

THESE DE DOCTORAT DE

L'UNIVERSITE DE NANTES

ECOLE DOCTORALE N° 596

Matière, Molécules, Matériaux

Spécialité : « Sciences des Matériaux »

Par

Maria Mitronika

Dépôt de couches minces de TiO_2 – SiO_2 par association plasma et sol-gel : impact du procédé de dépôt et de la composition sur les propriétés, application à l'optique intégrée

Thèse présentée et soutenue à « Nantes », le 08/09 /2020

Unité de recherche : Jean Rouxel Institut des Matériaux (IMN), UMR 6502

Rapporteurs avant soutenance :

Christelle Dublanche-Tixier	Professeur des universités, IRCER-UMR CNRS 7315 Université de Limoges
Khaled Hassouni	Professeur des universités, LSPM UPR CNRS 3407 Université Paris XIII, Villetaneuse

Composition du Jury :

Président :	Richard Clergereaux	Directeur de recherche, LAPLACE, CNRS
Examineurs :	Christelle Dublanche-Tixier	Professeur des universités, IRCER, Université de Limoges
	Khaled Hassouni	Professeur des universités, LSPM, Université Paris XIII
	Luc Stafford	Professeur des universités, Dép. de physique, Université de Montréal
	Agnés Granier	Directeur de recherche, IMN, CNRS

Dir. de thèse : Mireille Richard-Plouet
Co-dir. de thèse : Antoine Goullet

Directeur de recherche, IMN, CNRS
Professeur des universités, IMN, Université de Nantes

THESE DE DOCTORAT DE

L'UNIVERSITE DE NANTES

ECOLE DOCTORALE N° 596

Matière, Molécules, Matériaux

Spécialité : « Sciences des Matériaux »

Par

Maria Mitronika

Deposition of TiO₂ – SiO₂ thin films by associating plasma and sol-gel: impact of the deposition process and the composition on the properties, application to integrated optics

Thèse présentée et soutenue à « Nantes », le 08/09 /2020

Unité de recherche : Jean Rouxel Institut des Matériaux (IMN), UMR 6502

Rapporteurs avant soutenance :

Christelle Dublanche-Tixier	Professeur des universités, IRCER-UMR CNRS 7315 Université de Limoges
Khaled Hassouni	Professeur des universités, LSPM UPR CNRS 3407 Université Paris XIII, Villetaneuse

Composition du Jury :

Président :	Richard Clergereaux	Directeur de recherche, LAPLACE, CNRS
Examineurs :	Christelle Dublanche-Tixier	Professeur des universités, IRCER, Université de Limoges
	Khaled Hassouni	Professeur des universités, LSPM, Université Paris XIII
	Luc Stafford	Professeur des universités, Dép. de physique, Université de Montréal
	Agnés Granier	Directeur de recherche, IMN, CNRS
Dir. de thèse :	Mireille Richard-Plouet	Directeur de recherche, IMN, CNRS
Co-dir. de thèse :	Antoine Goullet	Professeur des universités, IMN, Université de Nantes

Wisdom begins in wonder...
Socrates

Acknowledgements

The present work was carried out in Jean Rouxel Institute of Materials (IMN) and more specifically in the Plasmas and Thin films group. First of all, I would like to tremendously thank my thesis supervisor Mireille RICHARD-PLOUET who allowed me to carry out this thesis in the best conditions and who was able to pass me over her knowledge, her academic and professional skills as well as his precious advices. I would like also to thank her for supporting me in all the ideas I had regarding the experimental system and encouraging me to attend several workshops and conferences. Nonetheless, I would like to thank my co-supervisor Antoine GOULLET for our numerous exchanges especially for Ellipsometry and his advices regarding the pedagogical skills needed when supervising a student. It really helped me evolve as a future potential teacher. A big thank you also to Agnès for replying to all my questions regarding Plasma and allowing me to adjust the specific plasma reactor to meet the requirements of our novel hybrid system. You have all been very supporting and caring to me, helped be improve scientifically, academically and personally. Thank you! I will also always bear in mind that meeting Friday afternoon, are never a good idea!!! 😊

I would like to thank the reporters and members of my jury, Christelle DUBLANCHE-TIXIER and Khaled HASSOUNI for devoting their precious time in creating the reports for my PhD manuscript. Moreover, I would like also to thank Richard CLERGERAUX, and Luc STAFFORD for being members of my jury. Finally, I would like to thank you all for being so interested in my work and having such an interesting and prosperous discussion the day of my presentation.

During these three years, I met and collaborated with several interesting people. Through the GDRi Nanomatériaux Multifonctionnels Contrôlés Network, which is based on a French Canadian collaboration, I was able to have short-term missions in the Physics Department of University of Montreal. There, I met and collaborated extensively with Jacopo PROFILI and Luc STAFORD. I would like to thank them for the exchanges, the beautiful papers we had together and the interaction we had in general. It was a pleasure to meet you. Apart from the short missions in Canada, under the SEEDS framework I had a fruitful collaborate with the LAPLACE laboratory, with which we were able to have a shared project. Therefore, I would like to thank Christina VILLENEUVE-FAURE and Marie-Paule BESLAND (from IMN) for this interesting collaboration.

Moreover, I would like thank the members of PCM team and especially Aurélie GIRARD for being my “Blast” partner. I would like to thank her for making my days more fun and interesting, exchanging several opinion about work and personally. Her office was always open for me (and all the PCM team), even when it should not! I

would like to also thank her for allowing me to teach microelectronics to her students in University of Nantes having almost 12 hours per year. In addition, from the PCM members, I would like to thank Christophe CARDINAUD, Pierre-Yves TESSIER, Ahmed RHALLABI, Maryline LE GRANVALET and Valérie BRIEN for the scientific discussions and PCM pic-nics.

I would like to thank enormously Franck PETITGAS for his help on the deposition reactor, for its reactivity, efficiency and his willingness to modify part of the reactor for the elaboration of the novel hybrid system. Even if we did not speak the same language, I believe we had an excellent collaboration. (Je remercie énormément Franck PETITGAS pour son aide sur le réacteur de dépôt, pour sa réactivité, son efficacité et sa volonté de modifier une partie du réacteur pour l'élaboration du nouveau système hybride. Même si nous ne parlions pas la même langue, je pense que nous avons eu une excellente collaboration.)

I would like to thank the CMC team, Nicolas STEPHANT at the SEM and Nicolas GAUTIER at the TEM, for their trust, their invaluable help as well as their wise advice the discussions about Greece and where it is in the map, the mythology and especially for the coffee breaks (analogue mode with an actual ring bell!). I also thank Bernard HUMBERT, Maxime BAYLE and Jean Yves MEVELLEC for their help on Raman diffusion, Vincent FERNANDEZ and Jonathan HAMON for the XPS, Benoit ANGLERAUD for the AFM, Françoise LARI for manipulations in the chemistry room. In addition, I would like to thank Cédric DOUTRIAUX for helping me with all the cool staff such as the 3D model of the reactor using designing tools and having some small project with students at the FabLab. Finally, I would like to thank Laurent GOURNEDE for all the help with the IT.

I would also like to thank Guylaine NICOLAS for her help and discussions in Greek(Ευχαριστώ) and in particular for the logistics part and all administrative services: Catherine ROCHAS, Richard BASCHERA and Françoise VIGOUROUX.

Leaving Greece to start my PhD in France was not always an easy decision. However, very shortly after my stay I started meeting wonderful people. IMN, its permanent staff, doctorates and post-docs helped a lot in that. Hence, I would like to thank my officemates Guillaume, Thibaut, Jordan, William and Joelle for sharing beautiful, fun and sometimes challenging moments. Guillaume thank you for all the jokes, even when the moments was not the right one, they really gave a different note to my days! Thibaut, thanks for the sport workout and for taking care my diet (always giving me quilts when I was eating chocolate :P). William, it was a pleasure working with you, making jokes sharing ideas and the reactor! Joelle, habibi, thank you for being close, understanding when my mood was off, being such a giving friend. I would like also to thank Lou and Feo, with whom, including William and Joelle we managed to create the IMN-Syra. I would like to thank my friends, Aurélie, Rezis and Maxime with whom I shared the funniest French-Chinese-Greek apero's even virtual ones sometimes due to COVID! I am going to miss these nights! In addition to this I would

like to thank Sandra and Angelica for being true friends from day one sharing beautiful moments in Nantes and in Barcelona. Hopefully in Greece as well. Raquel thank for being an awesome gym and lab buddy, for sharing the experience of the PhD together, all the thoughts, jokes and troubles. Yuman, I am really happy that I met you with Daniel, from day one, having all the multi-culti dinners at the beginning of my PhD (take care of Raquel, she is such a nice and true person). Manuela, my Italian friend, we only stayed for a short time together at the same city but it was long enough to establish a strong friendship. Thanks for all the skype calls. I would like to thank also Isabelle for being a cool friend and gym buddy and wish her all the best, as very shortly will be a mother. I would like to thank Adrien, Angelica, Emilie, Reine, Florent, Helène, Alix, Julien, Aurelie, Victor, Virgile and Thibault for our after work beer in Scène Michelet and all the events we had together.

Moreover, I would like to express my gratitude to my Greek “family” here in Nantes with whom this journey might have been not possible. First, I would like to thank Xenia, for introducing me, even before I arrive to Nantes, to this new environment and teaching me all the tricks. She has been such a good advisor, friend, colleague and role model sometimes. With her, I also met Matoula, a beautiful and smart person, which have been a great companion especially during COVID times. In addition, I would like to thank Angeliki for her support, funny moments, endless discussions and nights (with drinks of course). In addition, I would like to thank Theo, that arrived later in our life here in Nantes and made me always feel like a have an older brother, taking care of me. An important person during these three years has been Andriana, a loving, giving caring person, who has always been there discussing about the ups and downs of a PhD and life in general. The person through which I met Andriana was Bill. Bill (Vasilis) was my listener, endless coffees talking about memories, about the PhD, about science and life. Moving towards the end, I would like to thank my most recent friends, Timos, Giorgos and Alexandros, for our evenings all together, reminding my how cool it is to interact with engineers and more especially for our basketball events. Finally, I would like to thank Danai and Ntinios for their positive spirit!

I would like to specially thank Kyriakos, with whom I have experienced many stages of my journey before and during my PhD. I had endless talks, understanding and supporting each other. Very soon, he will be an excellent Doctor as well, with many prosperous things ahead of him.

I would like to thank my friends from Greece, Paulina, Nikos, Maria, Natalia, Yiota, Vicky, Eirini (Koumpara), Lena (Kyriakaina) and Ismini for not losing touch for discussing even for far away and for mentally supporting me.

Moving towards the end, I would like to thank my partner Christos, for being the greatest supporting system during these difficult times of writing the PhD and especially with COVID. Even from distanced we managed to preserve a healthy relationship and visit so many places around Europe. I still have to learn a lot about

stress and seeing things from a more positive perspective but I am sure that with him in my side it will be possible.

Finally, my greatest gratitude goes to my parents and my grandparents, who have let me grow to a person without fear, strong and independent. Mama and Mpampa thanks for letting me decide what I want to do even if it was far away from you. Now, if I would dedicate this PhD to someone that would be my brother, who has always been my younger/older brother, advising me and with who I have made endless discussion. I am sure he will have an excellent future.

General Table of Contents

Résumé en français	13
General Introduction	23
Chapter 1 Nanocomposite thin films and associated processes	27
1.1 Dielectric constant and optical index	29
1.2 Thin Dielectric Films and their applications	30
1.2.1 Dielectric Thin Films for Optics.....	31
1.2.1.1 Waveguides	31
1.2.1.2 Antireflective Coatings	33
1.2.2 Dielectric Thin Films for Microelectronics	34
1.2.2.1 Gate Dielectrics for active devices	34
1.2.2.2 Capacitor Dielectrics for passive devices.....	36
1.2.3 Configurations coupling two materials for achieving desirable characteristics.....	38
1.2.3.1 Multilayer TiO ₂ -SiO ₂ thin films	38
1.2.3.2 TiO ₂ -SiO ₂ mixed oxide films (Ti _x Si _{1-x} O ₂)	39
1.3 Interest of Nanocomposites	41
1.3.1 General definitions and trends	41
1.3.2 Focusing on the TiO ₂ NPs and the SiO ₂ matrix.....	43
1.4 Processes for the creation of Nanocomposite thin films and Nanomaterials.....	47
1.4.1 Liquid Phase Processes.....	48
1.4.2 Gas-Phase Processes	49
1.4.3 Hybrid Approaches coupling liquid and gas phase processes.....	51
1.4.3.1 Atmospheric Pressure based systems.....	52
1.4.3.2 Low-pressure-based systems	54
1.4.3.3 Characteristics of the produced nanomaterials through the hybrid approaches.....	57
1.5 Aim and Experimental Strategy of the Thesis.....	67
Conclusion.....	69
Bibliography	70
Chapter 2 Experimental Systems and Characterization Techniques	79
2.1 Preparation of the TiO ₂ colloidal solution	81
2.2 Experimental Systems for thin film deposition and treatment	82
2.2.1 Spin Coating.....	82
2.2.2 Low Pressure Plasma Reactor.....	83
2.2.2.1 O ₂ Plasma Treatment system.....	84

2.2.2.2 Plasma Enhanced Chemical Vapor Deposition (PECVD).....	85
2.2.2.3 Hybrid system for the Nanocomposite thin film deposition	86
2.5 In situ Characterization Techniques.....	87
2.5.1 Ellipsometry	87
2.5.2 Optical Emission Spectroscopy (OES)	92
2.6 <i>Ex situ</i> Characterization Techniques.....	93
2.6.1 Scanning Electron Microscopy (SEM).....	93
2.6.2 Atomic Force Microscopy (AFM)	95
2.6.3 Transmission Electron Microscopy (TEM).....	96
2.6.4 X-Ray Photoelectron Spectroscopy (XPS).....	97
2.6.5 Raman Spectroscopy.....	99
Conclusion.....	99
Bibliography.....	101
Chapter 3 Modification of the optical properties and nano-crystallinity of anatase TiO₂ nanoparticles thin film using low-pressure O₂ plasma treatment.....	103
Introduction	105
3.1 Material and Methods	106
3.1.1 Spin-coating of TiO ₂ nanoparticles	106
3.1.2 Plasma Treatment of spin-coated TiO ₂ nanoparticles	106
3.2. Results.....	107
3.2.1 Kinetics driving the plasma-induced modification of nanostructured TiO ₂ thin films.....	107
3.2.2 Morphological and crystallinity analysis of the plasma-treated nanostructured TiO ₂ thin films	110
3.2.3 Chemical analysis of the plasma-treated nanostructured TiO ₂ thin films.....	112
3.3. Discussion.....	114
3.3.1 Explanation of the two kinetics.....	114
3.3.2 Computation of the NPs Temperature upon Plasma Treatment using Energy Balance equation.....	116
Conclusion.....	119
Bibliography.....	121
Chapter 4 Multi-Step approach for the elaboration of TiO₂-SiO₂ multilayer thin film by spin coating and PECVD.....	125
Introduction	127
4.1 Materials and Methods.....	127
4.1.1 Deposition of the Nanoparticles.....	128
4.1.2 Implementation of the Bilayer and the Multilayer	128
4.2 Results.....	129

4.2.1 TEM characterization of the elaborated bilayer and multilayer.....	129
4.2.2 Investigation of the topographical characteristics of each layer.....	132
4.2.3 Evaluation of each layer's physical and optical characteristics through Ellipsometry.....	134
4.2.4 Comparison of the multi-step approach multilayer thin film with pure PECVD one.....	138
4.4 Discussion	145
4.4.1 Impact of the SiO ₂ infiltration and conformal behavior on the amorphous- crystalline interphase	145
4.4.2 Evaluation of the multilayer optical response based on the two implementation approaches	146
Conclusion.....	147
Bibliography.....	148
Chapter 5 Direct Liquid Injection of TiO₂ Nanoparticles colloidal solution in low pressure O₂ Plasma Reactor	151
Introduction	153
5.1 Material and Methods	154
5.2 Analysis of the Process - From the Atomization of the colloidal solution to the Deposition of the TiO ₂ NPs.....	154
5.2.1 Spraying/Atomization – Droplet Formation.....	154
5.2.1.1 The Injection System.....	154
5.2.1.2 Mean droplet size through Phase Doppler Anemometry (PDA).....	155
5.2.1.3 Mass rate of the injected solvent.....	157
5.2.2 Transport – Evaporation of Solvent	157
5.2.2.1 Travel time of droplets inside the heating pipe	157
5.2.2.2 Evaporation of liquid droplets inside a low-pressure environment.....	159
5.2.3 Droplet Interactions with Plasma – Estimation of the droplet temperature .	162
5.3 Deposition of the TiO ₂ NPs inside the O ₂ ICP plasma reactor: a first approach.....	171
5.3.1 Importance of the heating wire temperature on the deposited TiO ₂ thin films.....	172
5.3.2 Impact of the liquid injection parameters on the deposited TiO ₂ thin films and the low-pressure system	174
5.3.4 Plasma Characterization during Injection of the TiO ₂ Colloidal Solution inside the O ₂ ICP Reactor	176
5.4 Optimization Strategy – Improvement on the deposition of the TiO ₂ NPs	179
5.4.1 Dilution with more volatile solvents (Water, Ethanol and Methanol).....	180
5.4.2 Effect of system Geometry and the Temperature	182
5.4.3 Iterative Mode of Operation.....	183
5.5 Chemical Investigation of the optimized films through XPS and Raman	189

5.6 Characterization of the optimized films using Ellipsometry	191
5.6.1 <i>In situ</i> monitoring of the TiO ₂ NPs thin film growth	192
5.6.2 Optical and physical characteristics of the optimized films Ellipsometric Model	195
5.7 Discussion	199
5.7.1 Comparison between the deposited pristine and optimized TiO ₂ NPs thin films	199
5.7.2 Iterative Process	201
5.7.3 From the theoretical to the experimental point of view	202
Conclusion.....	203
Bibliography.....	205
Chapter 6 Novel one-step approach for the creation of TiO₂-SiO₂ NCs through PECVD and Sol Gel	209
Introduction	211
6.1 Materials and Methods.....	212
6.1.1 TiO ₂ NPs colloidal solution.....	212
6.1.2 Deposition of TiO ₂ -SiO ₂ NCs thin films through the hybrid approach	213
6.2 Elaboration of the PECVD made SiO ₂ matrix.....	214
6.2.1 Deposition conditions of the SiO ₂ matrix without any injection	214
6.2.2 Investigation of the SiO ₂ matrix characteristics during the creation of the NCs	217
6.2.3 Plasma behavior during the creation of the NCs	221
6.3 TiO ₂ -SiO ₂ NCs thin films through the hybrid approach.....	225
6.3.1 Structural characterization of the TiO ₂ -SiO ₂ NCs and TiO ₂ crystallinity.....	225
6.3.2 Morphological analysis of the TiO ₂ -SiO ₂ NC surface.....	227
6.3.3 Plasma characteristics during the TiO ₂ -SiO ₂ NC deposition.....	229
6.4 Chemical analysis of the NCs in various injection parameters using XPS.....	231
6.5 Characterization of the NCs using Ellipsometry	233
6.5.1 <i>In situ</i> monitoring of the NCs' growth.....	233
6.5.2 Optical and physical characteristics using Bruggeman Effective Medium Approximation (BEMA) Model.....	236
6.5.3 Following the growth and composition of a deposited layer within a one-minute sequence	239
6.6 Discussion	242
6.6.1 Estimation of the amount of NPs distribution in the matrix through the characterization techniques.....	242
6.6.2 Comparison with other studies	243
6.6.3 The outcome of this hybrid approach.....	244
Conclusion.....	245

Bibliography.....	247
General Conclusion & Perspectives.....	251

Résumé en français

Les matériaux diélectriques et les couches minces diélectriques ont fait l'objet d'études approfondies pour leur intérêt et leur utilisation dans de nombreuses applications industrielles, en particulier en microélectronique et en optique. Pour répondre à la demande constante de dispositifs technologiques plus efficaces, plus rentables et plus petits, ces matériaux, qui peuvent être facilement intégrés dans des dispositifs et des technologies à base de semi-conducteurs, ont été combinés dans différentes configurations telles que les oxydes mixtes et les couches minces multicouches. Dans ce contexte, les nanocomposites (NC) et les matériaux nanostructurés ont fait l'objet d'une grande attention, en raison de la gamme croissante de nouvelles propriétés qui sont découvertes. Comme ces matériaux composites présentent des interfaces plus développées par rapport aux constituants d'origine, le rapport surface/volume est un facteur clé pour contrôler leurs propriétés. Une motivation supplémentaire provient du fait que les propriétés physiques des matériaux sont également contrôlées par des phénomènes dont les dimensions critiques correspondent à l'échelle nanométrique. Cependant, l'un des principaux enjeux est de développer des procédés adaptés au dépôt de films NC minces, homogènes et polyvalents, qui puissent répondre aux exigences des applications. Par conséquent, un procédé donnant la liberté de régler le facteur de remplissage ainsi que de choisir la nature des nanoparticules (NP) et de contrôler séparément le dépôt de la matrice est d'un grand intérêt. Les techniques de dépôt permettant l'élaboration de nanocomposites impliquent généralement que les précurseurs réagissent en phase liquide ou en phase gazeuse. Récemment, afin de mettre au point un procédé polyvalent et sûr, certains travaux ont tenté de coupler les procédés mentionnés ci-dessus. Cette stratégie est décrite ici comme une approche hybride. La plupart de ces quelques travaux impliquent l'utilisation d'un système de plasma à pression atmosphérique et très rarement d'une plage de pression inférieure (100-500 mTorr). Aucun procédé à base de plasma n'a encore été mis au point qui pourrait conduire à des films NC homogènes mono-dispersés. En outre, la vitesse de dépôt mesurée ou estimée pour ces approches hybrides (supérieure à 1 nm. s⁻¹) est trop élevée pour répondre aux spécifications de la conception de films ultra-minces. Enfin, la plupart des études sont confrontées à une forte limitation concernant la quantité de NP qui peut être dispersée dans la matrice.

Dans cette thèse, nous visons à développer un nouveau type de procédé hybride couplant l'injection d'une solution colloïdale de TiO₂-NPs fabriquée au laboratoire avec un procédé plasma à très basse pression (3 mTorr), pour la création de films minces nanocomposites TiO₂-SiO₂ de composition homogène contrôlée.

Ces matériaux sont conçus pour former une gamme de matériaux accordables présentant des propriétés intéressantes pour les applications optiques (large gamme

d'indices optiques et transparence dans le domaine du visible et de l'IR) ainsi que pour les applications électriques (large gamme de permittivité).

En raison du manque de travaux expérimentaux et théoriques, cette étude entend répondre à certains points clés cruciaux. Ceux-ci concernent le maintien du plasma et son efficacité dissociative pendant l'injection de liquide (comme le solvant est injecté, une variation de pression est généralement observée) et les mécanismes qui régissent les interactions entre les gouttelettes en cours d'évaporation et le plasma. De plus, en ce qui concerne les NPs de TiO_2 , il s'agit de savoir si elles seront affectées par le plasma réactif spécifique (O_2). Une des clés est d'évaluer la capacité de cette approche à régler indépendamment les caractéristiques des NCs grâce à ses multiples paramètres. L'autre est d'évaluer comment ce nouveau procédé hybride peut limiter l'agrégation des nanoparticules et permettre le dépôt de couches très fines homogènes et accordables. L'objectif ultime serait de trouver les conditions de dépôt permettant d'obtenir des films nanocomposites riches en TiO_2 aux propriétés intéressantes et contrôlables.

Afin d'étudier ces points clés et de parvenir à la création de NC diélectriques TiO_2 - SiO_2 de la manière la plus efficace possible, cette thèse est divisée en six chapitres.

Sur la base du contexte mentionné ci-dessus, une étude bibliographique est fournie au **chapitre 1**. Dans un premier temps, l'importance des couches minces diélectriques et leurs principales applications sont analysées. En outre, les configurations de base couplant les matériaux TiO_2 et SiO_2 pour obtenir les caractéristiques souhaitées sont indiquées. Dans ce chapitre, l'accent est mis sur les processus menant à la création de nanocomposites en distinguant les processus impliquant la phase gazeuse, la phase liquide et l'approche hybride.

Dans le **chapitre 2**, la synthèse de TiO_2 NPs en laboratoire et les systèmes expérimentaux pour la production de couches minces de TiO_2 NPs ou les nanocomposites TiO_2 - SiO_2 sont expliqués. Différentes stratégies, notamment le procédé d'enduction centrifuge et les techniques de dépôt chimique en phase vapeur assisté par plasma (PECVD), sont analysées. Enfin, les principes de base des techniques de caractérisation utilisées pour évaluer les nanocomposites et étudier l'état chimique du plasma pendant l'injection de liquide sont présentés dans ce chapitre.

Dans le **chapitre 3**, la première étape de notre stratégie expérimentale a été réalisée. Dans ce chapitre, l'impact du plasma O_2 à couplage inductif (ICP) sur les NP TiO_2 est étudié. Pour ce faire, la solution colloïdale contenant les TiO_2 NP a été déposée par centrifugation sur un substrat de silice et a été traitée au plasma avec la source de plasma spécifique. En utilisant l'ellipsométrie, les modifications de la structure des NPs ont été suivies in situ. Les modifications induites ont également été vérifiées à l'aide de diverses autres techniques de caractérisation telles que le Raman et la

microscopie à force atomique (AFM). Pour tenter d'expliquer les résultats de cette étape expérimentale, nous avons proposé un modèle décrivant une seule NP sur le substrat à l'intérieur du volume de plasma. En utilisant ce modèle et l'équation du plasma d'énergie, nous avons identifié le flux de chaleur prédominant qui provoque l'élévation de la température des NP.

Dans le **chapitre 4**, la deuxième étape de la stratégie expérimentale a été réalisée. Ici, les NP TiO_2 déposées par induction centrifuge ont été exposées à un plasma O_2/HMDSO (technique PECVD) pour déposer une couche de silice. Cette étude visait à comprendre les interactions des NP TiO_2 avec la matrice SiO_2 en utilisant ces méthodes conventionnelles et à évaluer la possibilité de créer des structures multicouches en utilisant cette approche en plusieurs étapes. Les caractéristiques chimiques et physiques de ces échantillons multicouches de $\text{TiO}_2/\text{SiO}_2$ ont été évaluées et les caractéristiques optiques de chaque couche ont été définies. Enfin, une comparaison des caractéristiques de cette approche en plusieurs étapes couplant l'induction centrifuge et la PECVD a été effectuée avec un procédé entièrement PECVD.

Dans le **chapitre 5**, les principes fondamentaux de la production et de l'évaporation des gouttelettes sont analysés. En se basant sur la littérature, l'analyse théorique du plasma brumeux (plasma contenant des gouttelettes de liquide) est tentée et un modèle pour expliquer les interactions entre le plasma et la gouttelette de liquide est proposé. Sur la base des premiers résultats sur l'injection directe de la solution colloïdale liquide de NPs de TiO_2 dans le plasma O_2 à basse pression (3 mTorr) et des résultats théoriques, une stratégie d'optimisation des films homogènes déposés de TiO_2 est exposée avec les résultats obtenus.

Enfin, puisque les conditions optimisées pour l'injection des NPs de TiO_2 ont été identifiées, au **chapitre 6**, l'injection simultanée des NPs de TiO_2 et de la vapeur HMDSO à l'intérieur du plasma O_2 à basse pression a été établie. Avant de déposer les premiers NCs $\text{TiO}_2\text{-SiO}_2$, la matrice elle-même a été étudiée avec la seule injection de solvant (pas de NPs), afin d'évaluer sa qualité dans les conditions d'injection. Les NCs $\text{TiO}_2\text{-SiO}_2$ produits ont été caractérisés à l'aide de différentes techniques. La possibilité de régler leurs caractéristiques optiques (par l'approche, en ajustant le facteur de remplissage) a été évaluée par ellipsométrie.

Chapitre 1: Couches minces nanocomposites et procédés associés

Les matériaux diélectriques ont été utilisés dans une grande variété d'applications, notamment en microélectronique et en optique. La demande constante de dispositifs technologiques plus efficaces, plus rentables et plus petits a poussé la recherche à trouver des matériaux ou des procédés alternatifs qui combinent les matériaux existants. Un bref aperçu des tentatives d'utilisation du TiO_2 et du SiO_2 pour l'élaboration d'oxydes mixtes et de multicouches a été donné. Par ailleurs, plusieurs études récentes ont porté sur la mise en œuvre et la compréhension

des couches minces nanocomposites (NC), car elles peuvent être de bons candidats pour la demande susmentionnée. Il a été démontré que le TiO₂ à l'échelle nanométrique peut avoir des propriétés améliorées par rapport au matériau de base. Par conséquent, un processus donnant la liberté de régler le facteur de remplissage ainsi que de choisir la nature des NP est d'un grand intérêt. Ce chapitre est donc consacré à la connaissance des caractéristiques qu'un matériau diélectrique peut avoir, mais surtout aux approches qui peuvent permettre l'élaboration de nanocomposites diélectriques. Trois grandes catégories ont été décrites, à savoir les approches en phase liquide, en phase gazeuse et hybride. Une étude comparative de ces approches hybrides émergentes a permis de mettre en évidence l'intérêt de ces travaux et de soulever des questions clés auxquelles il faut répondre.

Chapitre 2: Systèmes expérimentaux et techniques de caractérisation

Pour l'élaboration des étapes expérimentales proposées au chapitre 1, plusieurs systèmes expérimentaux ont été utilisés. Dans toutes les expériences, des NPs de TiO₂ dispersés dans un solvant organique, et formant ainsi une solution colloïdale, ont été utilisés, et ses étapes de préparation sont analysées dans ce chapitre. Dans le chapitre 3, pour l'étude des interactions plasma-NP, un réacteur à plasma inductif O₂ à basse pression a été utilisé (ICP) sur des films de TiO₂ NP revêtus par centrifugation. Dans le chapitre 4, la possibilité d'acquérir des films multicouches fonctionnels en utilisant une combinaison de techniques de revêtement par centrifugation et de dépôt par plasma amélioré (PECVD) a été étudiée. Le plasma ICP O₂ et le PECVD élaboré dans le réacteur spécifique ont tous deux fait l'objet d'un examen approfondi dans le passé. Une brève description de ces deux techniques est donc donnée. Enfin, en vue de la mise en œuvre de l'approche hybride en une étape consistant à introduire directement les gouttelettes de liquide à l'intérieur du plasma basse pression O₂/HMDSO, une nouvelle configuration du système a été mise en place. C'est pourquoi, dans ce chapitre, tous les systèmes expérimentaux sont analysés. En outre, pour évaluer les caractéristiques physico-chimiques et optiques des films produits, plusieurs techniques de caractérisation ont été utilisées, qui sont expliquées dans ce chapitre.

Chapitre 3: Modification des propriétés optiques et de la nanocristallinité des nanoparticules d'anatase TiO₂ en couche mince par traitement plasma O₂ à basse pression

Dans ce chapitre, la première étape de la stratégie expérimentale est étudiée. Des couches minces de nanoparticules de TiO₂ d'une épaisseur de 50 nm et une nanostructure coeur-coquille ont été préparées par la technique d'enduction centrifuge et ont été traitées à l'aide d'un plasma d'O₂ à couplage inductif à basse pression. Bien qu'aucune évolution significative n'ait été observée pendant le pompage, deux cinétiques peuvent être identifiées pendant le traitement plasma en

utilisant l'ellipsométrie spectroscopique in situ. Pour des temps de traitement par plasma très courts, l'élimination des fractions organiques à base de solvant entourant les nanoparticules de TiO_2 produit une densification des films de TiO_2 inorganiques. Un tel effet de minéralisation par le traitement au plasma d' O_2 a été confirmé par XPS. Pour des échelles de temps plus importantes, la taille moyenne des NP de TiO_2 augmente et des changements significatifs des propriétés optiques se produisent. Alors qu'aucun changement significatif de la nanostructure du film n'a été observé par microscopie électronique à balayage, une augmentation de la taille des cristallites et une augmentation de l'agglomération des nanoparticules de TiO_2 ont été confirmées par la microscopie électronique à transmission et la microscopie à force atomique, respectivement. Les mécanismes impliqués dans cette modification induite par le plasma des couches minces de TiO_2 nanostructurées sont examinés en fonction des flux d'énergie des espèces générées par le plasma.

Chapitre 4: Approche en plusieurs étapes pour l'élaboration d'un film mince multicouche de TiO_2 - SiO_2 par revêtement par centrifugation et PECVD

Dans ce chapitre, la deuxième étape de la stratégie expérimentale est étudiée. Un film multicouche de TiO_2 - SiO_2 d'une épaisseur totale de 200 nm a été préparé en utilisant une approche en plusieurs étapes, couplant la technique d'enduction centrifuge et le procédé de dépôt chimique en phase vapeur assisté par plasma (PECVD). Les NP TiO_2 étudiés au chapitre 2 ont été utilisés pour les couches de TiO_2 déposées par enduction centrifuge et la vapeur HMDSO pour l'élaboration des couches de SiO_2 réalisées par PECVD. Alors que la microscopie électronique à transmission (MET) a démontré la structure multicouche claire sans couches mixtes dans la région d'interface (entre les couches), l'analyse par spectroscopie de rayons X à dispersion d'énergie (EDX) a révélé un degré d'infiltration du SiO_2 le long de celui du TiO_2 , se situant à environ 30%. La conformité des couches de SiO_2 a été identifiée grâce à la microscopie à force atomique (AFM), qui permet des balayages nanostructurés et une rugosité accrue (par rapport au SiO_2 déposé sur un substrat lisse). La réponse optique de ces couches a été caractérisée par l'ellipsométrie et il a été constaté que le SiO_2 agit comme un facteur de "guérison" concernant l'indice de réfraction. Enfin, les résultats obtenus ont été comparés et discutés avec des structures multicouches PECVD pures en termes de caractéristiques structurales et de réponse optique.

Chapitre 5: Injection liquide directe de solutions colloïdales de nanoparticules de TiO_2 dans un réacteur plasma d' O_2 à basse pression

Dans ce chapitre, la nouvelle approche utilisant le système d'injection directe de liquide (DLI) et le système de plasma d' O_2 à basse pression est présentée. Les principes de base, depuis la formation des gouttelettes jusqu'au dépôt des NP, sont étudiés. En utilisant un modèle théorique des interactions gouttelettes-plasma, la

durée de vie des gouttelettes en cours d'évaporation a été calculée et sa valeur a été trouvée dépendante de plusieurs facteurs, tels que la volatilité du solvant, la géométrie du système, les caractéristiques des espèces du plasma et la température entourant les gouttelettes. Dans une telle étude, il est crucial de comprendre comment ces facteurs peuvent provoquer des variations anormales de la pression, des hétérogénéités sur le film et une accumulation d'espèces issus du solvant dans le réacteur. Sur la base des résultats théoriques et des résultats expérimentaux préliminaires, nous avons pu optimiser le processus de dépôt de couches minces de TiO₂ NPs. Il a été contrôlé par ellipsométrie in situ, tandis que la spectroscopie d'émission optique (OES) a permis de mieux comprendre le processus d'oxydation du solvant organique par le plasma d'O₂. La structure du film a été étudiée à l'aide de la microscopie électronique à balayage (MEB), de la microscopie à force atomique (AFM) et de la spectroscopie Raman et son analyse chimique par XPS.

Chapitre 6: Nouvelle approche en une étape pour la création de NC TiO₂-SiO₂ par PECVD et Sol Gel

Des nanoparticules de TiO₂ (NP), d'une taille de 3 nm, ont été injectées à l'intérieur d'un réacteur plasma O₂/hexaméthylsiloxane à basse pression à l'aide d'un injecteur de liquide et suivant une séquence d'injection itérative. La condition initiale du plasma a été choisie parmi les expériences PECVD précédentes afin d'obtenir une matrice de SiO₂ dense de haute qualité et de produire finalement des couches minces de nanocomposites TiO₂-SiO₂ (NC). Cependant, pour vérifier la qualité du SiO₂ pendant le traitement de l'injection, une première série d'expériences a été réalisée. En fait, l'étude de l'élaboration de la matrice de SiO₂ en injectant uniquement le solvant sans les NP TiO₂ a révélé une bonne qualité de matrice, car il s'est avéré qu'elle présentait des propriétés optiques similaires à celles de la silice thermique, telle qu'elle est extraite de l'étude par ellipsométrie. La spectroscopie d'émission optique (OES) dans ces conditions a révélé l'impact de l'injection de liquide sur la chimie du plasma, indiquant que le plasma O₂ peut retrouver son équilibre après quelques secondes. En outre, sur la base des indications positives concernant la matrice SiO₂ et des conclusions du chapitre 5, les paramètres de l'injection de liquide et des précurseurs de vapeur ont été établis dans le but de relever les principaux défis observés lors de la création de NC. La microscopie électronique à transmission (TEM) a indiqué une bonne distribution et la non-agglomération des NP. La fraction des NP de TiO₂ à l'intérieur de la matrice de SiO₂ a été évaluée. Des résultats cohérents entre la microscopie électronique à balayage (MEB) et l'ellipsométrie ont été obtenus, avec un pourcentage volumique de 15% et 19%, respectivement pour le cas N=10. La spectroscopie de photoélectrons (XPS) a donné un pourcentage légèrement inférieur, 12 %, ce qui peut s'expliquer par la limitation de la mesure (en profondeur). Néanmoins, en faisant varier le paramètre d'injection, la composition de la surface peut être contrôlée. L'utilisation de données d'ellipsométrie in situ a permis de mettre en évidence le mode alterné de cette

approche, en identifiant en temps réel deux cinétiques différentes selon les phases d'injection de TiO₂ NPs dans SiO₂ ou non. Enfin, en utilisant l'ellipsométrie et le modèle approprié, la capacité de ce procédé à régler la composition des NC et la réponse optique en ajustant les paramètres d'injection a été prouvée.

En raison des nombreuses propriétés que peuvent avoir les nanocomposites (NC), un grand intérêt a été porté à leurs procédés de préparation. Deux d'entre eux sont les catégories principales et bien établies se déroulant en phase liquide et en phase gazeuse. La volonté de disposer d'un processus polyvalent et sûr a conduit à la tentative très récente de créer des approches hybrides couplant les phases gazeuse et liquide. Sur cette base, l'objectif de ce travail était la création de couches minces nanocomposites de TiO₂-SiO₂ par une approche hybride couplant les NPs synthétisés chimiquement au laboratoire, avec le procédé plasma. C'était la première fois que l'on tentait de le faire à une pression aussi basse (3 mTorr) en utilisant une source de plasma d'O₂ par couplage inductif (ICP), par rapport à la littérature. Grâce aux résultats théoriques et expérimentaux, des questions importantes ont été répondues. Nos travaux ont été séparés en quatre étapes expérimentales utilisant initialement des méthodes conventionnelles pour déposer les NP TiO₂ et la matrice SiO₂, afin d'évaluer toute modification des NP lors du traitement du plasma dans le plasma uniquement O₂ et dans le plasma O₂/hexamethydisiloxane. Les deux étapes suivantes ont ensuite été consacrées à la mise en œuvre de la nouvelle méthode hybride, dans laquelle les solutions colloïdales fabriquées en laboratoire ont été directement injectées dans deux plasmas à basse pression.

Comme ce travail est la première approche de notre groupe dans cette direction, de nombreuses perspectives peuvent être proposées. Elles sont regroupées ci-dessous en trois grandes catégories, à savoir la compréhension des mécanismes des interactions à l'intérieur du plasma, le processus et les nanocomposites produits.

Interactions

Il est très important de mieux comprendre les interactions qui se produisent au cours de ce processus, car cela peut fournir des informations utiles sur l'état du plasma, des nanoparticules et de la matrice. Il peut s'agir : a) des interactions entre les nanoparticules (dans la gouttelette), b) des interactions entre les particules et les espèces du plasma pendant leur transport vers le substrat et c) de l'interaction du plasma avec les nanoparticules et la matrice pendant le dépôt d) de l'interaction avec la surface du substrat et du film NC en croissance. Enfin, il est important d'étudier la réponse chimique et électrique (impédance du plasma) du plasma due à ces interactions. En particulier, en solution, les NPs présentent une charge positive à leur surface qui empêche les NPs de se déposer en maintenant des interactions répulsives entre elles. La stabilité de la solution colloïdale est un critère obligatoire pour son injection, mais des études supplémentaires sont nécessaires afin de comprendre comment la charge des NP à l'intérieur d'une gouttelette évolue (i) lors de

l'évaporation du solvant dans le réacteur, (ii) lors de l'interaction avec le plasma et en particulier avec la gaine et les espèces chargées jusqu'à (iii) la vaporisation totale de la solution avant de réagir avec le substrat ou le film de croissance.

Processus

Dans ce travail, l'optimisation du processus d'acquisition d'une distribution homogène des NP a constitué une partie importante de notre étude. Elle a permis d'améliorer considérablement nos dépôts. Comme il y a encore des possibilités d'amélioration, certaines modifications peuvent être proposées. Parmi celles-ci, le solvant de la solution colloïdale devrait être ajusté pour diminuer la durée de vie des gouttelettes, et la température dans laquelle ce processus se déroule devrait être augmentée (substrat chauffé et parois chauffées) pour aider le taux d'évaporation. La gestion de l'évaporation du solvant juste avant que la gouttelette n'atteigne la surface serait en fait la situation idéale. Il faut donc trouver un compromis entre la protection offerte aux NPs TiO_2 par le solvant peu volatil et son évaporation afin de limiter l'effet goutte de café auquel nous sommes encore confrontés. En outre, parvenir à réduire la taille des gouttelettes pourrait également constituer une amélioration. Ainsi, un système de réduction de la différence de pression (force motrice du système d'injection) entre le liquide et le réacteur pourrait être proposé, afin d'obtenir une vitesse et une taille moyenne plus faibles dans la gouttelette produite, ce qui donnerait aux gouttelettes plus de temps pour s'évaporer. Enfin, l'orifice de l'injecteur pourrait être ajusté afin de fournir moins de gouttelettes de liquide à chaque injection. Jusqu'à présent, l'injection de HMDSO était maintenue en mode continu, mais le contrôle de ses impulsions pendant le temps mort de l'injection de la solution pouvait également offrir de nouvelles possibilités et plus de degrés de liberté.

Nanocomposites

Nous avons déclaré que cette approche vise à créer un processus polyvalent dans lequel la nature des PN et de la matrice pourrait varier. Ici, il a été montré que grâce aux paramètres d'injection, le facteur de remplissage des NPs de TiO_2 peut être modifié. La modélisation par ellipsométrie spectroscopique a permis d'établir une corrélation linéaire entre l'indice de réfraction optique de la NC et sa fraction TiO_2 , indiquant le caractère agile du processus. Étant donné que la taille de la charge peut induire différentes caractéristiques sur les propriétés de la NC, les expériences utilisant différentes tailles de NPs pourraient être proposées. Enfin, la modification de la nature des NP et de la matrice devrait être tentée, afin de prouver la polyvalence du système.

Ces premiers travaux ouvrent tout un champ de recherche et de perspectives d'avenir concernant la possibilité de mettre en place des couches minces nanocomposites avec des propriétés diélectriques et optiques accordables. En effet, puisque l'injection des NP et le dépôt de la matrice peuvent être gérés dans le temps,

séparément, la production de couches minces avec des spécifications spécifiques devrait être rendue accessible, permettant une meilleure compréhension des mécanismes impliqués dans ce processus hybride couplant l'injection de solutions synthétisées au laboratoire et le dépôt chimique en phase vapeur assisté par plasma.

General Introduction

Dielectric materials and dielectric thin films have been extensively studied for their interest and use in many industrial applications, with a great emphasis in microelectronics and optics. To follow the on-going demand for more efficient, cost effective and smaller technological devices, these materials, which can be easily integrated in semiconductor devices and technologies, have been combined in different configurations such as mixed oxides and multilayered thin films. In this context, nanocomposites (NCs) and nanostructured materials have gained great attention, due to the expanding range of novel properties that are being discovered. As these composite materials exhibit enhanced interfaces, compared to the original constituents, the surface-area-to-volume ratio is a key factor for controlling their properties. Additional motivation originates from the fact that the physical properties of materials are also controlled by phenomena whose critical dimensions correspond to the nanoscale. However, one of the main issues is to develop processes suited for depositing thin homogeneous and versatile NC films which can fulfill the application requirements. Hence, a process giving the freedom to tune the filling factor as well as to choose the nature of the nanoparticles (NPs) and control separately the matrix deposition is of great interest. The deposition techniques allowing the elaboration of nanocomposites generally involve the precursors to react in the liquid phase or in the gas phase. Recently, in order to develop a versatile and safe-by-design process some works have attempted to couple the two above mentioned processes. Here, such strategy is described as hybrid approach. Most of these few works involve the use of an atmospheric pressure plasma system and only a few in lower pressure range (100-500 mTorr). Still no plasma-based process developed could lead to homogenous NC films, retaining the initial mono dispersity in size of the NPs. In addition, most of the studies are facing a strong limitation regarding the amount of NPs that could be dispersed in the matrix. Finally, the deposition rate measured or estimated for these hybrid approaches ($>1 \text{ nm} \cdot \text{s}^{-1}$) is too high to fulfill the specification of ultra-thin film design.

In this study, we aim to develop a novel type of hybrid process coupling the injection of a lab-made TiO_2 NPs colloidal solution with a very low-pressure (3 mTorr) plasma process, for the creation of controlled composition and homogenous TiO_2 - SiO_2 NCs. These materials are designed to form a range of tunable materials with interesting properties for optical applications (wide range of optical indexes and transparency in the visible and IR domain) together with electrical applications (broad range of permittivity).

Due to the lack of experimental and theoretical works, this study intends to reply to some crucial key points. The first one would be regarding the plasma efficiency to dissociate the molecules of the solvent and/or of the matrix precursor,

as upon injection of solution a variation of pressure is generally observed, possibly leading to a modification of the plasma species. Two other key points are concerning the mechanisms driving the interactions between the evaporating droplets and the plasma, and regarding the possibility of the TiO₂ NPs found inside these droplets to be affected by the specific reactive plasma (O₂). One supplementary key point is to evaluate the ability of this approach to tune independently the NCs characteristics through its multiple parameters. Another key point is to assess how this new hybrid process can limit the nanoparticles aggregation and allow the deposition of homogenous, tunable and very thin films. Finally, the ultimate objective would be to find deposition conditions leading to TiO₂ rich NC films with novel and interesting properties.

In order to investigate these key points and achieve the creation of TiO₂-SiO₂ dielectric NCs in the most efficient manner, this thesis is separated in six chapters.

Based on the above-mentioned context, in **Chapter 1**, a bibliographic study is provided. Initially, the importance of the dielectric thin films and their prominent applications are analyzed. In addition, the basic configurations coupling the TiO₂ and SiO₂ materials for achieving desirable characteristics are indicated. In this chapter, a great emphasis is given on the processes leading to the creation of the nanocomposites, discriminating the processes involving the gas-phase, the liquid-phase and the hybrid approach.

In **Chapter 2**, the synthesis of the lab-made TiO₂ NPs and the experimental systems for the production of TiO₂ NPs thin films or the TiO₂-SiO₂ nanocomposites are explained. Different strategies including, the spin coating process and the plasma enhanced chemical vapor deposition (PECVD) techniques are analyzed. The innovative approach of coupling the liquid injection with the low-pressure plasma system is described. Finally, the basic principles of the characterization techniques used to evaluate the nanocomposites and investigate the chemical state of the plasma during the liquid injection are given in this chapter.

In **Chapter 3**, the first step of our experimental strategy was realized. The impact of the O₂ Inductively Coupled Plasma (ICP) on the TiO₂ NPs is investigated. To achieve that, the colloidal solution with the TiO₂ NPs was spin coated on silica substrate and it was plasma treated with the specific plasma source. Using ellipsometry the modifications on the NPs structuration were monitored in situ. The induced modifications were also verified with various other characterization techniques such as Raman and Atomic Force Microscopy (AFM). In an attempt to explain the results of this experimental step, we proposed a model describing a single NP on the substrate inside the plasma volume. Using this model and the steady state between input and output energy fluxes, we identified the predominant heat flux causing the elevation of the NPs temperature.

In **Chapter 4**, the second step of the experimental strategy was achieved. Here, the spin coated TiO₂ NPs were exposed in the O₂/HMDSO plasma (PECVD technique). This study, aimed in understanding the interactions of the TiO₂ NPs with the SiO₂ matrix using these conventional methods and assess the possibility to create multilayer structures using this multistep approach. The chemical and physical characteristics of this TiO₂/SiO₂ multilayer samples were evaluated and the optical characteristics of each layer were defined. Finally, a comparison of the characteristics of this multistep approach coupling spin coating and PECVD were compared with a fully PECVD process.

In **Chapter 5**, the fundamentals of the droplet production and evaporation are analyzed. Based on literature, the theoretical analysis of the specific misty plasma (plasma containing liquid droplets) is attempted and a model to explain the interactions between the plasma and the liquid droplet is proposed. Based on the first results on direct injection of the liquid colloidal solution of TiO₂ NPs inside the low pressure (3 mTorr) O₂ plasma and the theoretical findings, an optimization strategy, for acquiring homogenous TiO₂ deposited films, is proposed along with the obtained results.

Finally, since the optimized conditions for the injection of the TiO₂ NPs were identified, in **Chapter 6**, the simultaneous injection of the TiO₂ NPs and the HMDSO vapor inside the low-pressure O₂ plasma was established. Before depositing the first TiO₂-SiO₂ NCs, the matrix itself under only solvent injection (no NPs) was studied, to assess its quality under the injection conditions. The produced TiO₂-SiO₂ NCs were characterized with various techniques. The possibility to tune their optical characteristics (through the approach, adjusting the filling factor) were evaluated using Ellipsometry.

Chapter 1

Nanocomposite thin films and associated processes

Dielectric materials have been used in a wide variety of applications, with an emphasis in microelectronics and optics. The on-going demand for more efficient, cost effective and smaller technological devices has urged research to find alternative materials or processes that combine the existing ones. A quick overview on the attempts using TiO_2 and SiO_2 for the elaboration of mixed oxides and multilayers was given. Apart from that, lately, several studies have focused on the implementation and understanding of nanocomposite (NC) thin films, as they can be good candidates for the above-mentioned demand. It has been shown that the nanoscale TiO_2 can have enhanced properties compared to the bulk material. Hence, a process giving the freedom to tune the filling factor as well as chose the nature of the NPs is of great interest. Therefore, this chapter is dedicated in getting acquainted with the characteristics that a dielectric material can have but more in importantly with the approaches that can allow the elaboration of dielectric nanocomposites. Three main categories were described, namely the liquid phase, the gas phase and the hybrid approaches. From a comparative study of these upcoming hybrid approaches, the interest of this work was further highlighted and key questions to be answered arose.

Table of Contents

1.1 Dielectric constant and optical index	29
1.2 Thin Dielectric Films and their applications	30
1.2.1 Dielectric Thin Films for Optics.....	31
1.2.1.1 Waveguides	31
1.2.1.2 Antireflective Coatings	33
1.2.2 Dielectric Thin Films for Microelectronics	34
1.2.2.1 Gate Dielectrics for active devices	34
1.2.2.2 Capacitor Dielectrics for passive devices.....	36
1.2.3 Configurations coupling two materials for achieving desirable characteristics.....	38
1.2.3.1 Multilayer TiO ₂ -SiO ₂ thin films.....	38
1.2.3.2 TiO ₂ -SiO ₂ mixed oxide films (Ti _x Si _{1-x} O ₂)	39
1.3 Interest of Nanocomposites	41
1.3.1 General definitions and trends	41
1.3.2 Focusing on the TiO ₂ NPs and the SiO ₂ matrix.....	43
1.4 Processes for the creation of Nanocomposite thin films and Nanomaterials.....	47
1.4.1 Liquid Phase Processes.....	48
1.4.2 Gas-Phase Processes	49
1.4.3 Hybrid Approaches coupling liquid and gas phase processes.....	51
1.4.3.1 Atmospheric Pressure based systems	52
1.4.3.2 Low-pressure-based systems	54
1.4.3.3 Characteristics of the produced nanomaterials through the hybrid approaches	57
1.5 Aim and Experimental Strategy of the Thesis.....	67
Conclusion.....	69
Bibliography.....	70

1.1 Dielectric constant and optical index

In 1834, Michael Faraday (1791-1867) appealed for William Whewell (1794-1866) for advice and suggestions when he found it impossible to expound his electrochemical researches in the existing vocabulary.[1] William Whewell was one of the most brilliant men in Cambridge starting initially as mathematician. Due to his versatile mind, he focused in addition in physics, philosophy, history of science and linguistics (mainly Greek and Latin). His interaction with Faraday led to the exchange of 156 letters in total and to the genesis of several terms such as *anode*, *cathode*, *anion*, *cation* etc. In 1836, the term **dielectric** was born. [2] The actual term originates from two words, with the first being *dia* (δία) and the second being *electric*. On the one hand, *dia* originates from Greek and it means “through” something. On the other hand, *electric* has origins that are more complex. It is a word first given by the “father of electricity and magnetism” William Gilbert (1544-1603) in 1600. The term is based on the Greek word of the amber stone, ἤλεκτρον (word which originates from the word ἠλέκτωρ meaning bright, luminous). This specific term was used as it was found that when this stone is rubbed, it becomes electrostatic. On this basis, what is the deeper meaning that Whewell wanted to describe, using the combination of these two words? Based on the etymologies above, he wanted to describe a material through which, electric field can be developed. More specifically, on an electric field, electric charges do not flow through the material, as in the case of conductor, but shift slightly from the equilibrium, creating the dielectric polarization. [3] All dielectric materials are insulating materials. The difference between a dielectric and an insulator lies in their applications. Hence, if the main function of non-conducting material is to provide electrical insulation, then they are called as insulator. On the other hand, if the main function of non-conducting material is to store electrical charges then they are called as dielectrics. The ability of the dielectric material to polarize and hold charge is called dielectric permittivity and is denoted with $\epsilon_r(\omega)$, where ω is the angular frequency ($\omega = 2\pi f$) of the applied source. When on this material a DC source is applied, the resulting dielectric constant is static. In contrary, when the applied field is an AC then this material dielectric characteristic is generally a complex value noted as

$$\epsilon_r = \epsilon_r' - j\epsilon_r'' \quad (\text{Equation 1.1})$$

The ϵ_r' term is the real part of the complex constant representing relative permittivity used to calculate the capacitance and therefore the ability of the dielectric to store energy. The ϵ_r'' term is the imaginary part representing the energy loss due to the dipole orientation to the applied field. As the applied AC field can have different frequencies, the polarization mechanisms are different leading to a variation of the complex dielectric ‘constant’. Therefore, the frequency dependence of the real and imaginary parts of the complex constant are given in Figure 1.1. In addition to this, in the same figure the type of polarization mechanism is given in accordance to the applied frequency.

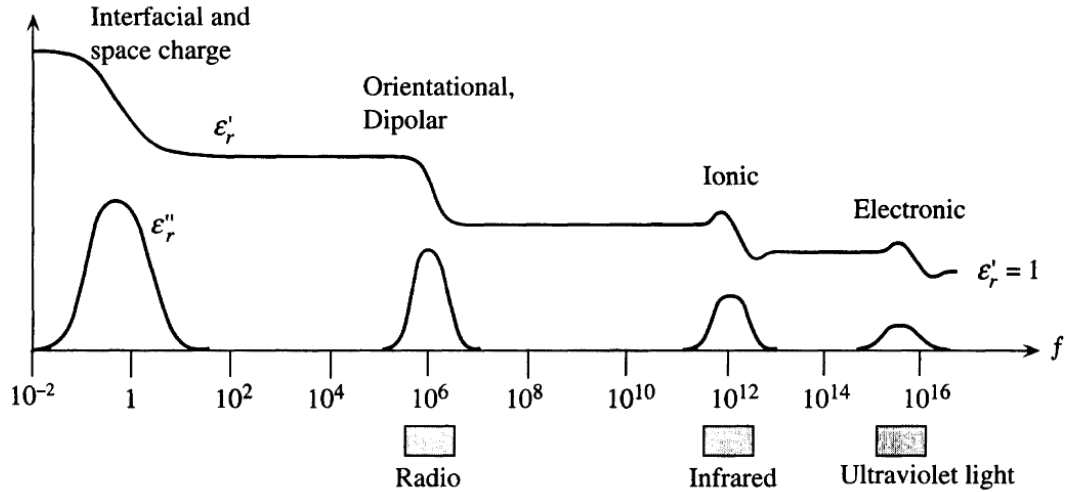


Figure 1.1: The frequency dependence of the real and imaginary parts of the dielectric constant in the presence of interfacial, orientational, ionic and electronic polarization mechanisms. [4]

When light propagates in a dielectric medium, it polarizes the molecules of the medium according to the specific frequency of the wave. The refractive index n of an optical or dielectric medium, is the ratio of the velocity of light (c) in vacuum to its velocity (v) in the medium. Hence, this is calculated with the following equation, $n = c/v$. Using this and Maxwell's equations, for non-magnetic medium, the $n = \sqrt{\epsilon_r}$ equation can be obtained, which is very useful for relating the dielectric properties of a material to its optical properties at any particular frequency of interest. However, we know that during the polarization of the molecules of the medium, losses occur and the complex dielectric constant of Equation 1.1 is used. In addition to this, as the electromagnetic wave (light) travels in the medium, it is attenuated due to absorption. Thus, the refractive index is also expressed by a complex refractive index as:

$$N = n - ik = \sqrt{\epsilon'_r - j\epsilon''_r} \quad (\text{Equation 1.2})$$

With n being the real part and k the imaginary (also call extinction coefficient).

1.2 Thin Dielectric Films and their applications

A thin film can be defined as a material in a geometric configuration in which two dimensions are macroscopic but the third one is microscopic. The typical thickness that a film can have in order to be considered thin can vary from 10 nm to 1 μm . In addition to this, depending on the targeted application, the exact size is adjusted. Dielectric thin films have been widely studied for the optics and electronics fields, aimed in this thesis.

In the field of optics, the refractive index n (as explained in Section 1.1) of the film is one of the main parameters for the evaluation of its optical response. In the

field of electronics, the term relative permittivity, or dielectric constant, is being used, to describe the electric polarizability of a dielectric. It is expressed as a ratio between the absolute to the vacuum permittivity. The term high- κ dielectric refers to a material with a higher dielectric constant, as compared to silicon dioxide ($\kappa > 3.9$). Some characteristics of high- κ materials along with their optical and electrical characteristics are given in Table 1.1. In detail, in the first column the material name is given whereas in the second and third one, the dielectric constant and refractive index at 633 nm wavelength are provided, accordingly. Finally, on the fourth column the energy band gap (E_g) of these materials are given and on the last column their typical breakdown strength for an applied field.

Based on these, in the next Sections 1.2.1 and 1.2.2, some prominent applications will be analyzed.

Table 1.1: Characteristics of typical high- κ dielectrics. [5–8]

Material	Dielectric constant (κ)	Refractive Index (n) @ 633 nm	Band gap E_g (eV)	Breakdown Strength (MV/cm)
SiO ₂	3.9	1.45	8.9-9	10
Al ₂ O ₃	9	1.76	6.7-8.7	7
HfO ₂	22	2.10	5.5-6.0	4
Ta ₂ O ₅	26	2.20	4.6	4.2
TiO ₂	80	2.20 - 2.50	3.05-3.3	2.7

1.2.1 Dielectric Thin Films for Optics

In this sub-Section, focus will be given on applications using the optical properties of dielectric thin films, such as the waveguides and the antireflective coatings.

1.2.1.1 Waveguides

An optical waveguide is a physical structure that guides electromagnetic waves in the optical spectrum (range from 10 nm to 1000 μ m, or frequencies in the range from 300 GHz to 3000 THz). Common types of optical waveguides include optical fibers and transparent dielectric waveguides made of plastic and glass (amorphous silica). The structures of optical waveguides are fundamentally similar to the optical fibers with the difference that the waveguides do not have circular symmetry.

The basic design of a waveguide device involves the incorporation of a film with high refractive index as the core layer and a low refractive index layer as the cladding layer. Based on this geometry, high light intensity confinement per unit power is achieved within the waveguide.[9] When referring to glass waveguides, typical values of the refractive index are 1.455 for the cladding and 1.470 for the core.

This small difference is important for long-haul communication because the optical loss at the interface is small.[10]

Optical waveguides deposited on a stable and thin substrate, which is typically made of low refractive index and glassy materials (such as SiO_2), can be classified in two types regarding their geometrical design, namely slab waveguides and channel waveguides (Figure 1.2). Slab waveguides are structures with a planar geometry, which guide light in only one transverse direction, as lateral modes become effectively infinite. Despite the relatively easy fabrication, another benefit of the slab waveguide is the absence of scattering between the transverse and lateral modes. Contrary to the slab waveguides, channel waveguides act as a conduit for the light in both transverse directions with a two dimensional optical confinement.[11]



Figure 1.2: Two different kinds of waveguides. Planar waveguides guide light only in the vertical direction, whereas channel waveguides guide in two dimensions.

The development of nanoscale optical waveguides with low losses has led to miniature, efficient photonic devices for applications in the fields of communications, computing, metrology, and sensing.[12] Since the minimum length scale, on which a beam of light can operate is equal to half its wavelength waveguides ($\lambda/2n$, λ :wavelength, n : refractive index of the core), a high refractive index contrast between core and cladding layers are highly required for further miniaturization. TiO_2 has a high refractive index ($n \approx 2.54$) at 633 nm wavelength, which allows for high-refractive-index-contrast waveguides and strong light confinement. Due to its large bandgap ($E_g = 3.2$ eV), TiO_2 is transparent over a broad wavelength range that includes the visible and near-infrared. An example is given in Figure 1.3, from Bradley et al. [12] work were both amorphous and anatase TiO_2 waveguides were attempted. In both cases, the refractive index was found similar in the studied wavelengths (633 - 1550 nm) and as expected differences were measured on the propagation losses. Amorphous TiO_2 had losses between 0.12 to 0.04 dB/mm whereas anatase between 2 to 0.42 at the same wavelengths. This occurred because the crystalline nature of the anatase TiO_2 can cause scattering of light.

In the past, several works involved the elaboration of waveguides using higher refractive indices materials or the mixture of existing ones (such as $\text{TiO}_2\text{-SiO}_2$) in order to tailor the optical response and structural morphology of the film (avoid grains or columns and thus scattering of light). An interesting comparison is given in Dayu Li's Thesis[13].

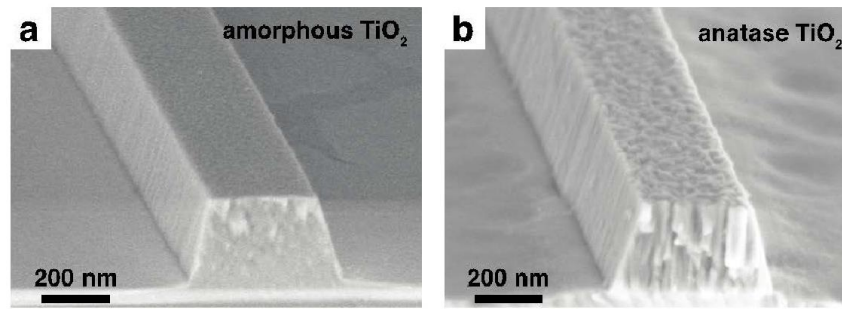


Figure 1.3: SEM images of 0.3- μm -wide (a) amorphous and (b) polycrystalline anatase TiO_2 waveguides fabricated on oxidized silicon wafers using e-beam lithography and reactive ion etching. [12]

1.2.1.2 Antireflective Coatings

Antireflective Coating or anti-reflection (AR) coating is a type of optical coating applied to the surface of lenses and other optical elements to reduce reflection. There are two main ways to induce antireflection. First, based on the coating topography, creating a porous surface to induce internal scattering of light and second based on the layer composition. Focusing on the latter, several configurations exist to induce anti-reflectance, such as one layer, bilayer, graded layer of multilayer films.[14]

AR coatings are designed so that the relative phase difference between the beam reflected at the upper and lower boundaries of a thin film is 180° . Destructive interference between the two reflected beams occurs, which cancels out both beams before they exit the surface (Figure 1.4). The optical thickness of the optical coating must be an odd integer multiple of $\lambda/4$, where λ is the targeted wavelength or wavelength being optimized for peak performance in order to achieve the desired path difference of $\lambda/2$ between the reflected beams. When achieved, this it will lead to the cancellation of the reflected beams intensity.

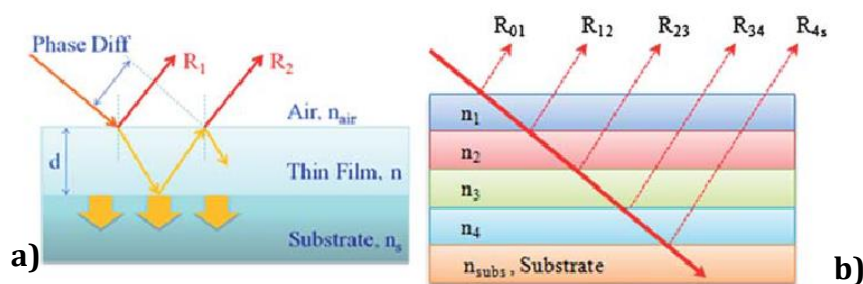


Figure 1.4: Propagation of light rays through (a) a single layer film on substrate ($n_s > n$) (b) multilayer film on substrate. [14]

For achieving a more broadband antireflectance, alternately varying high and low refractive index layers has been widely attempted. Hence, several works involve

dielectric materials such as TiO_2 and SiO_2 , as their refractive index ($n= 2.54$ for TiO_2 and $n=1.45$ for SiO_2 , at 633 nm) can serve this cause.[15]

1.2.2 Dielectric Thin Films for Microelectronics

Nowadays Internet of Things (IoT) and Industry 4.0 and in general the cutting-edge technological evolution has led to an on-going demand for faster, smaller and lower in consumption integrated systems. Since 1967, semiconductor industry and research have been measuring their technological evolution and performance based on the Moore's law. A remarkable example of this evolution is the case of the Metal–Oxide–Semiconductor Field-Effect Transistor (MOSFET) for which the technology node was at 10 μm whereas in 2020 is expected to reach the 5 nm. Based on this, Figure 1.5 shows how over the past five decades, Dynamic Random-Access Memories (DRAMs), flash memories, microprocessors, and graphics processors have tracked the curve Moore predicted.

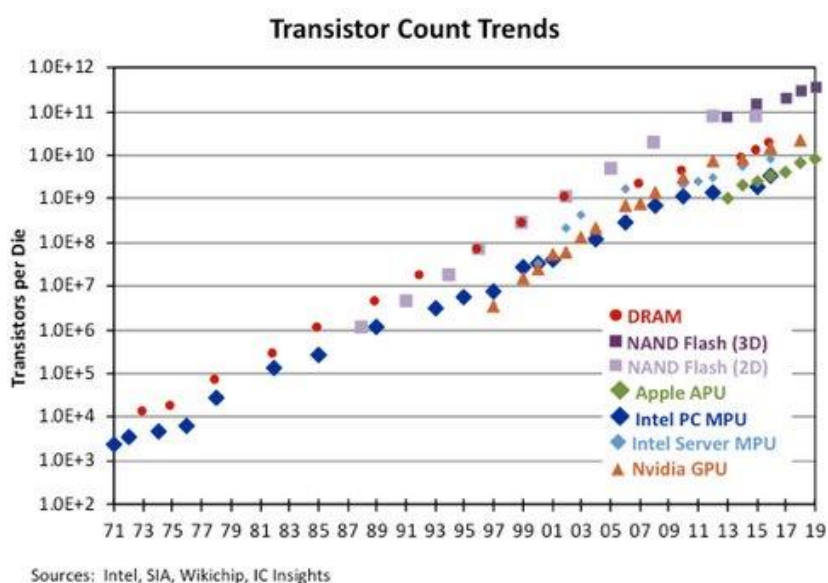


Figure 1.5: Transistors per Die of DRAMs, flash memories, microprocessors, and graphics processors from 1971 to 2019. A die, in the context of integrated circuits, is a small block of semiconducting material on which a given functional circuit is fabricated *Source:* <https://www.design-reuse.com/news/47652/transistor-count-trends.html>

Dielectric thin films play a crucial role in this technological evolution. Hence, in the next section, we will focus on two main applications, the gate dielectrics found in the active devices and the capacitor dielectrics found in the passive devices.

1.2.2.1 Gate Dielectrics for active devices

In this Section, as an active device the metal–oxide–semiconductor field-effect transistor (MOSFET) will be analysed. The schematic configuration of this device is

given in Figure 1.6. It works as a solid state switch when a voltage is applied across the source and the drain. In detail, as a voltage (positive for a NMOS and negative for a PMOS) is applied to the gate electrode, initially minority carriers are attracted to the surface of the Si channel and current can flow from the source to the drain. The current consequently depends on the gate capacitance and is expressed as:

$$I_{ds} = \frac{1}{2} \mu C \frac{W}{L} \left[(V_{GS} - V_t) V_{DS} - \frac{1}{2} V_{DS}^2 \right] \quad (\text{Equation 1.3})$$

$$C = \kappa \epsilon_o \frac{A}{t} \quad (\text{Equation 1.4})$$

where W is the width of the transistor channel, L is the channel length, μ is the channel carrier mobility (assumed to be constant in this analysis), and C is the capacitance with the gate dielectric when the underlying channel is in the inverted state. V_{GS} and V_{DS} are the voltages applied to the transistor gate and drain, respectively, and V_t is the threshold.

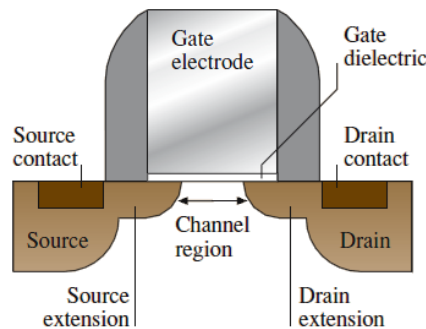


Figure 1.6: Schematic cross-sectional view of metal–oxide–semiconductor field-effect transistor (MOSFET), highlighting the important regions of such device. [5]

Silicon dioxide (SiO_2) has been almost exclusively used as the dielectric gate thin film material for semiconductor device fabrication and microelectronic applications. This is mainly because it is easy to prepare by various techniques and it has well-understood properties.[16] In addition, it has few electronic defects and forms a good interface with Si used as a substrate. It can also be etched and patterned to a nanometer scale. SiO_2 can exist both in crystalline and amorphous phase, with the non-crystalline and amorphous one being used as gate dielectric. For a thermally grown amorphous silica, its density is expected at 2.2 g cm^{-3} [5], and its electrical and optical characteristics are given in Table 1.1.

To follow the downscaling discussed (the Moore's law evolution), and fabricate more devices per wafer, several aspects of the devices are being constantly modified. Based on equation 1.4 by increasing the oxide capacitance on the gate, the drive current can be improved. Therefore, based on the oxide capacitance equation, the oxide thickness has been significantly decreased in order to increase the total gate capacitance. This has led the thickness to reach nanometric dimensions, reaching its dimensional limitation (near the atomic regime). As expected, physically thinning the

dielectric layer to the nanometer regime raises the prospect of tunneling effects through the dielectric, referred as leakage current.

To solve the problem of the leakage current induced by the decrease of the SiO₂ film thickness, researcher have focused their attention on a different term that can assist to the increase of the capacitance in equation 1.4. They would replace the thin SiO₂ film, with thicker and higher- κ dielectric. The physical thickness of a dielectric with higher κ value which would result in an equivalent capacitance can be written as: [5,16,17]

$$\frac{\kappa_{SiO_2}}{t_{SiO_2}} = \frac{\kappa_{high\ \kappa}}{t_{high\ \kappa}} \quad (\text{Equation 1.5})$$

Where $\kappa_{high\ \kappa}$ is the relative permittivity of a dielectric with higher value than the one of the SiO₂ and $t_{high\ \kappa}$ is the equivalent thickness as with the SiO₂ to achieve the same capacitance. An example of this strategy is shown in Figure 1.7.

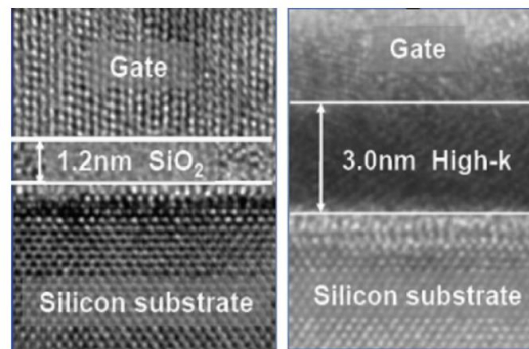


Figure 1.7: TEM image of Silica based gate stack vs. image of High- κ gate stack.[17]

1.2.2.2 Capacitor Dielectrics for passive devices

As defined in the Section 1.1, dielectrics are materials that are polarized with an applied field. This is translated in the dielectric constant representing the ability of the dielectrics to store charge. The equation of capacitance in Section 1.2.2.1 can explain this analogy. Hence, the role of dielectrics is important for the case of passive components such as capacitors and memories. In contrast to the metal-insulator-semiconductor MIS structure (or metal-oxide-semiconductor MOS) associated with transistors, in capacitors, the metal-insulator-metal (MIM) structure is more often found.

One of the widely used and known memory devices are the dynamic random-access memory (DRAM) in which capacitors play the crucial role for the storage of the information. More specifically, each bit of data is stored in a memory cell of a small capacitor and a transistor. The capacitor can be either charged or discharged, having therefore two states representing the 0 and 1. A schematic representation as illustrated by Kim et al.[18] is given in Figure 1.8a. Aiming to follow the scaling down evolution, DRAM's capacitor dimensions and configuration have been altered in the

past years. As seen in Figure 1.8b, the configuration of the capacitor has been involved from semiconductor-insulator-semiconductor (SIS) to metal-insulator-semiconductor (MIS), to finally reaching a metal-insulator-metal (MIM) configuration decreasing at the same time its dimension below 40 nm. Moreover, as observed, to maintain the same area (A) of the dielectric, and therefore the same capacitance (eq. 1.4), the height of the capacitor has been increased.

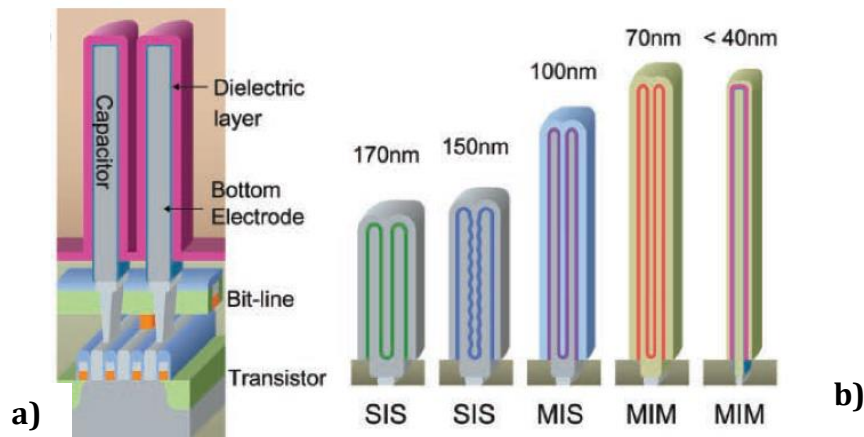


Figure 1.8: a) Schematic diagram of DRAM cells and b) a summary of the DRAM capacitor technology evolution. [18]

In microelectronics, the integrated circuits (ICs) comprise the front end of line (FEOL) where the active devices exist and the back end of line (BEOL) where mainly the integrated passive devices (IPDs) can be found. Following the same trend as with the storage cell of the DRAM, these capacitors should have the smallest possible thickness while preserving a high capacitance. These passive devices can be resistors, inductors or capacitors. Metal-insulator-metal (MIM) capacitors embedded in the backend inter-level dielectric layers as passive components are widely used in the integrated circuits. In this case, using the appropriate high- κ dielectric while preserving a high capacitance is of great importance. An example of a MIM capacitor using Al_2O_3 as a dielectric is given in Figure 1.9.

The issues that need to be addressed when using dielectric thin films for these passive devices are to maintain high capacitance densities, have low leakage current and maintain high electrical strength. At the same time being stable in temperature variations and insensitive to voltage variations is of great importance.

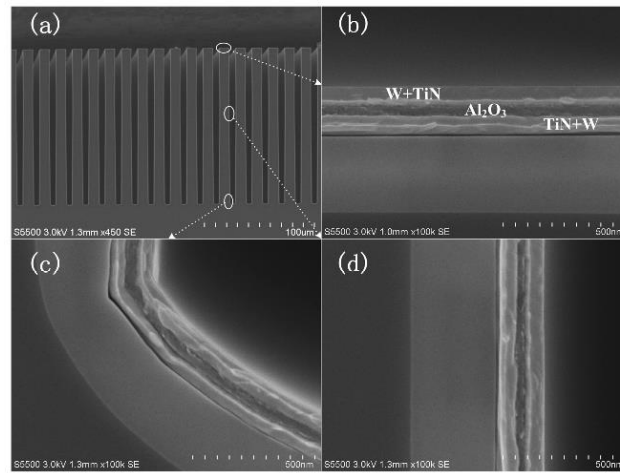


Figure 1.9: Cross-sectional SEM images of MIM capacitor A. (a) the overview images, (b) trench top, (c) trench bottom, (d) trench sidewall. [19]

1.2.3 Configurations coupling two materials for achieving desirable characteristics

In Section 1.1 different dielectric materials were introduced, and some examples of their utility in optic and electronic applications were analyzed in Section 1.2. In this study, the materials that we will focus on, are SiO_2 and TiO_2 . On the one hand, SiO_2 , is widely used in the semiconductor industry due to its low leakage current but associated to a low dielectric permittivity ($\kappa=3.9$), with a refractive index $n=1.46$ at 633 nm and an energy gap (E_g) of 8.5 eV.[20] On the other hand, TiO_2 is a highly investigated material exhibiting a high dielectric constant ($\kappa >50$) with the huge drawback of a high leakage current but associated to a higher refractive index of $n=2.45$ at 633 nm and an energy gap of 3.2 eV.[21] In an attempt to take advantage of the most desirable properties of these two materials, numerous works have been established from the scientific community, attempting their coupling in different configurations. Hence, in this Section we will indicate some works focusing on multilayer TiO_2 - SiO_2 structures and mixed oxide TiO_2 - SiO_2 (or $\text{Ti}_x\text{Si}_{1-x}\text{O}_2$) thin films.

1.2.3.1 Multilayer TiO_2 - SiO_2 thin films

Multilayer TiO_2 - SiO_2 thin films have been rigorously created in the past using sol-gel[22,23], ion beam sputtering[24,25], e-beam evaporation[26] or Atomic Layer Deposition (ALD)[27]. Over the last years, a great interest has been given in these multilayers due to their optical response.[24,25,28–32] Prominent application of these multilayer structures is the Antireflective coatings (AR) [14], as it is known that alternately varying high and low refractive index layers can enhance the antireflectance of the film. Towards this direction, Choi et al. [23] investigated the impact of the in-between SiO_2 layer characteristics on the near-infrared region reflectance of the total TiO_2 - SiO_2 multilayer thin film. In addition, Faustini et al. [33]

elaborated multilayer structures by sol-gel in a manner of acquiring not only anti-reflective properties but also hydrophobic and self-cleaning coating.

Nonetheless, studies have also been focusing in the dielectric response of these multilayer or stacked TiO₂-SiO₂ films and more specifically in the area of electronics using mainly vacuum processes. For instance, in an attempt to improve the tunneling effect caused by the SiO₂ layer, the time delays and the higher voltage needed when it is replaced by higher- κ materials, SiO₂/(TiO₂)_x (SiO₂)_{1-x} stacks were proposed by Oh et al.[27] for non-volatile memory applications. This approach is known as tunnel barrier engineering (TBE). Finally several works involved the introduction of a stack instead of a bulk film for the improvement of the capacitance in MIM and MOS configurations.[22,34,35]

1.2.3.2 TiO₂-SiO₂ mixed oxide films (Ti_xSi_{1-x}O₂)

TiO₂-SiO₂ mixed oxide films have been implemented through several approaches including wet processes[36,37] and more importantly gas phase deposition[38–48] ones. Several works annotate these films as Ti_xSi_{1-x}O₂ with the Ti atomic content calculated using the following formula $x = \frac{[Ti]}{[Ti]+[Si]}$ where [Ti] and [Si] are the atomic contents in titanium and silicon and the oxygen content can be calculated as, $y = \frac{[O]}{[Ti]+[Si]}$.

Focusing on the optical properties of the mixed oxide films, Larouche et al [39], studied the impact of the precursor ratio in a low pressure PECVD on the chemical and optical characteristics of the film, concluding that the resulting one-phase material can be good candidate for graded-index optical filters. Following this, Brassard et al. [43] investigated the impact of mixed oxide composition on the refractive index and the optical band gap. The results are given in Figure 10a. The linear evolution of the refractive index on the mixed oxide composition is clearly visible, varying from 1.46 for pure SiO₂ films to 2.45 for pure TiO₂ films. A noteworthy observation on this figure is the deduced optical energy gap of the film, which for the slightest amount of Ti, is shifted closer to the value of the TiO₂ film (4.2 eV for x=0.1). In the same manner, Li et al. [47] investigated the growth conditions, providing homogenous non columnar structures for optical applications. In the overall, the results attained followed a similar behavior concerning the linear dependency of the refractive index on the composition and the decreased optical gap. It was also shown in both works (using ellipsometry) that the film was possible to be modeled as a homogeneous film, using one dispersion law and without using an Effective Medium Approximation. This observation is an indirect proof regarding the prominent one phase character of these films at this macroscopic scale of observation. Finally, in an attempt to investigate the feasibility of TiO₂-SiO₂ mixed oxides avoiding vacuum systems, Gazal et al. [49] investigated the morphological and structural properties of these films made by atmospheric pressure PECVD.

Focusing in the dielectric properties of these mixed oxides, and aiming in acquiring high- κ materials while preserving a high breakdown strength, several works tested their compatibility, and investigated the films preparation parameters, in MIM and MOS configurations.[36,40–46,50,50] In the same work of Brassard et al. [43] as described in the previous paragraph, they investigated the variation of the dielectric constant measured at 1 MHz in regard to the film composition. As seen in Figure 10b, their dielectric constant is found to increase systematically as the Ti content increases. An increase of the value from 7 (for pure SiO_2) to 28 for $x=0.75$ and 42 for the pure TiO_2 is measured. In the inset of the figure, the dielectric constant and dissipation factor for the $x=0.75$ composition appears significantly stable for a range of frequency between 1 to 10 MHz revealing low dispersion of the dielectric constant together with very low dissipation factors. Finally, they conducted leakage current measurements. As expected, as the Ti content of the mixed oxide increased the electrical strength decreased accordingly. They concluded stating that, the strong variation of the leakage current and breakdown field of the mixed oxide films can be well correlated with the variation of their optical band gap (bandgap decreases significantly for the lowest amount of Ti). A reduction of the band gap definitely reduces the effective barrier against the injection of charges inside the dielectric and consequently leads to a deterioration of its insulating properties.

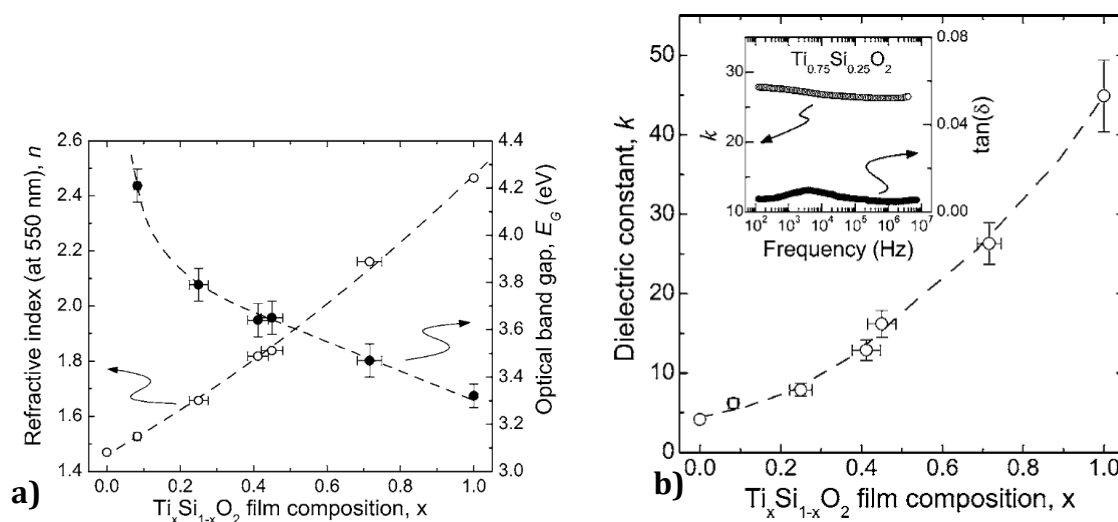


Figure 1.10: a) Refractive index (at 550 nm wavelength) and optical band gap variations with the composition of the co-sputtered $\text{Ti}_x\text{Si}_{1-x}\text{O}_2$ thin films. Dielectric constant of the co-sputtered thin films (measured at 1 MHz) as a function of their composition. The inset shows typical dielectric constant and dissipation factor vs frequency curves (in the case of $\text{Ti}_{0.75}\text{Si}_{0.25}\text{O}_2$ film).[43]

The identification of the mixed nature of these films is mostly elaborated using infrared (IR) absorption spectroscopy. The absorption around 950 cm^{-1} is attributed to the Ti–O–Si stretching vibrations indicating the mixed environment of the O atoms[39–46]. Some efforts using a statistical model have been attempted by Larouche et al.[39] to quantify the probabilities of the Si–O–Si, Si–O–Ti, and Ti–O–Ti

bonds occurrence in the film. Very recently, works conducted in the group supported by DFT calculations[48] quantified from XPS measurements the phase separation of amorphous thin $Ti_xSi_{1-x}O_2$ films prepared by PECVD. Hence, it was proven qualitatively and quantitatively that in mixed oxides like these, three components correspond to the local arrangement of TiO_2 , SiO_2 and main mixed environment of the O atoms, meaning that at the sub-nanometric scale, the films are not mixed oxides, at least at their very surface.

1.3 Interest of Nanocomposites

The tendency of both the scientific community and the industry to follow the Moore's law leading to smaller, faster integrated systems, as it has already been introduced in Section 1.2, has led researchers to search for new materials or processes that combine the existing ones. Nanocomposites and nanostructured materials have gained the attention, as the properties of the resulting composite are likely to differ from the original bulk ones. [51]

1.3.1 General definitions and trends

A more general term used for the nanocomposites or the nanoscale inclusions, is the term nanomaterials. Nanomaterial (NM) is defined as the "material with any external dimension in the nanoscale or having internal structure or surface structure in the nanoscale", with nanoscale defined as the "length range approximately from 1 nm to 100 nm". This includes both nano-objects, which are discrete pieces of material, and nanostructured materials, which have internal or surface structure on the nanoscale; a nanomaterial may be a member of both these categories (ISO/TS 80004-1:2015).

In 2000, Gleiter [52] made a classification based on the crystalline state and chemical composition of the nanomaterials. However, he did not consider their dimensions. In 2006, Pokropivny and Skorokhod [53] proposed a new scheme of the classification, for nanomaterials based on their geometrical shape, as they suggested that the later becomes a principal factor determining the properties of the nanomaterials. This classification is highly dependent on the electron movement along the dimensions in the NMs. In detail, as zero-dimensional nanomaterials (0D) can be considered as the materials with all external dimensions at the nanoscale (between 1 and 100 nm). This includes quantum dots, full spheres like anatase titanium dioxide. One-dimensional (1D) nanomaterials have two external dimensions at the nanoscale, the third one usually at the microscale. One-dimensional (1D) nanomaterials can be nanofibers, nanotubes, nanowires, and nanorods. Moreover, when only one external dimension at the nanoscale exists, 2D nanomaterials comprise thin films, nanocoatings, and nanoplates. The last dimensional category of nanomaterials, 3D nanomaterials, display internal nanoscale features but no external

dimension at the nanoscale. For example, coming back to Pokropivny and Slorokhod scheme, electrons in 0D NMs are entrapped in a dimensionless space whereas electrons in 1D NMs can move along the x-axis, which is less than 100 nm. Likewise, 2D and 3D NMs have electron movement along the x–y-axis, and x, y, z-axis respectively. Figure 1.11 provides this classification through SEM images of nanomaterials.

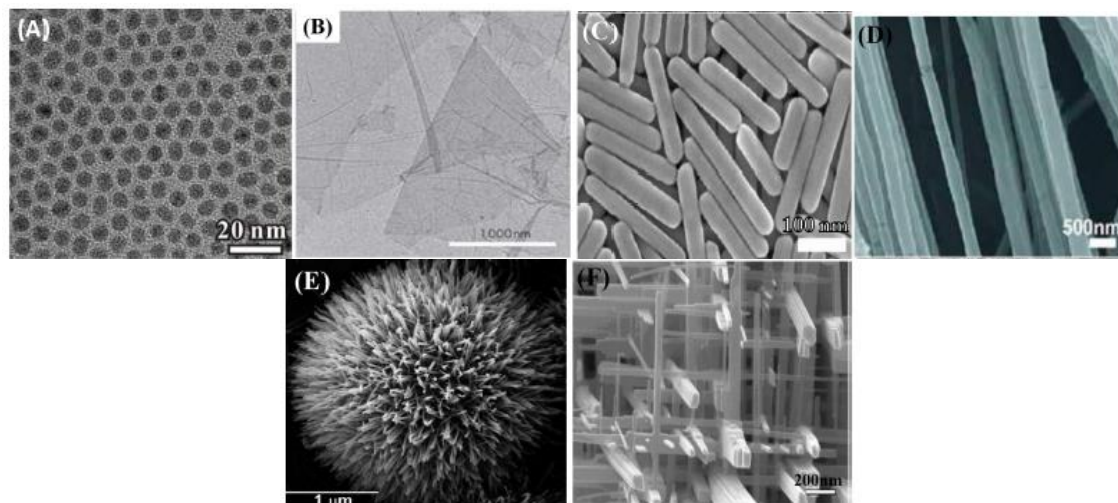


Figure 1.11: Nanomaterials with different morphologies: A) nonporous Pd NPs (0D), B) Graphene nanosheets (2D), C) Ag nanorods (1D), D) polyethylene oxide nanofibers (1D), E) urchin-like ZnO nanowires (3D) and F) WO₃ nanowire network (3D). [54]

3D NMs include nanocomposites and nanostructured materials.[55] Nanocomposites are solid materials that have multiple phase domains and at least one of these domains has a nanoscale structure. The surface-to-volume ratio due to the nanometric objects (up to 100 nm) is very high, and their behavior becomes controlled by surface properties, which are close to that of free atoms, rather than by volume properties. This can result in different properties than the bulk material. In addition to this, the interactions between the interfaces of the two phases become more important. Consequently, the materials can have novel chemical and physical properties that depend on the morphology and interfacial characteristics of the component materials. Since 1996, nanocomposites have been an emerging field providing in an exponential rate many scientific works, reaching in 2019 a total amount of 15.790 records. Their applications are rather broad with some of the most predominant ones being the packaging, insulations, antimicrobial, antireflective, self-cleaning, solar cells, sensors, and optics. [56–61]

Due to the versatile configuration these two phase materials can have some works focused in their theoretical study, using effective medium theories (EMT)[62,63], Volume Averaging Theory(VAT)[64]or the Lippmann-Schwinger equation[65]. Garahan et al. used the VAT model and finite elements to describe the boundary conditions of the nano-inclusion shapes, for the effective dielectric and

electrical properties and derived the effective index of refraction n_{eff} and absorption index k_{eff} of nanoporous materials. These results were used to predict the behavior of the optical properties of nanocomposite materials. It was found out that due to the presence of strongly absorbing dispersed phase such as metallic nanowires, the effective refractive index was much smaller than either of the two continuous or dispersed phases. Rao et al.[62], while comparing different EMTs for molecular NCs (TiO₂ NPs, polymer matrix) stressed out that the use of the effective medium can hold only when the two phases are chemically independent (no chemical binding between the neighboring constitutes). In addition, Lozovski et al. [65] indicated that the size of the filler, the thickness of the nanocomposite and the distance from the substrate can play a key role in the optical absorption of the NC.

The aim of these studies was to render it possible through this theoretical analysis to predict the properties of the final NCs, even if they were not implemented and characterized experimentally. In detail, it is proposed that knowing the tunable parameters that could affect the optical response (such as the filling factor, the nature of the NPs and matrix, the size and shape of the filler, the thickness of the NC, etc) can provide the guidelines for the design of the NCs oriented for the targeted applications. Also, the way (linear, parabolic etc) that the optical response is managed could additionally provide such guidelines.

1.3.2 Focusing on the TiO₂ NPs and the SiO₂ matrix

In this study, as nanoscale inclusions, 0D nanoparticles (NPs) will be used. In general, nanoparticles can be classified depending on their nature (for example, carbon-based, ceramic, metal, polymeric and semiconductor NPs[66]), size, morphology, physical and chemical characteristics, etc.

Among the different dielectric materials given in Section 1.1, TiO₂, as high- κ , stable and low cost semiconductor has been identified as an ideal candidate for its optical [67], dielectric[8-9] and photocatalytic[68] properties. Trying to expand these properties, TiO₂ NPs were extensively prepared in different configurations[69] and studied especially for cosmetic [70], antibacterial[71], solar cell[72–75], self-cleaning[76], hydrophobic [77] and dielectric-isolative[78] applications. It is known that when the diameter of the crystallite of a semiconductor particle falls below a critical radius of about 10 nm, each charge carrier appears to behave quantum mechanically. As a result of this quantum confinement, the band gap is enlarged (narrower valence and conduction bands as shown in Figure 1.12) and the band edges shift to larger redox potentials.[79,80]

Given the different properties that the nanoparticles can have compared to the bulk materials, some works focused on the influence that the diameter size can have on the band-gap. Enright et Fitzmaurice [81] predicted the size dependence for the energy of the valence and conduction bands, which is given in Figure 1.12b. Based on

this, for anatase nanocrystallites below 10 nm, a decrease in the band gap is observed. This decrease is more pronounced for nanocrystallite sizes below ~ 5 nm. Above the value of 10 nm, the band gap is expected to have similar behavior as the bulk material.

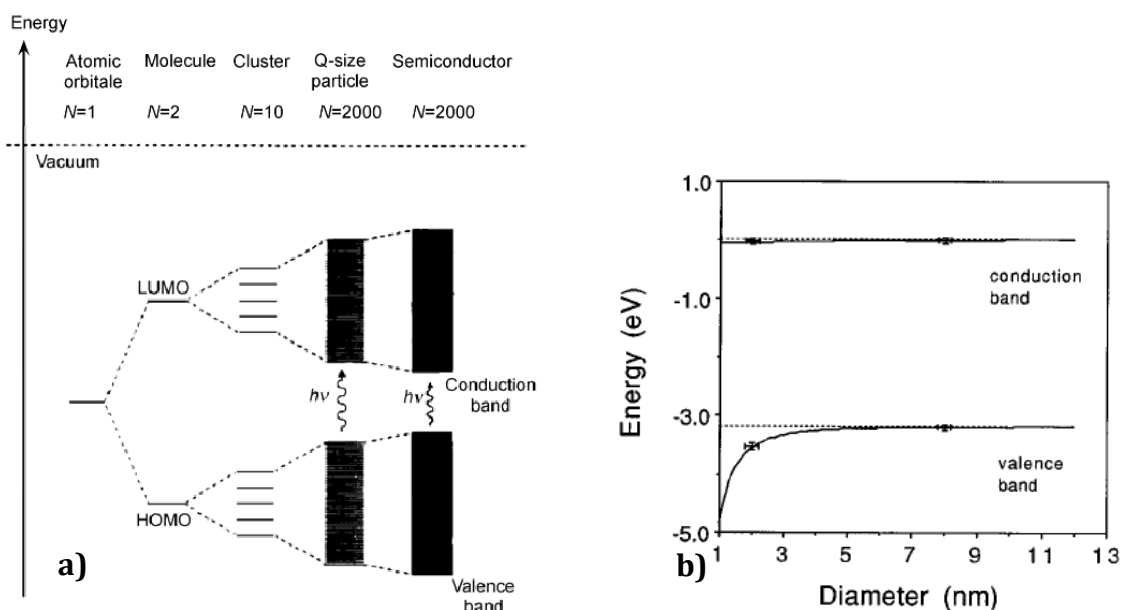


Figure 1.12: a) Molecular orbital (MO) model for particle growth of N monomeric units. The spacing of the energy levels (i.e., density of states) varies among systems. [79] On the right side of the images the bands of Q-size particles become narrower compared to the bulk semiconductor. b) Theoretical prediction of the E_g bandgap as a function of the particle radius. With bars, the experimentally determined changes in the energy of the valence and conduction band edges are plotted.[81]

A sensitive tool to follow the anatase nanocrystallite sizes is Raman spectroscopy. It is well-established experimentally that Raman spectra of low-dimensional crystals of semiconductors are modified in comparison to the corresponding bulk crystal spectra. More specifically, the Raman peaks are asymmetrically broadened and their positions are shifted [82,83]. An attempt to correlate the size of the TiO_2 crystallite with the Raman shift was carried out by Pighini et al.[84,85] collecting reports from other works shown in Figure 1.13. As observed in Figure 1.13a, the displacement of the E_g band is pronounced for lower diameters whereas for sizes above 10 nm is found very close to the reference one. In the same manner, in Figure 1.13b, the broadening of the band is more important in crystallite sizes below 5 nm.

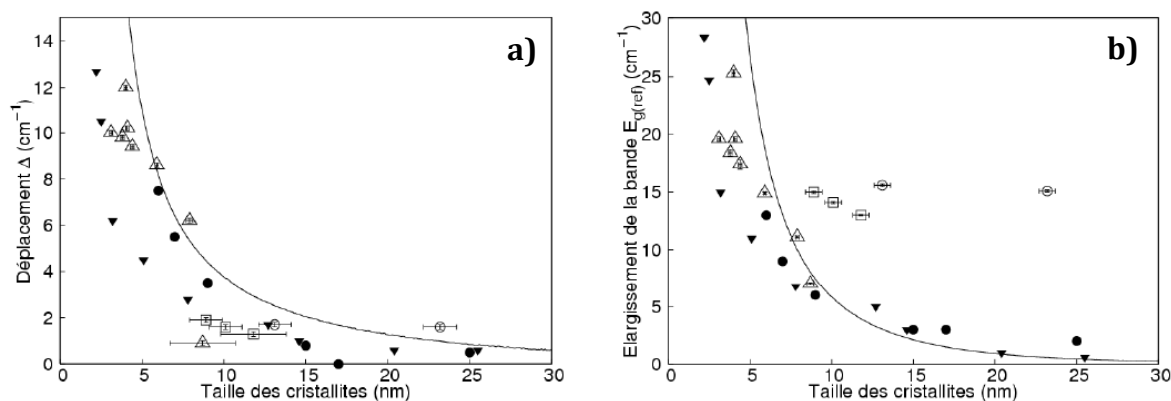


Figure 1.13: a) Displacement ($\Delta = E_g - E_{g(\text{ref})}$) of the measured position from the reference anatase Eg band (143 cm^{-1}) and b) enlargement of the reference Eg band, versus the anatase crystallite size. Different symbols correspond to different works, collected for comparison reasons by Pighini. [85].

Regarding the dielectric characteristics TiO_2 NPs can have, in comparison to bulk materials or different NPs diameter, the work of Zhang et al. [86] was one of the earliest reports. In this work, as shown in Figure 1.14, the real part of the dielectric constant ϵ_r' was measured in a frequency range of 10^1 to 10^5 Hz.

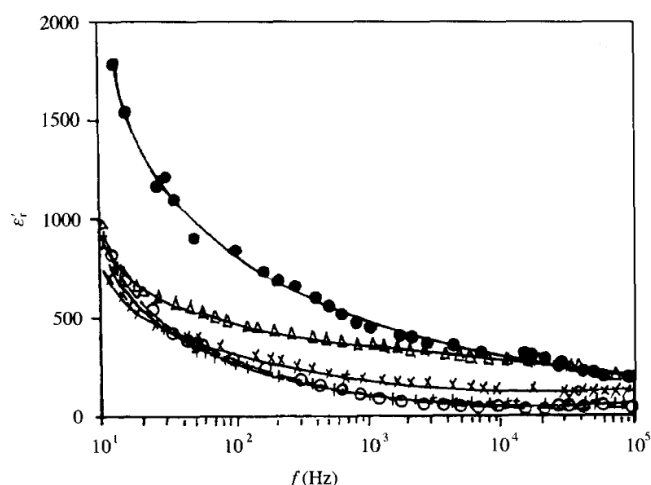


Figure 1.14: Spectra of dielectric constant vs. measuring frequency f at room temperature for nano- TiO_2 bulks with various particle diameters d . a) Anatase: (o) $d = 9.8 \text{ nm}$, (Δ) 14.4 nm , (\bullet) 17.8 nm , (x) 28.5 nm , (+) coarse grains ($\sim 1 \mu\text{m}$). [86]

Different size anatase nanoparticles were used and were compared with TiO_2 anatase coarse grains with a size of $\sim 1 \mu\text{m}$. The results indicated that in this frequency range, the TiO_2 NPs have equal or larger values than the coarse grain anatase TiO_2 . In addition to this, for larger diameter size (in the nanometer range) a higher value is observed especially in the low frequencies. As shown also in Figure 1.14, in this frequency range the polarization of the dielectric materials is based on interfacial and space charge mechanisms. Hence, under the action of an external electric field, positive and negative space charges in the interfaces move towards negative and

positive poles of the electric field, respectively. As a consequence, for coarse-grain TiO_2 NPs (large domains), the number of interfaces is very small and the space charge polarization becomes too weak. Contrary to this, for small nanoparticles (nanometer range), the volume fraction of interfaces is much larger, so that the contribution of space charge polarization in interfaces to ϵ_r' becomes obvious.

These findings were later verified by other works[87–89], and the general trend found for other materials is given in Figure 1.15. As observed for all the cases, the relative dielectric constant is 10 times higher for the nanopowder compacts than for the bulk materials.

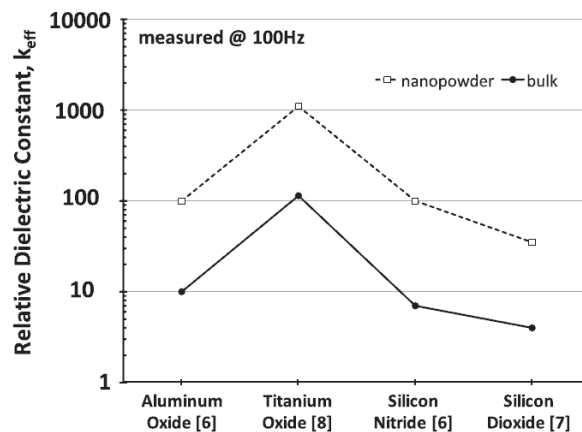


Figure 1.15: Relative dielectric constant of various materials in bulk form compared to materials existing as a nanopowder compact.[89]

As shown in Section 1.2, conventional dielectric materials are ceramics with large dielectric permittivity, coupled with high stiffness and excellent thermal stability. However, their applicability for passive components such as capacitors is largely impeded by their small breakdown strength and challenging processing conditions. Observing that these materials can exhibit enhanced characteristics in the nanoscale, attempts were carried out to disperse as fillers in matrix materials. The aim was to capitalize the high permittivity of such nanoparticles with the good electrical strength of the matrix resulting in the creation of nanocomposites with novel properties. Many works use polymer matrices as they exhibit high electrical strength, flexibility and can be easily processed.[90]. The drawback of these polymer matrices is that they lack in transparency or in high mechanical strength. Therefore, inorganic matrixes such as silica are a good alternative as they can exhibit significant isolative properties (high electrical strength), high mechanical strength and optical properties (transparent).

Since 2014, approximately 892 publications including the keywords of TiO_2 , SiO_2 and nanocomposites have been reported. The most cited applications of these works are regarding photocatalytic and antibacterial or dielectric and optical applications. Focusing mainly on the TiO_2 - SiO_2 nanocomposites (TiO_2 NPs, SiO_2

matrix), Sarkar et al.[91] attempted to investigate the TiO₂-SiO₂ nanocomposite thin films elaborated by sol gel. In this specific work, the size of the nanoparticles was varied from ~1 to 22 nm. At the same time for the larger NPs, a higher concentration of the Ti content was successfully achieved. Current density-electric field (J-E) measurements showed that for all the NPs sizes an ohmic conduction is observed in the low field. However, their low field resistivity is found depending on the size of the TiO₂ NPs to decrease by a factor of 10² Ωcm for the larger sizes. The explanation given by the authors was that in these cases; a percolated network of TiO₂ nanoparticles is created, controlling its conductivity. For higher electrical fields, as expected all compositions exhibit space-charge limited behavior. For the nanocomposite with NPs sizes as low as ~1 nm, some oscillations were observed and it was attributed to the single electron tunneling effect (SET) caused by the small nanocrystallites being isolated by the wide band amorphous silica matrix.

In recent years apart from studying the electrical response of such nanocomposites, nanoparticles have been used to make transparent nanocomposite structures having high refractive indices. If the NPs are small compared to the wavelength of light, scattering is avoided, and the nanocomposites are transparent even at high nanoparticle filling factors. Hence, it is possible for the refractive index to be tuned over a wide range by changing the filling factor and type of filler.[64,92,93] Following this direction Kermadi et al, examined the optical characteristics of sol-gel derived TiO₂-SiO₂ NCs with varying composition. The grain size of the TiO₂ NPs was between 4 nm for low fraction of TiO₂ in the NC and increased up to 10 nm for higher compositions. Using ellipsometry and Lorentz-Lorentz effective medium approximation he showed that as the fraction of TiO₂ increases the refractive index and in addition, the porosity of the film increases.[94,95] In a similar fashion Lopes de Jesus et al. [96] investigated both the porosity and the effective refractive index of the films using sol-gel derived TiO₂-SiO₂ NCs. Using Bruggeman effective medium approximation, it was possible to show the modulation of the refractive index (from 2.08 to 1.44 at $\lambda = 633$ nm), by varying the composition of the NC or its thickness (layered deposition with dip casting).

Based on these findings, the ability to choose the nature of the nanoparticles and more importantly their filling factor and size in the matrix is of great interest, as both the electrical and optical characteristics of the nanocomposite can vary.

1.4 Processes for the creation of Nanocomposite thin films and Nanomaterials

One of the most significant challenge in the development of such nanocomposites is the control of the growth mechanisms, the final morphology and the spatial distribution of the nanoparticles using reproducible, versatile and low-cost processes. Since nanocomposites and nanomaterials are an emerging scientific and

industrial field, several approaches enable their production. A good discrimination could be the bottom-up and top-down ones.[97] The top-down approaches start from the bulk material whereas the bottom-up start from the atoms.

In this Section we have decided to separate the processes for the creation of nanomaterials in three general categories, the liquid-phase, the gas-phase and the hybrid-approaches coupling the two previous ones.

1.4.1 Liquid Phase Processes

The term “liquid-phase” is used, to describe the condition when wet chemistry is needed for the fabrication of the nanomaterials. One of the most widely used process for the creation of nanomaterials is sol-gel. The sol-gel process is a chemical reaction that starts from an ionic or a molecular compound and forms a three-dimensional network through oxygen bond formation between the ions and the release of water or other small molecules. Some advantages of this technique is the low temperature during the process, the widely used precursors and the reproducibility. On the other hand, when drying (to create nanocomposite films), nanoparticles may be released arising several toxicity issues. [20,36] In case films are targeted, drying needs to be perfectly controlled in order to avoid cracks.

In more detail, sol-gel process is a chemical method which is based on hydrolysis and condensation reactions.[97–100] With the correct amount of reactants, nanosized particles precipitate. There are three basic steps in the sol-gel process: a) the partial hydrolysis of metal alkoxides (a widely used precursor given as an example here) to form reactive monomers, b) the condensation of these monomers to form colloid-like polymers (sol formation). At this step, the hydrolysis and condensation lead to the solid particles that are suspended in the liquid, a so-called sol. As the third step, the particles contain on their surface groups still active in condensation steps and therefore, they crosslink to a gel. The latter is defined as a solid network that contains liquid in its pores[101]. The last step involves drying the gel in order to produce a xerogel and consolidation can be obtained by annealing at high temperature if densification is needed to lead either to films, fibers or powders.

Figure 1.16 shows schematically all the steps needed to acquire a nanomaterial through sol-gel. As this technique has been investigated since 1800, there have been, as expected, numerous reports. Focusing on the materials of interest, meaning TiO_2 and SiO_2 , such reports target mainly on their photocatalytic[102–106], antireflective[74,105,107], hydrophobic[108,109] and dielectric[91] properties. To attain the final nanocomposite, three main experimental processes were followed. The preparation of two different sols and the mixture of them[74,103,104,110], the preparation of TiO_2 sol and the mixture with tetraethoxysilane (TEOS- SiO_2 precursor)[107–109] or the mixture of TiO_2 NPs inside the TEOS precursor[106].The

deposition of the produced nanocomposite sol-gel is taking place through spin coating, dip casting or drop casting.

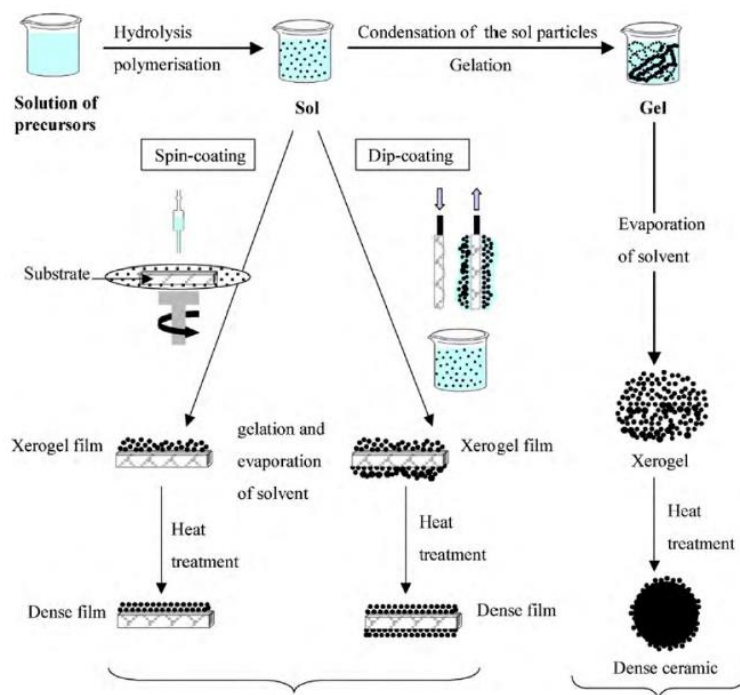


Figure 1.16: Different sol-gel process steps to control the final morphology of the product [111,112]

1.4.2 Gas-Phase Processes

The term “gas-phase” is used, to describe the state of the precursors in these processes being in a vapor or initially solid state inside the reactor/system.

Fanelli and Fracassi divided these processes in three categories. First, systems that use the same chemical source and strategy for the creation of NCs. This could be for example one PECVD system using a mixture of precursors. As shown in Section 1.2.3.2, this may produce mixed oxide one-phase film, rather than a nanocomposite. Second, the deposition using two independent chemical sources with one strategy such as co-sputtering[113], or co-evaporation[114]. Finally, the third category, were separated strategies and different sources are being followed. Over the last years, this category was proven more versatile in regard to the nature of the NPs and the matrix and a higher focus from the scientific community was given on this. Hence, for the elaboration of nanocomposite films through this category of processes, a combination of deposition systems is used for the simultaneous or step-by-step creation of the NPs and the matrix. For instance, in the past, several works involved the combination of Physical Vapor Deposition (PVD) and the Plasma Enhanced Chemical Vapor Deposition (PECVD) for the simultaneous deposition of the NPs and the matrix accordingly.[115–118] For the deposition of the NPs, sputter-deposition techniques have been utilized such as DC glow discharges, capacitively coupled RF discharges,

DC/RF magnetron plasma sources. Typical examples of successfully developed films consist of metallic (e.g., Ag, Au, Pt, Ti) or metal oxide (e.g., SiO₂, TiO₂, ZnO) NPs embedded in a large variety of polymeric matrices have been reported through these approaches.[92]

More recently, Gas Aggregation nanocluster Sources (GAS) have been used for the creation of metal nanoparticles.[119–125] The creation of these NPs is mainly based on vacuum metal evaporation or magnetron sputtering. This happens in an aggregation chamber enclosed by an orifice through which the expanding gas (usually an inert gas such as Ar or N₂) carries the clusters into the low pressure deposition chamber (typically Ultra High Vacuum one).[126] This chamber can be then used for the creation of the matrix using for instance plasma processes or using another magnetron configuration to create core-shell nanoparticles.

An example of gas-phase approaches is given in Figure 1.17. In this figure three different experimental strategies are followed for the creation of Ag/plasma polymer nanocomposites. In Figure 1.17a, the simultaneous sputtering and plasma polymerization of the NCs, in Figure 1.17b the deposition of the NCs from two independent magnetrons and experimental conditions related to the characteristics of the NPs and the matrix, and in Figure 1.17c a combination of a gas aggregation source and plasma polymerization.

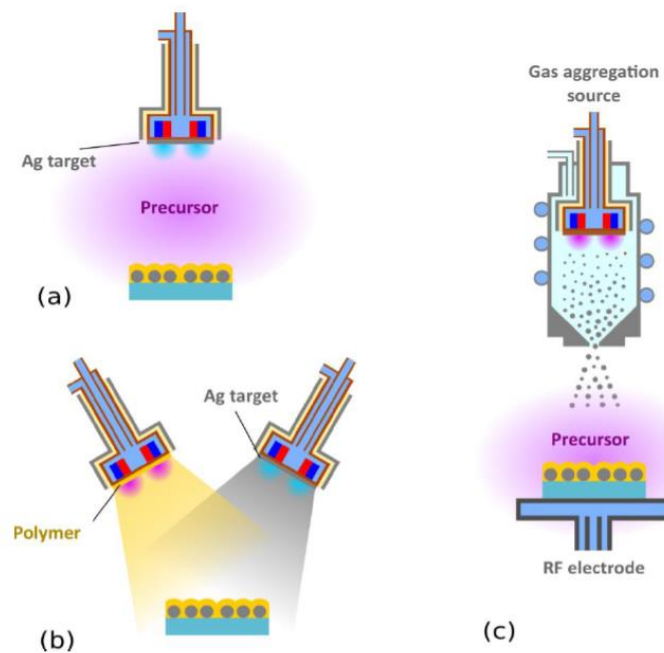


Figure 1.17: Different approaches for the production of Ag/plasma polymer nanocomposites: (a) Simultaneous sputtering and plasma polymerization, (b) deposition from two independent magnetrons, and (c) a combination of a gas aggregation source and plasma polymerization.[127]

Some appealing characteristics of these gas-phase approaches are the high purity of synthesized NPs and the environmentally friendly character (since no solvent or liquid precursors are needed). Contrary to that, the control of the NPs' characteristics is dependent on the system parameters with a small freedom for parametrization.

1.4.3 Hybrid Approaches coupling liquid and gas phase processes

Several liquid and gas-phase processes aim in the elaboration of nanomaterials or nanocomposite thin films. Liquid phase processes are well established involving mainly the sol-gel technique, indicating a high precision on the produced nanoparticles. The drawback of processes like this is the several steps until acquiring a nanocomposite thin film as well as the toxicity that the NPs can have during the drying of the film.[97] Moreover, through gas phase processes, it has been shown that a combination of vacuum techniques is being used. This allows the simultaneous creation of the nanoparticles and optionally the matrix without the manipulation of the actual nanoparticles from the user. Unfortunately, the size, form and other parameters of the produced nanoparticles are difficult to control by the process.

Hence, recently, an increasing tendency has appeared from the scientific community aiming to the creation of nanomaterials or nanocomposite thin films, by combining liquid and gas-phase processes. This is attempted by creating an aerosol of the NPs colloidal solution or directly injecting the colloidal solution inside a gas-phase system. The flexibility offered by aerosol-assisted deposition processes, in respect to those in which NPs are generated *in situ*, mainly resides in the possibility of using many preformed NPs in combinations with any compatible conventional precursor.[92]

The challenging part in approaches like these lies mainly in the droplet or aerosol production. Hence, a specific system will be needed to allow this droplet production in atmospheric or low-pressure gas-phase systems. Thanks to the spray drying[128,129] techniques, spray pyrolysis[130–132] or analytical techniques, such as inductively coupled plasma optical spectrometry (ICP-OES, ICP-MS)[133–137], the adaptation of these systems could be possible. Several droplet generation techniques exist involving different driving force to assist the atomization such as vaporization, pressure, centrifugal, electrostatic, and ultrasonic.[128]

In this section, these hybrid configurations will be introduced, being categorized by the working pressure of the gas process system (atmospheric or low pressure). At the end of this Section, an accumulative table with the hybrid approaches used and the film characteristics will be given in order to make a qualitative assessment of the produced films through these approaches.

1.4.3.1 Atmospheric Pressure based systems

Several attempts have been published over the past ten years aiming in the deposition of either nanoparticles only or nanocomposite thin films using hybrid approaches. In this part, some of the atmospheric pressure configurations will be analyzed along with their injection system. Three main categories have been found in literature. The Suspension Plasma Spray, the systems using non-equilibrium atmospheric pressure Plasma Jets and the ones using Dielectric Barrier Discharges (DBD).

Regarding the first category, the Suspension Plasma Spray[138–141], this process utilizes the high temperature and high velocity plasma jet to melt and spray nanometer-sized nanoparticles. As seen in Figure 1.18a, each drop of the liquid stream is fragmented into droplets ($< a \text{ few } \mu\text{m}$), which, after vaporization of the liquid phase, results in nano- or sub-micrometre-sized melted or partially melted particles, forming nanostructured coatings.[140] This process resembles the one of spray pyrolysis with the difference that the heat comes from the plasma (temperature up to 10 000 K) and not from a furnace. The resulted films have a melted like appearance with polydispersed in size deposited particles as seen in Figure 18b.

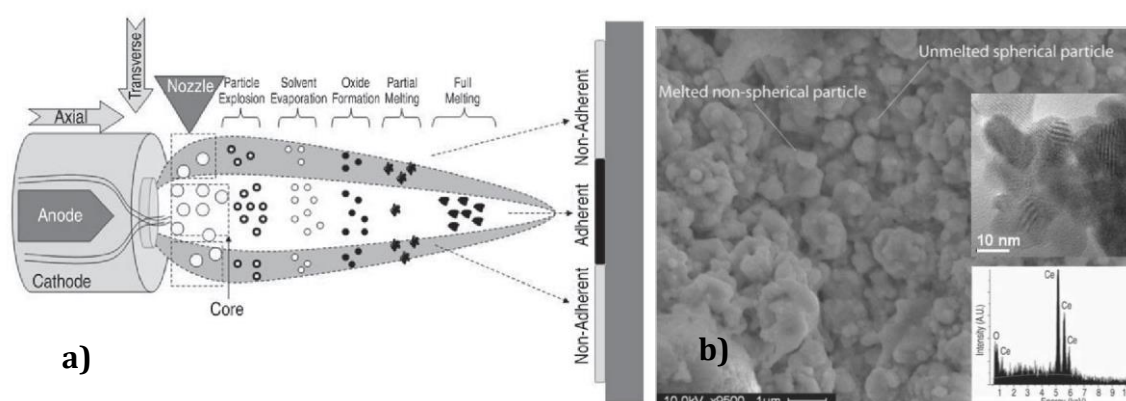


Figure 1.18: Schematic representation of precursor-plasma interaction and associated changes in various parts of the flame. Interaction in the core region of the flame leads to adherent coating. Axial and transverse represent the solution feed direction with respect to the plasma jet. [138]

Moreover, the approaches using non-equilibrium Plasma Jet configuration usually involve a system where the working gas along with the matrix precursor and the nebulized liquid are fed to the Plasma Jet.[142–144] For instance, as described by Liguori et al.[144] and given schematically in Figure 1.19a, at the same time the solution containing NPs is injected into the plasma source through the primary channel. Simultaneously, a second flow of Ar is introduced in a nebulizer system containing the dispersion of Ag NPs in ethanol (EtOH). The so-formed aerosol is injected into the plasma source through the secondary gas channel. The resulted films

were polymerized polyacrylic acid and silver nanoparticles (around 100 nm in size) having antimicrobial applications, an SEM image of which can be seen in Figure 1.19b.

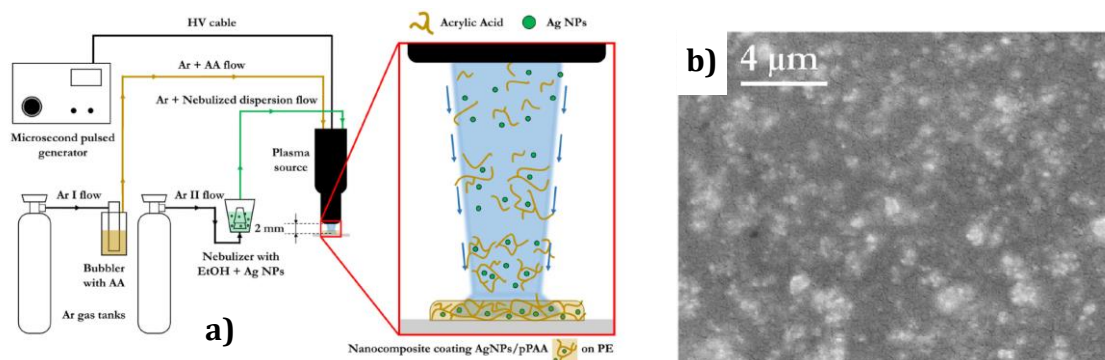


Figure 1.19: a) Experimental setup of the plasma co-deposition process. b) SEM images of the top views AgNPs/pPAA.[144]

Since 2006 many reports involve the Dielectric Barrier Discharge (DBD) systems, for the injection of the colloidal solution and the deposition of nanomaterial thin films.[92,145–153] For the efficient creation and injection of the liquid solution containing NPs, two main systems were used by the majority of the works, which are the nebulizer and the atomizer. In the case of the nebulizer, the flow rate of the colloidal solution is regulated by a syringe pump and then it is fed to the nebulizer. There the carrier gas for the production of the aerosol is introduced and based on the Venturi effect an aerosol is generated at the outlet of the nebulizer. [154] In the case of the atomizer, compressed air expands through an orifice to form a high-velocity jet. At the same time, liquid is drawn into the atomizing section through a vertical passage and is then atomized by the air jet. [155] Recently, using a DBD system with a nebulizer Profili et al. [149–152] reported several experiments for the deposition of nanocomposite thin films using the DBD reactor given in Figure 1.20a. This group attempted the deposition of TiO₂ NPs only (Figure 1.20b) or nanocomposite thin films through various approaches such as dissolving the NPs inside the HMDSO liquid and injecting it in the system or in a two-step approach injecting first the colloidal solution of NPs and second the SiO₂ matrix (introducing the vapor in the plasma).

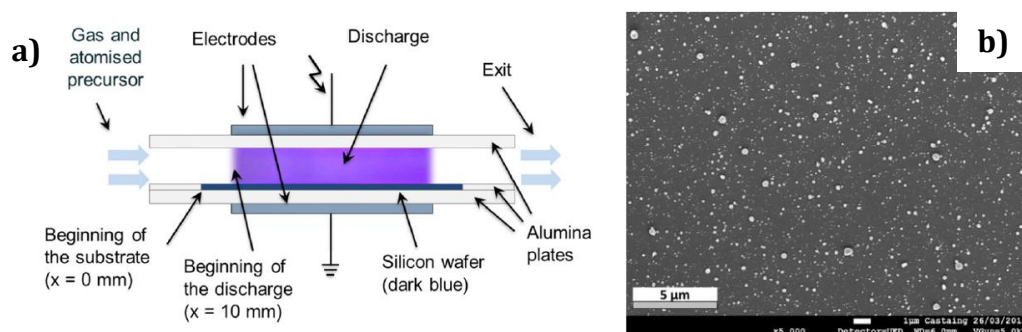


Figure 1.20: a) Schematic of the dielectric barrier discharge reactor used for the growth of nanocomposite thin films. [149–152] b) SEM images of the particles deposited on the silicon substrate using water as solvent. [150]

1.4.3.2 Low-pressure-based systems

A small number of scientific reports have been published involving low-pressure physical systems. This could be due to the fact that handling of aerosols or liquids at low pressure is challenging. These challenging conditions can be for instance the reactor contamination especially when working at room temperature, the degradation of the turbopump lifetime and plasma perturbation (if there is use of plasma) due to pressure variation caused by the solvent vaporization.[92,156] Two main categories will be given here, the thermally activated vacuum techniques such as the Chemical Vapor Deposition (CVD) and the ones based on plasma enhanced CVD (PECVD). Due to the scope of this work, the main focus will be given at the low-pressure plasma systems used, and their configuration to produce nanomaterials through this hybrid approach.

Some works involve the combination of the CVD systems with a direct liquid injector to produce nanomaterials.[157–159] An example of the configuration based on the direct liquid injection of the solvent containing nanoparticles is given in Figure 1.21a.

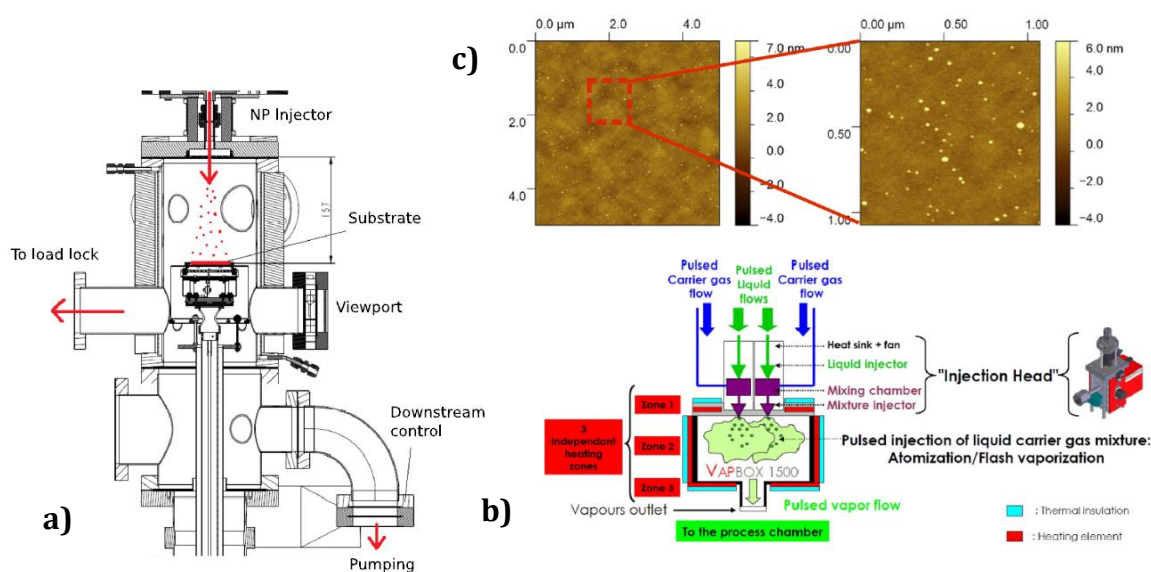


Figure 1.21: a) Schematic of the process chamber. b) Schematic of the Kemstream Vapbox 1500 injection head. c) AFM image of sample with a suspension flow rate of 0.25 g/min with a scanning area of 5 μm×5 μm and a zoom in of a region with a scanning area of 1 μm×1 μm. [159]

As observed in this scheme, the injector has been positioned at the top of the reactor facing the rotating substrate holder which is heated at 150 °C. The result from this hybrid system was the deposition of gold nanoparticles whose size was found to depend on the flow rate of the injected solution (having NPs inside). The AFM image of sample with the lowest attempted suspension flow rate (0.25 g/min) is given in Figure 1.21c. The gas used for this approach was N₂, in order to avoid any reactions

with the gold NPs. In Figure 1.21b a detailed diagram of the injection system is given, being comprised of an atomizer and a heated chamber. This allows the production of the aerosol with the help of a carrier gas.

Additional works have been found using a similar direct liquid injection (DLI) system for CVD[160–162] and Atomic Layer Deposition (ALD) [163,164] systems but without though the presence of nanoparticles in the injected liquid. They only capitalize the DLI process to atomize the injected liquid, vaporize it and generate the reactive vapor.

The first report using a low pressure plasma system, aiming at the simultaneous injection of the NPs in a solution and the injection of the matrix precursor using the PECVD technique has been proposed by Ross et Gleason [165] in 2006. In this report, the atomization of the solution is accomplished by a 40 kHz ultrasonic atomizer (Sonics and Materials, model VC134-AT with custom probe) located at the top of the reactor. The ultrasonic atomizers are based on the vibration of a quartz at high frequencies, typically 1 to 4 MHz. Vibrations created cause the surface liquid film to burst into very fine droplets. However, these devices are used in the case of a large flow of suspension. Through a distribution ring, the matrix precursor (HMDSO) was introduced inside the reactor. The produced plasma was created using O₂ as a working gas and an RF power supply as shown in Figure 1.22a.

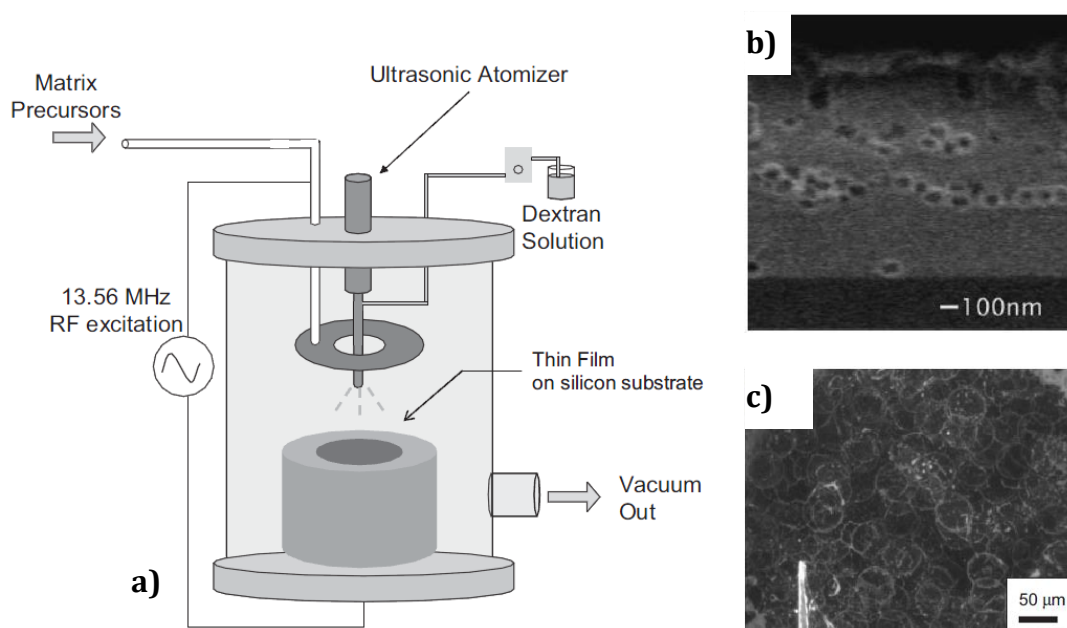


Figure 1.22: Reactor configuration for simultaneous plasma-enhanced deposition of matrix material and ultrasonic atomization deposition of particles. b) Cross section SEM image of 96 nm pores corresponding to the NPs, embedded inside the carbon-doped silicon dioxide matrix c) Deposited atomized droplets observed with fluorescent microscopy. [165]

The plasma was pulsed at an on-off rate of 10–40 ms, with a peak power of 300 W. For the deposition, the pressure was maintained between 100–500 mTorr. The

resulting films were polystyrene nanospheres with 96 nm diameter embedded inside the carbon-doped silicon dioxide matrix (Figure 1.22b). An interesting observation from this work was the appearance of droplets formed at the surface of the film (Figure 1.22c). Hence, the first attempts investigating how the volatility of the solvents can improve this phenomenon were established using water, ethylene glycol and labeled dextran (for fluorescent microscopy).

Three years later, in 2009, Ogawa et al. [166] introduced a complete experimental study of directly introducing the liquid inside the low pressure Ar Capacitively Coupled Plasma (CCP) powered by an RF power supply (Figure 1.23a). This was established using a Denso fuel injector (23209-0D040) in a pulsed mode and a produced droplet diameter estimated at 50 μm . The deposited Fe nanoparticles (brown rings) using this approach can be seen in Figure 1.23b.

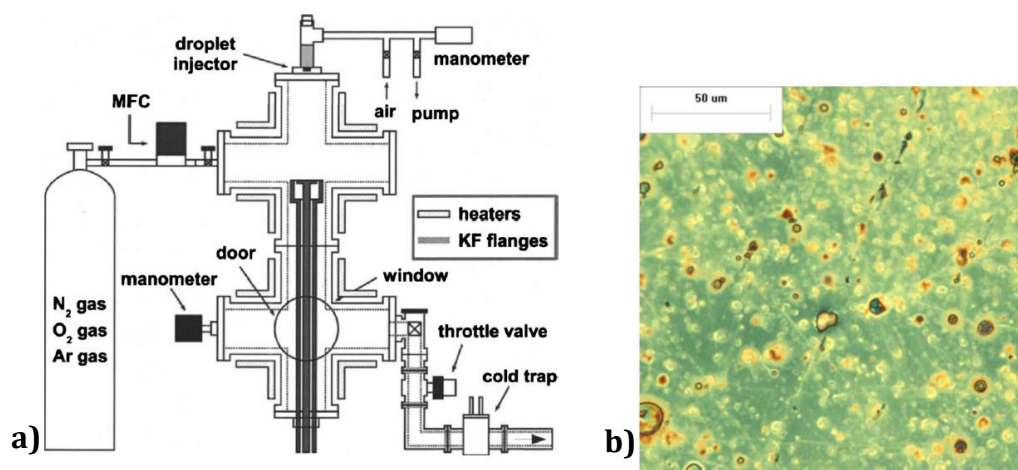


Figure 1.23: a) A schematic diagram of the experimental apparatus. b) The film produced by injection of Fe NPs in hexane into Ar plasma. Groups of Fe nanoparticles are visible as brown rings in the film. [166]

Furthermore, as discussed by a relative recent review of Bruggeman et al. [156] on plasma-liquid interactions, both the impact of the plasma to the droplets and vice versa has been poorly understood and studied. Ogawa's study was the first attempt to refer to the term misty plasmas, being plasmas that contain liquid droplets. This term was first proposed by Coppins [167,168] in 2004. Coppins stated also that these misty plasmas would not differ significantly from the dusty plasmas (plasma containing millimeter to nanometer particles) but that the liquid state of the droplets could allow droplet deformation and make surface tension forces more important. On this basis, Ogawa attempted the creation of a model (Figure 1.24) describing the energy fluxes entering and exiting the droplet under the specific plasma conditions. Using this model and the energy balance equation he was able to determine the parameters affecting the droplet evaporation in this low-pressure medium. Finally, in a following work [169] he investigated the transient effects caused by the liquid injection on the same low pressure plasma.

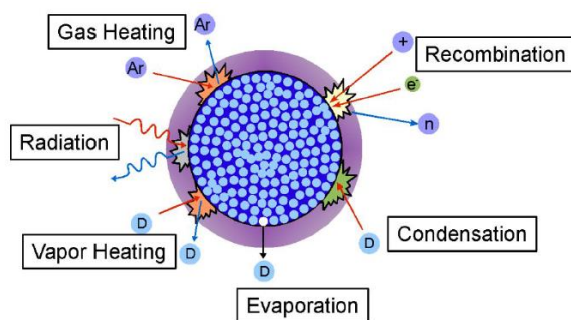


Figure 1.24: A schematic diagram of the different processes modeled at the droplet surface. [166,170]

Very recently, Clergereaux's group et al. [171,172] reported a new safer-by-design method for NC thin film plasma deposition. This method allowed to synthesize NPs from organometallic precursor in the reactor-injector prior to their injection in the RF low-pressure (750 mTorr) plasma reactor. The resulted nanocomposites consisted of small (6 ± 3 nm) and isolated (i.e. non-aggregated) ZnO NPs homogeneously dispersed in an amorphous hydrogenated carbon matrix. As seen in the top of Figure 1.25, they were able to control the chemical synthesis of the NPs inside the reactor-injector and the characteristics of the deposition, was controlled by the low pressure plasma reactor. During this work, studies to investigate the pulsed injection impact on the plasma were carried out.

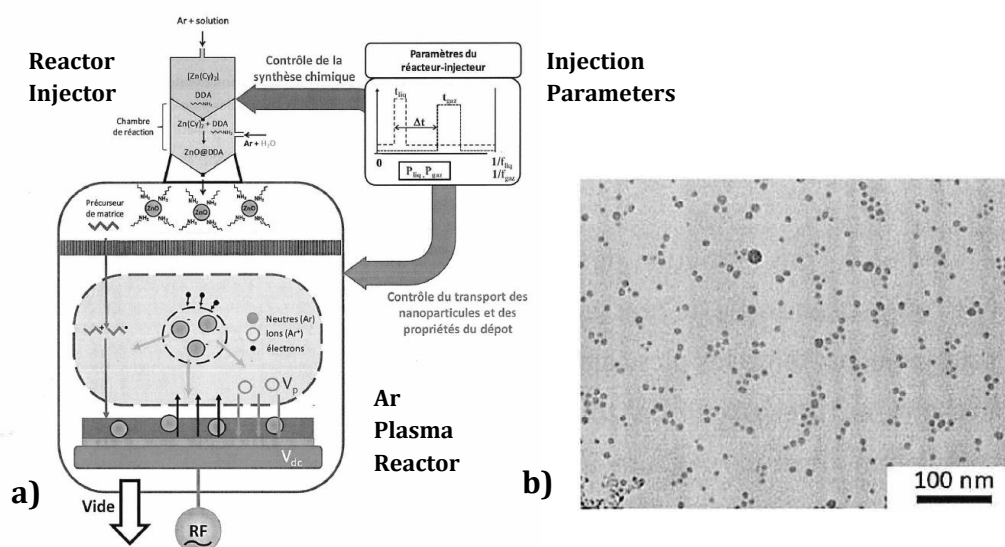


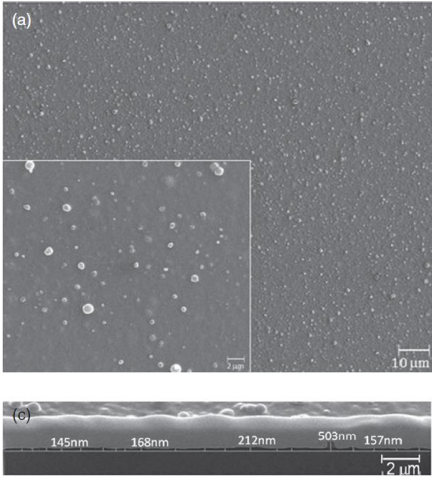
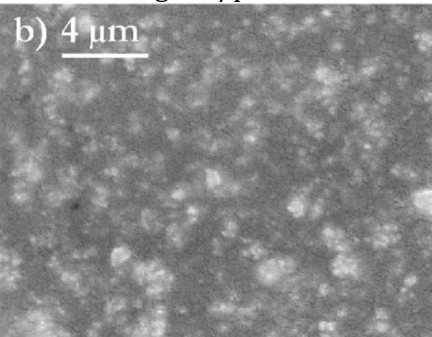
Figure 1.25: a) Reactor-injector and RF low-pressure plasma system used by Carnide et al. b) TEM view of the ZnO NPs using pentane as a solvent in the reactor injector. [171]

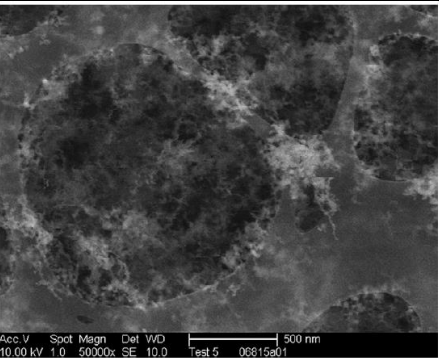
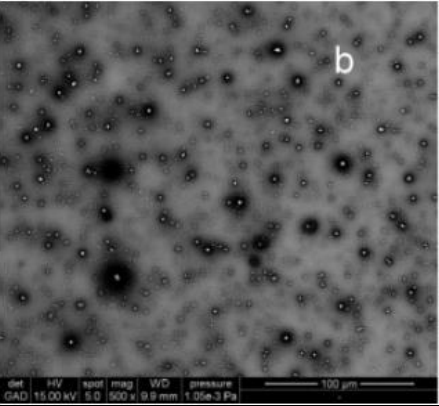
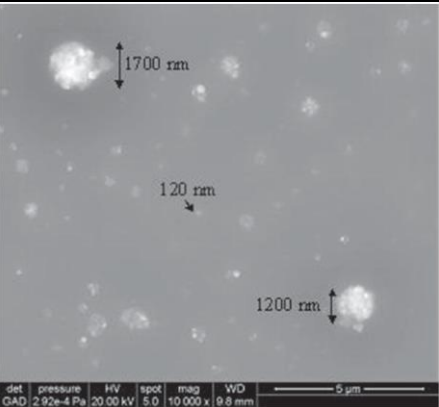
1.4.3.3 Characteristics of the produced nanomaterials through the hybrid approaches

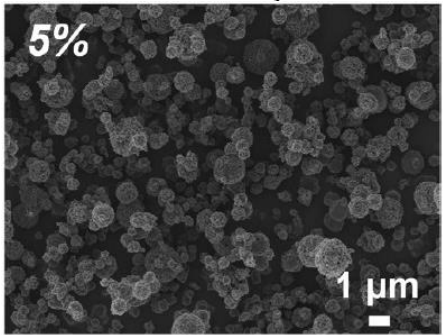
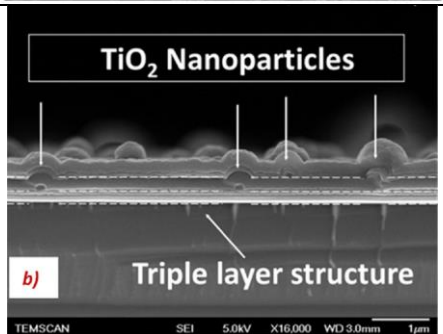
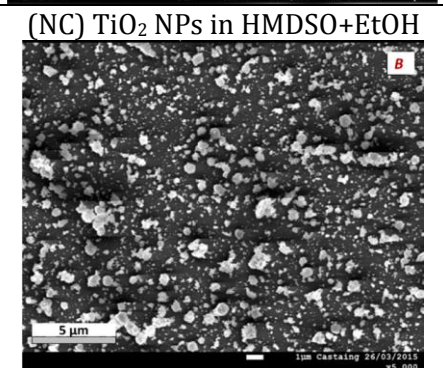
Due to the originality of this hybrid approach coupling the gas and liquid phase processes, Table 1.2 was produced, indicating a majority of the works since 2006. In

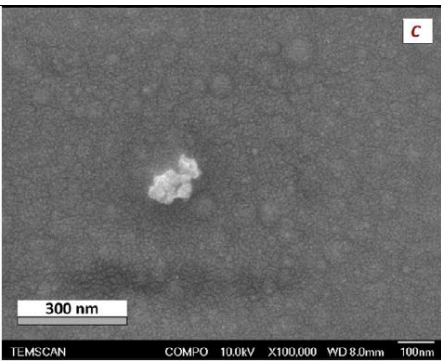
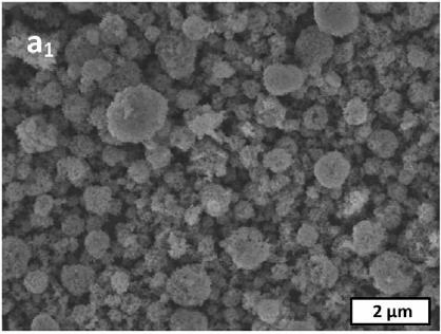
this table, details regarding the process parameters, the system used, the precursors and working pressure are given. Moreover, the characteristics of the produced films and the evolution of the NPs size upon deposition are discussed.

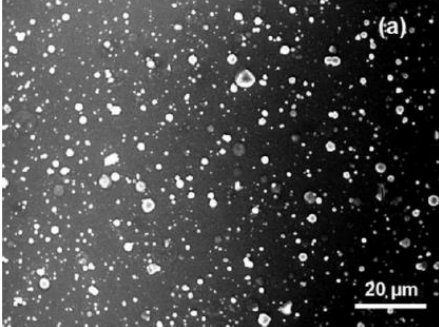
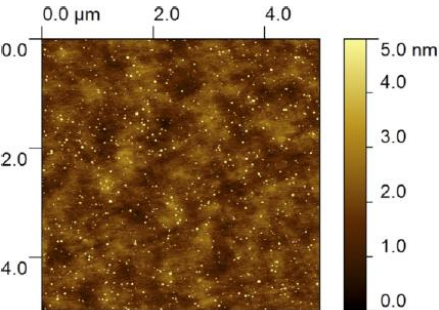
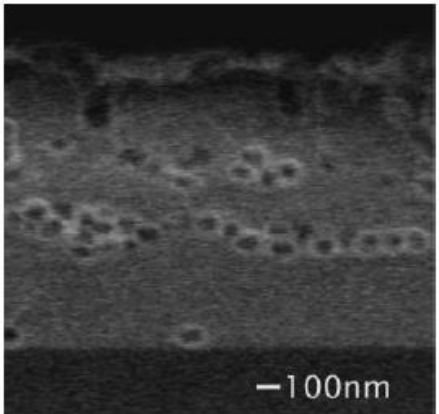
Table 1.2: Comparative table of the hybrid systems used and the characteristics of the produced nanomaterials.

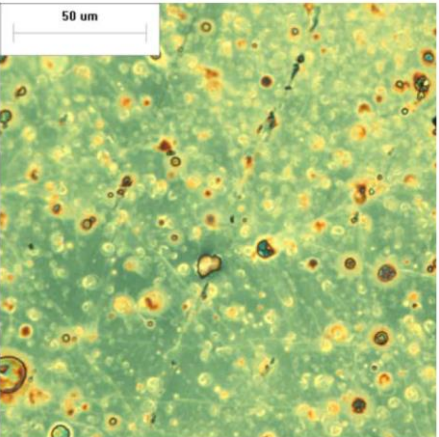
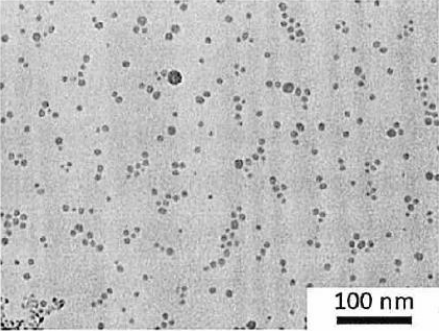
System Configuration	Precursors	Pressure	NPs evolution during deposition	Produced nanomaterial	View of the Nanomaterials	Ref.
Ar Plasma Jet + nebulizer	Admixtures with alcohols for solution stability TiO ₂ NPs/ tetramethoxysilane, TMOS/methanol TiO ₂ NPs /TMOS/pentanol TiO ₂ NPs/ TMOS/octanol <u>NPs Origin:</u> Commercial	Atm.	<u>Initially:</u> 30–80 nm <u>After Deposition:</u> 50–700 nm	Hybrid Organic–Inorganic Composite	TiO ₂ NPs/TMOS/methanol 	[142]
Ar Plasma Jet +nebulizer (Ar carrier gas)	Acrylic Acid + Ag NPs in ethanol, EtOH (Co-deposition) <u>NPs Origin:</u> Commercial	Atm.	<u>Initially:</u> (mean diameter < 100 nm) <u>After Deposition:</u> characteristic dimension around 100 nm	0.9 at.% Ag NPs in polymerized polyacrylic acid (pPAA)	AgNPs/pPAA 	[144]

Ar DBD + nebulizer(Ar carrier gas)	CuO nanoparticles are suspended in acetone or methyl methacrylate (MMA) <u>NPs Origin:</u> -	Atm.	<u>Initially:</u> 30 nm <u>After Deposition:</u> Agglomerated and single needle like particles 200-500 nm	CuO NPs with a carbon coating		[145]
DBD +atomizer (N ₂ /O ₂ carrier gas)	AlCeO ₃ in HMDSO solution and admixture with ethanol to improve NPs distribution <u>NPs Origin:</u> Commercial	Atm.	<u>Initially:</u> 25 - 200 nm <u>After Deposition:</u> -	1-4% AlCeO ₃ NPs (agglomerates) in ppHMDSO matrix (NC)		[146]
	AlCeO ₃ in HMDSO solution <u>NPs Origin:</u> Commercial	Atm.	<u>Initially:</u> 25 - 200 nm <u>After Deposition:</u> 100 nm to several μm	1-4% AlCeO ₃ NPs (agglomerates) in ppHMDSO matrix (NC)		[147]

<p>He DBD + pneumatic atomizer (He carrier gas)</p>	<p>ZnO NPs in n-octane solution <u>NPs Origin:</u> Commercial</p>	<p>Atm.</p>	<p><u>Initially:</u> ~36 nm <u>After Deposition:</u> ~640 nm</p>	<p>ZnO NPs (agglomerates) polyethylene-like polymer matrix (NC) -The NPs concentration varied in the solution, 0.5 to 5 wt %. Led 0.5% -4.5 at% and 19 ± 3 wt % to 78 ± 4 wt % loading.</p>	<p>Oleate-capped ZnO NPs in n-octane at a concentration of 0.5, 3, and 5 wt % (deposition time = 10 min)</p>	<p>[148]</p>
<p>DBD + nebulizer(N2 + N2O carrier gas)</p>	<p>HMDSO in vapor + TiO2 NPs colloidal suspension</p>	<p>Atm.</p>	<p>Initially: ~30 nm with some agglomerates 100 nm After Deposition: 100 nm range</p>	<p>2 step deposition of TiO₂ NPs and silica like matrix (NC)</p>		<p>[149]</p>
<p>TiO₂ NPs colloidal suspension in HMDSO <u>NPs Origin:</u> Lab-made</p>	<p>Atm.</p>	<p>Atm.</p>	<p><u>Initially:</u>20–120 nm <u>After Deposition:</u> 30– 500 nm</p>	<p>TiO₂ NPs 3% in weight (agglomerates) in silica-like matrix (NC)</p>		<p>[150]</p>
						

	<p>ZnO NPs in pentane+HMDSO solution <u>NPs Origin:</u> Commercial</p>	<p>Atm.</p>	<p><u>Initially:</u> 7.7 nm, FWHM of 6 nm <u>After Deposition:</u> agglomeration Due to agglomeration in the suspension when HMDSO is added</p>	<p>ZnO NPs (agglomerates) in silica-like matrix (NC)</p>		<p>[151]</p>
	<p>TiO₂ NPs in water</p>	<p>Atm.</p>	<p>TiO₂ NPs Interaction of atomized colloid with the DBD AC electric field. Effect on their size distribution</p>			<p>[152]</p>
<p>DBD + nebulizer (Ar carrier gas)</p>	<p>TiO₂ NPs coated by TMOS added to 50 ml of isopropanol (IPA) <u>NPs Origin:</u> Commercial</p>	<p>Atm.</p>	<p><u>Initially:</u> 20 nm <u>After Deposition:</u> clusters with ~25 nm</p>	<p>TiO₂ NPs in a polymer matrix (NC) NPs only: Increasing the power supply frequency from 1 to 50 kHz, a decrease on the NPs coverage is observed. At % from 23 to 0.5 for the Ti content (XPS)</p>	<p>TiO₂ NPs @1 kHz AC</p> 	<p>[153]</p>

MOCVD + Kemstream (N ₂ carrier gas)	TTiP vapor + α-Al ₂ O ₃ in isopropyl alcohol solution <u>NPs Origin:</u> Commercial	7.5 Torr	<u>Initially:</u> 40 nm <u>After Deposition:</u> 1245 ± 75 nm (aggregates)	a-Al ₂ O ₃ particles in TiO ₂ matrix (NC)		[158]
CVD + Vapsoft 1500 Kemstream (N ₂ carrier gas)	Gold NPs in solution[173] <u>NPs Origin:</u> Lab-made	-	<u>Initially:</u> 2 ± 0.6 nm. <u>After Deposition:</u> 5.2 ± 1 nm.	Gold NPs Solvent mass rate affects the NPs size (agglomerates)		[159]
Low Pressure O ₂ Plasma + 40 kHz ultrasonic atomizer	Tetraethoxysilane, TEOS in vapor (PECVD) + dextran/ aqueous dextran/ ethylene glycol polystyrene NPs/aqueous suspensions <u>NPs Origin:</u> Commercial	100- 500 mTorr	<u>Initially:</u> 96 ± 9 nm. A variation on the size upon deposition was not observed	carbon-doped silicon dioxide (OSG) matrix, polystyrene NPs 96 nm (NC)		[165]

<p>Low Pressure Ar Plasma + Fuel Injector</p>	<p>Fe NPs in hexane solution <u>NPs Origin:</u> -</p>	<p>400 mTo rr</p>	<p><u>Initially:</u> 2 nm <u>After deposition:</u> agglomerations range from 2 to 20 μm</p>	<p>Fe fraction per unit volume ~ 3.9% in hydrocarbon matrix</p>		<p>[166]</p>
<p>Low Pressure Ar plasma + reactor- injector</p>	<p>$\text{Zn}(\text{C}_6\text{H}_{11})_2 + \text{H}_2\text{O}$ in Pentane, Cyclohexane, Toluene or Heptane <u>NPs Origin:</u> Lab-made</p>	<p>750 mTo rr</p>	<p><u>Initially:</u> liquid precursor <u>After deposition:</u> 6 ± 3 nm</p>	<p>ZnO NPs in an amorphous hydrogenated carbon matrix. Small mean diameter size and homogeneous distribution.</p>		<p>[155, 156]</p>

A first observation from this table is that the majority of the provided works were conducted at atmospheric pressure. This could be linked to the relative easier set up as there is no turbomolecular pump and the injection of the aerosol is facilitated by the geometry of the system and the gas flow configuration. The preponderant use of DBD configurations over plasma jets could be linked to the lower temperature the first exhibits, and the possibility to deposit on higher surface area. Moreover, an issue occurring frequently in these works is the agglomeration of the initial NPs upon deposition. Some more recent works, such as from Profili et al.[152] investigated the impact of the ac voltage parameters of the DBD power supply on the deposited size distribution of the NPs. In addition to this, regarding the low pressure system Vervaele et al. [159] showed that for a low pressure CVD system, the mass flow rate of the introduced solvent significantly affects the size of the deposited NPs. Furthermore, three general categories of experimental strategies were identified for the production of nanomaterials. First, the NPs colloidal solution was injected only in the plasma system for the deposition of NPs. In this scenario, when the solvent is organic, a carbon-like matrix could be observed surrounding the NPs. Second, for the creation of NC thin films, the NPs were dissolved in the liquid precursor of the matrix. Third, the deposition of the matrix precursor and the NPs took place from two separate sources. Two works were identified with this latter experimental strategy. The first by Profili et al. [149] where two steps were followed namely the deposition of the TiO₂ NPs (from the aerosol) and after the injection of the HMDSO vapor precursor in the DBD reactor. The created film was a layered nanocomposite. The second work was from Ross et Gleason [165] where the colloidal solution with the NPs was injected simultaneously with the HMDSO vapor precursor in the low pressure (100-500 mTorr) reactor. From the characteristics regarding the produced nanomaterials in Table 1.2, it appears that the majority of the works have an organic matrix. This could be linked with the transient effects happening during the liquid vaporization (pressure variation, discharge perturbation etc) or the released organic species that can affect the inorganic quality of the deposited matrix (in case it is preferred for the application of the produced films). Finally, the concentration of the distributed NPs has propelled the curiosity of the researchers. For the majority of the works the NPs content remains in low levels (less than 5%). Brunet et al.[153] attempted to control the coverage percentage through the power supply frequency of the DBD (adjusting the process) whereas Fanelli et al.[148] chose to increase the NPs concentration in the solution (adjusting the precursor).

To conclude, from this comparative study, the challenge and difficulties to develop NC films, retaining the initial mono dispersity in size of the NPs, with controlled composition and homogeneous NPs dispersion in the matrix through plasma-based hybrid processes is clearly highlighted.

1.5 Aim and Experimental Strategy of the Thesis

In Section 1.3 the interest and importance of the nanocomposites and nanomaterials were discussed. Due to complexity to produce well defined nanomaterials, several processes have been used. The most famous and prominent one is the sol-gel process. Unfortunately, the several steps needed, the fine control required at the drying step and dangers that may arise from NPs manipulation during the drying process, urge scientists to search different approaches. Hence, wouldn't it be ideal to have a versatile and safe-by-design process that could give us the ability to tune and adjust the nanocomposite characteristics?

Through this work, what we propose is the coupling of the Chemical Synthesis and Plasma process to create nanocomposites. We focus here the study in creating TiO₂-SiO₂ NCs although different NPs and matrix precursors could be used. Thus, our aim is binary, first to establish an approach like this, in quite low pressures (a few mTorr), that could provide an inorganic matrix of a good optical quality and second, investigate whether it is possible to tune the NCs' characteristics through the process. In Figure 1.26, a scheme of the aim of this work is given. In detail, we attempt the direct injection of the colloidal solution containing TiO₂ NPs, inside the low pressure 3 mTorr Inductively Coupled Plasma (ICP) reactor. Simultaneously, from a different source HMDSO vapor is added, for the creation of the SiO₂ matrix.

Based on the information extracted from previous works, in Section 1.4.3 and 1.5, there are several key questions that need to be addressed:

- Given that the published works have been carried out in atmospheric or a few hundred mTorr, will it be possible **to maintain the efficiency of the low-pressure plasma** during the injection (as solvent is injected a variation of pressure is generally observed)?
- If plasma is maintained, how will its chemistry be affected by the droplet evaporation?
- Do we understand what are the main mechanisms driving the interactions between the evaporating droplets and the plasma?
- Will the introduced NPs be affected or degraded by the low pressure ICP?
- Will this approach result in agglomerations of NPs?
- Providing that most works have organic matrixes or silica-like ones, will it be possible using this low-pressure system to deposit an inorganic matrix?
- Finally, will it be possible, in the future, to have an agile process (through this approach) in a way to tune and adjust the NCs' characteristics oriented for integrated optics applications?

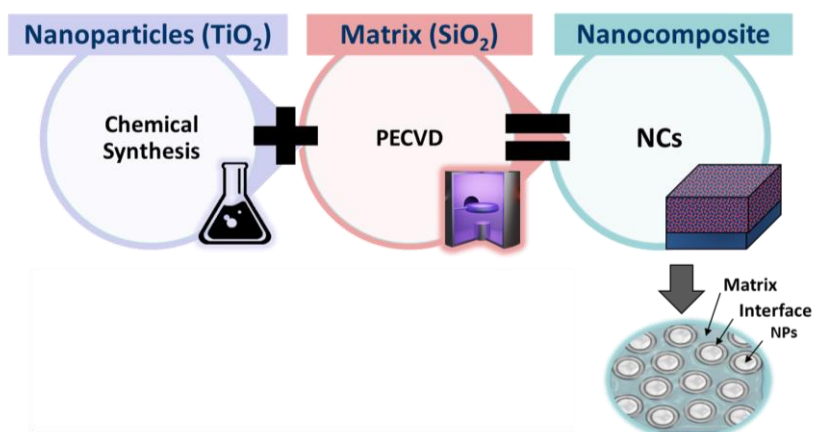


Figure 1.26: Schematic of the principle idea of the approach attempted in this work.

In order to reply to these questions in the most efficient manner, we separated this work in four parts. Therefore, Figure 1.27 indicates schematically the experimental strategy followed. After presenting the experimental techniques in Chapter 2, Chapter 3 is dedicated to investigate the impact of the O₂ ICP plasma on the NPs, we spin coated using conventional techniques the TiO₂ NPs and plasma treated them with the specific plasma source. We chose to inject lab-made stable colloidal solution that allowed us to control the size and dispersion in the initial suspension. For understanding the interphase between the TiO₂ NPs (in a nanocrystalline phase) with the amorphous SiO₂ matrix, a two-step approach was followed preparing a multilayer thin film. Hence, in Chapter 4, the deposition of the TiO₂ NPs layers is established using spin coating and the SiO₂ layers using PECVD. This result, is compared with a one-step fully PECVD made multilayer film. Once these two studies were concluded, the selection and implementation of a compatible, with our system, injector was finalized and the experiments using the hybrid approach were carried out. Consequently, in Chapter 5, the direct injection of the liquid droplets containing NPs was attempted in an O₂ plasma. Both the injection system and the produced samples were characterized and optimized. An important point in this Chapter is the computational investigation of the interactions between the evaporating droplets and the plasma, using a dedicated model. Finally, once the optimized conditions for the injection of the TiO₂ NPs were achieved in Chapter 5, the simultaneous introduction of the HMDSO vapor in the O₂ plasma was conducted in Chapter 6. The results presented in this Chapter, show how it is possible to monitor dynamically this hybrid approach and understand the parameters affecting the growth, the distribution of the NPs and the quality of the produced NCs.

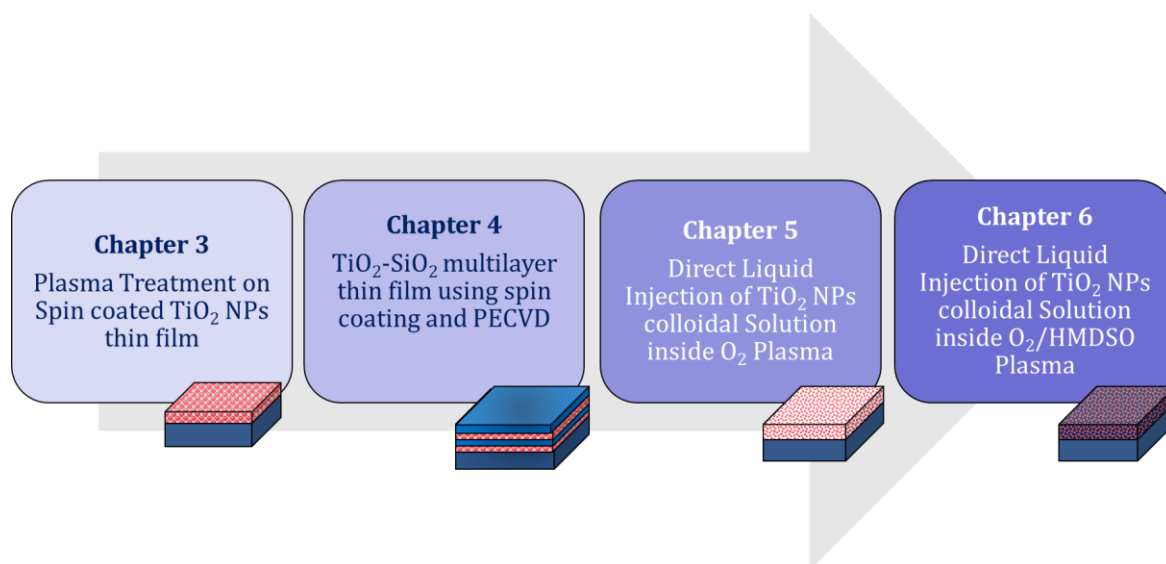


Figure 1.27: Schematic of the experimental strategy followed in this work (dark blue corresponds to the substrate, light blue to the SiO₂ layer or matrix and red to the TiO₂ NPs).

Conclusion

The aim of this work is the creation of TiO₂-SiO₂ NCs thin films through a hybrid approach coupling chemically synthesized NPs with plasma process. Due to the nature of the materials used, the basic principles of dielectric materials were given. The parameters characterizing their ability to store electrical energy or reflect/guide light were explained, and prominent applications towards microelectronics and optics were described. To assess the technological evolution and the on-going demand more functional materials, nanocomposites and nanomaterials in general, have emerged. Nanocomposites are solid materials that have multiple phase domains and at least one of these domains has a nanoscale structure. They can have novel chemical and physical properties that depend on the morphology and interfacial characteristics of the component materials. In this work, the process to create well controlled homogenous nanocomposites is the main issue. Hence, emphasis was given on the general trends found in literature, which were separated in three main categories: the liquid phase, the gas phase and the hybrid approaches. Finally, from a thorough comparison between the existing hybrid approaches, important questions arose and the importance of the present work was solidified.

Bibliography

- [1] R.E. Oesper, M. Speter, The Faraday-Whewell Correspondence Concerning Electro-Chemical Terms, *Sci. Mon.* 45 (1937) 535–546.
- [2] Faraday consults the scholars: the origins of the terms of electrochemistry, *Notes Rec. R. Soc. Lond.* 16 (1961) 187–220. <https://doi.org/10.1098/rsnr.1961.0038>.
- [3] R.P. Deshpande, *Capacitors*, McGraw-Hill Education, New York Chicago San Francisco, 2015.
- [4] S.O. Kasap, *Principles of electronic materials and devices*, McGraw-Hill, Boston, 2006.
- [5] S. Kasap, ed., *Springer handbook of electronic and photonic materials: with 168 tables*, Springer, New York, NY, 2006.
- [6] J. Yota, H. Shen, R. Ramanathan, Characterization of atomic layer deposition HfO_2 , Al_2O_3 , and plasma-enhanced chemical vapor deposition Si_3N_4 as metal–insulator–metal capacitor dielectric for GaAs HBT technology, *J. Vac. Sci. Technol. Vac. Surf. Films.* 31 (2013) 01A134. <https://doi.org/10.1116/1.4769207>.
- [7] H. Shin, M.R. De Guire, A.H. Heuer, Electrical properties of TiO_2 thin films formed on self-assembled organic monolayers on silicon, *J. Appl. Phys.* 83 (1998) 3311–3317. <https://doi.org/10.1063/1.367132>.
- [8] K.-C. Tsai, W.-F. Wu, C.-G. Chao, C.-C. Wu, Improving Electrical Characteristics of $\text{Ta/Ta}_2\text{O}_5/\text{Ta}$ Capacitors Using Low-Temperature Inductively Coupled N_2/O Plasma Annealing, *J. Electrochem. Soc.* 154 (2007) H512. <https://doi.org/10.1149/1.2719624>.
- [9] A.D. Li, W.C. Liu, Optical properties of ferroelectric nanocrystal/polymer composites, in: *Phys. Prop. Appl. Polym. Nanocomposites*, Elsevier, 2010: pp. 108–158. <https://doi.org/10.1533/9780857090249.1.108>.
- [10] K. Ohashi, Silicon (Si) and germanium (Ge) in optical devices, in: *Silicon–Germanium SiGe Nanostructures*, Elsevier, 2011: pp. 551–574. <https://doi.org/10.1533/9780857091420.4.551>.
- [11] P. Kozma, F. Kehl, E. Ehrentreich-Förster, C. Stamm, F.F. Bier, Integrated planar optical waveguide interferometer biosensors: A comparative review, *Biosens. Bioelectron.* 58 (2014) 287–307. <https://doi.org/10.1016/j.bios.2014.02.049>.
- [12] J.D.B. Bradley, C.C. Evans, J.T. Choy, O. Reshef, P.B. Deotare, F. Parsy, K.C. Phillips, M. Lončar, E. Mazur, Submicrometer-wide amorphous and polycrystalline anatase TiO_2 waveguides for microphotonic devices, *Opt. Express.* 20 (2012) 23821. <https://doi.org/10.1364/OE.20.023821>.
- [13] D. Li, *Synthèse par PECVD et caractérisation de couches minces de TiO_2 et de TiSiO pour applications optiques*, Nantes, 2013.
- [14] H.K. Raut, V.A. Ganesh, A.S. Nair, S. Ramakrishna, Anti-reflective coatings: A critical, in-depth review, *Energy Environ. Sci.* 4 (2011) 3779. <https://doi.org/10.1039/c1ee01297e>.
- [15] A.S. Sarkın, N. Ekren, Ş. Sağlam, A review of anti-reflection and self-cleaning coatings on photovoltaic panels, *Sol. Energy.* 199 (2020) 63–73. <https://doi.org/10.1016/j.solener.2020.01.084>.
- [16] K.H. Zaininger, Chih-Chun Wang, Thin film dielectric materials for microelectronics, *Proc. IEEE.* 57 (1969) 1564–1570. <https://doi.org/10.1109/PROC.1969.7337>.
- [17] J. Robertson, R.M. Wallace, High-K materials and metal gates for CMOS applications, *Mater. Sci. Eng. R Rep.* 88 (2015) 1–41. <https://doi.org/10.1016/j.mser.2014.11.001>.
- [18] S.K. Kim, S.W. Lee, J.H. Han, B. Lee, S. Han, C.S. Hwang, Capacitors with an Equivalent Oxide Thickness of <0.5 nm for Nanoscale Electronic Semiconductor Memory, *Adv. Funct. Mater.* 20 (2010) 2989–3003. <https://doi.org/10.1002/adfm.201000599>.
- [19] J. Mu, X. Chou, Z. Ma, J. He, J. Xiong, High-Performance MIM Capacitors for a Secondary Power Supply Application, *Micromachines.* 9 (2018) 69. <https://doi.org/10.3390/mi9020069>.
- [20] C.M. Herzinger, B. Johs, W.A. McGahan, J.A. Woollam, W. Paulson, Ellipsometric determination of optical constants for silicon and thermally grown silicon dioxide via a multi-sample, multi-wavelength, multi-angle investigation, *J. Appl. Phys.* 83 (1998) 3323–3336. <https://doi.org/10.1063/1.367101>.
- [21] D. Li, M. Carette, A. Granier, J.P. Landesman, A. Goulet, In situ spectroscopic ellipsometry study of TiO_2 films deposited by plasma enhanced chemical vapour deposition, *Appl. Surf. Sci.* 283 (2013) 234–239. <https://doi.org/10.1016/j.apsusc.2013.06.091>.
- [22] X.-X. Zhang, S. Cai, D. You, L.-H. Yan, H.-B. Lv, X.-D. Yuan, B. Jiang, Template-Free Sol-Gel Preparation of Superhydrophobic ORMOSIL Films for Double-Wavelength Broadband

- Antireflective Coatings, *Adv. Funct. Mater.* 23 (2013) 4361–4365.
<https://doi.org/10.1002/adfm.201203059>.
- [23] J. Choi, K. Han, J.H. Kim, Enhanced near infrared reflectance of TiO₂/SiO₂/TiO₂ multilayer structure using a base-catalyzed SiO₂ film, *Thin Solid Films*. 569 (2014) 100–103.
<https://doi.org/10.1016/j.tsf.2014.08.036>.
- [24] M. Mazur, D. Wojcieszak, J. Domaradzki, D. Kaczmarek, S. Song, F. Placido, TiO₂/SiO₂ multilayer as an antireflective and protective coating deposited by microwave assisted magnetron sputtering, *Opto-Electron. Rev.* 21 (2013). <https://doi.org/10.2478/s11772-013-0085-7>.
- [25] M. Magnozzi, S. Terreni, L. Anghinolfi, S. Uttiya, M.M. Carnasciali, G. Gemme, M. Neri, M. Principe, I. Pinto, L.-C. Kuo, S. Chao, M. Canepa, Optical properties of amorphous SiO₂-TiO₂ multilayered coatings for 1064-nm mirror technology, *Opt. Mater.* 75 (2018) 94–101.
<https://doi.org/10.1016/j.optmat.2017.09.043>.
- [26] D. Bhattacharyya, N.K. Sahoo, S. Thakur, N.C. Das, Spectroscopic ellipsometry of multilayer dielectric coatings, *Vacuum*. 60 (2001) 419–424. [https://doi.org/10.1016/S0042-207X\(00\)00222-0](https://doi.org/10.1016/S0042-207X(00)00222-0).
- [27] J. Oh, H. Na, I.-S. Mok, J. Kim, K. Lee, H. Sohn, Physical and electrical properties of band-engineered SiO₂/(TiO₂)_x(SiO₂)_{1-x} stacks for nonvolatile memory applications, *Appl. Phys. A*. 108 (2012) 679–684. <https://doi.org/10.1007/s00339-012-6950-2>.
- [28] C. Battaglin, F. Caccavale, A. Menelle, M. Montecchi, E. Nichelatti, F. Nicoletti, P. Polato, Characterisation of antireflective TiO₂/SiO₂ coatings by complementary techniques, *Thin Solid Films*. (1999) 4.
- [29] K. Yu-Zhang, G. Boisjolly, J. Rivory, L. Kilian, C. Colliex, Characterization of TiO₂/SiO₂ multilayers by high resolution transmission electron microscopy and electron energy loss spectroscopy, *Thin Solid Films*. 253 (1994) 299–302. [https://doi.org/10.1016/0040-6090\(94\)90337-9](https://doi.org/10.1016/0040-6090(94)90337-9).
- [30] W. Lin, J. Zheng, L. Yan, X. Zhang, Sol-gel preparation of self-cleaning SiO₂-TiO₂/SiO₂-TiO₂ double-layer antireflective coating for solar glass, *Results Phys.* 8 (2018) 532–536.
<https://doi.org/10.1016/j.rinp.2017.12.058>.
- [31] I. Pana, C. Vitelaru, A. Kiss, N.C. Zoita, M. Dinu, M. Braic, Design, fabrication and characterization of TiO₂-SiO₂ multilayer with tailored color glazing for thermal solar collectors, *Mater. Des.* 130 (2017) 275–284. <https://doi.org/10.1016/j.matdes.2017.05.063>.
- [32] J. Wang, J. Ge, H. Hou, M. Wang, G. Liu, G. Qiao, Y. Wang, Design and sol-gel preparation of SiO₂/TiO₂ and SiO₂/SnO₂/SiO₂-SnO₂ multilayer antireflective coatings, *Appl. Surf. Sci.* 422 (2017) 970–974. <https://doi.org/10.1016/j.apsusc.2017.06.133>.
- [33] M. Faustini, L. Nicole, C. Boissière, P. Innocenzi, C. Sanchez, D. Grosso, Hydrophobic, Antireflective, Self-Cleaning, and Antifogging Sol-Gel Coatings: An Example of Multifunctional Nanostructured Materials for Photovoltaic Cells, *Chem. Mater.* 22 (2010) 4406–4413.
<https://doi.org/10.1021/cm100937e>.
- [34] M.K. Bera, C.K. Maiti, Electrical properties of SiO₂/TiO₂ high-k gate dielectric stack, *Mater. Sci. Semicond. Process.* 9 (2006) 909–917. <https://doi.org/10.1016/j.mssp.2006.10.008>.
- [35] H. Báez, M. Estrada, J.C. Tinoco, Electrical Characterization of MOS Capacitors with SiO₂-TiO₂ Dielectric Stack Made by Room Temperature Plasma Oxidation, in: *Fifth IEEE Int. Caracas Conf. Devices*, Dominican Republic, 2004: p. 4.
- [36] D.K. Sarkar, D. Brassard, M.A.E. Khakani, L. Ouellet, Dielectric properties of sol-gel derived high-k titanium silicate thin films, *Thin Solid Films*. 515 (2007) 4788–4793.
<https://doi.org/10.1016/j.tsf.2006.11.155>.
- [37] P. Karasiński, C. Tyszkiewicz, R. Rogoziński, J. Jaglarz, J. Mazur, Optical rib waveguides based on sol-gel derived silica-titania films, *Thin Solid Films*. 519 (2011) 5544–5551.
<https://doi.org/10.1016/j.tsf.2011.02.064>.
- [38] S. Chao, W.-H. Wang, M.-Y. Hsu, L.-C. Wang, Characteristics of ion-beam-sputtered high-refractive-index TiO₂-SiO₂ mixed films, *J Opt Soc Am A*. 16 (1999) 1477–1483.
<https://doi.org/10.1364/JOSAA.16.001477>.
- [39] S. Larouche, H. Szymanowski, J.E. Klemberg-Sapieha, L. Martinu, S.C. Gujrathi, Microstructure of plasma-deposited SiO₂/TiO₂ optical films, *J. Vac. Sci. Technol. Vac. Surf. Films*. 22 (2004) 1200–1207. <https://doi.org/10.1116/1.1763912>.
- [40] D. Brassard, D.K. Sarkar, M.A. El Khakani, L. Ouellet, High-k titanium silicate thin films grown by reactive magnetron sputtering for complementary metal-oxide-semiconductor applications, *J. Vac. Sci. Technol. Vac. Surf. Films*. 22 (2004) 851. <https://doi.org/10.1116/1.1722530>.

- [41] D. Brassard, D.K. Sarkar, M.A. El Khakani, L. Ouellet, Tuning the electrical resistivity of pulsed laser deposited TiSiO_x thin films from highly insulating to conductive behaviors, *Appl. Phys. Lett.* 84 (2004) 2304–2306. <https://doi.org/10.1063/1.1688999>.
- [42] D. Brassard, M.A. El Khakani, Pulsed-laser deposition of high-k titanium silicate thin films, *J. Appl. Phys.* 98 (2005) 054912. <https://doi.org/10.1063/1.2039274>.
- [43] D. Brassard, D.K. Sarkar, M.A. El Khakani, L. Ouellet, Compositional effect on the dielectric properties of high-k titanium silicate thin films deposited by means of a cosputtering process, *J. Vac. Sci. Technol. Vac. Surf. Films.* 24 (2006) 600–605. <https://doi.org/10.1116/1.2180267>.
- [44] D. Brassard, L. Ouellet, M.A. El Khakani, Room-Temperature Deposited Titanium Silicate Thin Films for MIM Capacitor Applications, *IEEE Electron Device Lett.* 28 (2007) 261–263. <https://doi.org/10.1109/LED.2007.891754>.
- [45] D. Brassard, M.A. El Khakani, L. Ouellet, Substrate biasing effect on the electrical properties of magnetron-sputtered high-k titanium silicate thin films, *J. Appl. Phys.* 102 (2007) 034106. <https://doi.org/10.1063/1.2759196>.
- [46] D. Brassard, M.A. El Khakani, Thermal behavior of the microstructure and the electrical properties of magnetron-sputtered high-k titanium silicate thin films, *J. Appl. Phys.* 103 (2008) 114110. <https://doi.org/10.1063/1.2937241>.
- [47] D. Li, S. Elisabeth, A. Granier, M. Carette, A. Goulet, J.-P. Landesman, Structural and Optical Properties of PECVD TiO₂-SiO₂ Mixed Oxide Films for Optical Applications: Structural and Optical Properties of PECVD TiO₂-SiO₂ ..., *Plasma Process. Polym.* 13 (2016) 918–928. <https://doi.org/10.1002/ppap.201600012>.
- [48] P. Ondračka, D. Nečas, M. Carette, S. Elisabeth, D. Holec, A. Granier, A. Goulet, L. Zajíčková, M. Richard-Plouet, Unravelling local environments in mixed TiO₂-SiO₂ thin films by XPS and ab initio calculations, *Appl. Surf. Sci.* 510 (2020) 145056. <https://doi.org/10.1016/j.apsusc.2019.145056>.
- [49] Y. Gazal, C. Dublanche-Tixier, A. Antoine, M. Colas, C. Chazelas, P. Tristant, Elaboration of nanostructured TiO₂/SiO₂ films by plasma enhanced chemical vapor deposition at atmospheric pressure, *Thin Solid Films.* 619 (2016) 137–143. <https://doi.org/10.1016/j.tsf.2016.11.010>.
- [50] S. Kim, M.-H. Ham, B.-Y. Oh, H.J. Kim, J.-M. Myoung, High-k TixSi1-xO2 thin films prepared by co-sputtering method, *Microelectron. Eng.* 85 (2008) 100–103. <https://doi.org/10.1016/j.mee.2007.04.145>.
- [51] J.K. Nelson, ed., *Dielectric polymer nanocomposites*, Springer, New York, 2010.
- [52] H. Gleiter, *NANOSTRUCTURED MATERIALS: BASIC CONCEPTS AND MICROSTRUCTURE* p, *NANOSTRUCTURED Mater.* (n.d.) 29.
- [53] V.V. Pokropivny, V.V. Skorokhod, Classification of nanostructures by dimensionality and concept of surface forms engineering in nanomaterial science, *Mater. Sci. Eng. C.* 27 (2007) 990–993. <https://doi.org/10.1016/j.msec.2006.09.023>.
- [54] J. Jeevanandam, A. Barhoum, Y.S. Chan, A. Dufresne, M.K. Danquah, Review on nanoparticles and nanostructured materials: history, sources, toxicity and regulations, *Beilstein J. Nanotechnol.* 9 (2018) 1050–1074. <https://doi.org/10.3762/bjnano.9.98>.
- [55] P.I. Dolez, *Nanomaterials Definitions, Classifications, and Applications*, in: *Nanoengineering*, Elsevier, 2015: pp. 3–40. <https://doi.org/10.1016/B978-0-444-62747-6.00001-4>.
- [56] C. Sanchez, B. Julián, P. Belleville, M. Popall, Applications of hybrid organic–inorganic nanocomposites, *J. Mater. Chem.* 15 (2005) 3559. <https://doi.org/10.1039/b509097k>.
- [57] X.-Y. Zhang, H.-P. Li, X.-L. Cui, Y. Lin, Graphene/TiO₂ nanocomposites: synthesis, characterization and application in hydrogen evolution from water photocatalytic splitting, *J. Mater. Chem.* 20 (2010) 2801. <https://doi.org/10.1039/b917240h>.
- [58] J.-W. Rhim, H.-M. Park, C.-S. Ha, Bio-nanocomposites for food packaging applications, *Prog. Bionanocomposites Green Plast. Biomed. Appl.* 38 (2013) 1629–1652. <https://doi.org/10.1016/j.progpolymsci.2013.05.008>.
- [59] H. Dong, Z. Wu, F. Lu, Y. Gao, A. El-Shafei, B. Jiao, S. Ning, X. Hou, Optics–electrics highways: Plasmonic silver nanowires@TiO₂ core–shell nanocomposites for enhanced dye-sensitized solar cells performance, *Nano Energy.* 10 (2014) 181–191. <https://doi.org/10.1016/j.nanoen.2014.09.011>.
- [60] J. Xu, Y. Wang, S. Hu, Nanocomposites of graphene and graphene oxides: Synthesis, molecular functionalization and application in electrochemical sensors and biosensors. A review, *Microchim. Acta.* 184 (2017) 1–44. <https://doi.org/10.1007/s00604-016-2007-0>.

- [61] K. Müller, E. Bugnicourt, M. Latorre, M. Jorda, Y. Echegoyen Sanz, J. Lagaron, O. Miesbauer, A. Bianchin, S. Hankin, U. Bölz, G. Pérez, M. Jesdinszki, M. Lindner, Z. Scheuerer, S. Castelló, M. Schmid, Review on the Processing and Properties of Polymer Nanocomposites and Nanocoatings and Their Applications in the Packaging, Automotive and Solar Energy Fields, *Nanomaterials*. 7 (2017) 74. <https://doi.org/10.3390/nano7040074>.
- [62] Y. Rao, S. Chen, Molecular Composites Comprising TiO₂ and Their Optical Properties, *Macromolecules*. 41 (2008) 4838–4844. <https://doi.org/10.1021/ma800371v>.
- [63] R. Belka, Analysis of optical properties of fullerene-palladium nanostructures using effective medium theory, in: R.S. Romaniuk (Ed.), Wilga, Poland, 2013: p. 89030B. <https://doi.org/10.1117/12.2032015>.
- [64] A. Garahan, L. Pilon, J. Yin, I. Saxena, Effective optical properties of absorbing nanoporous and nanocomposite thin films, *J. Appl. Phys.* 101 (2007) 014320. <https://doi.org/10.1063/1.2402327>.
- [65] V. Lozovski, G. Strilchuk, Optical properties of nanocomposite films with inclusions of the same dimensions as the film thickness, in: 2015 IEEE 35th Int. Conf. Electron. Nanotechnol. ELNANO, IEEE, Kyiv, Ukraine, 2015: pp. 158–160. <https://doi.org/10.1109/ELNANO.2015.7146860>.
- [66] I. Khan, K. Saeed, I. Khan, Nanoparticles: Properties, applications and toxicities, *Arab. J. Chem.* 12 (2017) 908–931. <https://doi.org/10.1016/j.arabjc.2017.05.011>.
- [67] D. Li, M. Carette, A. Granier, J.P. Landesman, A. Goulet, Effect of ion bombardment on the structural and optical properties of TiO₂ thin films deposited from oxygen/titanium tetraisopropoxide inductively coupled plasma, *Thin Solid Films*. 589 (2015) 783–791. <https://doi.org/10.1016/j.tsf.2015.07.015>.
- [68] D. Li, S. Bulou, N. Gautier, S. Elisabeth, A. Goulet, M. Richard-Plouet, P. Choquet, A. Granier, Nanostructure and photocatalytic properties of TiO₂ films deposited at low temperature by pulsed PECVD, *Appl. Surf. Sci.* 466 (2019) 63–69. <https://doi.org/10.1016/j.apsusc.2018.09.230>.
- [69] J.-P. Jolivet, S. Cassaignon, C. Chanéac, D. Chiche, O. Durupthy, D. Portehault, Design of metal oxide nanoparticles: Control of size, shape, crystalline structure and functionalization by aqueous chemistry, *Comptes Rendus Chim.* 13 (2010) 40–51. <https://doi.org/10.1016/j.crci.2009.09.012>.
- [70] M. Auffan, M. Pedeutour, J. Rose, A. Masion, F. Ziarelli, D. Borschneck, C. Chaneac, C. Botta, P. Chaurand, J. Labille, J.-Y. Bottero, Structural Degradation at the Surface of a TiO₂-Based Nanomaterial Used in Cosmetics, *Environ. Sci. Technol.* 44 (2010) 2689–2694. <https://doi.org/10.1021/es903757q>.
- [71] K. Jamuna-Thevi, S.A. Bakar, S. Ibrahim, N. Shahab, M.R.M. Toff, Quantification of silver ion release, in vitro cytotoxicity and antibacterial properties of nanostructured Ag doped TiO₂ coatings on stainless steel deposited by RF magnetron sputtering, *Vacuum*. 86 (2011) 235–241. <https://doi.org/10.1016/j.vacuum.2011.06.011>.
- [72] T. Homola, M. Shekargoftar, P. Dzik, R. Krumpolec, Z. Ďurašová, M. Veselý, M. Černák, Low-temperature (70 °C) ambient air plasma-fabrication of inkjet-printed mesoporous TiO₂ flexible photoanodes, *Flex. Print. Electron.* 2 (2017) 035010. <https://doi.org/10.1088/2058-8585/aa88e6>.
- [73] B. O'Regan, M. Grätzel, A low-cost, high-efficiency solar cell based on dye-sensitized colloidal TiO₂ films, *Nature*. 353 (1991) 737–740. <https://doi.org/10.1038/353737a0>.
- [74] D. Adak, S. Ghosh, P. Chakrabarty, A. Mondal, H. Saha, R. Mukherjee, R. Bhattacharyya, Self-cleaning V-TiO₂:SiO₂ thin-film coatings with enhanced transmission for solar glass cover and related applications, *Sol. Energy*. 155 (2017) 410–418. <https://doi.org/10.1016/j.solener.2017.06.014>.
- [75] D. Adak, S. Ghosh, P. Chakraborty, K.M.K. Srivatsa, A. Mondal, H. Saha, R. Mukherjee, R. Bhattacharyya, Non lithographic block copolymer directed self-assembled and plasma treated self-cleaning transparent coating for photovoltaic modules and other solar energy devices, *Sol. Energy Mater. Sol. Cells*. 188 (2018) 127–139. <https://doi.org/10.1016/j.solmat.2018.08.011>.
- [76] S. Guldin, P. Kohn, M. Stefik, J. Song, G. Divitini, F. Ecarla, C. Ducati, U. Wiesner, U. Steiner, Self-Cleaning Antireflective Optical Coatings, *Nano Lett.* 13 (2013) 5329–5335. <https://doi.org/10.1021/nl402832u>.
- [77] H. Bellanger, T. Darmanin, E. Taffin de Givenchy, F. Guittard, Chemical and Physical Pathways for the Preparation of Superoleophobic Surfaces and Related Wetting Theories, *Chem. Rev.* 114 (2014) 2694–2716. <https://doi.org/10.1021/cr400169m>.

- [78] Y. Du, Y. Lv, F. Wang, X. Li, C. Li, Effect of TiO₂ nanoparticles on the breakdown strength of transformer oil, in: 2010 IEEE Int. Symp. Electr. Insul., IEEE, San Diego, CA, USA, 2010: pp. 1–3. <https://doi.org/10.1109/ELINSL.2010.5549772>.
- [79] M.R. Hoffmann, S.T. Martin, Wonyong. Choi, D.W. Bahnemann, Environmental Applications of Semiconductor Photocatalysis, *Chem. Rev.* 95 (1995) 69–96. <https://doi.org/10.1021/cr00033a004>.
- [80] S.M. Gupta, M. Tripathi, A review of TiO₂ nanoparticles, *Chin. Sci. Bull.* 56 (2011) 1639–1657. <https://doi.org/10.1007/s11434-011-4476-1>.
- [81] B. Enright, D. Fitzmaurice, Spectroscopic Determination of Electron and Hole Effective Masses in a Nanocrystalline Semiconductor Film, *J. Phys. Chem.* 100 (1996) 1027–1035. <https://doi.org/10.1021/jp951142w>.
- [82] A.G. Rolo, M.I. Vasilevskiy, Raman spectroscopy of optical phonons confined in semiconductor quantum dots and nanocrystals, *J. Raman Spectrosc.* 38 (2007) 618–633. <https://doi.org/10.1002/jrs.1746>.
- [83] Y. Gao, X. Zhao, P. Yin, F. Gao, Size-Dependent Raman Shifts for nanocrystals, *Sci. Rep.* 6 (2016). <https://doi.org/10.1038/srep20539>.
- [84] C. Pighini, D. Aymes, N. Millot, L. Saviot*, Low-frequency Raman characterization of size-controlled anatase TiO₂ nanopowders prepared by continuous hydrothermal syntheses, *J. Nanoparticle Res.* 9 (2007) 309–315. <https://doi.org/10.1007/s11051-005-9061-6>.
- [85] C. Pighini, Synthèses de nanocristaux de TiO₂ anatase à distribution de taille contrôlée. Influence de la taille des cristallites sur le spectre Raman et étude des propriétés de surface, (n.d.) 207.
- [86] L.D. Zhang, H.F. Zhang, G.Z. Wang, C.M. Mo, Y. Zhang, Dielectric behaviour of nano-TiO₂ bulks, *Phys. Status Solidi A.* 157 (1996) 483–491. <https://doi.org/10.1002/pssa.2211570232>.
- [87] G. Liu, W. Jian, H. Jin, Z. Shi, G. Qiao, A high dielectric constant in nano-TiO₂ ceramic prepared by a rapid and high-pressure sintering process, *Scr. Mater.* 65 (2011) 588–591. <https://doi.org/10.1016/j.scriptamat.2011.06.031>.
- [88] A.B. S., C.V. S., N.C. S., R.M. P., J.H. S., A.R. Lamani, Influence of particle size on band gap and dielectric properties of TiO₂ nanomaterials, in: Bikaner, India, 2016: p. 020347. <https://doi.org/10.1063/1.4946398>.
- [89] J.A. Davis, Energy Density Limits of Multiphase Composites With Dielectric Nanoparticles, *IEEE Trans. Nanotechnol.* 17 (2018) 250–260. <https://doi.org/10.1109/TNANO.2018.2790955>.
- [90] Z.-M. Dang, J.-K. Yuan, S.-H. Yao, R.-J. Liao, Flexible Nanodielectric Materials with High Permittivity for Power Energy Storage, *Adv. Mater.* 25 (2013) 6334–6365. <https://doi.org/10.1002/adma.201301752>.
- [91] D.K. Sarkar, D. Brassard, M.A. El Khakani, L. Ouellet, Single-electron tunneling at room temperature in Ti_xSi_{1-x}O₂ nanocomposite thin films, *Appl. Phys. Lett.* 87 (2005) 253108. <https://doi.org/10.1063/1.2147729>.
- [92] F. Fanelli, F. Fracassi, Aerosol-Assisted Atmospheric Pressure Cold Plasma Deposition of Organic–Inorganic Nanocomposite Coatings, *Plasma Chem. Plasma Process.* 34 (2014) 473–487. <https://doi.org/10.1007/s11090-013-9518-9>.
- [93] P.M. Ajayan, L.S. Schadler, P.V. Braun, Nanocomposite science and technology, 2nd repr, Wiley-VCH, Weinheim, 2005.
- [94] S. Kermadi, N. Agoudjil, S. Sali, M. Boumaour, S. Bourgeois, M.C. Marco de Lucas, Sol-gel synthesis of xTiO₂(100-x)SiO₂ nanocomposite thin films: Structure, optical and antireflection properties, *Thin Solid Films.* 564 (2014) 170–178. <https://doi.org/10.1016/j.tsf.2014.05.068>.
- [95] S. Kermadi, N. Agoudjil, S. Sali, L. Zougar, M. Boumaour, L. Broch, A. En Naciri, F. Placido, Microstructure and optical dispersion characterization of nanocomposite sol-gel TiO₂-SiO₂ thin films with different compositions, *Spectrochim. Acta. A. Mol. Biomol. Spectrosc.* 145 (2015) 145–154. <https://doi.org/10.1016/j.saa.2015.02.110>.
- [96] M.A.M. Lopes de Jesus, G.H. de Magalhães Gomes, A.S. Ferlauto, L.M. Seara, A. de Mello Ferreira, N. Della Santina Mohallem, A systematic study of multifunctional xTiO₂/(100-x)SiO₂ thin films prepared by sol-gel process, *J. Sol-Gel Sci. Technol.* 89 (2019) 380–391. <https://doi.org/10.1007/s10971-018-4867-8>.
- [97] C.A. Charitidis, P. Georgiou, M.A. Koklioti, A.-F. Trompeta, V. Markakis, Manufacturing nanomaterials: from research to industry, *Manuf. Rev.* 1 (2014) 11. <https://doi.org/10.1051/mfreview/2014009>.
- [98] L.L. Hench, J.K. West, The sol-gel process, *Chem. Rev.* 90 (1990) 33–72. <https://doi.org/10.1021/cr00099a003>.

- [99] K. Kwiatkowski, C. Lukehart, Nanocomposites prepared by sol-gel methods Synthesis and characterization, in: *Handb. Nanostructured Mater. Nanotechnol.*, Elsevier, 2000: pp. 387–421. <https://doi.org/10.1016/B978-012513760-7/50011-3>.
- [100] A.V. Nikam, B.L.V. Prasad, A.A. Kulkarni, Wet chemical synthesis of metal oxide nanoparticles: a review, *CrystEngComm*. 20 (2018) 5091–5107. <https://doi.org/10.1039/C8CE00487K>.
- [101] M. Guglielmi, G. Kickelbick, A. Martucci, eds., *Sol-Gel Nanocomposites*, Springer New York, New York, NY, 2014. <https://doi.org/10.1007/978-1-4939-1209-4>.
- [102] W. Dong, C.W. Lee, X. Lu, Y. Sun, W. Hua, G. Zhuang, S. Zhang, J. Chen, H. Hou, D. Zhao, Synchronous role of coupled adsorption and photocatalytic oxidation on ordered mesoporous anatase TiO₂-SiO₂ nanocomposites generating excellent degradation activity of RhB dye, *Appl. Catal. B Environ.* 95 (2010) 197–207. <https://doi.org/10.1016/j.apcatb.2009.12.025>.
- [103] A. Nilchi, S. Janitabar-Darzi, A.R. Mahjoub, S. Rasouli-Garmarodi, New TiO₂/SiO₂ nanocomposites—Phase transformations and photocatalytic studies, *Colloids Surf. Physicochem. Eng. Asp.* 361 (2010) 25–30. <https://doi.org/10.1016/j.colsurfa.2010.03.006>.
- [104] A. Nilchi, S. Janitabar-Darzi, S. Rasouli-Garmarodi, Sol-Gel Preparation of Nanoscale TiO₂/SiO₂ Composite for Eliminating of Con Red Azo Dye, *Mater. Sci. Appl.* 02 (2011) 476–480. <https://doi.org/10.4236/msa.2011.25064>.
- [105] W. Dong, Y. Sun, Q. Ma, L. Zhu, W. Hua, X. Lu, G. Zhuang, S. Zhang, Z. Guo, D. Zhao, Excellent photocatalytic degradation activities of ordered mesoporous anatase TiO₂-SiO₂ nanocomposites to various organic contaminants, *J. Hazard. Mater.* 229–230 (2012) 307–320. <https://doi.org/10.1016/j.jhazmat.2012.06.002>.
- [106] L. Pinho, M.J. Mosquera, Photocatalytic activity of TiO₂-SiO₂ nanocomposites applied to buildings: Influence of particle size and loading, *Appl. Catal. B Environ.* 134–135 (2013) 205–221. <https://doi.org/10.1016/j.apcatb.2013.01.021>.
- [107] Q. Mao, D. Zeng, K. Xu, C. Xie, Fabrication of porous TiO₂-SiO₂ multifunctional anti-reflection coatings by sol-gel spin coating method, *RSC Adv.* 4 (2014) 58101–58107. <https://doi.org/10.1039/C4RA10424B>.
- [108] C. Holtzinger, L. Rapenne, P. Chaudouët, G. Berthomé, J.C. Joud, M. Langlet, Influence of sol composition on natural superhydrophilicity of sol gel-derived TiO₂-SiO₂ nanocomposite thin films, *Emerg. Mater. Res.* 1 (2012) 127–135. <https://doi.org/10.1680/emr.11.00024>.
- [109] E. Pakdel, W.A. Daoud, X. Wang, Self-cleaning and superhydrophilic wool by TiO₂/SiO₂ nanocomposite, *Appl. Surf. Sci.* 275 (2013) 397–402. <https://doi.org/10.1016/j.apsusc.2012.10.141>.
- [110] M.L.V. de Chiara, S. Pal, A. Licciulli, M.L. Amodio, G. Colelli, Photocatalytic degradation of ethylene on mesoporous TiO₂/SiO₂ nanocomposites: Effects on the ripening of mature green tomatoes, *Biosyst. Eng.* 132 (2015) 61–70. <https://doi.org/10.1016/j.biosystemseng.2015.02.008>.
- [111] P.G. Kudryavtsev, O.L. Figovsky, NANOCOMPOSITES BASED ON HYBRID ORGANO-SILICATE MATRIX, (2016) 23.
- [112] V. Kondratiev, Processing and characterization of transparent electrode materials, (2017). <https://doi.org/10.13140/RG.2.2.34906.24008>.
- [113] E.-T. Hu, X.-X. Liu, Q.-Y. Cai, Y. Yao, K.-Y. Zang, K.-H. Yu, W. Wei, X.-X. Xu, Y.-X. Zheng, S.-Y. Wang, R.-J. Zhang, L.-Y. Chen, Tunable optical properties of co-sputtered Ti-SiO₂ nanocomposite thin films, *Opt. Mater. Express.* 7 (2017) 2387. <https://doi.org/10.1364/OME.7.002387>.
- [114] J.-S. Chen, S. Chao, J.-S. Kao, H. Niu, C.-H. Chen, Mixed films of TiO₂-SiO₂ deposited by double electron-beam coevaporation, *Appl. Opt.* 35 (1996) 90. <https://doi.org/10.1364/AO.35.000090>.
- [115] T. Ghodselahe, M.A. Vesaghi, A. Shafiekhani, A. Baradaran, A. Karimi, Z. Mobini, Co-deposition process of RF-Sputtering and RF-PECVD of copper/carbon nanocomposite films, *Surf. Coat. Technol.* 202 (2008) 2731–2736. <https://doi.org/10.1016/j.surfcoat.2007.10.009>.
- [116] A.A. El Mel, B. Angleraud, E. Gautron, A. Granier, P.Y. Tessier, Microstructure and composition of TiC/a-C:H nanocomposite thin films deposited by a hybrid IPVD/PECVD process, *Surf. Coat. Technol.* 204 (2010) 1880–1883. <https://doi.org/10.1016/j.surfcoat.2009.09.045>.
- [117] K.L. Kolipaka, V. Brueser, R. Schlueter, A. Quade, J. Schaefer, H. Wulff, T. Strunskus, F. Faupel, Simple method of hybrid PVD/PECVD to prepare well-dispersed cobalt-plasma polymerized hexamethyldisilazane nanocomposites, *Surf. Coat. Technol.* 207 (2012) 565–570. <https://doi.org/10.1016/j.surfcoat.2012.07.073>.
- [118] L. Bedel, C. Cayron, M. Jouve, F. Maury, Embedded layer of Ag nanoparticles prepared by a combined PECVD/PVD process producing SiO_xC_y-Ag nanocomposite thin films, *Nanotechnology*. 23 (2012) 015603. <https://doi.org/10.1088/0957-4484/23/1/015603>.

- [119] O. Kylián, R. Štefaníková, A. Kuzminova, J. Hanuš, P. Solař, P. Kúš, M. Cieslar, H. Biederman, In-flight plasma modification of nanoparticles produced by means of gas aggregation sources as an effective route for the synthesis of core-satellite Ag/plasma polymer nanoparticles, *Plasma Phys. Control. Fusion*. 62 (2020) 014005. <https://doi.org/10.1088/1361-6587/ab4115>.
- [120] H. Biederman, O. Kylian, M. Drabik, A. Choukourov, O. Polonskyi, P. Solar, Nanocomposite and nanostructured films with plasma polymer matrix, *Surf. Coat. Technol.* 211 (2012) 127–137. <https://doi.org/10.1016/j.surfcoat.2011.09.011>.
- [121] H. Biederman, Nanocomposites and nanostructures based on plasma polymers, *Surf. Coat. Technol.* 205 (2011) S10–S14. <https://doi.org/10.1016/j.surfcoat.2011.03.115>.
- [122] N. Patelli, A. Migliori, V. Morandi, L. Pasquini, One-Step Synthesis of Metal/Oxide Nanocomposites by Gas Phase Condensation, *Nanomaterials*. 9 (2019) 219. <https://doi.org/10.3390/nano9020219>.
- [123] D. Nikitin, J. Hanuš, S. Ali-Ogly, O. Polonskyi, J. Drewes, F. Faupel, H. Biederman, A. Choukourov, The evolution of Ag nanoparticles inside a gas aggregation cluster source, *Plasma Process. Polym.* 16 (2019) 1900079. <https://doi.org/10.1002/ppap.201900079>.
- [124] T. Košutová, L. Horák, A. Shelemin, M. Vaidulych, J. Hanuš, H. Biederman, O. Kylián, P. Solař, M. Cieslar, A. Choukourov, M. Dopita, Synthesis and microstructure investigation of heterogeneous metal-plasma polymer Ag/HMDSO nanoparticles, *Surf. Interface Anal.* (2020). <https://doi.org/10.1002/sia.6779>.
- [125] P. Solař, J. Hanuš, M. Cieslar, T. Košutová, K. Škorvánková, O. Kylián, P. Kúš, H. Biederman, Composite Ni@Ti nanoparticles produced in arrow-shaped gas aggregation source, *J. Phys. Appl. Phys.* 53 (2020) 195303. <https://doi.org/10.1088/1361-6463/ab7353>.
- [126] Y. Huttel, ed., *Gas-phase synthesis of nanoparticles*, Wiley-VCH, Weinheim, Germany, 2017.
- [127] J. Kratochvíl, A. Kuzminova, O. Kylián, State-of-the-Art, and Perspectives of, Silver/Plasma Polymer Antibacterial Nanocomposites, *Antibiotics*. 7 (2018) 78. <https://doi.org/10.3390/antibiotics7030078>.
- [128] A.B.D. Nandiyanto, K. Okuyama, Progress in developing spray-drying methods for the production of controlled morphology particles: From the nanometer to submicrometer size ranges, *Adv. Powder Technol.* 22 (2011) 1–19. <https://doi.org/10.1016/j.apt.2010.09.011>.
- [129] A. Suhendi, A.B.D. Nandiyanto, M.M. Munir, T. Ogi, L. Gradon, K. Okuyama, Self-Assembly of Colloidal Nanoparticles Inside Charged Droplets during Spray-Drying in the Fabrication of Nanostructured Particles, *Langmuir*. 29 (2013) 13152–13161. <https://doi.org/10.1021/la403127e>.
- [130] X. Wang, H. Masumoto, Y. Someno, T. Hirai, Microstructure and optical properties of amorphous TiO₂-SiO₂ composite @lms synthesized by helicon plasma sputtering, *Thin Solid Films*. (1999) 5.
- [131] W.-N. Wang, Y. Itoh, I.W. Lenggoro, K. Okuyama, Nickel and nickel oxide nanoparticles prepared from nickel nitrate hexahydrate by a low pressure spray pyrolysis, *Mater. Sci. Eng. B*. 111 (2004) 69–76. <https://doi.org/10.1016/j.mseb.2004.03.024>.
- [132] W.-N. Wang, A. Purwanto, I.W. Lenggoro, K. Okuyama, H. Chang, H.D. Jang, Investigation on the Correlations between Droplet and Particle Size Distribution in Ultrasonic Spray Pyrolysis, *Ind. Eng. Chem. Res.* 47 (2008) 1650–1659. <https://doi.org/10.1021/ie070821d>.
- [133] G. Schaldach, L. Berger, I. Rrazilov, H. Berndt, Characterization of a cyclone spray chamber for ICP spectrometry by computer simulation, *J. Anal. At. Spectrom.* 17 (2002) 334–344. <https://doi.org/10.1039/b106024b>.
- [134] C.S. Westphal, K. Kahen, W.F. Rutkowski, B.W. Acon, A. Montaser, Demountable direct injection high efficiency nebulizer for inductively coupled plasma mass spectrometry, *Spectrochim. Acta Part B At. Spectrosc.* 59 (2004) 353–368. <https://doi.org/10.1016/j.sab.2004.01.004>.
- [135] H. Matusiewicz, M. Ślachciński, Simultaneous determination of As, Bi, Sb, Se and Sn by microwave induced plasma spectrometry using a quadruple-mode microflow ultrasonic nebulizer for in situ hydride generation with internal standardization, *Microchem. J.* 131 (2017) 70–78. <https://doi.org/10.1016/j.microc.2016.11.017>.
- [136] J. Giersz, M. Bartosiak, K. Jankowski, Sensitive determination of Hg together with Mn, Fe, Cu by combined photochemical vapor generation and pneumatic nebulization in the programmable temperature spray chamber and inductively coupled plasma optical emission spectrometry, *Talanta*. 167 (2017) 279–285. <https://doi.org/10.1016/j.talanta.2017.02.018>.
- [137] H. Matusiewicz, M. Ślachciński, Analytical evaluation of a quadruple-mode micro-flow ultrasonic nebulizer for sample introduction in microwave induced plasma spectrometry, *Microchem. J.* 130 (2017) 345–352. <https://doi.org/10.1016/j.microc.2016.10.010>.

- [138] E. Brinley, K.S. Babu, S. Seal, The solution precursor plasma spray processing of nanomaterials, *JOM*. 59 (2007) 54–59. <https://doi.org/10.1007/s11837-007-0090-8>.
- [139] N.D. Boscher, P. Choquet, D. Duday, N. Kerbellec, J.-C. Lambrechts, R. Maurau, Luminescent lanthanide-based hybrid coatings deposited by atmospheric pressure plasma assisted chemical vapour deposition, *J. Mater. Chem.* 21 (2011) 18959. <https://doi.org/10.1039/c1jm14659a>.
- [140] P. Fauchais, A. Joulia, S. Goutier, C. Chazelas, M. Vardelle, A. Vardelle, S. Rossignol, Suspension and solution plasma spraying, *J. Phys. Appl. Phys.* 46 (2013) 224015. <https://doi.org/10.1088/0022-3727/46/22/224015>.
- [141] J. Haapanen, M. Aromaa, H. Teisala, M. Tuominen, M. Stepien, J.J. Saarinen, M. Heikkilä, M. Toivakka, J. Kuusipalo, J.M. Mäkelä, Binary TiO₂/SiO₂ nanoparticle coating for controlling the wetting properties of paperboard, *Mater. Chem. Phys.* 149–150 (2015) 230–237. <https://doi.org/10.1016/j.matchemphys.2014.10.011>.
- [142] A. Dembele, M. Rahman, I. Reid, B. Twomey, J.M.D. MacElroy, D.P. Dowling, Deposition of Hybrid Organic–Inorganic Composite Coatings Using an Atmospheric Plasma Jet System, *J. Nanosci. Nanotechnol.* 11 (2011) 8730–8737. <https://doi.org/10.1166/jnn.2011.3459>.
- [143] J. Schäfer, K. Fricke, F. Mika, Z. Pokorná, L. Zajíčková, R. Foest, Liquid assisted plasma enhanced chemical vapour deposition with a non-thermal plasma jet at atmospheric pressure, *Thin Solid Films*. 630 (2017) 71–78. <https://doi.org/10.1016/j.tsf.2016.09.022>.
- [144] A. Liguori, E. Traldi, E. Toccaceli, R. Laurita, A. Pollicino, M.L. Focarete, V. Colombo, M. Gherardi, Co-Deposition of Plasma-Polymerized Polyacrylic Acid and Silver Nanoparticles for the Production of Nanocomposite Coatings Using a Non-Equilibrium Atmospheric Pressure Plasma Jet: Co-Deposition of Plasma-Polymerized Polyacrylic Acid and Silver Nanoparticles..., *Plasma Process. Polym.* 13 (2016) 623–632. <https://doi.org/10.1002/ppap.201500143>.
- [145] E. Marino, T. Huijser, Y. Creyghton, A. van der Heijden, Synthesis and coating of copper oxide nanoparticles using atmospheric pressure plasmas, *Surf. Coat. Technol.* 201 (2007) 9205–9208. <https://doi.org/10.1016/j.surfcoat.2007.04.091>.
- [146] J. Bardon, J. Bour, D. Del Frari, C. Arnoult, D. Ruch, Dispersion of Cerium-Based Nanoparticles in an Organosilicon Plasma Polymerized Coating: Effect on Corrosion Protection, *Plasma Process. Polym.* 6 (2009) S655–S659. <https://doi.org/10.1002/ppap.200931710>.
- [147] D. Del Frari, J. Bour, J. Bardon, O. Buchheit, C. Arnoult, D. Ruch, Hybrid Layers Deposited by an Atmospheric Pressure Plasma Process for Corrosion Protection of Galvanized Steel, *J. Nanosci. Nanotechnol.* 10 (2010) 2611–2619. <https://doi.org/10.1166/jnn.2010.1460>.
- [148] F. Fanelli, A.M. Mastrangelo, F. Fracassi, Aerosol-Assisted Atmospheric Cold Plasma Deposition and Characterization of Superhydrophobic Organic–Inorganic Nanocomposite Thin Films, *Langmuir*. 30 (2014) 857–865. <https://doi.org/10.1021/la404755n>.
- [149] J. Profili, O. Levasseur, J.-B. Blaisot, A. Koronai, L. Stafford, N. Gherardi, Nebulization of Nanocolloidal Suspensions for the Growth of Nanocomposite Coatings in Dielectric Barrier Discharges, *Plasma Process. Polym.* 13 (2016) 981–989. <https://doi.org/10.1002/ppap.201500223>.
- [150] J. Profili, O. Levasseur, N. Naudé, C. Chaneac, L. Stafford, N. Gherardi, Influence of the voltage waveform during nanocomposite layer deposition by aerosol-assisted atmospheric pressure Townsend discharge, *J. Appl. Phys.* 120 (2016) 053302. <https://doi.org/10.1063/1.4959994>.
- [151] J. Profili, O. Levasseur, A. Koronai, L. Stafford, N. Gherardi, Deposition of nanocomposite coatings on wood using cold discharges at atmospheric pressure, *Surf. Coat. Technol.* 309 (2017) 729–737. <https://doi.org/10.1016/j.surfcoat.2016.10.095>.
- [152] J. Profili, S. Dap, O. Levasseur, N. Naude, A. Belinger, L. Stafford, N. Gherardi, Interaction of atomized colloid with an ac electric field in a dielectric barrier discharge reactor used for deposition of nanocomposite coatings, *J. Phys. Appl. Phys.* 50 (2017) 075201. <https://doi.org/10.1088/1361-6463/aa515f>.
- [153] P. Brunet, R. Rincón, J.-M. Martinez, Z. Matouk, F. Fanelli, M. Chaker, F. Massines, Control of composite thin film made in an Ar/isopropanol/TiO₂ nanoparticles dielectric barrier discharge by the excitation frequency, *Plasma Process. Polym.* (2017) n/a-n/a. <https://doi.org/10.1002/ppap.201700049>.
- [154] P. Brunet, Procédé de dépôt de couches minces nanocomposites par décharge à barrière diélectrique : de l'aérosol d'une suspension colloïdale à la morphologie du dépôt, (n.d.) 187.
- [155] Model 3076 Constant Output Atomizer Instruction Manual, (n.d.) 63.
- [156] P.J. Bruggeman, M.J. Kushner, B.R. Locke, J.G.E. Gardeniers, W.G. Graham, D.B. Graves, R.C.H.M. Hofman-Caris, D. Maric, J.P. Reid, E. Ceriani, D. Fernandez Rivas, J.E. Foster, S.C. Garrick, Y. Gorbanev, S. Hamaguchi, F. Iza, H. Jablonowski, E. Klimova, J. Kolb, F. Krcma, P. Lukes, Z.

- Machala, I. Marinov, D. Mariotti, S. Mededovic Thagard, D. Minakata, E.C. Neyts, J. Pawlat, Z.L. Petrovic, R. Pflieger, S. Reuter, D.C. Schram, S. Schröter, M. Shiraiwa, B. Tarabová, P.A. Tsai, J.R.R. Verlet, T. von Woedtke, K.R. Wilson, K. Yasui, G. Zvereva, Plasma-liquid interactions: a review and roadmap, *Plasma Sources Sci. Technol.* 25 (2016) 053002. <https://doi.org/10.1088/0963-0252/25/5/053002>.
- [157] E. Hemmer, I. Kumakiri, N. Lecerf, R. Bredesen, S. Barth, J. Altmayer, N. Donia, C. Cavalius, K. Soga, S. Mathur, Nanostructured ZrO₂ membranes prepared by liquid-injection chemical vapor deposition, *Microporous Mesoporous Mater.* 163 (2012) 229–236. <https://doi.org/10.1016/j.micromeso.2012.06.057>.
- [158] L. Avril, J. Boudon, M.C. Marco de Lucas, L. Imhoff, Alumina particle reinforced TiO₂ composite films grown by direct liquid injection MOCVD, *Vacuum.* 107 (2014) 259–263. <https://doi.org/10.1016/j.vacuum.2014.02.020>.
- [159] M. Vervaele, B. De Roo, O. Deschaume, M. Rajala, H. Guillon, M. Sousa, C. Bartic, C. Van Haesendonck, J.W. Seo, J.-P. Locquet, Development of a new direct liquid injection system for nanoparticle deposition by chemical vapor deposition using nanoparticle solutions, *Rev. Sci. Instrum.* 87 (2016) 025101. <https://doi.org/10.1063/1.4940937>.
- [160] Z. Li, R.G. Gordon, V. Pallem, H. Li, D.V. Shenai, Direct-Liquid-Injection Chemical Vapor Deposition of Nickel Nitride Films and Their Reduction to Nickel Films, *Chem. Mater.* 22 (2010) 3060–3066. <https://doi.org/10.1021/cm903636j>.
- [161] M. Vervaele, B. De Roo, J. Debehets, M. Sousa, L. Zhang, B. Van Bilzen, S. Seré, H. Guillon, M. Rajala, J.W. Seo, J.-P. Locquet, A Novel Direct Liquid Injection Low Pressure Chemical Vapor Deposition System (DLI-LPCVD) for the Deposition of Thin Films: A Novel Direct Liquid Injection Low Pressure Chemical..., *Adv. Eng. Mater.* 19 (2017) 1700193. <https://doi.org/10.1002/adem.201700193>.
- [162] M. Vervaele, B. De Roo, J. Debehets, M. Sousa, L. Zhang, B. Van Bilzen, S. Seré, H. Guillon, M. Rajala, J. Won Seo, J.-P. Locquet, Direct Liquid Injection – Low Pressure Chemical Vapor Deposition of Silica Thin Films from Di-t-butoxydiacetoxysilane, *Adv. Eng. Mater.* (2017) 1700425. <https://doi.org/10.1002/adem.201700425>.
- [163] L. Avril, J.M. Decams, L. Imhoff, Pulsed Direct liquid Injection ALD of TiO₂ Films Using Titanium Tetraisopropoxide Precursor, *Phys. Procedia.* 46 (2013) 33–39. <https://doi.org/10.1016/j.phpro.2013.07.063>.
- [164] L. Avril, S. Reymond-Laruinaz, J.M. Decams, S. Bruyère, V. Potin, M.C.M. de Lucas, L. Imhoff, TiO₂ anatase films obtained by direct liquid injection atomic layer deposition at low temperature, *Appl. Surf. Sci.* 288 (2014) 201–207. <https://doi.org/10.1016/j.apsusc.2013.10.007>.
- [165] A.D. Ross, K.K. Gleason, The CVD of Nanocomposites Fabricated via Ultrasonic Atomization, *Chem. Vap. Depos.* 12 (2006) 225–230. <https://doi.org/10.1002/cvde.200506368>.
- [166] D. Ogawa, I. Saraf, A. Sra, R. Timmons, M. Goeckner, L. Overzet, The direct injection of liquid droplets into low pressure plasmas, *J. Vac. Sci. Technol. Vac. Surf. Films.* 27 (2009) 342–351. <https://doi.org/10.1116/1.3081965>.
- [167] M. Coppins, The critical droplet size in a misty plasma, (n.d.) 4.
- [168] M. Coppins, Electrostatic Breakup in a Misty Plasma, *Phys. Rev. Lett.* 104 (2010). <https://doi.org/10.1103/PhysRevLett.104.065003>.
- [169] D. Ogawa, C.W. Chung, M. Goeckner, L. Overzet, Transient effects caused by pulsed gas and liquid injections into low pressure plasmas, *Plasma Sources Sci. Technol.* 19 (2010) 034013. <https://doi.org/10.1088/0963-0252/19/3/034013>.
- [170] M. Goeckner, D. Ogawa, I. Saraf, L. Overzet, Progress report: Direct injection of liquids into low-pressure plasmas, *J. Phys. Conf. Ser.* 162 (2009) 012014. <https://doi.org/10.1088/1742-6596/162/1/012014>.
- [171] G. Carnide, Procédé de dépôt couplant un réacteur-injecteur et un plasma basse pression - vers le dépôt de couches minces multifonctionnelles pour l'aéronautique, Toulouse 3, 2020.
- [172] M. Kahn, Y. Champouret, R. Clergereaux, C. Vahlas, A.-F. Mingotaud, G. Carnide, Procédé de préparation de nanoparticules, WO 2018/019862 Al, n.d.
- [173] M. Brust, M. Walker, D. Bethell, D.J. Schiffrin, R. Whyman, Synthesis of thiol-derivatised gold nanoparticles in a two-phase Liquid-Liquid system, *J Chem Soc Chem Commun.* 0 (1994) 801–802. <https://doi.org/10.1039/C39940000801>.

Chapter 2

Experimental Systems and Characterization Techniques

For the successful elaboration of the experimental steps proposed in Chapter 1, several experimental systems were used. In all the experiments, TiO₂ NPs dispersed in an organic solvent forming a colloidal solution were used, the preparation steps of which, are analyzed in this Chapter. In Chapter 3, for the investigation of the plasma-NPs interactions, a low pressure O₂ Inductively Coupled Plasma reactor was used (ICP) on Spin Coated TiO₂ NPs films. In Chapter 4, the possibility of acquiring functional multilayer films using a combination of spin coating and Plasma Enhanced Deposition (PECVD) techniques were investigated. Both the ICP O₂ plasma and the PECVD elaborated in the specific reactor have been extensively examined in the past. Thus, a brief description of them is given. Finally, aiming towards the implementation of the hybrid one-step approach of directly introducing the liquid droplets inside the O₂/HMDSO low pressure plasma, a new system configuration was set up. Hence, in this chapter all the experimental systems are being analyzed. Furthermore, to assess the physical, chemical and optical characteristics of the produced films, several characterization techniques were used, which are explained in this Chapter.

Table of Contents

2.1 Preparation of the TiO ₂ colloidal solution.....	81
2.2 Experimental Systems for thin film deposition and treatment.....	82
2.2.1 Spin Coating	82
2.2.2 Low Pressure Plasma Reactor	83
2.2.2.1 O ₂ Plasma Treatment system	84
2.2.2.2 Plasma Enhanced Chemical Vapor Deposition (PECVD)	85
2.2.2.3 Hybrid system for the Nanocomposite thin film deposition.....	86
2.5 In situ Characterization Techniques	87
2.5.1 Ellipsometry.....	87
2.5.2 Optical Emission Spectroscopy (OES).....	92
2.6 <i>Ex situ</i> Characterization Techniques	93
2.6.1 Scanning Electron Microscopy (SEM)	93
2.6.2 Atomic Force Microscopy (AFM).....	95
2.6.3 Transmission Electron Microscopy (TEM)	96
2.6.4 X-Ray Photoelectron Spectroscopy (XPS)	97
2.6.5 Raman Spectroscopy	99
Conclusion	99
Bibliography	101

2.1 Preparation of the TiO₂ colloidal solution

The lab-made colloidal solution of TiO₂ NPs used in all the experiments that are analyzed in the following Chapters, has been already developed and analyzed in a previous study of our group[1]. Briefly, the colloidal solution was prepared using titanium precursor [Ti₈O₁₂(H₂O)₂₄]Cl₈.HCl.7H₂O, denoted Ti₈O₁₂, 4-methyl-1,3-dioxolan-2-one also known as propylene carbonate (PC) (Sigma-Aldrich 99.7%) and ultrapure milli-Q water. Before synthesis, the crystals of titanium precursor were eluted several times by ethanol and dried in nitrogen flow. For each synthesis, Ti₈O₁₂ crystals were dissolved in the appropriate amount of water by vigorous stirring. This led to the dissolution of the TiO₂ precursor. After this step, Propylene Carbonate was added. The mixture was heated in an autoclave, at 120°C for 24 hours. This step led to the consumption of water and the conversion of PC into 1,2-propanediol or propylene glycol (PG).

As synthesized, the solvent of this solution is a mixture of propylene carbonate and or propylene glycol, with a molar fraction in PC, $x_{PC}=0.27$, where $x_{PC} = [PC]/([PC] + [PG])$. In order to deposit a highly-concentrated and sufficiently-thick layer of TiO₂ NPs by spin coating (Chapter 3, 4), the solution was concentrated by evaporating part of the solvent at 120 °C. Consequently, due to the lower volatility of PC with respect to PG, x_{PC} increases by enrichment in PC. As shown in Figure 2.1, such change in x_{PC} also modifies the viscosity of the solution (determined using a Lovis 2000 ME-Anton-Paar viscometer). For the deposition of TiO₂ NPs layers using spin coating in Chapter 3 and 4, $x_{PC}=0.6$ was used. Thus upon further evaporation during spin coating, the viscosity remains in a narrow range of values [2] from 4.4 to 2.7 mPa s for $x= 0.6$ to 1, respectively. For the direct injection of the colloidal solution (Chapter 5 and 6), the colloidal solution was used as-synthesized i.e., with the initial $x_{PC}=0.27$.

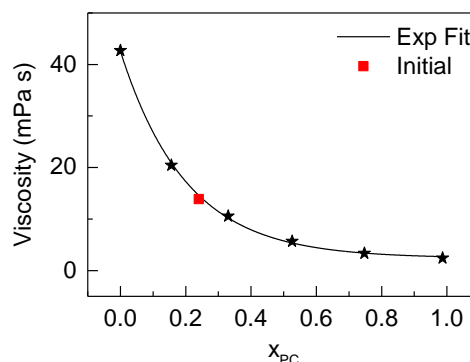


Figure 2.1: Graph of viscosity to the x_{pc} value. The values indicated by black stars are experimental ones using reference solutions with different starting x_{pc} values; the red square corresponds to as-synthesized colloidal solution.

A variation in the water content during the synthesis may change the size of the NPs. Smaller NPs were selected for the direct injection of the colloidal solution inside the low-pressure plasma system (Chapter 5 and 6) than for the spin coated thin films (Chapter 3 and 4), in order to limit possible clogging of the injector nozzle.

2.2 Experimental Systems for thin film deposition and treatment

In this Section, the experimental systems will be analyzed. As explained in the strategy of the thesis, there are different experiments giving access to the final target of this work, named the hybrid one-step approach creating nanocomposite thin films. Hence, for Chapter 3, the spin coating deposition technique and the plasma treatment with O_2 low pressure Inductive Coupled Plasma (ICP) will be used. Furthermore, in Chapter 4 the combination of spin coating and Plasma Enhanced Chemical Vapor Deposition (PECVD) will be attempted to create multilayer films. Finally, for the injection of the TiO_2 NPs and the creation of the SiO_2 matrix, a combination of systems will be presented here.

2.2.1 Spin Coating

In Chapter 3 and 4, the spin coating process is used, in order to identify the interactions induced by the plasma on the NPs film and create a multilayer structure, accordingly. In order to achieve a homogeneous layer of TiO_2 NPs, a two-step spin coating program was chosen. More precisely, using Spin Processor Laurell WS-650Mz-23NPPB, the first step was set to a spinning speed of 1000 rotations per minute (rpm) for 30 seconds to ensure a homogeneous spread of the solution on the substrate surface. In the second step, a speed of 2000 rpm for 1 minute was used to activate the drying process of the spin-coated layer. After each spin-coating set, the substrate was dried at $150^\circ C$ for 10 minutes. To acquire a thickness of 40-50 nm (thickness used in the experiments of Chapter 3 and 4), three spin-coating sets were performed. The schematic illustration of this process is given in Figure 2.2. The substrate used was silicon with 500 nm thermally grown silica on top, as it was found experimentally that the deposition is more homogeneous than using silicon one due to better wettability of the solution.

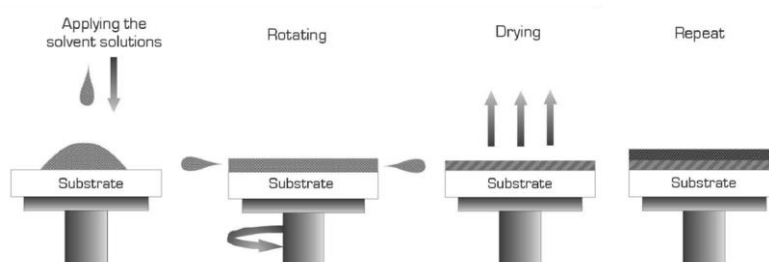


Figure 2.2: Schematic illustration of the spin coating stages [3]

2.2.2 Low Pressure Plasma Reactor

For the elaboration of our experimental strategy three systems were used. An O₂ ICP Plasma Source, a PECVD system and a hybrid configuration for the creation of the NC thin films coupling the colloidal solution with the plasma process. All these were implemented under the same reactor given as a 3D schematic in Figure 2.3.

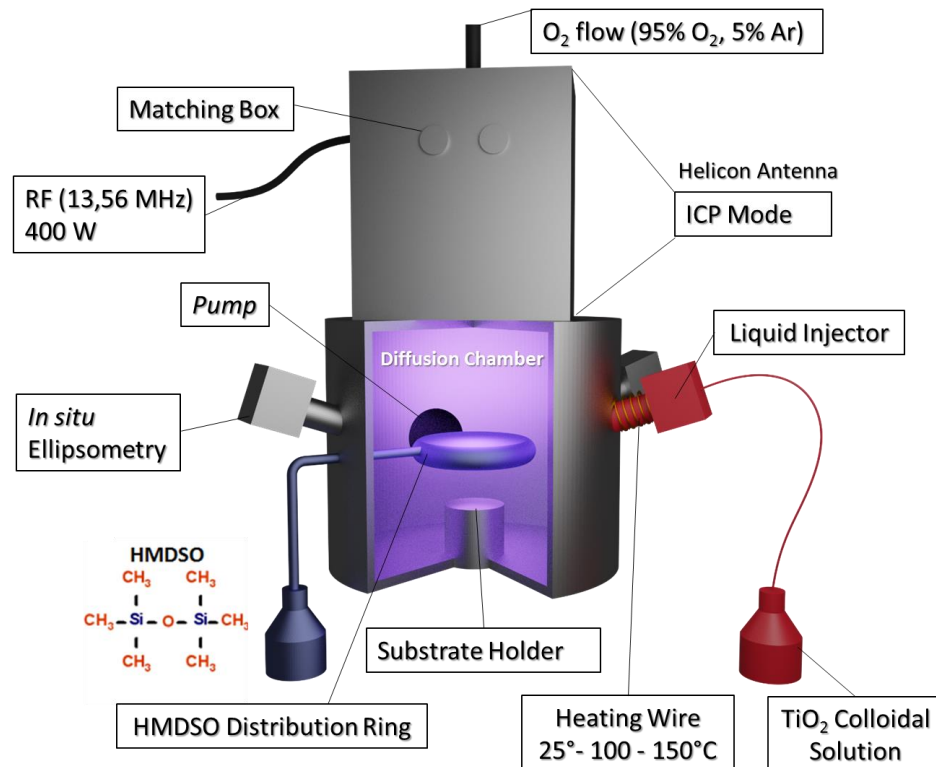


Figure 2.3: 3D Schematic of the reactor used system used for the plasma treatment, the Plasma Enhanced Chemical Vapor Deposition and the Implemented hybrid approach that are explained in Section 2.2.2.1, 2.2.2.2 and 2.2.2.3.

In this Figure the configuration of the different apparatus can be seen. At the top of the reactor the O₂ working gas of the system is introduced and in the helicon antenna, the Inductively Coupled Plasma Source is produced. At the bottom backside of the reactor, the output connected to the turbomolecular pump can be seen (black hole in the Figure 2.3). Before the turbomolecular pump, a cold trap was used to avoid contaminating the pump with the injected NPs. With blue color, the system corresponding to the HMDSO vapor is presented allowing the PECVD to take place. With red, the attached novel system that will allow us the direct injection of the liquid droplets containing the NPs can be seen. The selection of this system and its addition to the reactor was carried out during the first year of this work. During all the experiments an *in situ* ellipsometer was mounted on the reactor orientated towards the substrate and an OES system could be connected using an optical fiber and a small window port. In the next Sections, each of these systems will be further analyzed. In

Annex A, a scheme of this new system is given, including the in situ characterization systems and all the technical/geometrical considerations.

2.2.2.1 O₂ Plasma Treatment system

For the elaboration of the plasma treatment of the spin coated TiO₂ NPs (Chapter 3) and the injection of the colloidal solution of TiO₂ NPs (Chapter 5), a low pressure O₂ Inductively Coupled Plasma (ICP) was used.

Inductively coupled plasma (ICP) reactors using RF as a power source are used for plasma processing being able to have high-density plasmas. ICP can be generated by a coil that surrounds the cylindrical dielectric wall of the source region. The RF current flowing in the coil launches an evanescent disturbance that decays over a distance of a few centimeters into the plasma. This induces RF current in the plasma and transfers energy to electrons; *i.e.*, it controls the plasma density. A magnetic field of 50-100 G is often applied for the efficient confinement of the electrons towards the diffusion chamber. A schematic illustration of this, is given in Figure 2.4. [4]

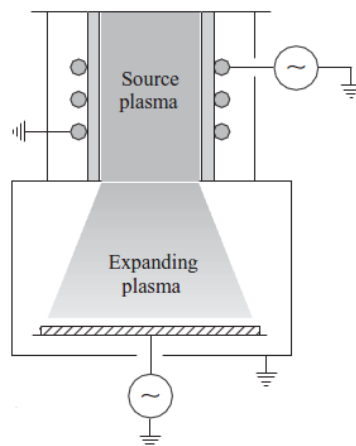


Figure 2.4: Inductively coupled plasma reactor with cylindrical source tube with an expanding chamber. [4]

The reactor comprises a very-low-pressure high-density Inductively Coupled Plasma (ICP) source created at 13.56 MHz (400 W) in a fused silica discharge tube using a helicon antenna which is also connected to a matching network. The particular configuration of this antenna, allows three modes of different couplings according to RF power: capacitive coupling (<100 W), inductive, as in our case (100-1000 W) or helicon (> 1 kW in the presence of a static magnetic field). A static magnetic field (50 G) is applied to the source in order to confine the electrons and densify the plasma. The plasma then expands into a stainless-steel processing chamber where the substrate holder is located. The substrate holder is 17 cm in diameter located in the middle of the reactor with a distance of 16.8 cm from the ICP antenna. The Si substrates used, which were positioned in the middle of the substrate holder, were 1 cm x 2 cm in dimension and their temperature was measured at 400 K through

temperature-sensitive labels located at the substrate's backside. In this system, plasma gases (95% O₂, 5% Ar here) are introduced at the top of the plasma source and the high-vacuum pumping system is located 11 cm from the bottom of the processing chamber. The outlet of the vacuum pumping system that includes also a cold trap, is 10 cm in diameter. The pressure was maintained in high vacuum, 10⁻⁶ Torr.

Using, *in situ* spectroscopic ellipsometry (Section 2.5.1), the modifications or growth of the film were monitored. The plasma chemistry was characterized using Optical Emission Spectroscopy (OES) that will be analyzed in Section 2.5.2. The basic reactions taking place under the specific conditions, gathered by previous works of our group are summarized in Annex B.

2.2.2.2 Plasma Enhanced Chemical Vapor Deposition (PECVD)

For the creation of the SiO₂ layers in the multilayer structure in Chapter 3 and the SiO₂ matrix of the nanocomposite films in Chapter 6, the Plasma Enhanced Chemical Vapor Deposition (PECVD) technique was used. In Figure 2.3, the schematic of the reactor used was given. It is based on the configuration of the reactor explained in Section 2.2.2.1 with the addition of a heated container and a showerhead distributing the vapor precursor located 8 cm above the substrate holder (bleu apparatus in Figure 2.3). PECVD utilizes the high chemical reactivity of the plasma (high electron density) environment to dissociate the vapor precursor at low temperatures (less than 100°C), rendering it possible to deposit on thermally sensitive substrates such as polymers.

In our experimental study, a mixture between O₂ and Hexamethyldisiloxane (HMDSO) was used. The process of depositing inorganic films of SiO₂ using this system can be separated in two steps, the dissociation of the initial HMDSO molecules and the oxidation of the deposited fragments [5] (Figure 2.5).

In detail, in a first step, as the HMDSO vapor molecules enter the low-pressure reactor, they are being dissociated by the electrons of the O₂ plasma. The result of this interaction is the production of fragments from the initial HMDSO molecules. In a second step, these fragments are being deposited on the surface of the substrate. The oxidation of the carbon containing deposited fragments occurs by the interaction with the produced O atoms. As by-products of this oxidation process, volatile species are formed such as CO, H₂O and CO₂. From this process, SiOH has been formed on the surface of the substrate with O₂⁺ ions (dominant ions) possibly assessing (breaking the OH bonds) in the creation Si-O-Si bonds. This process is also given schematically in Figure 2.5. In this example, a Si substrate is considered with a native oxide.

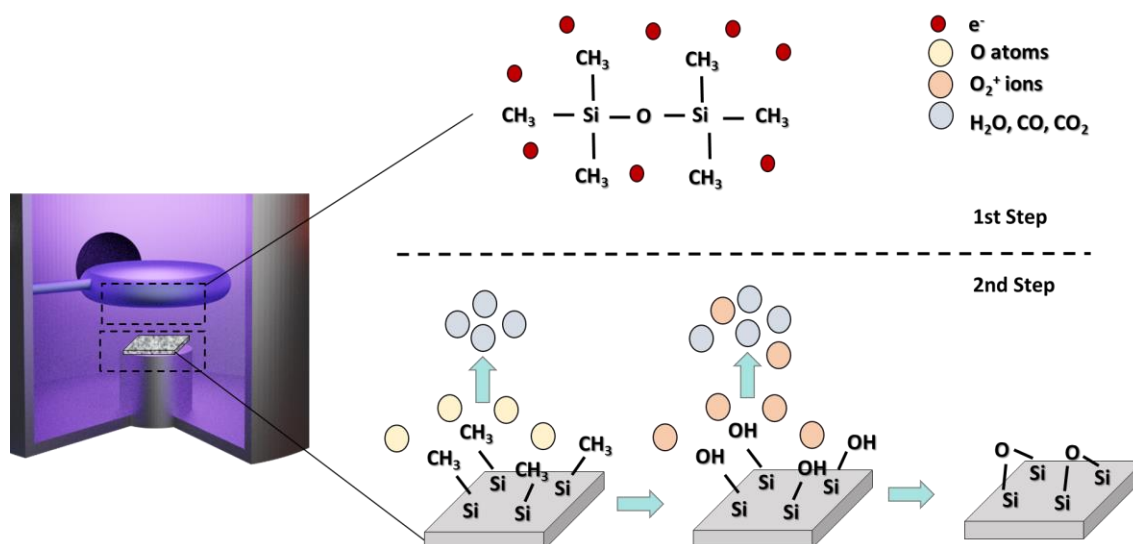


Figure 2.5: Schematic of the PECVD reactor and the two-step process leading to the deposition of the SiO₂ (substrate for this example could be an Si with a native oxide).

2.2.2.3 Hybrid system for the Nanocomposite thin film deposition

For the implementation of the hybrid one-step approach for the creation of NC thin films, a combination of systems was used. A schematic of this apparatus was given in Figure 2.3.

Explicitly, to the O₂ ICP reactor explained in Section 2.2.2.1, a liquid injection system was mounted with 45° angle targeting the substrate holder (red apparatus). For Chapter 5, in O₂ ICP only, liquid droplets containing TiO₂ NPs were introduced in order to establish the injection conditions and investigate the droplet interactions with the O₂ plasma. In Chapter 6, in this O₂ ICP reactor, HMDSO precursor was added from a showerhead linked to a heated container (bleu apparatus), as in PECVD method explained in Section 2.2.2.2. During the O₂/HMDSO ICP plasma, TiO₂ NPs were introduced and the TiO₂-SiO₂ nanocomposites were created.

In order to directly inject the solution and create droplets several systems exist, which have to be chosen depending on the specifications of the experiment. The driving force to create these droplets and assist the atomization can be pressure difference, centrifugal, electrostatic and ultrasonic energy. For maintaining the low pressure (3 mTorr) a system with low injection rate is needed. Thus, the use of carrier gas to assist the atomization was not an option in our case. Therefore, an industrial injector (Liquid Dozer) without carrier gas was selected in order to introduce the liquid solution containing the NPs. It is an injection system from Kemstream that features a normally closed fast solenoid valve (or injector), with a small conductance (flow coefficient), commonly called Cv. This valve is controlled in pulsed regime. A photograph of this injector and other parts of the system are given in Figure 2.7.

As observed in this photograph and the 3D schematic of Figure 2.7, the injector is connected to the reactor through a pipe. Around this pipe, we have positioned a

heating wire, allowing the variation of the temperature, from room temperature (25° C) to 150°C. During Chapter 5, based on computational and experimental findings this parameter was determined for the acquisition of homogeneous and reproducible films. In addition to this, the pipe connecting the injector and the reactor will be extended to 15 cm, in order to better assess the droplet evaporation. Finally, the principle of operation of this approach, and the mechanisms involved in the atomization of the liquid colloidal solution, its transport and its interactions with the O₂ plasma, will be extensively analyzed in Chapter 5.

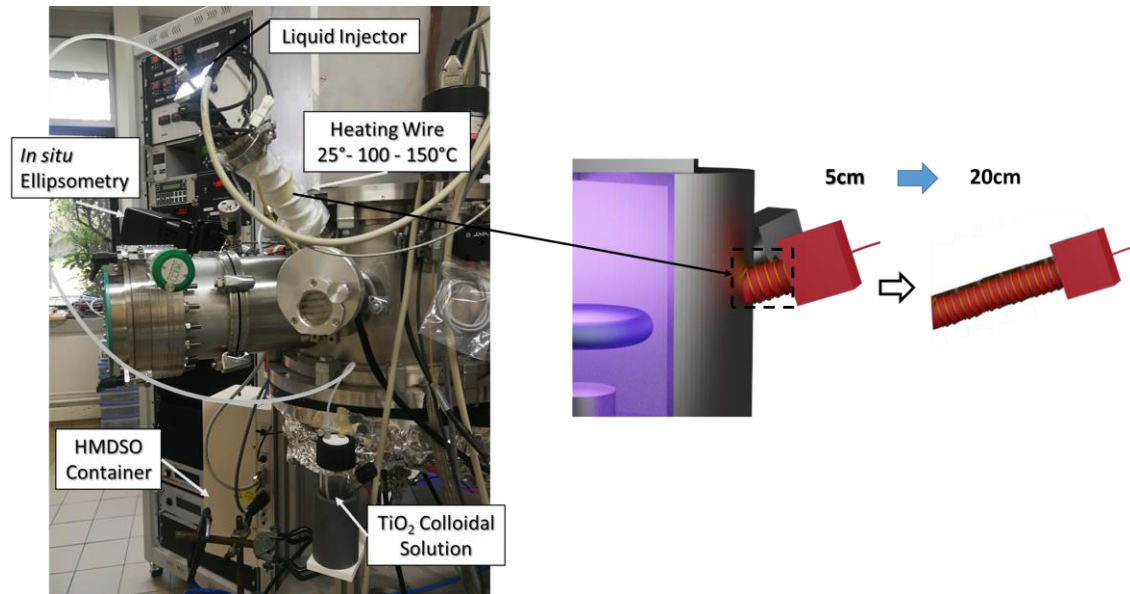


Figure 2.7: Photograph of the injection system mounted on the reactor and schematic illustrate of the pipe enlargement, indicating on the top the distance of the injector from the reactor wall.

2.5 In situ Characterization Techniques

In this Section, the *in situ* ellipsometry technique used to monitor in real time, the growth or treatment of the films is presented. The basic principles of ellipsometry measurement and simulation are given in Section 2.5.1. In addition to this, apart from the *in situ* recording of the films modifications the impact of the liquid droplets on the plasma chemistry upon injection is studied with Optical Emission Spectroscopy (OES) which is further explained in Section 2.5.2.

2.5.1 Ellipsometry

Light is a transverse electromagnetic wave with wavelengths ranging from 1 μm to 10 nm (with the visible range being from 400 to 700 nm). The light wave in a medium is linked to the induced motion of the electric charges of electrons and atomic nuclei, constituting macroscopic electric currents. It is mostly safe to neglect the induced magnetization, since the motion of magnetic moments of electrons and nuclei

is too slow to follow the rapid optical oscillations. Thus, the most important quantity describing the light wave is the vector of its electric-field intensity, E . [6]

Ellipsometry is a non-destructive characterization technique that can provide information regarding the optical and physical characteristics of the film. It is based on the change in the polarization of incident light after reflection by the system under investigation (thin film) and its principle of operation is given in Figure 2.8.

In detail, the polarization states of incident and reflected light waves are described by the coordinates of p- (meaning parallel to the plane) and s-polarizations (meaning perpendicular to the plane). Upon reflection on the sample, p- and s-polarizations show different changes in amplitude and phase.[7] Consequently, Psi and Delta ($^{\circ}$) measured values express the amplitude ratio and phase difference between p- and s-polarizations (Figure 2.8). Finally, the ellipsometric ratio can be written as:

$$\rho = \frac{\frac{E_{rp}}{E_{ip}}}{\frac{E_{rs}}{E_{is}}} = \frac{r_p}{r_s} \tan(\Psi) \exp(i\Delta)$$

where E_{ip} and E_{is} are the incident vectors and E_{rp} and E_{rs} are the reflected ones, of the p- and s-polarizations. r_p and r_s are the amplitude of reflection coefficient of the p- and s-polarizations. The ratio of the latter can give access to the Psi and Delta ellipsometric parameters.

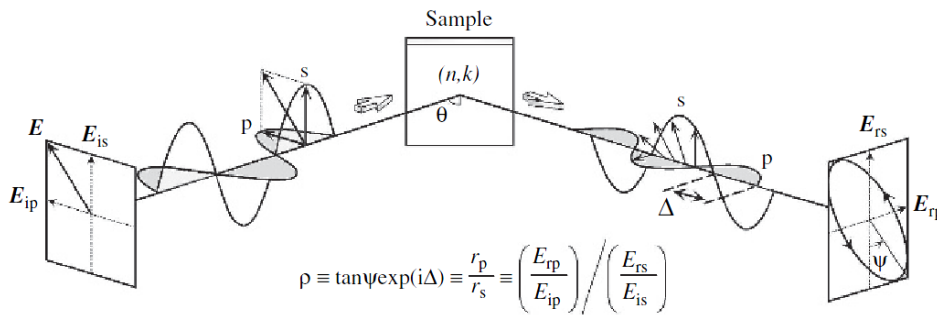


Figure 2.8: Measurement principle of ellipsometry. [7]

Another way to view the ellipsometric data is based on the Mueller-matrix formulation. The non-zero elements of this matrix, are the I_s , I_c and I_N , which are linked with Psi and Delta values as following: $I_s = \sin(2\Psi)\sin(\Delta)$, $I_c = \sin(2\Psi)\cos(\Delta)$ and $I_N = \cos(2\Psi)$. Some advantages of representing the ellipsometric data with this notation is that these values are always bounded between -1 and 1 and that they are linearly related to the intensity harmonics measured by any ellipsometer.

Two approaches can be used to study a film. The first one is the Kinetic Ellipsometry (KE) where the growth or treatment of the film can be dynamically

monitored at a fixed wavelength. This type of study can provide information regarding the continuous or not growth of the film as well as information regarding its homogeneity (concerning the growth axis). For instance, in Figure 2.9a, the trajectory plots (I_s , I_c), of mixed TiO_2 - SiO_2 oxide films with varying Si concentration is given. The retrace of cyclic curves upon time (and thus upon film growth), indicate that homogeneous films have been obtained. The change of the I_s/I_c trajectory shape is related to the evolution of the film optical indices. [8] Hence, the pure TiO_2 ($R_{\text{Si}}=0$ and black dashed line) exhibits a rather circular trace. For higher amount of Si a flatening of the curve for the mixed TiO_2 - SiO_2 oxide films is observed reaching finally (for the highest Si content) trajectory plots close to the pure SiO_2 plot ($R_{\text{Si}}=1$ and orange dashed line). Furthermore, in Figure 2.9b, another approach for the use of the KE results is reported. In this case, due to the high sensitivity of this technique, the Atomic Layer Deposition (ALD) cycles of the TiO_2 growth are identified, by monitoring the state of the Psi and Delta ellipsometric parameters.

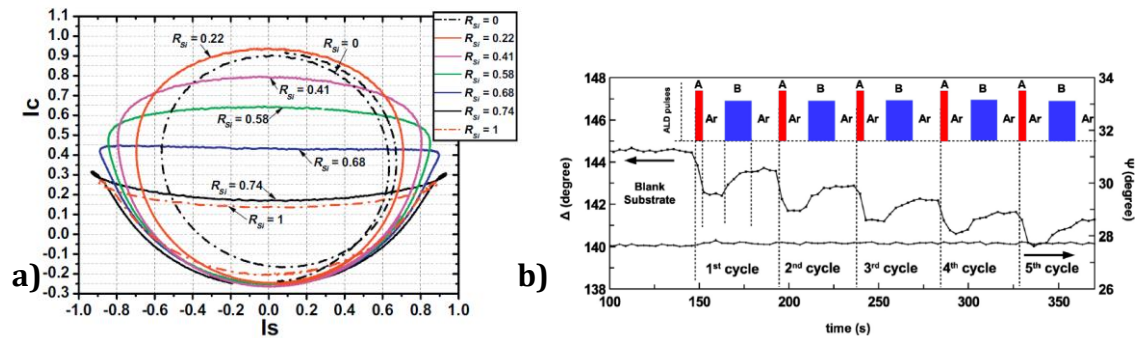


Figure 2.9: Trajectory plot of mixed oxide films with varying amount of Si [8] and dynamic Psi and Delta plots versus time monitoring the growth of ALD grown TiO_2 film [9].

The second and more conventional approach is the Spectroscopic Ellipsometry (SE), where the ellipsometric data are being recorded over a range of wavelengths (or photon energies). Since the measured ellipsometric parameters (Psi, Delta) cannot directly be related to the information of interest (optical constants, physical characteristics of the film etc.), some mathematical analysis should be done to extract these information. Knowing the nature (or estimating it initially) of the film, the appropriate dispersion law have to be selected to describe its dielectric function. Using a model describing each layer of the film with a particular dispersion law and comparing the produced (simulated) ellipsometric parameters, can lead us to a conclusion of whether or not this model is the appropriate one. The determination of the discrepancy between measured and simulated data (indicating also the quality of the fit) is validated by the Mean Square Error (MSE) expressed as:

$$MSE = \frac{1}{2N - M - 1} \sum_{i=1}^N [(Psi_i^{sim} - Psi_i^{meas}) + (Delta_i^{sim} - Delta_i^{meas})]^2$$

where N and M are the total number of data points and the number of fitted parameters, respectively, Psi^{sim} or $Delta^{sim}$ are the simulated ellipsometric data and Psi^{meas} or $Delta^{meas}$ the measured ellipsometric data.[10] For the description of TiO_2 films, several dispersion laws have been proposed, depending on the deposition method. Among them Tauc-Lorentz and Cody-Lorentz were reported to be the most appropriate ones. Tauc Lorentz (TL) [11] dispersion law is well known to parametrize the amorphous and nanocrystalline semiconductors optical constant in both the inter-band and the transparent regions. It combines the Tauc expression for the band edge onset [12] with the broadening given by the classic Lorentz oscillator [13]. The imaginary part ϵ_r'' of the dielectric function has the following expression:

$$\epsilon_r''(E) = \begin{cases} \frac{1}{E} \frac{ACE_o(E - E_g)^2}{(E^2 - E_o^2) + C^2E^2} & E > E_g \\ 0 & E < E_g \end{cases}$$

where E is the photon energy, E_g is the band gap, E_o the peak transition energy, C the broadening parameter and the factor A represents the optical transition matrix elements. These values can be adjusted or fitted before or after the fitting to represent the dielectric function of the specific material. As the relationship between the real part ϵ_r' of the dielectric function and the imaginary ϵ_r'' is described by the Kramers–Kronig relations, then ϵ_r' can be written as:

$$\epsilon_r'(E) = \epsilon_r'(\infty) + \frac{2}{\pi} P \int_{E_g}^{\infty} \frac{\xi \epsilon_r''(\xi)}{\xi^2 - E^2} d\xi$$

where $\epsilon_r'(\infty)$ represents the contribution of the optical transitions at higher energies and appears as an additional fitting parameter. P stands for the Cauchy principal part of the integral, E_g is the band gap and E the photon energy.

An example of this spectroscopic ellipsometry approach is given in Figure 2.10. In this figure, the Tauc Lorentz law representing a PECVD made TiO_2 layer has been used to describe the spin coated TiO_2 NPs. As expected, the discrepancy between the Psi and $Delta$ measured (colored) and the simulated (black dashed) data is high and therefore the model can not lead to reliable optical results. If the fit is good and the MSE has low values the optical constant such as the refractive index (n) and extinction coefficient (k) can be extracted based on the following equation.

$$n - jk = \sqrt{\epsilon_r' - j\epsilon_r''}$$

For the representation of SiO_2 , the Cauchy dispersion law was used. The classical Cauchy dispersion formula for the refractive index is an empirical formula that may be used to describe transparent and amorphous films. [6,14] It is written as:

$$n(\lambda) = A + \frac{B}{\lambda^2} + \frac{C}{\lambda^4}$$

where A, B, C are parameters adjusted to describe the film characteristics and λ the wavelength.

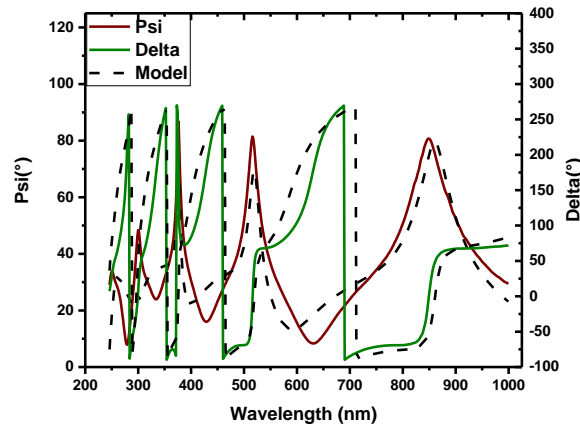
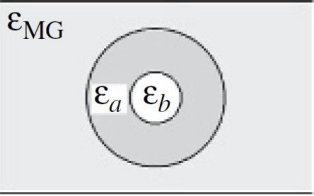
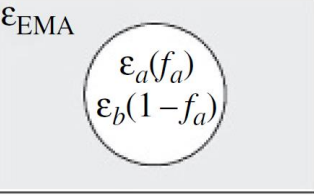


Figure 2.10: Example of measure and theoretical Psi and Delta Plots based on Tauc-Lorentz model with high discrepancies and therefore high MSE.

When the studied film is not composed by one phase material and it is a mixture of two or more, then the material can be considered as a composite of regions each of which has its own dielectric response. The identification of the volume fractions of these composite materials can be accomplished using the Effective Medium Approximation (EMA) theory. The purpose of EMA theory is to accommodate the screening charge that develops at the boundaries between regions. Two theories are distinguished which are based on the geometry of the composite film. The Maxwell-Garnett (MG) theory applies to cermet microstructures, where the inclusions are completely surrounded by the host material, have a specific shape (usually spherical), and are well separated. The Bruggeman effective-medium theory applies to aggregates, where any region may be adjacent to regions with the same or different dielectric responses. [15] Table 2.1, provides the expressions of these two approximations and a physical model of what they represent (ϵ_a and ϵ_b correspond to the dielectric constant of the material a and b. Based on the physical model and the expression given, the MG model assumes a structure in which the phase of ϵ_b is surrounded by the phase of ϵ_a , and their volume ratio determines f_a . Bruggeman on the other hand, assumes the mixture of the two materials with the f_a and $(1 - f_a)$ representing the probabilities of finding ϵ_a and ϵ_b in a spherical space. For these approximations, the maximum size of the inclusions should be typically less than $\lambda / 10$.

During all the experiments, an *in situ* monitoring of the thin films was conducted with a rotating compensator spectroscopic ellipsometer (J.A. Woollam M-2000). It was mounted on the plasma system (Figures 2.6, 2.4 and 2.7) and aligned with the substrate surface. Measurements were conducted between 245 and 1000 nm at 71.7° incident and collected angle.

Table 2.1: Effective Medium approximations

EMA	Expression	Physical Model
Maxwell-Garnett	$\frac{\varepsilon - \varepsilon_a}{\varepsilon + 2\varepsilon_a} = (1 - f_a) \frac{\varepsilon_b - \varepsilon_a}{\varepsilon_b + 2\varepsilon_a}$	 <p style="text-align: right;">[15]</p>
Bruggeman	$f_a \frac{\varepsilon_a - \varepsilon}{\varepsilon_a + 2\varepsilon} + (1 - f_a) \frac{\varepsilon_b - \varepsilon}{\varepsilon_b + 2\varepsilon} = 0$	 <p style="text-align: right;">[15]</p>

2.5.2 Optical Emission Spectroscopy (OES)

Optical Emission Spectroscopy (OES) is one of the most widely used techniques for the chemical investigation of the plasma. It is based on the capture of the light emitted by the plasma. This light originates from the radiative de-excitation of the excited species. These species can be atoms, ions or molecules.

The wavelengths of photons emitted by the plasma species during their transition from an excited state to a lower energy state are specific and unique. Therefore, by capturing them using a specific system they can be used afterwards for the identification of each of the species.

The emitted light by the plasma system is collected through a quartz window (at the middle of the reactor), using an optical fiber. The optical emission spectrum is detected by a Jobin–Yvon monochromator (HR460) with the focal length of 0.46 m. It is equipped with two gratings (2400 and 1200 grooves mm^{-1} used for the 180–500 and 500–900 nm spectral range, respectively), and a photomultiplier (R928 Hamamatsu). The entrance and exit slits can be adjusted to have a good compromise between signal light intensity and spectral resolution. The acquisition of spectra is monitored by Jobin–Yvon software using OriginPro software. Under standard acquisition conditions the resolution was fixed at 0.1 nm.

Using this system, initially a wide spectrum was captured in a wavelength range of 250 to 500 nm. Then specific peaks were followed versus time in order to investigate the impact of the liquid injection on the O_2 (in Chapter 5) or O_2/HMDSO plasma (in Chapter 6). The peaks followed are given in Table 2.2.

Table 2.2: Systems and transitions of the studied peaks

Atom/Molecule	Transition	System	Emission (nm)
CO	$B^3\Sigma^+ \rightarrow a^3\Pi$	3 rd positive system	297.7
OH	$A^2\Sigma^+ \rightarrow X^2\Sigma$	3065 Å system	306.4
O	$4p^5P \rightarrow 3s^5S^0$		394.5
H _δ	6 → 2	Balmer Series	410
Ar	$5p^2[5/2] \rightarrow 4s^2[5/2]^0$		419.8

2.6 *Ex situ* Characterization Techniques

The *ex situ* characterization techniques being analysed in this Section involve the physical and chemical characterization of the produced films. They can be categorized as destructive and non-destructive methods, indicating the necessity to manipulate and fragmentize the produced films.

2.6.1 Scanning Electron Microscopy (SEM)

Scanning Electron Microscopy (SEM) is a technique for the morphology investigation of a surface with resolution down to 10 nm. It uses a high voltage focused beam of high-energy electrons to generate a variety of signals after their impact with the solid specimen. All these signals are the product of strong electron-matter interactions, which depend on the energy of the incident electrons and the nature of the specimen. When the surface is a dielectric, polymer and a nonconductive material in general, sputtering with gold or platinum very thin film is needed in order the electrons to interact with the surface. A scanning electron microscope (SEM) consists of an electron optical column (having the detection lenses and an electron gun on the top of the column), a vacuum system, electronics, and software.

There are three types of electrons that can be emitted from the electron-specimen interactions: secondary electrons with energies <50 eV, Auger electrons produced by the decay of the excited atoms, and backscattered electrons that have energies close to those of the incident electrons. [16] All these signals can be used to form images. In secondary electron imaging (SEI), the secondary electrons are emitted from very close to the specimen surface. Consequently, SEI can produce very high-resolution images of a sample surface and an image representative of the topology. Back-scattered electrons (BSE) are beam electrons that are reflected from the sample by elastic scattering. They emerge from deeper locations within the specimen and, consequently, the resolution of BSE images is less than SE images. However, BSE are often used in analytical SEM, along with the spectra made from the characteristic X-rays, because the intensity of the BSE signal is strongly related to the atomic number (Z) of the specimen. Consequently, the contrast of the BSE image enclose a chemical information. The de-excitation of atoms that are excited by the

primary electrons also produces continuous and characteristic X-rays as well as visible light. These signals can be utilized to provide qualitative, semi-quantitative, or quantitative information on the elements present in the regions of interest. [16]

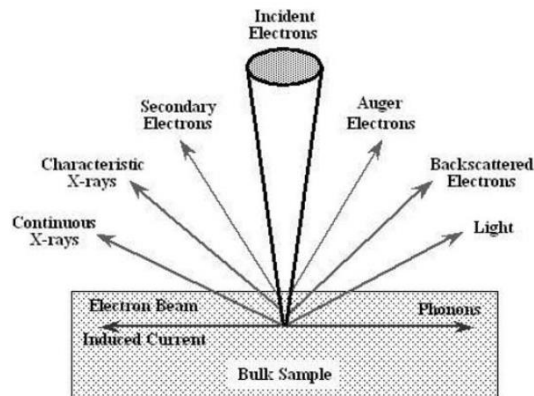


Figure 2.11: Schematic drawing illustrates the signals generated inside a scanning electron microscope when an electron beam interacts with a specimen. [16]

The surface morphology of the films was monitored using the JEOL JSM 7600F, in a secondary electron mode, operating at 5 kV. The initial samples were fragmented using a diamond pen and were attached (using silver paste) on specific SEM sample holder. Before the sample introduction in the SEM vacuum system, they were coated with platinum.

Energy-dispersive X-ray spectroscopy (EDX) was conducted with a SAMx SDD system on a SEM JEOL JSM 5800LV. As the incident electron beam interacts inelastically with the atoms of the sample, electrons are ejected from the inner shells of the atoms. The electron vacancies are then filled by the outer shell electrons which possess higher energy states. This transition is followed by an X-ray emission of equivalent energy to the energy state transition. In Chapter 6, for the chemical analysis of the produced TiO₂-SiO₂ NCs, dedicated thicker films were prepared (270 nm) in order to increase the EDX signals. Since the emission depth of the X-rays depends on the accelerating voltage (typical 1 μ m at 15 kV) the 224 nm thick film was deposited on Tin doped Indium oxide deposited on polyethylene terephthalate (ITO(50nm)/PET(125 μ m), Sheldahl) substrate. This allowed to avoid any additional Si signal coming from the substrate (that would have interfere with the quantification of the SiO₂ matrix). In order to probe different thicknesses, we recorded the EDX spectra at three accelerating voltages: 15 kV, 10 kV and 7 kV and chose a magnification of 1000 to smooth the local heterogeneities of chemical concentrations. In case of multilayered samples, the software Stratagem was designed to improve the determination of chemical composition of the topmost layer from EDX measurements [17].

The atomic percentages in Ti and Si were determined with this software allowing us to take into account the multilayered (nanocomposite/ITO/PET) nature of the probed zone.[18] Actually, the latter was modelled by three layers: first, 270

nm of NC including Ti, Si, O, second, 50 nm of ITO constituted of Sn, In and O and third PET incorporating C and O. The effective analysed thickness of PET depends on the accelerating voltage. The best accuracy of this method is obtained when the thicknesses of the layers are well known as well as the density of the top layer. The different atomic percentages were fitted in order to reproduce the intensity of EDX signals, as a function of the accelerating voltage, accounting for the thicknesses of the NC and ITO and attenuation of signals throughout the different layers.[17,18] As usual for EDX and because the corresponding signals may come from PET and ITO underneath, the determination of carbon and even oxygen is not reliable. However, the precautions taken before acquisition and the good fit obtained after several tries between simulated curves generated by Stratagem and experimental values make it possible to rely on the results concerning silicon and titanium atomic percentages.

2.6.2 Atomic Force Microscopy (AFM)

Atomic Force Microscopy (AFM) is a technique used for the surface topography of a material. The principle of operation is based on a mechanical probe cantilever and a tip “tapping” the surface. The precise scanning of the film is facilitated by piezoelectric elements that allow the accurate and precise movements. A laser beam is reflected from the back of the cantilever and directed to the position-sensitive detector. A graphical depiction of this is given in Figure 2.12. Apart from the ability of this technique to follow the topography of the film with a nanometric accuracy (1-5 nm), another advantage would be that it is a non-destructive method, as no fragmentation of the samples is needed. The samples only require to be positioned below the AFM, fixed with an adhesive sticker.

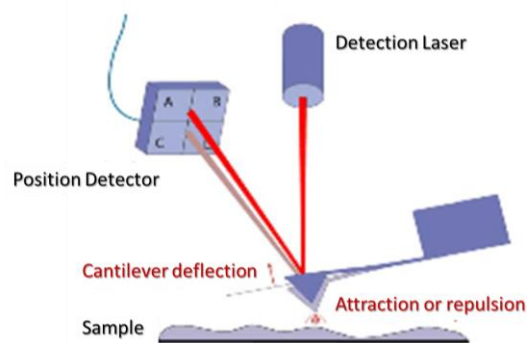


Figure 2.12: Descriptive schematic illustrating the AFM principle of operation [19]

The experiments were conducted in tapping mode with AFM Nanowizard II (JPK Instruments) and an Al-coated cantilever (PPP-NCHR-50 from NANOSENSORS). A free resonance frequency of 330 kHz and a typical spring constant of about 42 N/m. Using the ImageJ software and the AFM scans, after adjustment of the image's threshold and transformation in a binary format, the size distribution of the NPs was extracted.

2.6.3 Transmission Electron Microscopy (TEM)

To investigate the structure, crystallinity and cross section of the produced films Transmission Electron Microscopy (TEM) was employed. In principle, this technique uses an electron beam that passes through a very thin sample (less than 100 nm in thickness). [20] The images are formed based on the interaction between the sample and the transmitted electron beam. TEM lies in the category of destructive methods, as a particular preparation of the sample is needed to have such a small thickness.

The microscope consists of an electron gun, emitting an electron beam, which is accelerated to energies typically ranging between 80 and 300 keV (even up to 1200 keV). The way these electrons impinge on the sample differs for the conventional TEM (CTEM) and the scanning TEM (STEM) modes. These two modes are given in Figure 2.13a, b. In TEM mode, the specimen is irradiated with a parallel electron beam whereas in STEM with a focused one. Using the conventional TEM mode, high resolution images and electron diffraction can be performed. Hence, from Selected Area Electron Diffraction (SAED) can be deduced priding information about the crystallinity of the sample. More specifically, when a parallel electron beam is scattered at a crystalline specimen, a part of the electrons is diffracted at atomic planes. All electrons transmitted by the specimen are imaged by the objective lens into the image plane. In order to confine the diffraction pattern to a specific region of interest, an aperture may be positioned on the corresponding position in the image plane (2.13c).

Lastly, electrons transmitted through the sample in the STEM mode can be detected by the use of High Angular Dark Field (HADF) detector, residing on the optical axis of the microscope, which has the form of a ring and is therefore termed annular. By varying the camera length of the ADF detector, it is possible to image using mostly Bragg-diffracted electrons (large camera lengths), obtaining a crystallographic contrast. An image of this topology is given in Figure 2.13d.

In all the experiments analyzed in the following chapters, High-resolution TEM was conducted (S/TEM Themis Z G3, 300kV, Thermo Fisher Scientific). In Chapter 3, to examine the crystallinity of TiO₂ NPs and assess any evolution of their size due to the plasma treatment the films were scratched and the produced NPs were deposited on a carbon grid. In Chapter 4 for effective analysis of the multilayer films' cross-section, the samples were prepared by creating "sandwich" of two pieces stuck with each other with epoxy resin. The fine thin films were created by cutting the "sandwiches" with a Focused Ion Beam device (FIB). This preparation was elaborated by the Department of Physics in University of Montreal. In chapter 6, for the identification of the TiO₂ NPs inside the SiO₂ matrix, an elemental mapping was performed using high-angle annular dark-field scanning transmission electron microscopy (HAADF-STEM, 28.5 mrad, probe corrected) mode combined with energy dispersive X-ray spectrometry (EDX). For the effective characterization of the

samples through TEM, the deposition was carried on Tin doped Indium oxide deposited on polyethylene terephthalate (ITO(50nm)/PET(125 μ m), Sheldahl). Thus, the samples were suitable for preparation of cross-sections using an ultramicrotome (Leica UC7/FC7) equipped with diamond knife (Diatome).

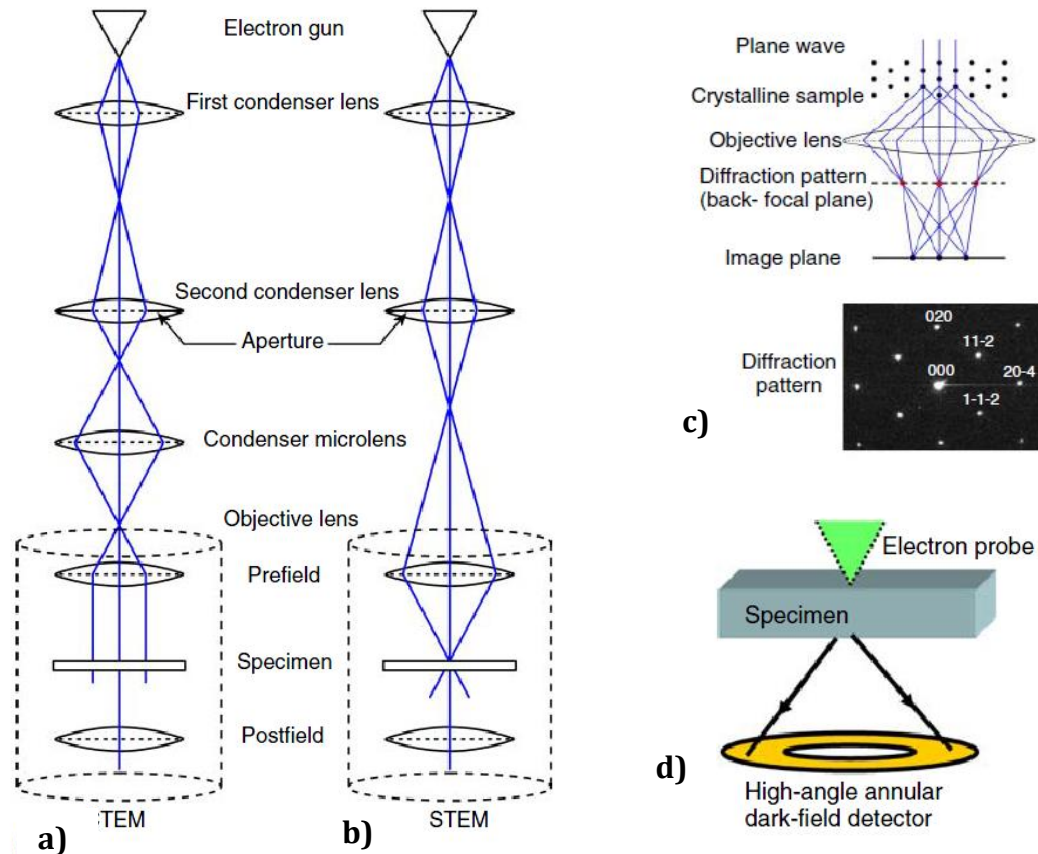


Figure 2.13: Schematic of the a) TEM and b) STEM configuration. c) Description of the diffraction pattern d) HAADF topology [21]

2.6.4 X-Ray Photoelectron Spectroscopy (XPS)

The chemical composition of the topmost surface was investigated with X-ray Photoelectron Spectroscopy (XPS) technique. It is typically accomplished by exciting a sample's surface with mono-energetic Al $K\alpha$ X-rays causing electrons from the surface to be emitted, due to the photoelectric effect.[22] The photoelectric effect was first presented by Einstein in 1905, where it was proposed that light involves "energy packets" having energy equal to $E_{ph}=h\nu$, called *photons*. As a photon collides with an electron, it transfers its energy.[23] A schematic representation of this is given in Figure 2.14.

A typical XPS spectrum is a plot of the number of electrons detected (Y-axis) versus the binding energy of the electrons detected (X-axis). Each element produces a characteristic set of XPS peaks at characteristic binding energy values that directly identify each element that exists at the surface of the material being analyzed.[24] The

kinetic energies (KEs) of the emitted electrons are measured using an electrostatic charged-particle energy analyzer, from which their electron binding energies (BEs) can be calculated from the following equation:

$$E_{\text{phot}}(\text{xrays}) = BE(\text{calculate}) + KE(\text{measured}) + W_a$$

where E_{phot} is the energy of the emitted photons by the X-ray source, BE is the value calculated, KE is the kinetic energy of the electrons emitted by the surface of the material and W_a is the work function.

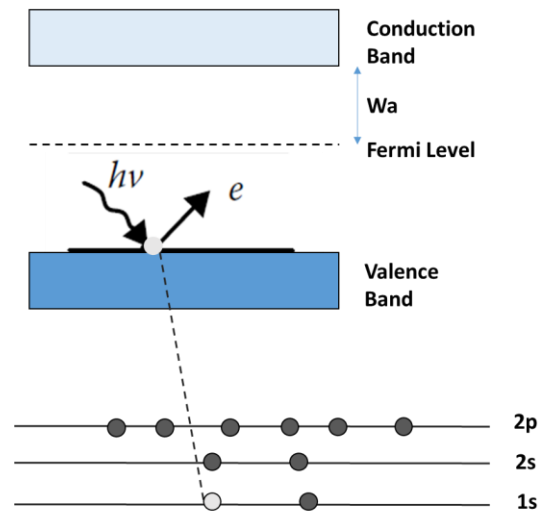


Figure 2.14: Schematic illustration of the photoelectron emission occurring during the XPS technique.

The system used was the Kratos Nova spectrometer with Al $K\alpha$ radiation at 1486.6 eV. One of the problems during the analysis of insulating materials is the appearance of positive electrical charges on their surface. This positive electric charges can modify the kinetic energy of the photoelectrons emitted by the sample. To avoid this problem, a neutralizer was used. The neutralizer is a low energy electron gun that removes positive charges accumulated on the surface of the sample. In some cases only a portion of the sample is insulating with some discrete areas or layers of the sample being conducting or semi-conducting. In these cases a phenomenon known as differential charging effect can occur. The spectral features from these areas will be shifted to lower binding energies by the action of the charge neutralizer whereas the spectral features of the underlying material will not be shifted. This may be complicated if the islands or domain structures behave as semi-conductors and their conductivity varies with thickness. The resulting spectra may be broadened significantly as a result.

One excellent way to combat differential charging effects is to electrically isolate (or "float") the entire sample from the specimen holder. For this reason, all the

samples were completely isolated from the plate by a piece of polymer for all the analyses in order to use the same neutralization parameters throughout our analyzes.

Survey spectra were measured from 1200 to -2 eV (Binding Energy) using a pass energy of 160 eV while high-resolution spectra over specific regions of interest were recorded with a pass energy of 40 eV. Short time measurements were undertaken (dwell of 100 per 0.1 eV step-scan for O 1s, Ti 2p and 200 ms for C 1s). After checking that no X-ray damage was induced, the scans were summed up in order to increase the signal over noise ratio. The decomposition and fitting of the measured XPS peaks was carried out using CasaXPS software [25]. After accounting for the background using a U2-Tougaard background, Gaussian-Lorentzian (30-70%) functions were selected to model the different components. The calibration in binding energy was conducted using the C 1s as a reference at 284.5 eV.

2.6.5 Raman Spectroscopy

The chemical analysis of the film was conducted using Raman Spectroscopy. Raman spectroscopy consists in analyzing the frequency shift of the light scattered by a sample when it is exposed to monochromatic illumination. In detail, most of the incident light is elastically scattered from the matter (Rayleigh scattering) and thus the incident light has the same energy as the scattered light. The Rayleigh scattering does not give any information on the elemental composition or crystallinity of the sample. The spectrometer is equipped with a special filter that removes the Rayleigh scattering. However, a small fraction of the incident beam is inelastically scattered (Raman scattering) and thus the scattered light possesses a different frequency than the excitation photon frequency. This shift of scattered light is characteristic of the material considered and corresponds to the vibrations of its atomic bonds.[26]

The Raman spectroscopy measurements were performed using a microconfocal Raman microscope (Renishaw inVia). The instrument was equipped with a double edge filter to eliminate the Rayleigh scattering and a charged couple device (CCD) camera working at a temperature of 220 K with a 1024-by-256 pixel array. The setup was composed of a confocal microscope that was equipped with an automated XYZ table and an $\times 50$ magnification objective. The laser excitation source used was set at 514 nm and the focused power was checked to avoid any degradation of the samples. Therefore, the power was selected at 1.5 mW and a recording time of 1 s with an accumulation of 10 measurements was used.

Conclusion

As a conclusion, we have shown in this chapter the various experimental systems used in the following experimental studies. Both the ICP O₂ plasma and the PECVD systems created in the specific reactor have been extensively examined in the

past. These two well established systems along with spin coating will provide us with significant information (in Chapter 3 and 4) that will assess the implementation of the hybrid one step approach for the creation of NC thin films. The setup proposed to elaborate these NCs thin films is introduced here along with some important technical-geometrical aspects that will be modified (heating wire temperature, distance of the pipe) in order to acquire homogeneous and reproducible thin films. For the investigation of the physical chemical and optical characteristics of the produced films as well as for the investigation of the injected liquid impact on the plasma chemistry, several characterization techniques were used. Hence, their principle of operation has been introduced in this chapter.

Bibliography

- [1] A. Karpinski, Couches interfaciales TiO₂ et NiO déposées par CSD et PVD, pour cellules solaires organiques, Nantes, 2011.
- [2] N. Sahu, B. Parija, S. Panigrahi, Fundamental understanding and modeling of spin coating process: A review, *Indian J. Phys.* 83 (2009) 493–502. <https://doi.org/10.1007/s12648-009-0009-z>.
- [3] L.A. Dobrzański, M. Szindler, Sol gel TiO₂ antireflection coatings for silicon solar cells, *J. Achiev. Mater. Manuf. Eng.* 52 (2012) 9.
- [4] P. Chabert, N. Braithwaite, *Physics of Radio-Frequency Plasmas*, (n.d.) 395.
- [5] A. Bousquet, Dépôt de couches minces par plasma pulsé radiofréquence et basse pression en mélange hexaméthylsiloxane / oxygène, Thesis Manuscript, 2005.
- [6] H.G. Tompkins, ed., *Handbook of ellipsometry*, Repr, Andrew [u.a.], Norwich, NY, 2010.
- [7] H. Fujiwara, *Spectroscopic Ellipsometry*, *Spectrosc. Ellipsom.* (n.d.) 6.
- [8] D. Li, S. Elisabeth, A. Granier, M. Carette, A. Goulet, J.-P. Landesman, Structural and Optical Properties of PECVD TiO₂-SiO₂ Mixed Oxide Films for Optical Applications: Structural and Optical Properties of PECVD TiO₂-SiO₂ ..., *Plasma Process. Polym.* 13 (2016) 918–928. <https://doi.org/10.1002/ppap.201600012>.
- [9] T. Muneshwar, K. Cadien, Probing initial-stages of ALD growth with dynamic in situ spectroscopic ellipsometry, *Appl. Surf. Sci.* 328 (2015) 344–348. <https://doi.org/10.1016/j.apsusc.2014.12.044>.
- [10] D. Li, Synthèse par PECVD et caractérisation de couches minces de TiO₂ et de TiSiO pour applications optiques, Nantes, 2013.
- [11] G.E. Jellison, F.A. Modine, Parameterization of the optical functions of amorphous materials in the interband region, *Appl. Phys. Lett.* 69 (1996) 371–373. <https://doi.org/10.1063/1.118064>.
- [12] J. Tauc, R. Grigorovici, A. Vancu, Optical Properties and Electronic Structure of Amorphous Germanium, *Phys. Status Solidi B.* 15 (1966) 627–637. <https://doi.org/10.1002/pssb.19660150224>.
- [13] M. Fox, G.F. Bertsch, Optical Properties of Solids, *Am J Phys.* 70 (2002) 9.
- [14] C.M. Herzinger, B. Johs, W.A. McGahan, J.A. Woollam, W. Paulson, Ellipsometric determination of optical constants for silicon and thermally grown silicon dioxide via a multi-sample, multi-wavelength, multi-angle investigation, *J. Appl. Phys.* 83 (1998) 3323–3336. <https://doi.org/10.1063/1.367101>.
- [15] H. Wormeester, M. Losurdo, The case of Nanostructured Noble Metal Films, (2010).
- [16] N. Yao, ed., *Handbook of microscopy for nanotechnology*, Kluwer Acad. Publ, Boston, 2005.
- [17] J.-L. Pouchou, X-Ray Microanalysis of Thin Surface Films and Coatings, *Microchim. Acta.* 138 (2002) 133–152. <https://doi.org/10.1007/s006040200020>.
- [18] F. Christien, E. Ferchaud, P. Nowakowski, M. Allart, The Use of Electron Probe MicroAnalysis to Determine the Thickness of Thin Films in Materials Science, in: S.K. Sharma (Ed.), *X-Ray Spectrosc.*, InTech, 2012. <https://doi.org/10.5772/28877>.
- [19] *NanoWizard AFM Handbook*, (2012).
- [20] R.F. Egerton, *Physical Principles of Electron Microscopy*, Springer International Publishing, Cham, 2016. <https://doi.org/10.1007/978-3-319-39877-8>.
- [21] D. Abou-Ras, T. Kirchartz, U. Rau, eds., *Advanced characterization techniques for thin film solar cells*, 2nd, extended edition ed., Wiley-VCH Verlag, Weinheim, 2016.
- [22] J.C. Rivière, S. Myhra, eds., *Handbook of surface and interface analysis: methods for problem-solving*, 2. ed, CRC Press, Boca Raton, Fla., 2009.
- [23] S.O. Kasap, *Principles of electronic materials and devices*, 3. ed, McGraw-Hill, Boston, 2006.
- [24] J.F. Moulder, W.F. Stickle, P.E. Sobol, K.D. Bomben, J. Chastain, R.C. King Jr., *Physical Electronics, Incorporation*, eds., *Handbook of X-ray photoelectron spectroscopy: a reference book of standard spectra for identification and interpretation of XPS data*, Physical Electronics, Eden Prairie, Minn., 1995.
- [25] Neal Fairley, Copyright© 2005 Casa Software Ltd, 2005.
- [26] I.R. Lewis, ed., *Handbook of Raman spectroscopy: from the research laboratory to the process line*, 4. print, CRC Press, New York, 2001.

Chapter 3

Modification of the optical properties and nano-crystallinity of anatase TiO₂ nanoparticles thin film using low-pressure O₂ plasma treatment

In this chapter, the first step of the experimental strategy is being studied. Core shell TiO₂ nanoparticles thin films with a thickness of 50 nm were prepared using the spin coating technique and were treated using an inductively coupled O₂ plasma at low pressure. While no significant features were observed during pumping, two kinetics can be identified during plasma processing using *in situ* spectroscopic ellipsometry. For very short plasma treatment times, the removal of solvent-based organic moieties surrounding TiO₂ nanoparticles produces a densification of the inorganic TiO₂ films. Such mineralization effect by the O₂ plasma treatment was confirmed by X-ray photoelectron microscopy. For larger time scales, the average size of TiO₂ NPs rises and significant changes of the optical characteristics occur, evidenced by ellipsometry. While no significant changes in the film nanostructure were observed by Scanning Electron Microscopy, a rise in the crystallite size and an increase in the agglomeration of TiO₂ nanoparticles were confirmed by Transmission Electron Microscopy and Atomic Force Microscopy, respectively. The mechanisms involved in such plasma-induced modification of nanostructured TiO₂ thin films are discussed in line with the energy fluxes of plasma-generated species.

Table of Contents

Introduction.....	105
3.1 Material and Methods.....	106
3.1.1 Spin-coating of TiO ₂ nanoparticles.....	106
3.1.2 Plasma Treatment of spin-coated TiO ₂ nanoparticles.....	106
3.2. Results.....	107
3.2.1 Kinetics driving the plasma-induced modification of nanostructured TiO ₂ thin films	107
3.2.2 Morphological and crystallinity analysis of the plasma-treated nanostructured TiO ₂ thin films	110
3.2.3 Chemical analysis of the plasma-treated nanostructured TiO ₂ thin films	112
3.3. Discussion.....	114
3.3.1 Explanation of the two kinetics	114
3.3.2 Computation of the NPs Temperature upon Plasma Treatment using Energy Balance equation	116
Conclusion	119
Bibliography	121

Introduction

Nanoparticles (NPs) have been widely investigated by the scientific community, as they give flexibility to a wide variety of applications, including photovoltaics [1,2], electrical insulation systems [3], electronic[4], photonic devices [5] and sensors[6]. The importance of NPs was especially realized when it was discovered that the size of the NPs can have an influence on the final properties compared to the bulk material. TiO₂, as high-*k*, stable and low cost semiconductor has been identified as an ideal candidate for its optical [7], dielectric[8-9] and photocatalytic[10] properties.

Today, the most common ways to deposit a layer of NPs dispersed in colloidal solution are dip casting, drop casting, spin coating and inkjet printing. While wet processes represent fast and low-cost deposition methods, they often result in poor-quality films due to the presence of solvent residues inside the sample. In an attempt to counterbalance this effect, a few studies have investigated the impact of weakly ionized, non-thermal plasma treatments on these wet-processed thin films of NPs. In particular, Homola et al. [11] have reported the mineralization effect of atmospheric pressure dielectric barrier discharge (DBD) on the inkjet-printed TiO₂ NPs film. In particular, they have indicated the possibility of acquiring high-quality inorganic TiO₂ films by removing the organic moieties of the binder. Chang et al. [12,13] have investigated the sintering effect of atmospheric pressure plasma jet (APPJ) on screen-printed TiO₂ NPs paste. Finally, there have been some reports aiming in the effective nitrogen doping of ordered, mesoporous TiO₂ thin films using nitrogen/argon (N₂/Ar) plasmas at low pressure [14].

In this framework, this study examines the treatment of thin films formed of spin-coated 5 nm anatase TiO₂ NPs [15] by an inductively coupled plasma operated in O₂ at low pressure as has been reported in our most recent published work[16]. More precisely, through judicious control of the plasma properties and using both *ex situ* and *in situ* analysis of plasma-processed thin films, we studied the influence of the plasma treatment time on the organic solvent, the TiO₂ crystallites and the nanostructuring of spin-coated TiO₂ NPs. This study was also conducted in view of qualifying if the NPs were affected by a plasma treatment and get a picture of the induced modification if any when they are further injected in the plasma. In line with the experimental data and the energy fluxes of plasma-generated species at the substrate surface, the mechanisms involved in such plasma-induced modification are discussed.

3.1 Material and Methods

3.1.1 Spin-coating of TiO₂ nanoparticles

For the wet deposition of TiO₂ thin films, the colloidal solution of crystallized anatase TiO₂ NPs was spin-coated on thermally oxidized silicon substrates (500 nm SiO₂ on 500 μm Si wafer). Before deposition, the SiO₂/Si substrates were cleaned in an ultrasonic bath with distilled water, ethanol and isopropanol. The colloidal solution, synthesized according to ref. [2] and [15], comprises TiO₂ NPs with a well-defined monodispersed mean hydrodynamic diameter centered at 5 nm. As explained in Chapter 2, in order to deposit a highly-concentrated and sufficiently-thick layer of TiO₂ NPs by spin coating, the solution was concentrated by evaporating part of the solvent.

3.1.2 Plasma Treatment of spin-coated TiO₂ nanoparticles

TiO₂ NPs spin-coated on SiO₂/Si substrates were exposed to a low-pressure inductively coupled O₂ plasma. All details on this plasma source can be found in previous publications that are indicated in Chapter 2. The operating conditions (along with the corresponding plasma characteristics recorded close to the substrate surface) used in this study are summarized in Table 3.1. SiO₂/TiO₂ thin films were positioned in the centre of the substrate holder located in the processing chamber. As detailed below, *in situ* spectroscopic ellipsometry (SE) measurements were recorded during pumping as well as during the 20 minutes plasma treatment (PT) in order to monitor any possible vacuum- and plasma-induced modification.

Table 3.1: Low-Pressure O₂ Plasma Characteristics [7,17,18]

RF power	400 W
O ₂ flow rate	16 sccm
Working Pressure	25 mTorr
Positive Ion (O ₂ ⁺) / Electron Density (n _i =n _e)	1.6 x10 ⁹ cm ⁻³
Positive Ion Energy (E _{ion})	7 eV
Electron Temperature (T _e)	2 eV
Density of O atoms (n _o)	1.7x10 ¹⁴ cm ⁻³
Neutral Gas temperature (T _g)	~450 K
Substrate Temperature (T _s)	<150°C

3.2. Results

3.2.1 Kinetics driving the plasma-induced modification of nanostructured TiO₂ thin films

As mentioned above, *in situ* SE measurements were recorded during pumping as well as during the 20 minutes plasma treatment in order to monitor possible vacuum- and plasma-real time induced modification. Spectroscopic Ellipsometry is based on change in the polarization of incident light after reflection by the system under investigation, the ellipsometric ratio $\rho = \tan(\text{Psi}) \cdot \exp(j\text{Delta})$ is typically analyzed from the measured angles Psi and Delta. The corresponding evolution of Psi and Delta values with plasma treatment time at 633 nm wavelength is plotted in Figure 3.1.

Here, the measurement was initialized at the beginning of the reactor pumping. After about 97 minutes, the plasma was turned on (time 0 on the x-axis of Figure 3.1) for 20 minutes and then SE measurements were stopped. While the Psi and Delta values remain stable during pumping, significant changes of both Psi and Delta can be seen during the first two minutes of the plasma treatment. During the 2nd to 10th minute, signal variation becomes less pronounced and a saturation is reached between 10 and 20 minutes.

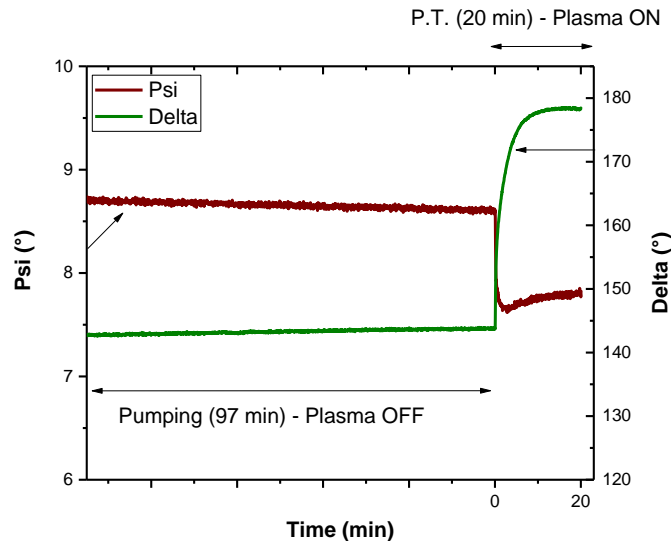


Figure 3.1: *In situ* evolution of Psi and Delta values with time, during the pumping and the 20-minutes plasma treatment. Results are shown for only one sample although comparable values were observed for other samples.

Aiming at further understanding this kinetic evolution, especially in the first minutes of the plasma treatment, the *in situ* SE data recorded at each plasma treatment time were fitted using a model. The validity of this model, and therefore the evaluation of the accuracy of the fit, was estimated by the Mean Square Error (MSE)

[19]. Initially, the ellipsometric model used for the before plasma treatment condition (time 0) was the one illustrated in Figure 3.2a. This model, typically used for plasma-deposited anatase TiO₂ thin films, is based on Tauc-Lorentz dispersion law with an optical energy gap (E_g) of 3.2 eV [20]. As seen in Figure 3.2a, this model reveals significant discrepancy (MSE=273) between the experimental (coloured) and simulated (dashed) lines. Therefore, a different model was required to adequately represent a film containing spin-coated anatase TiO₂ NPs. As mentioned in the experimental section, the colloidal solution with TiO₂ NPs contains PG and PC. In such conditions, Karpinsky et al. [15] have proposed a core shell configuration of these NPs. In detail, it was calculated that for 5nm TiO₂ anatase NPs, a 4.7 Å hydroxylated and organic shell is surrounding a crystalline core. In this framework, the TiO₂ nanostructured layer was modelled using Bruggeman Effective Medium Approximation (BEMA) with two materials: the TiO₂ anatase NPs expressed with the Tauc-Lorentz dispersion law [19] with an optical energy gap at 3.4 eV (due to the nanometer size of the TiO₂ [21,22]) and the low-density thin shell inducing separation between the nanoparticles and thus expressed as voids. As highlighted in Figure 3.2b, the BEMA model provides much better agreement between experimental and simulated values (MSE=11) and thus seems very well suited for the spin-coated TiO₂ NPs system, at least from the optical point of view. Similar very-good-quality fits were observed for all operating conditions (not shown here).

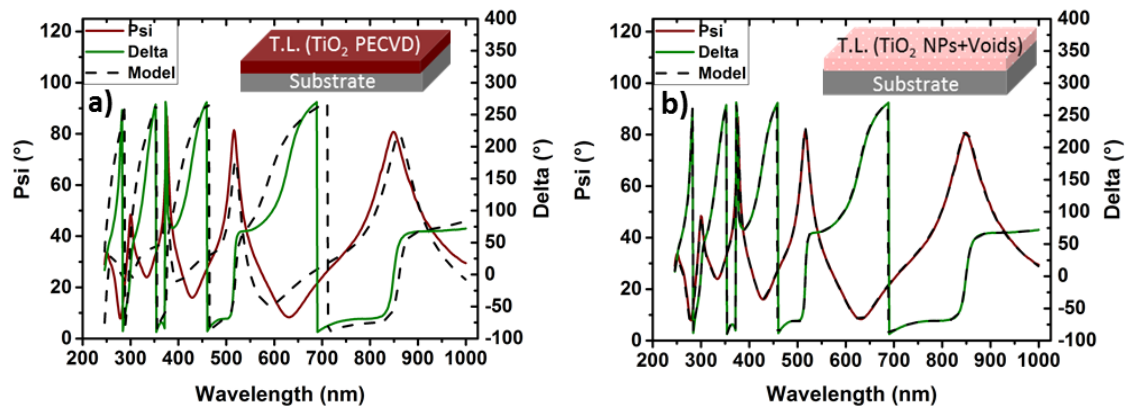


Figure 3.2: Psi-Delta values obtained from *in situ* spectroscopic ellipsometry before plasma treatment (full lines) and from simulations (dashed lines). The results are shown as a function of the photon wavelength. In a), the model is based on a plasma-deposited anatase TiO₂ material (TL, for Tauc-Lorentz dispersion law) whereas in b) the model relies on a combination of TiO₂ NPs and void (BEMA, for Bruggeman Effective Medium Approximation). The schematic representation of the models are also shown in the topmost figures.

From the fit of Psi and Delta spectra recorded at each plasma treatment time, a variety of information such as the optical thickness of the film, the fraction of voids, the energy gap (E_g), the refractive index of the layer (n_{eff}) and the extinction coefficient (k_{eff}) can be extracted. Information on the optical roughness of the layer could also be analysed. However, due to the rather small thickness of the films examined in this

work and their very small roughness, roughening effects in Psi and Delta analysis can only be estimated. Over the range of experimental conditions examined, optical roughness values deduced by spectroscopic ellipsometry were ~round 2 nm. By fitting and extracting the spectral data as a function of treatment time, the plots given in Figure 3.3 were obtained. Focusing on the 20 first minutes of the plasma treatment, the time evolution of the film thickness, the fraction of voids and the energy gap (E_g) are displayed in Figure 3.3a while the optical constants as a function of wavelength for various plasma treatment times are presented in Figure 3.3b.

As a general trend, the film thickness, the fraction of voids and E_g decrease with plasma treatment time and then reach steady-state after 10 minutes of plasma treatment. However, further analysis reveals that two timeframes can be identified during the first 10 minutes. Between 0 and 2 minutes, the film thickness sharply decreases by almost 6 nm (14% of the total thickness) and the fraction of voids rapidly reaches 0. This means that the shells and the empty spaces (which can be detected by ellipsometry) separating TiO₂ NPs are removed: this brings TiO₂ NPs closer together. Over this time frame, the energy gap remains more or less constant. On the other hand, between the 2nd and the 10th minute, the fraction of voids remains 0, the film thickness only slightly decreases and the energy gap (E_g) now decreases significantly. As reported elsewhere for TiO₂ systems [22,23], there is a clear dependence between the size of TiO₂ crystallites and the energy bandgap of the film. Therefore, the decrease in E_g , as evidenced by spectroscopic ellipsometry between the 2nd and the 10th minute, suggests an increase in the crystallite size of the spin-coated TiO₂ crystallites during plasma treatment over this specific time frame.

Regarding the optical parameters of the nanostructured TiO₂ layer, Figure 3.3b reveals that the effective refractive index (n_{eff}) and the effective extinction coefficient (k_{eff}) both increase during plasma treatment, with a more prominent increase in the UV (240-340nm) zone. In terms of spectroscopic ellipsometry, the observed plasma-induced modification during the first two minutes (fraction of voids becomes 0, reduction in the film thickness, NPs become closer) implies that the initial layer incorporating voids in between the NPs (modelled by a BEMA) becomes an actual TiO₂ NPs layer. Then, this TiO₂ layer is further treated, resulting in an additional increase of the effective refractive index, as observed in Figure 3.3a. In the same manner, the shift in the onset of the extinction coefficient can be related to the decrease of E_g [24,25]. Nevertheless, both the refractive index and the extinction coefficient have lower values than the ones obtained for bulk, plasma-deposited TiO₂ films ($n = 2.3$ at 633 nm) due to the nanometric size of TiO₂ NPs in the nanostructured TiO₂ film obtained by spin coating [20].

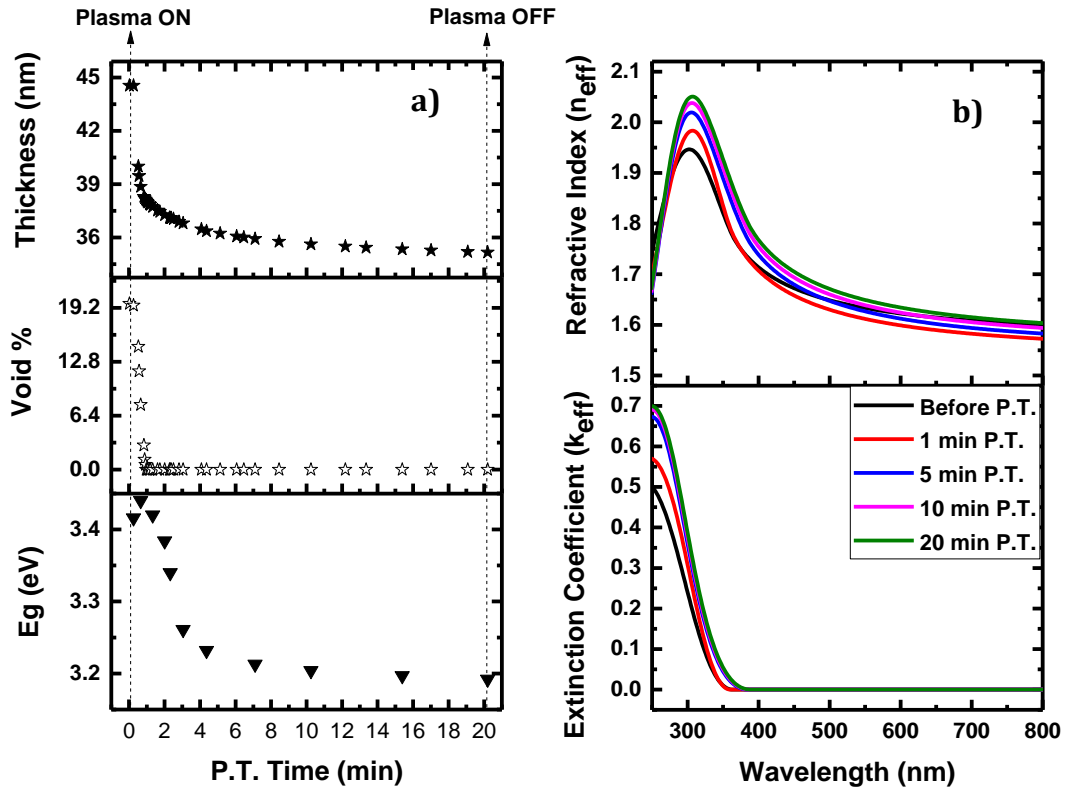


Figure 3.3: (a) *In situ* spectroscopic ellipsometry results indicating the thickness evolution, the percentage of void, and the energy gap during the 20 minutes of the plasma treatment. (b) Evolution of the effective refractive index (n_{eff}) and effective extinction coefficient (k_{eff}) for different times during the 20 minutes plasma treatment. Black, red, blue, purple and green lines correspond to Before P.T., 1 min, 5 min, and 10 min.

3.2.2 Morphological and crystallinity analysis of the plasma-treated nanostructured TiO₂ thin films

Morphological analysis of nanostructured, spin-coated TiO₂ thin films were realized by SEM and AFM in order to better understand the optical changes observed in the previous section. Further investigations on the crystallinity of TiO₂ NPs were achieved by TEM. Typical SEM images, TEM images and AFM scans obtained before and after plasma treatment are shown in Figure 3.4. At the scale of SEM images (left-hand-side column in Figure 3.4), the film seems globally homogeneous even if some darker contrasts are detected. At this scale, we deduce that these features could be attributed to cracks allowing the solvent to be expelled during the spin-coating process. After the plasma treatment, the nanostructuring of the film globally remains intact. However, the number of the cracks seems slightly increased. Since the resolution of the SEM is at 10 nm, one can understand that the exact identification of the 5 nm NPs is impossible. From TEM images (presented on the middle side column of Figure 3.4), the basal TiO₂ planes indicate crystallized TiO₂ NPs before and after plasma treatment. Before exposure to the low-pressure O₂ plasma, typical crystallite sizes can be estimated at 3.5 ± 0.6 nm whereas after the plasma treatment the typical crystallite sizes increases to 4.5 ± 0.9 nm.

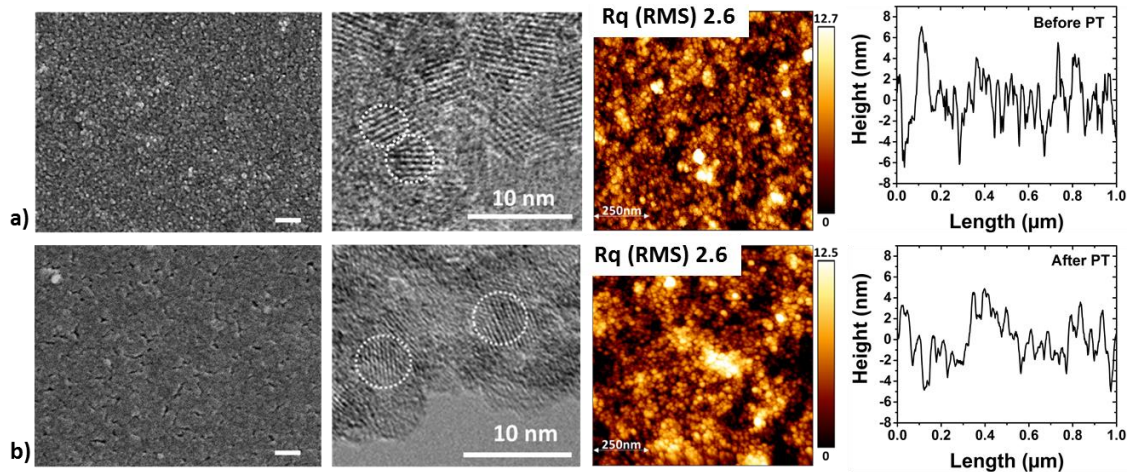


Figure 3.4: (from the left) Surface Scanning Electron Microscopy (SEM) Images, Transmission Electron Microscopy images, Atomic Force Microscopy (AFM) scans and cross section AFM of the a) non treated spin coated TiO₂ nanoparticles (NPs) thin film and b) 20 minutes plasma treated TiO₂ NPs thin film. Scale bar for SEM: 100 nm and Root Mean Square (RMS) Rq roughness values are indicated on the AFM scans.

AFM was used as a local probe first to have access to the roughness and second to the size distribution of the NPs. As shown in Figure 3.4 (right-hand-side column), the root-mean-square (RMS, Rq) roughness of as-deposited and plasma-treated TiO₂ coatings is 2.6 nm. These values are consistent with those estimated from spectroscopic ellipsometry (Section 3.2.1). Before the plasma treatment, Figure 3.4a reveals that AFM scans at low magnification are kind of fuzzy and blurry. Such feature can most likely be ascribed to the presence of solvent expelled throughout the film thickness that remains on the film surface after spin-coating of the colloidal solution. In contrary, after the plasma treatment, the quality of the image is significantly improved such that the shape and size of TiO₂ NPs can now readily be identified from both low and high magnification images.

Cross sectional line profile from the same AFM scans are given in Figure 3.4 (right-hand-side column). Despite the fact that these two profiles have the same Rq (RMS) roughness, which is extracted from the total area of the scan, they reveal some differences. From the as-deposited film, the height variation is more pronounced. Contrary, after the plasma treatment, the height variation is smoothed and the variation is less frequent. From these two particular profiles, the peak-to-valley Rt reaches 14.6 and 11.4 nm, before and after plasma treatment, respectively. This indicates that the surface of the NPs is affected by the treatment.

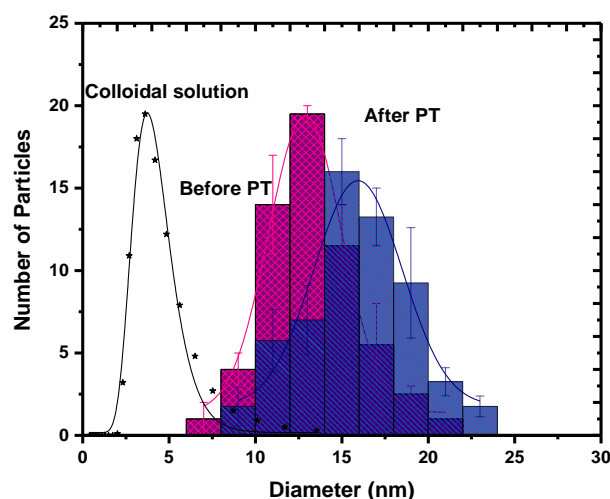


Figure 3.5: Size distribution of nanostructures deduced from AFM scans before (magenta) and after (blue) plasma treatment for 20 minutes. The size distribution of TiO₂ NPs obtained from DLS in the colloidal solution (black) before spin coating is also shown for comparison.

From detailed analysis of multiple AFM scans at low and high magnification, the mean size of spin-coated nanostructures before and after plasma treatment were extracted. The results are plotted as histograms in Figure 3.5. Size distribution obtained from Dynamic Light Scattering (DLS) in the colloidal solution is also shown for comparison. From the plots, Gaussian fits were realized to obtain the mean size and the standard deviation. Compared to the DLS results of TiO₂ NPs in volume, the hydrodynamic diameter increases after the spin-coating process. In the colloidal solution, the hydrodynamic diameter is estimated at 4.0 nm and the standard deviation is at 0.3 nm. After the spin-coating process, these values increase to 13 nm and 4 nm, respectively. Such feature was also observed by other authors (see, for example, [26,27]) and was ascribed to the agglomeration of TiO₂ NPs during deposition and evaporation of the solvent. Therefore, the objects observed and measured by AFM are aggregated TiO₂ NPs. After the plasma treatment, there is a slight shift of these aggregations to higher values, with a mean size of 16 nm and a standard deviation of 5 nm. The fact that the mean size increases with a relatively low standard deviation in AFM scans is consistent with previous observations that there is a shift towards higher NPs sizes of TiO₂ NPs after plasma treatment, observed from SE (section 3.2.1) associated to an increase in crystallite size as stated from High Resolution TEM observations (Middle of Figure 3.4).

3.2.3 Chemical analysis of the plasma-treated nanostructured TiO₂ thin films

For the chemical analysis of the spin-coated TiO₂ NPs before and after the plasma treatment, Raman spectroscopy and XPS were used. Figure 3.6 presents the Raman spectra of TiO₂ NPs before and after plasma treatment with a focus on the Eg band anatase peak. Raman modes can be assigned to the Raman spectra of the anatase crystal: 144 (Eg), 200 (Eg), 400 (B1g), 513 (A1g), 518 (B1g) and 642 cm⁻¹ (Eg) [28,29].

Regarding the spin-coated films before plasma treatment, it can be observed that the Eg peak lies at 154 cm⁻¹: this value is shifted from the expected anatase 144 cm⁻¹ Eg peak [30,31]. Since commenting Raman intensities of very thin films requires to be cautious, the analysis was limited to the peak positions. It is well-established experimentally that Raman spectra of low-dimensional crystals of semiconductors are modified when compared to the corresponding bulk crystal spectra namely, (1) the Raman peaks are asymmetrically broadened and (2) their positions are shifted [32,33]. In this context, the results presented in Figure 3.6 confirm that spin-coated TiO₂ NPs are anatase crystallites and small in size. Moreover, after the plasma treatment, the Eg band peak maintains a similar asymmetrical shape but shifts to 150 cm⁻¹; such feature still typical for nanometric TiO₂, can be related to an increase in the mean crystallite size of TiO₂ NPs [31,34], in very good agreement with the conclusions of *in situ* spectroscopic ellipsometry (Section 3.2.1) and TEM (middle of Figure 3.4) in Section 3.2.2.

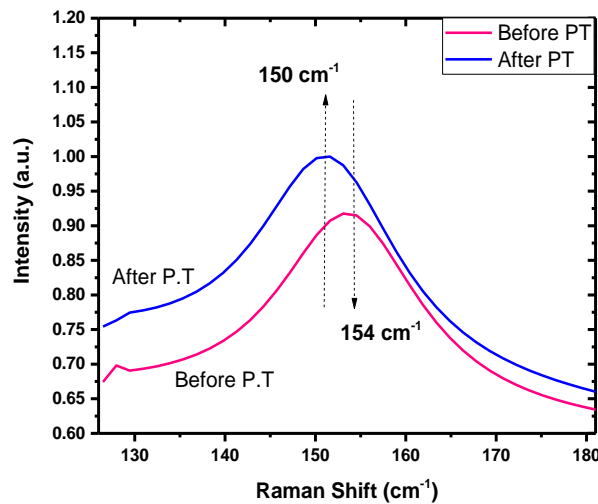


Figure 3.6: Anatase Eg Raman band before (pink) and after plasma treatment (blue).

Further chemical analysis was obtained through XPS. As reported by many authors (see, for example, [2,35,36]), the signal of titanium element in XPS results from two separated peaks that can be attributed to Ti 2p_{3/2} and Ti 2p_{1/2}. The 2p_{3/2} peak lies at 458.5 eV as expected for Ti⁴⁺ cations in TiO₂. The contribution of oxygen bonded to titanium atoms and noted as Ti-O appears at 530.0 eV. Since the colloidal solution of TiO₂ NPs was synthesized in an organic solvent, the contribution of carbon element was considered. Therefore, three peaks were identified. The first, at 284.8 eV, is usually assigned to C-C bonds of both adventitious elemental carbon and the solvent, while the second, at 286.0 eV, and the third, 288.5 eV, can be related to -C-O bonds and C=O bonds, respectively, corresponding to PG and PC. Fitting these peaks with CasaXPS software can then provide information on the atomic percentage of the various contributions in nanostructured TiO₂ films. The results are presented in Figure 3.7 before and after plasma treatment. As expected, the pristine surface reveals

a rather significant amount of organic species (40% in total). After the O₂ plasma treatment, this contribution significantly decreases (22% in total) due to the removal of solvent-based organic moieties.

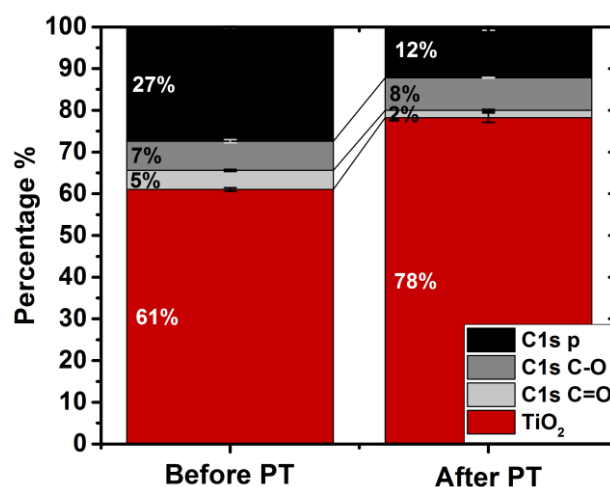


Figure 3.7: Stacked columns (%) of the chemical composition of the TiO₂ thin film surface before and after the plasma treatment.

3.3. Discussion

3.3.1 Explanation of the two kinetics

Based on the experimental data presented in Section 3.2, the main effects observed after the O₂ plasma treatment of the spin-coated TiO₂ nanostructured thin film are (i) a mineralization of the coating due to the removal of solvent-based organic moieties surrounding TiO₂ NPs (evidenced by XPS and AFM), (ii) a densification of the film (evidenced by *in situ* SE) and (iii) an increase of the crystallite size (evidenced by *in situ* SE, TEM, and Raman spectroscopy) and of the agglomeration of TiO₂ NPs (evidenced AFM). A way to explain these features is by understanding both the nanoparticles and the O₂ plasma itself. On the one hand, as already mentioned, Karpinsky et al. [15] have proposed a core shell configuration for TiO₂ NPs synthesized according to ref. [2] and [15]. As a result, for the case of 5 nm TiO₂ anatase NPs dispersed in PC and PG, a 4.7 Å hydroxylated and organic shell exists around TiO₂ NPs. On the other hand, over the range of experimental plasma conditions investigated (see all details in Table 3.1, [18]), the population of O atoms ($n_o=1.7 \times 10^{14} \text{ cm}^{-3}$) is much larger than the O₂⁺ ion density ($n_i=1.6 \times 10^9 \text{ cm}^{-3}$). This predominance of O atoms in the low-pressure plasma promotes their interaction with the film and thus provides a smooth and selective chemical etching rather than rapid and non-selective ion bombardment. Based on these features, an attempt to illustrate the effect of the O₂ plasma treatment on TiO₂ NPs is presented in Figure 9.

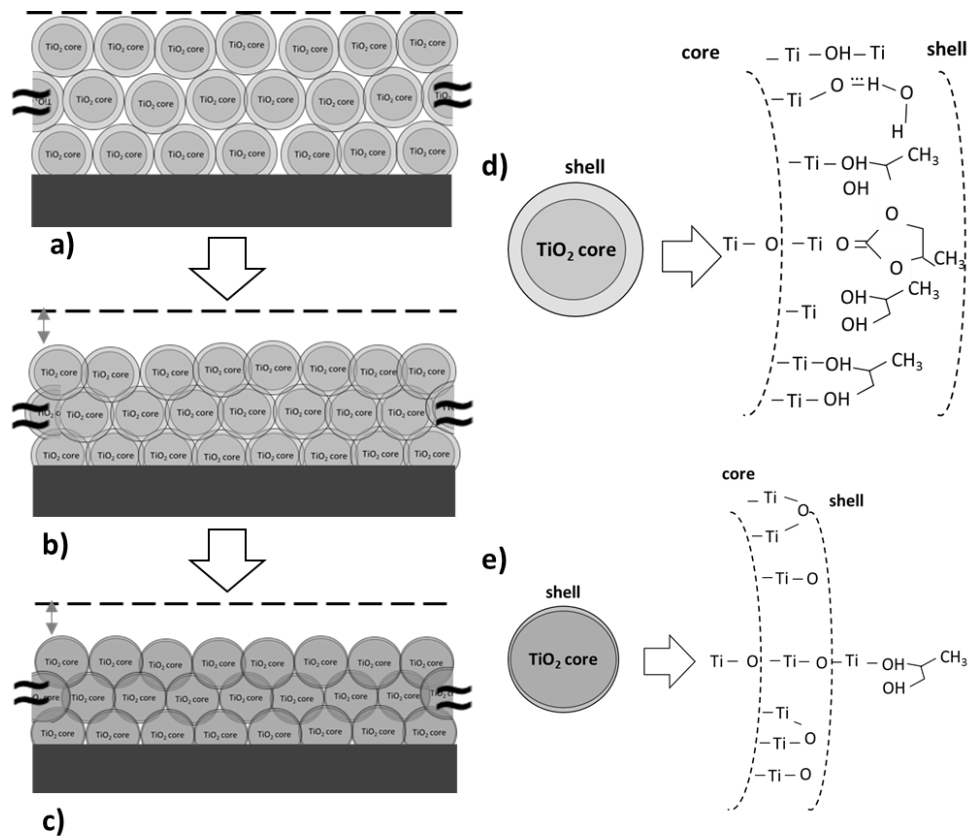


Figure 3.8: Schematic illustration of the spin-coated TiO₂ NPs a) before the plasma treatment, b) during the first kinetics (1-2min) and c) during the second kinetics (3-15min). Schematic illustration of the d) as synthesized, TiO₂ NPs, in core-shell configuration and e) after the plasma treatment.

During the first kinetics characterized by a fairly constant energy gap (and thus crystallite size) and a significant decrease of the film thickness and of the fraction of voids (0-2min, see Figure 3.4), chemical etching of the organic part of the NPs' shell occurs, densifying the layer and leading to the production of CO, CO₂ and H₂O volatile by-products in the plasma volume [18]. This behaviour, depicted in Figure 3.8b, can be confirmed by the decrease of the fraction of organic species measured by XPS. During the second kinetics characterized by a decrease of the energy gap (and thus a rise of the crystallite size) and of the film thickness (2-10min, see Figure 3.4), the O atoms have better access to the total thickness of the film such that they become able to reorganize the remaining shell with the core (for each NP). This reorganization leads to an even thinner shell and to the addition of a TiO₂ layer surrounding the initial TiO₂ core by the formation of O-Ti-O bonds. These aspects are illustrated in Figures 3.8c and 3.8d and ultimately lead to the configuration displayed in Figure 3.8e. Through both *in situ* SE and Raman spectroscopy, it can be verified that this layer is contributing to the growth of the total TiO₂ crystallites, meaning that they remain in an anatase and not amorphous phase.

In this section, we proposed to explain the mechanisms leading to the two kinetics observed in Section 3.2. For these, the main parameter identified causing the alterations was the much higher density of the O atom species. However, is the energy brought by the plasma species high enough to condense the framework and induce the formation of O-Ti-O bonds? This, we will attempt to reply in the next Section.

3.3.2 Computation of the NPs Temperature upon Plasma Treatment using Energy Balance equation

Many groups have attempted to investigate the mechanism leading to the crystallization of amorphous NPs in weakly ionized, non-thermal plasmas [37–39]. The plasma-particle interactions leading to the heating of the TiO₂ NPs could be a suitable explanation to this phase transformation in O₂ plasmas at low pressure. In order to estimate the temperature of the NPs (T_{NPs}) over the range of experimental conditions examined, a steady-state power balance equation $Q_{IN} = Q_{OUT}$ was used [37,38]. In this case, the simple model of a single NP on the substrate surface was used (Figure 3.9). Here, the total input power Q_{IN} and total output power Q_{OUT} at the NPs' surface can be obtained from the corresponding energy fluxes J_{IN} and J_{OUT} , $Q_{IN} = \int_A J_{IN} dA = \int_A J_{OUT} dA$, where the integrals are performed over the studied surface area.

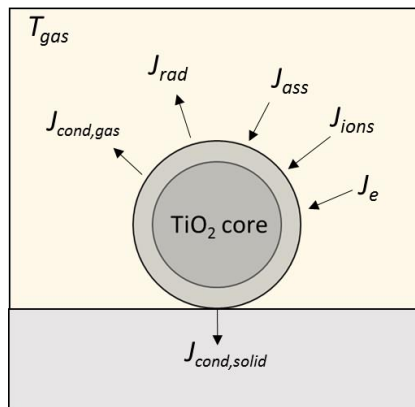


Figure 3.9: Schematic illustration of the model used for the energy balance equation with the corresponding input and output energy fluxes.

During the O₂ plasma treatment, the total input energy flux includes the contributions of positive ions (J_{ions}) following either their acceleration in the plasma sheath surrounding the NP at floating potential or their neutralization at the NP surface. In addition, electrons (J_e) as a result of their random motion around the NP at floating potential and O atoms (J_{ass}) following their recombination-association event at the NP surface. In this framework, the total energy flux towards the NPs can be written as [37,38]:

$$J_{IN} = J_{ions} + J_e + J_{ass} = n_i \sqrt{\frac{k_B T_e}{m_i}} (E_{ion} + \Gamma_i E_i) + n_e \sqrt{\frac{k_B T_e}{m_i}} 2k_B T_e + \frac{1}{4} n_O \sqrt{\frac{8k_B T_g}{\pi m_O}} \Gamma_O E_{diss} \quad (\text{Equation 3.1})$$

where k_B is the Boltzmann constant, m_i is the mass of O₂⁺, $E_{ion} = e (V_p - V_f)$ is the sheath potential (where V_p is the plasma potential, V_f is the floating potential and e is the electron charge), Γ_i is the recombination coefficient of the positive ions on the NP surface (here, $\Gamma_i = 1$ is assumed), E_i is the ionization energy (12.06 eV for O₂), m_O is the mass of O atoms, E_{diss} is the dissociation energy (5 eV for O₂), and Γ_O is the recombination coefficient of O atoms on the TiO₂ NP surface. Over the range of experimental conditions investigated, the Γ_O value can be estimated between 0.4 and 1 [40] (here, a maximum contribution was assumed such that $\Gamma_O = 1$). For the 25 mTorr, O₂ plasma investigated in this study, all of these contributions can be calculated using the plasma characteristics ($n_i, n_e, n_O, E_{ion}, T_e, T_g, T_s$) listed in Table 3.1. As shown in Table 3.2, the main contribution to the total input energy flux is J_{ass} .

Table 3.2: Calculated energy fluxes towards the TiO₂ NP inside the reactor during the 25 mTorr O₂ plasma

Energy flux (Jcm ⁻² s ⁻¹)			
$J_{ions} = 0.001$	$J_e = 0.0025$	$J_{ass} = 2.8$	$J_{IN} = 3.03$

To highlight the significance of the O atom energy flux to the total input flux, the J_{ions} , J_{ass} , J_e and J_{IN} were calculated for different pressure conditions inside the specific reactor and the results are given in Figure 3.10. The plasma conditions used for each pressure were extracted from previous studies.[18]

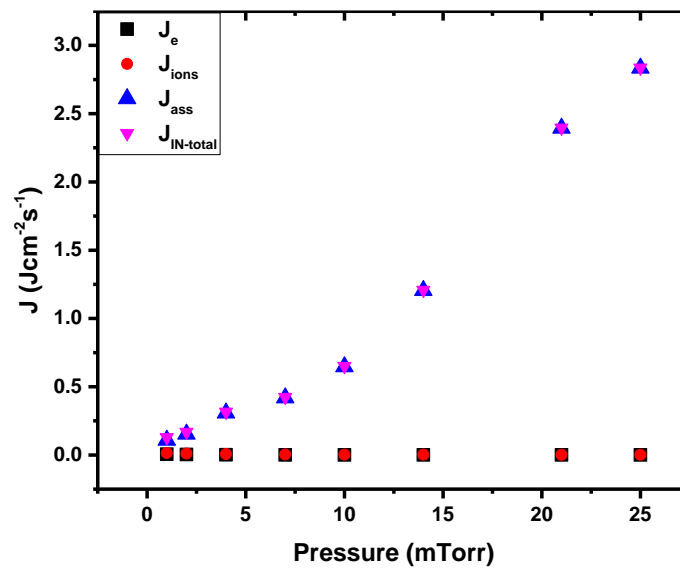


Figure 3.10: Calculated energy fluxes (J_{ions}, J_{ass}, J_e) towards the NPs for different pressure inside the reactor, during O₂ plasma and the calculated total J_{IN} energy flux.

In the present study, it was found that as the oxygen plasma pressure is increasing it yields both an increase of the oxygen atom flux and a decrease of the density, flux and energy of the positive oxygen ions. Indeed, by calculating the energy fluxes based on these data, the dependence of the total energy flux on the oxygen atoms for pressure from 3-25 mTorr is clarified (fig. 11-blue pink symbols). For lower pressure values, the flux obtained from the O atoms decreases which is linked to the decrease of the Oxygen atom density. In addition, a slight increase on the positive ions is also observed. Consequently, the chosen pressure directly affects the total energy brought to the surface of the NPs.

Regarding the total output energy flux J_{OUT} (heat loss term), the contributions include thermal conduction with the neutral gas species striking onto the NP surface ($J_{cond,gas}$), thermal conduction with atoms from the solid substrate ($J_{cond,solid}$) and radiation cooling (J_{rad}). For the 25 mTorr, O₂ plasma, the mean free path of the gas molecules (λ_{gas}) is much higher than the diameter of TiO₂ NPs such that the equation used for thermal conduction effects is the one for the free-molecule regime [41]. In this context, J_{OUT} can be written as follows [42]:

$$J_{OUT} = J_{cond,gas} + J_{cond,solid} + J_{rad} = \frac{\gamma+1}{16(\gamma-1)} \alpha \frac{p}{\sqrt{T_g}} \sqrt{\frac{8k_B}{\pi m}} (T_{NPs} - T_g) + \frac{\lambda_s}{d_s} (T_{NPs} - T_s) + \epsilon \sigma (T_{NPs}^4 - T_g^4) \quad (\text{Equation 3.2})$$

where γ is the adiabatic coefficient ($\gamma = 1.4$ for oxygen), α is the accommodation coefficient ($\alpha = 0.9$ for oxygen), p is the pressure, m is the mass of gas molecules, ϵ is the emissivity of the TiO₂ NPs, and σ is the Stefan-Boltzmann constant. For the heat loss by thermal conduction with the solid, d_s is the thickness of the substrate ($d_s = 500 \mu\text{m}$ for SiO₂/Si substrate) and λ_s is the heat conductivity of Si which is the main material of the substrate ($\lambda_s = 130 \text{ Wm}^{-1}\text{K}^{-1}$). In the last term of Equation (3.2), the emissivity is $\epsilon = 0.8$ [43]. For the 25 mTorr, O₂ plasma examined in this study, the main contribution to the total output energy flux J_{OUT} comes from $J_{cond,solid}$ and from $J_{cond,gas}$. In this context, assuming $Q_{IN} = Q_{OUT}$ Equations (3.1) and (3.2) can be simplified as

$$Q_{IN} = A_p \frac{1}{4} n_O \sqrt{\frac{8k_B T_g}{\pi m_O}} E_{diss} = A_{cont} \frac{\lambda_s}{d_s} (T_{NPs} - T_s) + A_p \frac{\gamma+1}{16(\gamma-1)} \alpha \frac{p}{\sqrt{T_g}} \sqrt{\frac{8k_B}{\pi m}} (T_{NPs} - T_g) = Q_{OUT} \quad (\text{Equation 3.3})$$

where A_p is the surface integral of the NP area i.e. $A_p = 4\pi r_p^2$, with a NPs's radius $r_p = 2.5 \text{ nm}$ for the case of $\sim 5 \text{ nm}$ TiO₂ anatase NPs and A_{cont} the cross-sectional area between the NP and the plane substrate. Assuming a round sphere in contact with a plane (Fig. 10), based on Hertz equation, $a = \sqrt[3]{\frac{3Wr_p}{4E^*}}$ [44], the radius of the spherical

cap in contact can be deduced. W is the weight of the NP, r_p its radius and E^* is the effective elasticity modulus between the TiO₂ NP and the SiO₂/Si substrate. The resulting radius is significantly low verifying the assumption that the contact between the NP and the substrate is a single point.

For a typical substrate temperature of $T_s=400\text{K}$ (as measured by temperature-sensitive labels located at the substrate's backside [7]), the temperature of the NPs can be estimated to $T_{NPS}=744\text{ K}$. This value indicates that the conduction of the substrate is negligible due to the geometry (small contact area) of the system under consideration, the main cooling parameter is the one of the conduction with the gas and T_{NPS} becomes comparable to the temperature achieved for NPs in the gas phase of dusty plasmas [37,38,45]. Crystallization of amorphous TiO₂ NPs or nanotubes (NT) has been studied by several authors using either thermal annealing (furnaces) or hydrothermal treatment techniques. In such conditions, crystallization temperatures in the 720-1070 K and 320-470 K ranges have been reported for thermal annealing and hydrothermal treatments, respectively [15,46–49]. Ohsaki et al [50] have also investigated the transformation of sol-gel derived TiO₂ films by RF plasma at a substrate temperature lower than 400 K and a duration of treatment at 2 min. From these studies, it seems that the energy fluxes of plasma-generated species, and thus the corresponding values of T_{NPS} (especially on the topmost surface), obtained over the range of plasma conditions investigated are sufficient to induce a transformation of the additional TiO₂ thin amorphous layer to form anatase TiO₂ NPs with larger crystallite sizes than in as-deposited, spin-coated TiO₂ thin films.

Conclusion

Through this study, we have investigated the impact of a low pressure O₂ plasma on thin films formed of spin-coated anatase TiO₂ nanoparticles with a core shell configuration. It was shown that the pumping process for acquiring a low-pressure environment in the plasma reactor does not affect the optical properties of the films measured by *in situ* spectroscopic ellipsometry. In contrast, two kinetics were identified during O₂ plasma processing. For very short plasma treatment times, chemical etching of the hydroxyl and organic shell by O atoms induces a mineralization of the nanostructured TiO₂ film with no significant change in the film morphology and nano-crystallinity. For larger time scales, a rise in the crystallite size of anatase TiO₂ NPs was first suggested from *in situ* spectroscopic ellipsometry and then confirmed by TEM and Raman analysis. In line with this finding, a rise of the size of TiO₂ agglomerates was also observed by AFM. In addition, a significant increase of the effective refractive index and extinction coefficient was highlighted. Based on this complete set of data, it was proposed that following chemical etching of the hydroxyl and organic shell, the O₂ plasma treatment can produce an additional TiO₂ layer surrounding the initial TiO₂ core through the formation of O-Ti-O bonds. In addition,

given the relatively high temperature of TiO₂ nanoparticles provided by the energy balance between input energy fluxes (mostly through heterogeneous recombination of O atoms on the nanoparticles surface) and output energy fluxes (mostly through thermal conduction with atoms from the surrounding gas), it was concluded that they are in an anatase and not amorphous phase. Overall, low-pressure O₂ plasma treatments represent fast and efficient post-deposition tools for tailoring, with a degree of control, the optical properties and nano-crystallinity of the TiO₂ thin films formed of spin-coated anatase TiO₂ nanoparticles. Based on these results, we infer that tuning the plasma parameters (change the plasma species) could possibly give additional degrees of freedom to clean and heal the surface of oxide NPs without degrading them, especially in case they are prepared in solution.

Bibliography

- [1] A. Karpinski, S. Berson, H. Terrisse, M. Mancini-Le Granvalet, S. Guillerez, L. Brohan, M. Richard-Plouet, Anatase colloidal solutions suitable for inkjet printing: Enhancing lifetime of hybrid organic solar cells, *Sol. Energy Mater. Sol. Cells.* 116 (2013) 27–33. <https://doi.org/10.1016/j.solmat.2013.04.006>.
- [2] M. El Kass, L. Brohan, N. Gautier, S. Béchu, C. David, N. Lemaitre, S. Berson, M. Richard-Plouet, TiO₂ Anatase Solutions for Electron Transporting Layers in Organic Photovoltaic Cells, *ChemPhysChem.* 18 (2017) 2390–2396. <https://doi.org/10.1002/cphc.201700306>.
- [3] J.K. Nelson, ed., *Dielectric polymer nanocomposites*, Springer, New York, 2010.
- [4] S. Sun, Monodisperse FePt Nanoparticles and Ferromagnetic FePt Nanocrystal Superlattices, *Science.* 287 (2000) 1989–1992. <https://doi.org/10.1126/science.287.5460.1989>.
- [5] J.D.B. Bradley, C.C. Evans, J.T. Choy, O. Reshef, P.B. Deotare, F. Parsy, K.C. Phillips, M. Lončar, E. Mazur, Submicrometer-wide amorphous and polycrystalline anatase TiO₂ waveguides for microphotonic devices, *Opt. Express.* 20 (2012) 23821. <https://doi.org/10.1364/OE.20.023821>.
- [6] T. Bora, Recent Developments on Metal Nanoparticles for SERS Applications, in: M.S. Seehra, A.D. Bristow (Eds.), *Noble Precious Met. - Prop. Nanoscale Eff. Appl.*, InTech, 2018. <https://doi.org/10.5772/intechopen.71573>.
- [7] D. Li, M. Carette, A. Granier, J.P. Landesman, A. Goulet, Effect of ion bombardment on the structural and optical properties of TiO₂ thin films deposited from oxygen/titanium tetraisopropoxide inductively coupled plasma, *Thin Solid Films.* 589 (2015) 783–791. <https://doi.org/10.1016/j.tsf.2015.07.015>.
- [8] D.K. Sarkar, D. Brassard, M.A.E. Khakani, L. Ouellet, Dielectric properties of sol-gel derived high-k titanium silicate thin films, *Thin Solid Films.* 515 (2007) 4788–4793. <https://doi.org/10.1016/j.tsf.2006.11.155>.
- [9] D. Brassard, D.K. Sarkar, M.A. El Khakani, L. Ouellet, Compositional effect on the dielectric properties of high-k titanium silicate thin films deposited by means of a cosputtering process, *J. Vac. Sci. Technol. Vac. Surf. Films.* 24 (2006) 600–605. <https://doi.org/10.1116/1.2180267>.
- [10] D. Li, S. Bulou, N. Gautier, S. Elisabeth, A. Goulet, M. Richard-Plouet, P. Choquet, A. Granier, Nanostructure and photocatalytic properties of TiO₂ films deposited at low temperature by pulsed PECVD, *Appl. Surf. Sci.* 466 (2019) 63–69. <https://doi.org/10.1016/j.apsusc.2018.09.230>.
- [11] T. Homola, P. Dzik, M. Veselý, J. Kelar, M. Černák, M. Weiter, Fast and Low-Temperature (70 °C) Mineralization of Inkjet Printed Mesoporous TiO₂ Photoanodes Using Ambient Air Plasma, *ACS Appl. Mater. Interfaces.* 8 (2016) 33562–33571. <https://doi.org/10.1021/acsami.6b09556>.
- [12] H. Chang, Y.-J. Yang, H.-C. Li, C.-C. Hsu, I.-C. Cheng, J.-Z. Chen, Preparation of nanoporous TiO₂ films for DSSC application by a rapid atmospheric pressure plasma jet sintering process, *J. Power Sources.* 234 (2013) 16–22. <https://doi.org/10.1016/j.jpowsour.2013.01.113>.
- [13] H. Chang, C.-M. Hsu, P.-K. Kao, Y.-J. Yang, C.-C. Hsu, I.-Chun. Cheng, J.-Z. Chen, Dye-sensitized solar cells with nanoporous TiO₂ photoanodes sintered by N₂ and air atmospheric pressure plasma jets with/without air-quenching, *J. Power Sources.* 251 (2014) 215–221. <https://doi.org/10.1016/j.jpowsour.2013.11.051>.
- [14] S.Z. Islam, A. Reed, D.Y. Kim, S.E. Rankin, N₂/Ar plasma induced doping of ordered mesoporous TiO₂ thin films for visible light active photocatalysis, *Microporous Mesoporous Mater.* 220 (2016) 120–128. <https://doi.org/10.1016/j.micromeso.2015.08.030>.
- [15] A. Karpinski, S. Berson, H. Terrisse, M. Mancini-Le Granvalet, S. Guillerez, L. Brohan, M. Richard-Plouet, Anatase colloidal solutions suitable for inkjet printing: Enhancing lifetime of hybrid organic solar cells, *Sol. Energy Mater. Sol. Cells.* 116 (2013) 27–33. <https://doi.org/10.1016/j.solmat.2013.04.006>.
- [16] M. Mitronika, J. Profili, A. Goulet, L. Stafford, A. Granier, M. Richard-Plouet, Modification of the optical properties and nano-crystallinity of anatase TiO₂ nanoparticles thin film using low pressure O₂ plasma treatment, *Thin Solid Films.* 709 (2020) 138212. <https://doi.org/10.1016/j.tsf.2020.138212>.
- [17] F. Nicolazo, A. Goulet, A. Granier, C. Vallee, G. Turban, B. Grolleau, Study of oxygen/TEOS plasmas and thin SiO_x films obtained in an helicon diffusion reactor, *Surf. Coat. Technol.* 98 (1998) 1578–1583.

- [18] A. Granier, G. Borvon, A. Bousquet, A. Goullet, C. Leteinturier, A. van der Lee, Mechanisms Involved in the Conversion of ppHMDSO Films into SiO₂-Like by Oxygen Plasma Treatment, *Plasma Process. Polym.* 3 (2006) 365–373. <https://doi.org/10.1002/ppap.200600022>.
- [19] D. Saha, R.S. Ajimsha, K. Rajiv, C. Mukherjee, M. Gupta, P. Misra, L.M. Kukreja, Spectroscopic ellipsometry characterization of amorphous and crystalline TiO₂ thin films grown by atomic layer deposition at different temperatures, *Appl. Surf. Sci.* 315 (2014) 116–123. <https://doi.org/10.1016/j.apsusc.2014.07.098>.
- [20] D. Li, M. Carette, A. Granier, J.P. Landesman, A. Goullet, In situ spectroscopic ellipsometry study of TiO₂ films deposited by plasma enhanced chemical vapour deposition, *Appl. Surf. Sci.* 283 (2013) 234–239. <https://doi.org/10.1016/j.apsusc.2013.06.091>.
- [21] S.M. Gupta, M. Tripathi, A review of TiO₂ nanoparticles, *Chin. Sci. Bull.* 56 (2011) 1639–1657. <https://doi.org/10.1007/s11434-011-4476-1>.
- [22] B. Enright, D. Fitzmaurice, Spectroscopic Determination of Electron and Hole Effective Masses in a Nanocrystalline Semiconductor Film, *J. Phys. Chem.* 100 (1996) 1027–1035. <https://doi.org/10.1021/jp951142w>.
- [23] R. Vijayalakshmi, V. Rajendran, Synthesis and characterization of nano-TiO₂ via different methods, (2012) 8.
- [24] H.G. Tompkins, ed., *Handbook of ellipsometry*, Repr, Andrew [u.a.], Norwich, NY, 2010.
- [25] S.O. Kasap, *Principles of electronic materials and devices*, McGraw-Hill, Boston, 2006.
- [26] J. Profili, O. Levasseur, J.-B. Blaisot, A. Koronai, L. Stafford, N. Gherardi, Nebulization of Nanocolloidal Suspensions for the Growth of Nanocomposite Coatings in Dielectric Barrier Discharges: Nebulization of Nanocolloidal Suspensions..., *Plasma Process. Polym.* 13 (2016) 981–989. <https://doi.org/10.1002/ppap.201500223>.
- [27] A.B.D. Nandiyanto, K. Okuyama, Progress in developing spray-drying methods for the production of controlled morphology particles: From the nanometer to submicrometer size ranges, *Adv. Powder Technol.* 22 (2011) 1–19. <https://doi.org/10.1016/j.apt.2010.09.011>.
- [28] W.F. Zhang, Y.L. He, M.S. Zhang, Z. Yin, Q. Chen, Raman scattering study on anatase TiO₂ nanocrystals, *J. Phys. Appl. Phys.* 33 (2000) 912–916. <https://doi.org/10.1088/0022-3727/33/8/305>.
- [29] T. Ohsaka, F. Izumi, Y. Fujiki, Raman spectrum of anatase, TiO₂, *J. Raman Spectrosc.* 7 (1978) 321–324. <https://doi.org/10.1002/jrs.1250070606>.
- [30] W. Ma, Z. Lu, M. Zhang, Investigation of structural transformations in nanophase titanium dioxide by Raman spectroscopy, *Appl. Phys. Mater. Sci. Process.* 66 (1998) 621–627. <https://doi.org/10.1007/s003390050723>.
- [31] C. Pighini, D. Aymes, N. Millot, L. Saviot*, Low-frequency Raman characterization of size-controlled anatase TiO₂ nanopowders prepared by continuous hydrothermal syntheses, *J. Nanoparticle Res.* 9 (2007) 309–315. <https://doi.org/10.1007/s11051-005-9061-6>.
- [32] Y. Gao, X. Zhao, P. Yin, F. Gao, Size-Dependent Raman Shifts for nanocrystals, *Sci. Rep.* 6 (2016). <https://doi.org/10.1038/srep20539>.
- [33] A.G. Rolo, M.I. Vasilevskiy, Raman spectroscopy of optical phonons confined in semiconductor quantum dots and nanocrystals, *J. Raman Spectrosc.* 38 (2007) 618–633. <https://doi.org/10.1002/jrs.1746>.
- [34] J. Profili, O. Levasseur, N. Naudé, C. Chaneac, L. Stafford, N. Gherardi, Influence of the voltage waveform during nanocomposite layer deposition by aerosol-assisted atmospheric pressure Townsend discharge, *J. Appl. Phys.* 120 (2016) 053302. <https://doi.org/10.1063/1.4959994>.
- [35] D. Li, S. Elisabeth, A. Granier, M. Carette, A. Goullet, J.-P. Landesman, Structural and Optical Properties of PECVD TiO₂-SiO₂ Mixed Oxide Films for Optical Applications: Structural and Optical Properties of PECVD TiO₂-SiO₂ ..., *Plasma Process. Polym.* 13 (2016) 918–928. <https://doi.org/10.1002/ppap.201600012>.
- [36] J.F. Moulder, W.F. Stickle, P.E. Sobol, K.D. Bomben, J. Chastain, R.C. King Jr., Physical Electronics, Incorporation, eds., *Handbook of X-ray photoelectron spectroscopy: a reference book of standard spectra for identification and interpretation of XPS data*, Physical Electronics, Eden Prairie, Minn., 1995.
- [37] G.H.P.M. Swinkels, H. Kersten, H. Deutsch, G.M.W. Kroesen, Microcalorimetry of dust particles in a radio-frequency plasma, *J. Appl. Phys.* 88 (2000) 1747–1755. <https://doi.org/10.1063/1.1302993>.
- [38] N.J. Kramer, R.J. Anthony, M. Mamunuru, E.S. Aydil, U.R. Kortshagen, Plasma-induced crystallization of silicon nanoparticles, *J. Phys. Appl. Phys.* 47 (2014) 075202. <https://doi.org/10.1088/0022-3727/47/7/075202>.

- [39] A.-L. Thomann, A. Caillard, M. Raza, M. El Mokh, P.A. Cormier, S. Konstantinidis, Energy flux measurements during magnetron sputter deposition processes, *Surf. Coat. Technol.* 377 (2019) 124887. <https://doi.org/10.1016/j.surfcoat.2019.08.016>.
- [40] A. Granier, S. Jacq, D. Li, M. Carette, A. Goulet, Investigation of plasma surface interactions in pulsed O₂/TTIP low pressure ICP plasma by time resolved optical emission spectroscopy, in: *ESCAMPIG XXI*, Viana do Castelo, Portugal, 2010: p. 2.
- [41] R. Piejak, V. Godyak, B. Alexandrovich, N. Tishchenko, Surface temperature and thermal balance of probes immersed in high density plasma, *Plasma Sources Sci. Technol.* 7 (1998) 590–598. <https://doi.org/10.1088/0963-0252/7/4/016>.
- [42] H. Kersten, H. Deutsch, H. Steffen, G.M.W. Kroesen, R. Hippler, The energy balance at substrate surfaces during plasma processing, *Vacuum.* 63 (2001) 385–431. [https://doi.org/10.1016/S0042-207X\(01\)00350-5](https://doi.org/10.1016/S0042-207X(01)00350-5).
- [43] Y. Qi, B. Xiang, J. Zhang, Effect of titanium dioxide (TiO₂) with different crystal forms and surface modifications on cooling property and surface wettability of cool roofing materials, *Sol. Energy Mater. Sol. Cells.* 172 (2017) 34–43. <https://doi.org/10.1016/j.solmat.2017.07.017>.
- [44] Popov, Kottusch, *Handbook of Contact Mechanics*, Springer Berlin Heidelberg, Place of publication not identified, 2019. <https://link.springer.com/book/10.1007/978-3-662-58709-6> (accessed February 16, 2020).
- [45] S. Prasanna, A. Michau, K. Hassouni, S. Longo, Effect of charge fluctuation on nanoparticle heating in dusty plasma, *Plasma Sources Sci. Technol.* 28 (2019) 03LT03. <https://doi.org/10.1088/1361-6595/ab094d>.
- [46] A. Lamberti, A. Chiodoni, N. Shahzad, S. Bianco, M. Quaglio, C.F. Pirri, Ultrafast Room-Temperature Crystallization of TiO₂ Nanotubes Exploiting Water-Vapor Treatment, *Sci. Rep.* 5 (2015). <https://doi.org/10.1038/srep07808>.
- [47] L. Yang, M. Zhang, S. Shi, J. Lv, X. Song, G. He, Z. Sun, Effect of annealing temperature on wettability of TiO₂ nanotube array films, *Nanoscale Res. Lett.* 9 (2014) 621. <https://doi.org/10.1186/1556-276X-9-621>.
- [48] F. Hilario, V. Roche, R.P. Nogueira, A.M.J. Junior, Influence of morphology and crystalline structure of TiO₂ nanotubes on their electrochemical properties and apatite-forming ability, *Electrochimica Acta.* 245 (2017) 337–349. <https://doi.org/10.1016/j.electacta.2017.05.160>.
- [49] S. Kundu, V. Polshettiwar, Hydrothermal Crystallization of Nano-Titanium Dioxide for Enhanced Photocatalytic Hydrogen Generation, *ChemPhotoChem.* 2 (2018) 796–800. <https://doi.org/10.1002/cptc.201800101>.
- [50] H. Ohsaki, Y. Shibayama, N. Yoshida, T. Watanabe, S. Kanemaru, Room-temperature crystallization of amorphous films by RF plasma treatment, *Thin Solid Films.* 517 (2009) 3092–3095. <https://doi.org/10.1016/j.tsf.2008.11.086>.

Chapter 4

Multi-Step approach for the elaboration of TiO₂-SiO₂ multilayer thin film by spin coating and PECVD

In this chapter, the second step of the experimental strategy is being studied. TiO₂-SiO₂ multilayer film with total thickness of 200 nm was prepared using a multi-step approach, coupling the spin coating technique and the Plasma Enhanced Chemical Vapor Deposition (PECVD) process. The TiO₂ NPs studied in Chapter 2, were used for the spin coated TiO₂ layers and the HMDSO vapor for the elaboration of the PECVD-made SiO₂ layers. While Transmission Electron Microscopy (TEM) proved the clear multilayer structure without mixed layers at the interface region (between the layers), Energy-dispersive X-ray spectroscopy (EDX) analysis revealed a degree of infiltration of the SiO₂ along the TiO₂ one, lying at approximately 30 %. The conformity of the SiO₂ layers was identified through Atomic Force Microscopy (AFM) providing nanostructured scans and increased roughness (compared to SiO₂ deposited on smooth substrate). The optical response of these layers was characterized with Ellipsometry and it was found that SiO₂ acts like a “healing” factor concerning the refractive index. Finally, the obtained results were compared and discussed with pure PECVD multilayer structures in terms of structural characteristics and optical response.

Table of Contents

Introduction.....	127
4.1 Materials and Methods.....	127
4.1.1 Deposition of the Nanoparticles	128
4.1.2 Implementation of the Bilayer and the Multilayer	128
4.2 Results.....	129
4.2.1 TEM characterization of the elaborated bilayer and multilayer	129
4.2.2 Investigation of the topographical characteristics of each layer	132
4.2.3 Evaluation of each layer's physical and optical characteristics through Ellipsometry	134
4.2.4 Comparison of the multi-step approach multilayer thin film with pure PECVD one	138
4.4 Discussion.....	145
4.4.1 Impact of the SiO ₂ infiltration and conformal behavior on the amorphous- crystalline interphase.....	145
4.4.2 Evaluation of the multilayer optical response based on the two implementation approaches.....	146
Conclusion	147
Bibliography	148

Introduction

Multilayer TiO₂-SiO₂ thin films have been rigorously created in the past focusing mainly on the optical and dielectric[1] properties of these two materials in the multilayer structures. On the one side, TiO₂ is an interesting semiconductor due to its optical, dielectric and photocatalytic properties having a refractive index of $n = 2.5$ at 633 nm, dielectric constant at 80 and an energy gap at $E_g = 3.2$ eV, when in anatase phase [2]. On the other side, SiO₂, used especially in the semiconductor industry is a good insulator having lower refractive index at $n = 1.46$, dielectric constant at 3.9 but higher energy gap at 9 eV. Prominent application of these multilayer structures is the Antireflective Coatings (AR)[3], as it is known that alternately varying high and low refractive index layers can enhance the anti-reflectance of the film. Towards this direction, several works include sol-gel made TiO₂-SiO₂ multilayered thin films. Choi et al. [4] investigated the impact of the in-between SiO₂ layer characteristics on the near-infrared region reflectance of the total TiO₂-SiO₂ multilayer thin film. In addition, Faustini et al. [5] elaborated sol-gel multilayer structures in a manner of acquiring not only anti-reflective properties but also hydrophobic and self-cleaning. Nonetheless, studies have also been focusing in the dielectric response[6] of these TiO₂-SiO₂ films and more specifically in the area of electronics and optoelectronics using mainly vacuum processes such as Atomic Layer Deposition (ALD)[7] and Ion Sputtering[8].

Based on these, this chapter is focusing on the elaboration of multilayer thin films, by a multi-step approach coupling Plasma Enhanced Chemical Vapor Deposition (PECVD) and Sol- Gel. This study will help us understand the interactions between the spin coated TiO₂ NPs and the PECVD made SiO₂ matrix and possibly assess the creation of NCs thin films in the next chapters. Here, a multi-step approach will be used, using more conventional deposition techniques than the hybrid approach described in chapter 5 of this thesis. Using Transmission Electron Microscopy (TEM) and Energy Dispersive X-ray spectrometry (EDX) we will investigate the structural and chemical nature of the multilayer cross section. Using Scanning Electron Microscopy (SEM) and Atomic Force Microscopy (AFM) the surface of the final film was characterized. Since several works using multilayer TiO₂-SiO₂ structured are oriented towards optical applications, the optical characteristics of the films were evaluated with ellipsometry. Finally, these results will be compared with multilayer films obtained only by PECVD (both TiO₂ and SiO₂ layers).

4.1 Materials and Methods

The multilayer thin film was created following an experimental protocol explained as follows, where each layer was created and then characterized in order to verify its thickness. The alternation of the layer started first by depositing the TiO₂ NPs one (1st)

through spin coating and then followed by the PECVD SiO₂ one (2nd). This was repeated once more for the creation of the double bilayer (or multilayer) structure.

4.1.1 Deposition of the Nanoparticles

For the creation of the 1st and 3rd spin coated TiO₂ NPs layer (denoted TiO_{2sp}), the colloidal solution of crystallized anatase TiO₂ nanoparticles described in Chapter 2 was spin coated on thermally oxidized SiO₂ silicon substrates, SiO_{2th}. This colloidal solution is being synthesized according to ref. [9,10], enclosing nanoparticles, exhibiting a well-defined monodispersed mean size centered on 5 nm. The conditions for an effective and reproducible spin coated layer which were used are explained in detail in Chapter 2 and had been already used in Chapter 3. To acquire a thickness of 40-50nm of TiO₂ layers, three spin coating sets were performed and the achieved thickness was measured with Ellipsometry.

4.1.2 Implementation of the Bilayer and the Multilayer

For the elaboration of the 2nd and 4th layer, the sample was introduced in the low-pressure PECVD reactor. The reactor comprises a diffusion chamber and a low-pressure high-density Inductive Coupled Plasma (ICP) created at 13.56 MHz (400 W) via a helicon antenna and oxygen was introduced at the top of the plasma source. A detailed description of this reactor is given in Chapter 2. The monitoring of the growth of each SiO₂ layer (denoted SiO_{2PECVD}), for achieving the required thickness of 50 nm, was carried out with *in situ* ellipsometry.

For the deposition of the SiO₂ layer Hexamethyldisiloxane (HMDSO) vapor was introduced from the heated container (at 35.8 °C) without a carrier gas through a distribution ring, located 8 cm above the substrate. During the deposition, the pressure value was set at 25 mTorr by adjusting the valve position of the turbopump. The oxygen flow of the working gas was set at 16 sccm while the HMDSO flow at 0.33 sccm. The ratio between the HMDSO flow and the O₂ was therefore set at 2:88, in order to facilitate sufficiently the dissociation of the HMDSO molecules from the O₂ plasma species.[11] The reactor and the deposition conditions for acquiring SiO₂ films are gathered in Table 4.1.

Table 4.1: Experimental Conditions for the SiO₂ layer deposition

RF power coupled to the ICP source	400 W
O ₂ flow rate	16.1 sccm
Working Pressure	25 mTorr
HMDSO	0.33 sccm
Deposition time	20 minutes
Deposition rate	2.5 nm/min
Substrate	Si/SiO _{2thermal} /TiO ₂ NPs spin coated
Substrate Temperature	<150°C

4.2 Results

4.2.1 TEM characterization of the elaborated bilayer and multilayer

The elaborated structures were evaluated with TEM. Both the bilayer (Substrate/TiO_{2sp}/SiO_{2PECVD}) and the multilayer (two bilayers - Substrate/TiO_{2sp}/SiO_{2PECVD}/TiO_{2sp}/SiO_{2PECVD}) are given in Figure 4.1a,1b respectively. In both images, each layer can be clearly distinguished so that the sample exhibits a contrasted multilayer structure and not a mixed oxide film. The first interesting observation is the fact that the interface between the SiO₂ substrate and the 1st layer (TiO₂ spin coated NPs) is well defined (*i.e.* abrupt). In contrary, as we move to the interface between the 1st and 2nd layer, the interface is defined but in a rougher way, following the surface pattern of the layer below.

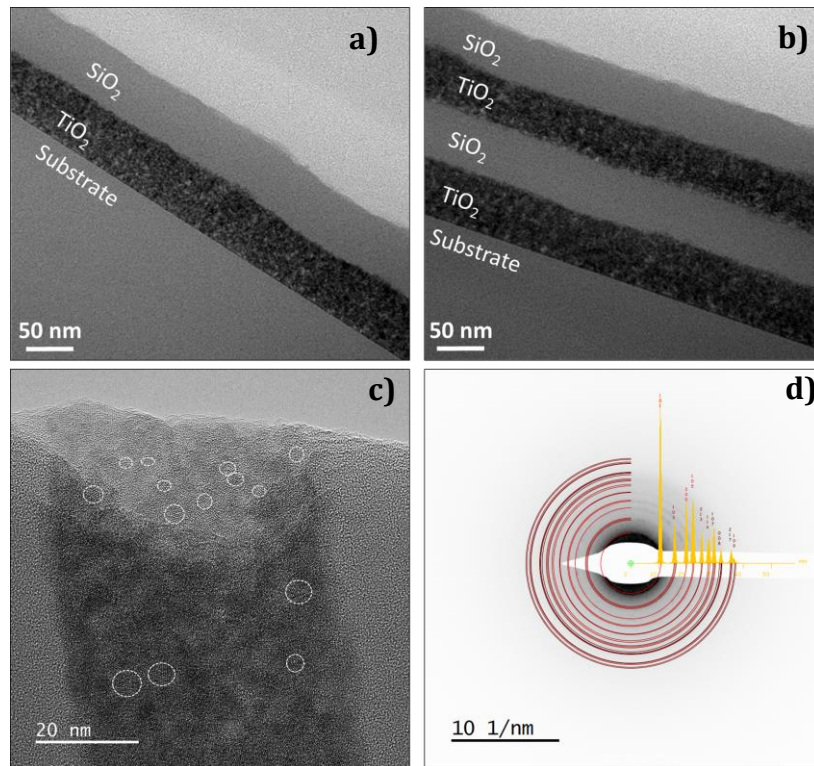


Figure 4.1: TEM investigation of the bilayer structure (SiO_{2th}/TiO_{2sp}/SiO_{2PECVD}) and the multilayer one (SiO_{2th}/TiO_{2sp}/SiO_{2PECVD}/TiO_{2sp}/SiO_{2PECVD}). Cross section views of the a) bilayer and b) multilayer. c) High resolution image of the 1st TiO₂ NPs layer revealing the crystalline nature of the NPs and their size and d) the SAED experimental pattern (grey), the simulated ones (red rings and yellow histogram) from the JCPDF file N° 89-4971 for anatase.

From the resulted cross section, the mean thickness of the layers was deduced through multiple measurements, and the result can be seen in Table 4.3. As a general trend, the 50 nm thickness for each layer has been achieved. From a higher resolution (Fig. 4.1c) the basal planes of the nanocrystals can be identified, which are noted with

contour rounded shapes. In addition to this, the anatase phase of these crystals was verified through the SAED pattern, depicted in Figure 4.1d.

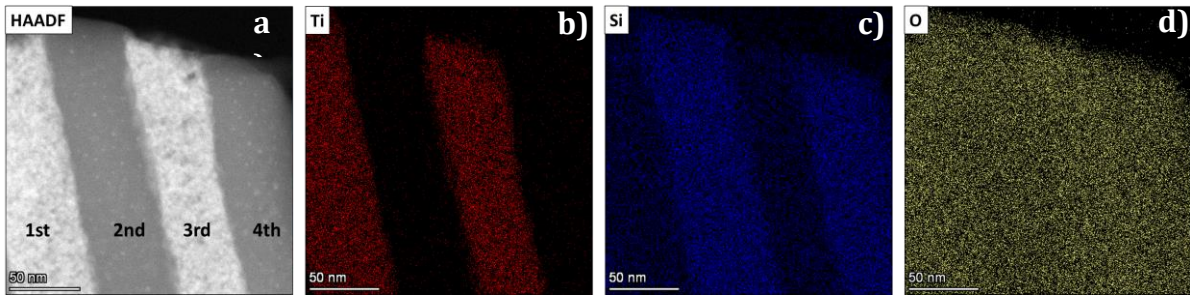


Figure 4.2: HAADF-STEM images of the SiO₂-TiO₂ multilayer a) in a selective area. Elemental mapping for b) Ti, c) Si and d) O.

As shown in Chapter 3, especially from spectroscopic ellipsometry, the spin coated layer of nanoparticles contains voids. Thus, as the SiO₂ layer is deposited on top, one would expect that some infiltration of SiO₂ along the TiO₂ nanostructured film takes place. To investigate the possible infiltration of SiO₂ among the TiO₂ layer, Figure 4.2a shows the high-angle annular dark-field (HAADF) scanning TEM image of the TiO₂-SiO₂ multilayer, while Figure 4.2b, c, d are the elemental mappings of Ti, Si, and O, respectively. The TiO₂ layers are clearly identified with red colour (Ti element) whereas the SiO₂ (Si element) ones are depicted with blue. Indeed, for the case of SiO₂, the color is intense as expected in the 2nd and 4th layer, whereas a rather significant amount is detected among the TiO₂ ones. To quantify this infiltration, using the EDX results the atomic percentage of each element was extracted along the thickness of the film. The exact area that these data were acquired is given in Figure 4.3a following the direction of the black arrow. Due to the lower efficiency of the EDX technique to collect the oxygen element and the possibility to discard this lighter element during the film preparation using a Focused Ion Beam (FIB) device, the oxygen element was not evaluated.

From the atomic percentages of the Ti and Si elements, the atomic fraction of Ti over Ti+Si and the atomic fraction of Si over Ti + Si in percentage (%) are given in Figure 4.3b. From this plot it appears that for the 1st (position from 0 to 50 nm) and for the 3rd (position from 100 to 150 nm) layer, a significant infiltration of Si exists. In detail, around 60% to 70% of Ti is found in these parts and 30 to 40 % of Si. Contrary to this, the 2nd (position from 50 to 100 nm) and 4th (position from 100 to 150 nm) layers only contain Si.

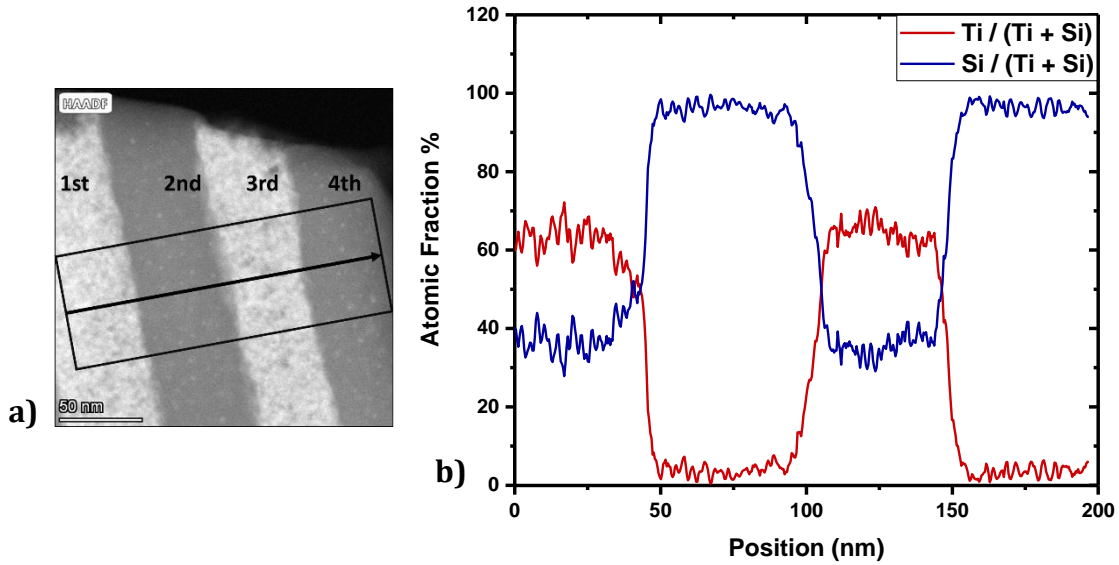


Figure 4.3: a) HAADF-STEM image indicating the area of the EDX analysis and b) atomic fraction of Ti from the total Ti + Si given with red color and atomic fraction of Si over the total Ti + Si given with blue color.

The extraction of the mean size of the TiO₂ nanoparticles contained in the 1st layer was based on the high-resolution images shown in Figure 4.1c, observing the diffracting TiO₂ planes indicating the crystallized nanoparticles. This is given in Figure 4.4 with a mean diameter centered at 4.5 nm and a standard deviation of 0.8 nm. In the same figure, with black, the size distribution of the NPs in the colloidal solution can be seen, having a smaller mean hydrodynamic diameter (3.7 nm). Consequently, only a slight shift towards higher mean size occurs after the deposition, showing that the oxidizing HMDSO/O₂ plasma does not significantly affect the NPs size.

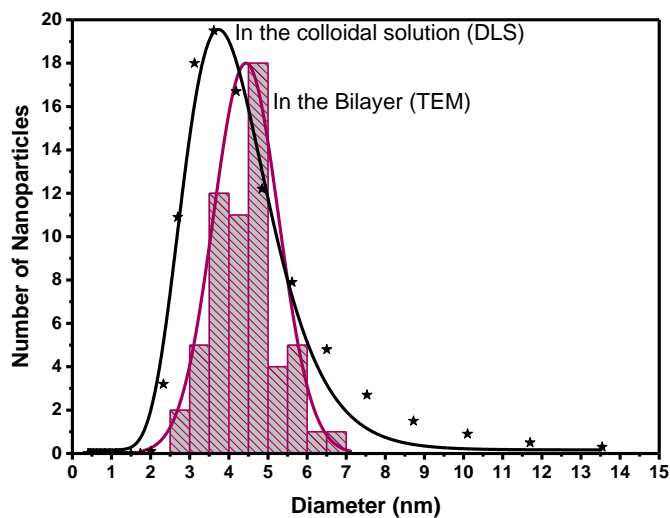


Figure 4.4: Size distribution of the TiO₂ NPs extracted using DLS in volume, of the colloidal solution (black) and using the TEM images and ImageJ software in the bilayer.

Regarding the spin coated layer, it has been shown that the produced TiO₂ NPs thin film consists of TiO₂ NPs and voids. In addition to this, it has been shown in the past[12], and also studied further in Chapter 3, that at the pressure of 25 mTorr, the Oxygen atoms in the plasma during the first minutes, are capable of diffusing along the TiO₂ NPs layer causing its densification. Thus, an explanation of this significant infiltration of the SiO₂, could be that the O atoms diffuse inside the layer providing the “path” to the SiO₂ molecules to penetrate as well the TiO₂ layer. To further investigate the impact of this infiltration on the physical characteristics of each layer, in the next Section, SEM and AFM will be conducted.

4.2.2 Investigation of the topographical characteristics of each layer

The surface morphology of each elaborated layer was evaluated with SEM. Figure 4.5 depicts the secondary electron high magnification top view images of each layer, starting with the 1st TiO₂ one. As expected, the spin coated TiO₂ NPs layer has a nanostructured morphology. In a more unexpected way, the 2nd SiO₂ layer, follows this nanostructured morphology. The 3rd and 4th layers exhibit the same nanostructured features. This morphology is very different from the amorphous characteristics of a SiO₂ PECVD-made layer when deposited on a smooth substrate, as given in Figure 4e.

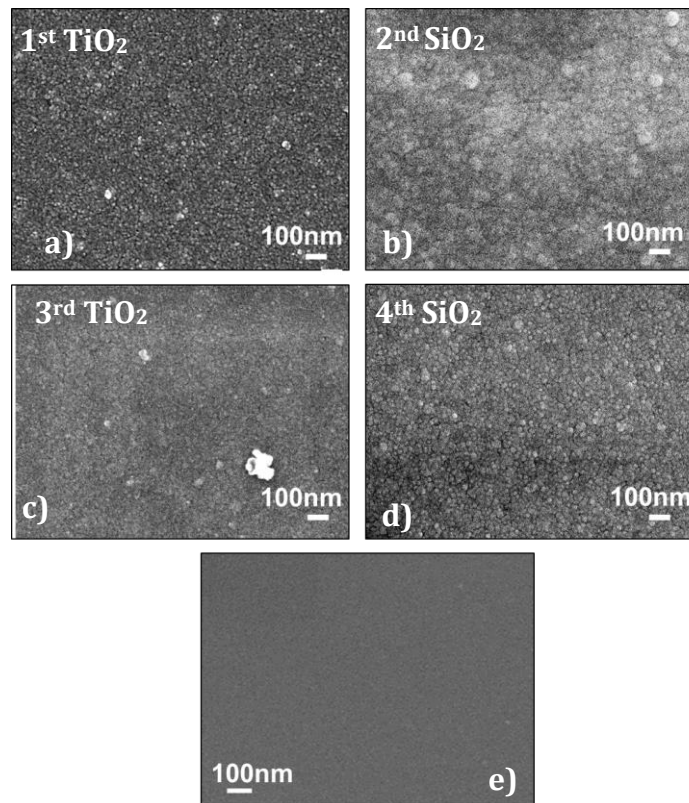


Figure 4.5: SEM (secondary electron) images of the top view of the a) 1st b) 2nd c) 3rd and d) 4th layer of the multilayer structure. e) Top view of PECVD deposited SiO₂ on SiO₂ thermal substrate.

To acquire the topography and roughness of these layers in a nanometric scale, AFM was employed. In Figure 4.6, the surface images in an area 1 μm x 1 μm are given for all the layers including for an amorphous SiO₂ PECVD made one on a smooth surface. For the 1st and 3rd layer, the small TiO₂ nanoparticles are identified. In addition, for the 2nd and 4th layer the surface appears nanostructured and the SiO₂ grains seem larger in size than the TiO₂ NPs. Therefore, the contrast between the SiO₂ layer deposited on a smooth substrate (Fig 4.6e) and the one we obtain on the multilayer structure are obviously very different with a clear nanometric contrast for the former.

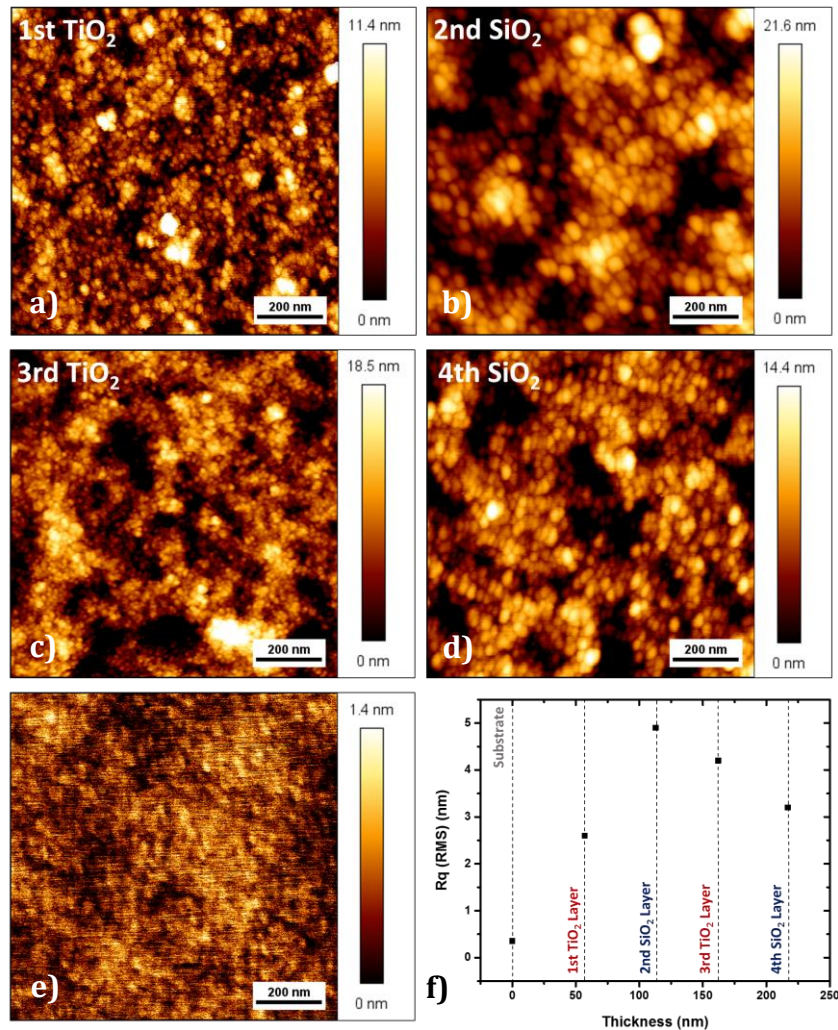


Figure 4.6: AFM images of the top view of the a) 1st TiO₂ b) 2nd SiO₂ c) 3rd TiO₂ and d) 4th SiO₂ layer of the multilayer structure. e) Top view of PECVD deposited SiO₂ on SiO₂ thermal substrate. f) Roughness Rq (RMS) for each layer of the multilayer structure.

In Figure 4.6f, the roughness Rq (RMS) obtained from these scans is given for each layer. In detail, for the 1st the roughness was found at 2.6 nm, a value expected as it is known also from Chapter 3 that the spin coated TiO₂ NPs induce nanostructuring and a small roughness. Despite the fact that the second layer is SiO₂ and it would have been expected to have a very smooth surface as in Figure 4.6e (when deposited to thermal silica substrate), the second layer reveals a roughness Rq (RMS) = 4.9 nm. This higher value

could be linked to the excellent conformal behavior of the SiO₂ layer and the infiltration observed in Section 4.2.1. Finally, the 3rd TiO₂ layer has slightly higher roughness than the 1st at 4.2 nm and the 4th and final, at 3.2 nm.

An accumulative table with the R_q (RMS) roughness obtained by this characterization technique, is given in Table 4.3, and it is compared with the ones obtained with ellipsometry in the next Section. From both SEM and AFM we have seen that the SiO₂ layer follows the nanostructured pattern of the TiO₂ NPs. This effect is probably linked to the highly conformal character of the SiO₂ deposition.

Both from Section 4.2.2 and 4.2.1 it is rather clear that this infiltration affects the structuration of the multilayer structure and it is important to understand how its optical characteristics are affected as well. Hence, in the next Section, *in situ* ellipsometry will be discussed.

4.2.3 Evaluation of each layer's physical and optical characteristics through Ellipsometry

After each layer was created, ellipsometry (*ex situ*) measurements were carried out, identifying the characteristics of the layer such as its thickness, roughness and interface with the layer below. To assess the optical characteristics of the layers, we needed to create a model to fit the ellipsometric data. The validity of this model, and therefore the evaluation of the accuracy of the fit, was estimated by the Mean Square Error (MSE) [13]. In Figure 4.7, the schematic models used for the fitting of each layer are illustrated. These models were inspired by the cross-section images obtained from TEM and the atomic ratios of EDX. Every step, until acquiring the multilayer structure, is illustrated in Figures 4.7a,b,c and d. Each model A, B, C, D was fitted separately and gradually until reaching finally the multilayer. On the top of each scheme, the process used for the elaboration of the last layer is noted, as well as the name of the Model.

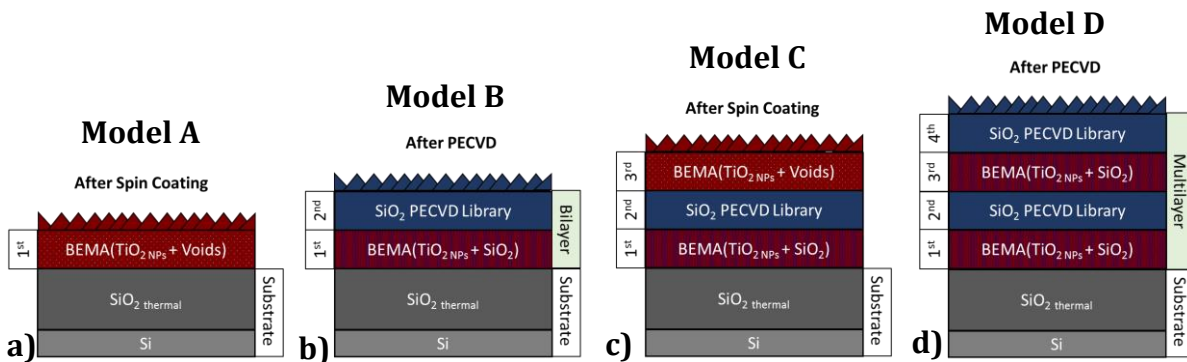


Figure 4.7: Schematic representation of the ellipsometric models used to fit the data of each elaborated layer reaching the bilayer and multilayer structure.

The TiO₂ layers based on what was previously mentioned in Chapter 3 regarding the nature of the colloidal solution and the organic shell surrounding the NPs, were modelled using BEMA with two materials. These were the TiO₂ anatase NPs expressed

with the Tauc-Lorentz (TL) dispersion law (with higher energy gap E_g determined at 3.4 eV to the nanometric scale of the anatase, as already evidenced in chapter 3)[14] and the low density thin shell inducing separation between the nanoparticles, accounted for with voids. Since it has been observed from TEM and EDX, that a significant infiltration of SiO₂ inside the TiO₂ NPs layer exists, the BEMA layer after the deposition of the 2nd (Model B - Bilayer) and 4th (Model D - Multilayer) was actually implemented with TiO₂ NPs plus SiO₂ incorporation. For the SiO₂ layers, classical thermal SiO₂ material expressed with the Cauchy dispersion law was used. [15] Based on the AFM findings, the roughness of each layer was accounted for as a second contribution modeled as a Bruggeman Effective Medium Approximation (BEMA)[16] consisting of 50% the material below and 50% void (fixed proportion).

During the fitting, the thickness, the BEMA fraction (between TiO₂ NPs and Voids or TiO₂ NPs and SiO₂) and the TL dispersion law parameters describing the TiO₂ NPs were fitted. Since the produced PECVD SiO₂ matrix was found very close to the thermal silica, its parameters were not fitted. It has to be mentioned that no intermix of graded layer led to a converging solution.

In Table 4.2 the results of each fitted layer are given. This table has been separated horizontally in four parts (double line). Each part corresponds to the results obtained from the Model A, the Model B (Bilayer), the Model C and the Model D (Multilayer) the notation of which is given in the second column. In the 3rd column, the thickness of each layer is given. If the TiO₂ NPs thin film is the top layer (Model A and C), then in the 4th column the fraction of voids is given. If the TiO₂ NPs thin layer is located below the SiO₂ one, then infiltration has occurred, and the fraction of SiO₂ is given in 5th column. Finally, the roughness of the top layer of each model and the MSE are given in the last columns of Table 4.2. In the model, roughness is accounted as a BEMA material with 50 % the top material and 50 % voids. [2] As the number of layer increases, the error of the fit necessarily increases but remains low enough to lead to reliable results.

Table 4.2: Results obtained from ellipsometry based on Figure 4.7.

Layer	Model	Thickness (nm)	Void vol%	SiO ₂ vol%	Roughness (nm)	MSE
1 st TiO ₂	A	48	27	--	2	12
1 st TiO ₂	B (Bilayer)	44	--	32	10	14
2 nd SiO ₂		56				
1 st TiO ₂	C	47	--	27	5	21
2 nd SiO ₂		62	x	x		
3 rd TiO ₂	D (Multilayer)	48	35	--	5	23
1 st TiO ₂		45	--	29		
2 nd SiO ₂		60				
3 rd TiO ₂		45	--	27		
4 th SiO ₂		53				

From the results of Table 4.2, we observe that the thickness of most of the layers lies close to the targeted 50 nm. In addition, we see that the first and third layers before any infiltration (Model A and C) have between 27 and 35 % voids. Moreover, after the deposition of the SiO₂ layer (Models B and D) the fraction of SiO₂ infiltrated in the TiO₂ layer is estimated by ellipsometry between 29 and 32%. This percentage is a result significantly consistent with the EDX ratios given in Figure 4.3.

Fitting the ellipsometry data can lead to the optical characteristics of each layer such as the refractive index (n). Thus, in Figure 4.8, the refractive index at the wavelength of 633 nm is plotted as a function of the thickness of the multilayer, based on the models in Figure 4.7 and the results in Table 4.2. On the top x axis of the plot, the number and the material of each layer are also given. In order to analyze the impact of the voids or the SiO₂ infiltration on the refractive index of the TiO₂ NPs thin film, multiple colored lines are identified in Figure 4.8. Therefore, the pink line represents the effective index of the spin coated TiO₂ NPs layer expressed with BEMA of TiO₂ NPs and void, for Models A and C, where the TiO₂ NPs are in the top layer and before the silica infiltration. The purple line corresponds to the effective refractive index of the spin coated TiO₂ NPs layer expressed with BEMA of TiO₂ NPs and SiO₂, for Models B and C, and after the silica deposition. Finally, the black dotted line corresponds to the actual refractive index of the TiO₂ NPs without any void or SiO₂ infiltration, before the fitting (Model A and C) and the red line after the fitting (Model C and D). For the 2nd and 4th SiO₂ layer, the refractive index is given with blue line lying at 1.46 as the refractive index of the thermal silica.

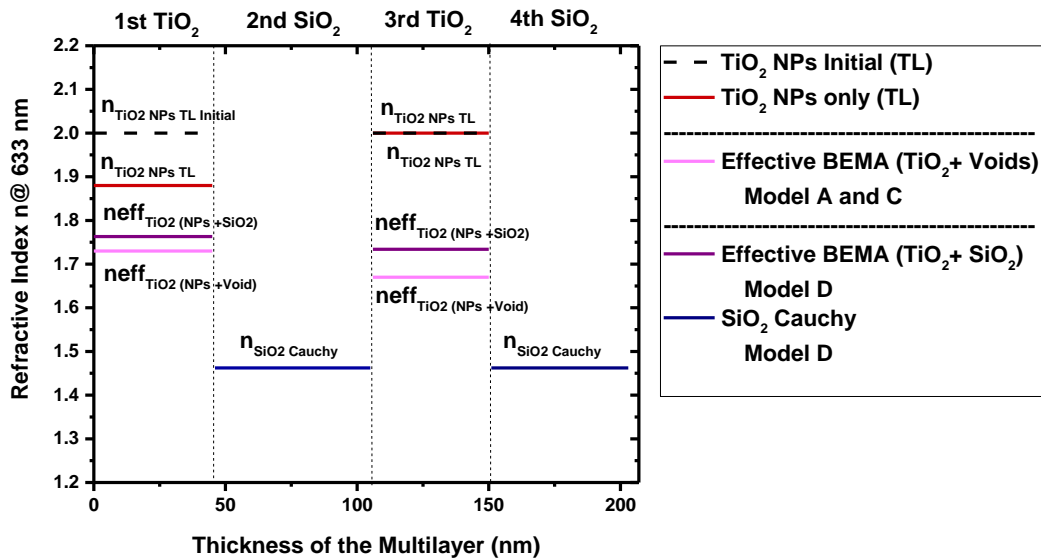


Figure 4.8 Refractive index at 633 nm (of the four layers) as a function of the multilayer thickness according to the models A, B, C, D used in Figure 4.7. Pink line represents the effective index of the spin coated TiO₂ NPs layer expressed with BEMA of TiO₂ NPs and void (Models A and C). Purple line corresponds to the effective refractive index of the spin coated TiO₂ NPs layer expressed with BEMA of TiO₂ NPs and SiO₂ (Models B and D). Black dotted line corresponds to the actual refractive index of the TiO₂ NPs without any void or SiO₂ infiltration, before the fitting (Model A and C) and the red line after the fitting (Model C and D). Blue line for the SiO₂ layers.

The great interest of the Figure 4.8 lies on the TiO₂ layers. Initially, if we consider the Models A and B, the focus should be given in the black dashed and pink lines. The TiO₂ NPs only index for both models lies at the value of 2. A value slightly smaller than the one of the dense TiO₂ PECVD films ($n=2.45$) as already indicated in Chapter 3. The existence of voids in this layer unfortunately decreases even more the effective refractive index of the layer. Hence, with pink we observe the refractive index lying at 1.74 for the first layer and 1.65 for the second. Subsequently, considering the Models B and D, when SiO₂ has been deposited on top of the TiO₂ NPs layers, the attention should be drawn in the red and purple lines. This time, since the TiO₂ NPs are exposed to the O₂/HMDSO plasma, both the SiO₂ fraction and the TL material expressing the NPs were fitted. Therefore, we observe for the red line that for the 1st layer the refractive index of the TiO₂ NPs only has been slightly decreased from 2 to 1.9. Contrary to this, for the 3rd layer the index of the TL after the infiltration remained the same. In both cases, the optical E_g of the TiO₂ NPs remained close to the 3.4 eV. Finally, due to the SiO₂ infiltration the effective refractive index of the 1st layer is found at 1.76 and for the 3rd at 1.74. This is a reasonable and positive outcome of this infiltration as SiO₂ has a higher refractive index than void.

Since the physical characteristics of the film have been deduced with several characterization techniques apart from ellipsometry, in Table 4.3 all the results are accumulated for comparison. Regarding the thickness of each layer some small discrepancies between TEM and ellipsometry exist. TEM reveals slightly larger thicknesses with the most pronounced difference being the one on the 1st and 3rd TiO₂ layers. The discrepancies between AFM and ellipsometry roughness layer thickness can be linked to the different area of measurement, as AFM is in a more local scale.

Table 4.3: Thickness and roughness obtained by TEM, Ellipsometry and AFM

Layer	Thickness(nm)		Roughness (nm)	
	TEM	Ellipsometry	AFM	Ellipsometry
1 st	57 ± 1	45 ± 0.1	2.6	2
2 nd	56 ± 1	60 ± 0.2	4.9	10
3 rd	49 ± 3	45 ± 0.2	4.2	5
4 th	55 ± 2	53 ± 0.1	3.2	5

The combination of characterization techniques given in Sections 4.2.1, 4.2.2 and 4.2.3, allowed us to gain insight in the interactions of the TiO₂ NPs with the SiO₂ layer and investigate the impact of the latter on the structural and optical characteristics of a multilayer film. From the mean diameter size of Figure 4.4 and the optical E_g, found both close to the initial one we observe that their interaction is not detrimental. In addition through the elemental mapping using STEM and EDX we observed an infiltration of ~30 % of SiO₂ in the TiO₂ layers. This percentage was also verified by ellipsometry. From these results, the capacity of the SiO₂ matrix to infiltrate among the TiO₂ NPs is identified. Finally, the positive outcome of this infiltration would be that the effective refractive index

was slightly improved compared to the spin coated one, and that the multilayer consists of abrupt layers.

4.2.4 Comparison of the multi-step approach multilayer thin film with pure PECVD one

For the evaluation of the multilayer thin films through this multi-step approach, a comparison with PECVD made TiO₂-SiO₂ multilayer films was attempted. It was realized in the same PECVD reactor, under the standard PECVD deposition conditions established by the group, and the precursors used for the deposition of the TiO₂ and SiO₂ layer were Titanium Tetraisopropoxide (TTiP) and Hexamethyldisiloxane (HMDSO) vapor accordingly. The TTiP vapor (at 104 °C) and HMDSO vapor (at 35.8°C) were introduced from the heated containers without a carrier gas through the distribution ring. During the deposition, the pressure value was set at 3 mTorr. A synopsis of the deposition parameters can be seen in Table 4.4. The 1st deposited layer was TiO₂ and its growth was monitored with *in situ* ellipsometry. As the targeted thickness was achieved, both the O₂ ICP plasma and TTiP injection system were switched off. In the same manner, the plasma was ignited using oxygen and the HMDSO precursor to deposit the 2nd SiO₂ layer. For the 3rd TiO₂ layer and 4th SiO₂ layer, the same protocol was used.

Table 4.4: Experimental condition for the SiO₂/TiO₂ layer deposition

RF power	400 W
O ₂ flow rate	16 sccm
TTiP flow rate	0.2 sccm
HMDSO flow rate	0.33 sccm
Deposition time for TiO ₂	45 min
Deposition rate for TiO ₂	1.2 nm/min
Deposition time for SiO ₂	6 min
Deposition rate for SiO ₂	8 nm/min
Working Pressure	3 mTorr
Substrate	Si (100)
Substrate Temperature	<150°C

The cross section of the PECVD deposited TiO₂-SiO₂ multilayer thin film was investigated with TEM. In Figure 4.9a the total multilayer film can be seen. The columnar structure of the TiO₂ layer can be identified as shown in the past from previous studies of the group.[17] From multiple measurements along the layers, the thickness of each one was deduced having a thickness of: 59 ± 3 nm for the 1st, 50 ± 4 nm for the 2nd, 57 ± 4 nm for the 3rd and 52 ± 4 nm for 4th layer.

From a higher magnification image (Fig. 4.9b), the interface between each layer is identified. The one between the substrate and the TiO₂ layer is well defined whereas the one between the 1st TiO₂ and the 2nd SiO₂ layer appears to have a rougher pattern. Another significant observation is the fact that during the first 20 nm of the TiO₂ layer (dotted white

line on Figure 4.9b), a dense sublayer appears, followed by the columnar structure. In addition to this, in-between the columns of the TiO₂ a small infiltration of SiO₂ is distinguished indicated with rounded contour black shapes. The anatase phase of the TiO₂ layer was verified through the diffraction pattern (SAED) given in Figure 4.9d.

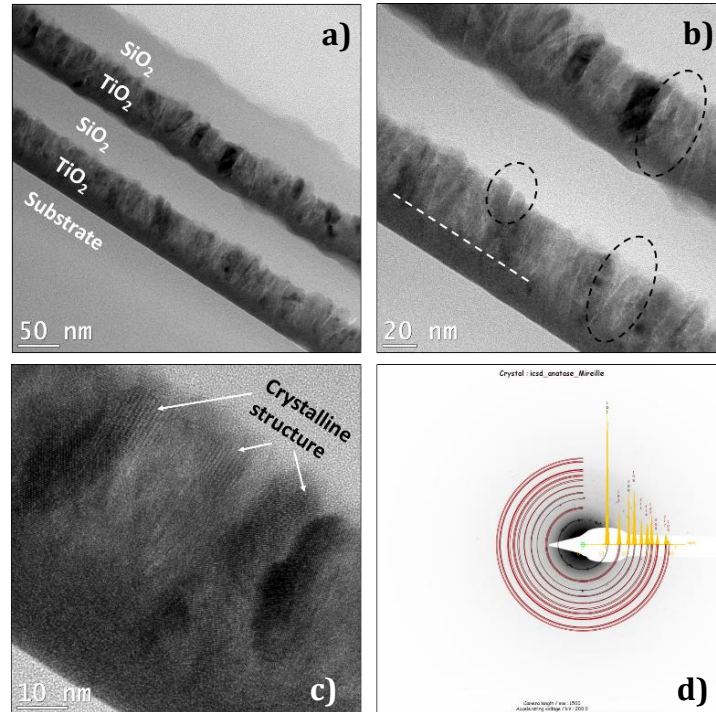


Figure 4.9: TEM investigation of the multilayer structure (SiO₂th/TiO₂^{PECVD}/SiO₂^{PECVD}/TiO₂^{PECVD}/SiO₂^{PECVD}). a) Low magnification image of the cross section, b) image focusing on the interface between the TiO₂ columns and the SiO₂ amorphous layer and c) higher resolution image of the TiO₂ crystallized columnar structure and d) SAED pattern use the caption of the cross-section for spin coating and PECVD to describe grey, red and yellow.

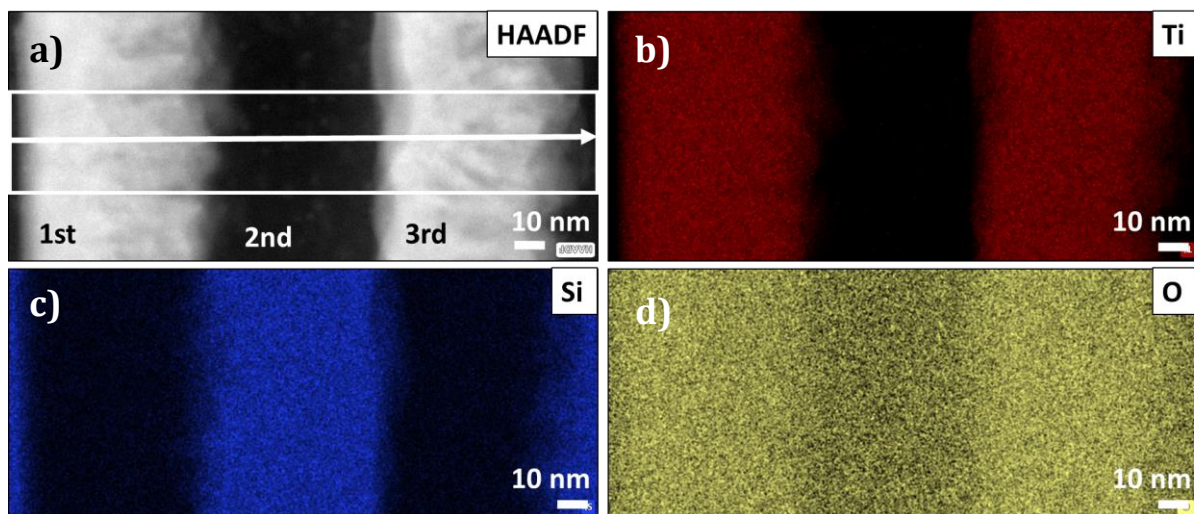


Figure 4.10: HAADF-STEM images of the SiO₂-TiO₂ multilayer a) in a selective area. Elemental mapping for b) Ti, c) Si and d) O.

To verify the infiltration of the SiO₂ along the TiO₂ layer, HAADF-STEM was conducted. As shown in Figure 4.10, a specific area was chosen, (Fig 4.10a) Focusing on the 1st, 2nd and 3rd layer. In Figure 4.10b (with red), the Ti element of the 1st and 3rd layer appears, following a rough pattern at the top of each layer. In-between, Ti is not identified. Figure 4.10c (with blue), is linked to the Si content. The most significant observation on that image, is the fact that Si appears to be present among the Ti layers, being more prominent in the top-columnar part of the TiO₂ ones. Finally, the oxygen content is given in Figure 4.10d, revealing a higher concentration of the TiO₂ layers. This could be linked to the oxygen over Ti ratio for TiO₂ grown PECVD being larger than 2 [11] providing a higher total content or the preparation of the TEM samples using FIB, as oxygen is element that may be sputtered with a different rate than this other ones.

To quantify this infiltration of the SiO₂, using the EDX results the atomic percentage of each element was extracted along the thickness of the film. The exact area that these data were acquired is given in Figure 4.11a following the direction of the white arrow. From these data the Ti fraction and Si fraction over the total Ti and Si were calculated, the results of which are given in Figure 4.11b. Again, this time, the oxygen element was not assessed as its detecting especially in EDX need cautious handling. From this plot it appears that for the 1st (position from 20 to 700 nm) and for the 3rd (position from 120 to 170 nm) layer, a significant infiltration of Si exists. In detail, around 80% of Ti is found in these films and around 20 % of Si. Contrary to this, the 2nd (position from 50 to 100 nm) and 4th (position from 100 to 150 nm) layers only contain Si. Therefore, if compared with the results in Section 4.2.1, in the case of the PECVD made multilayers less infiltration exists. From this plot it is also verified that between the 1st and 2nd layer as well as between the 3rd and 4th a grading between TiO₂ and SiO₂ layer exists.

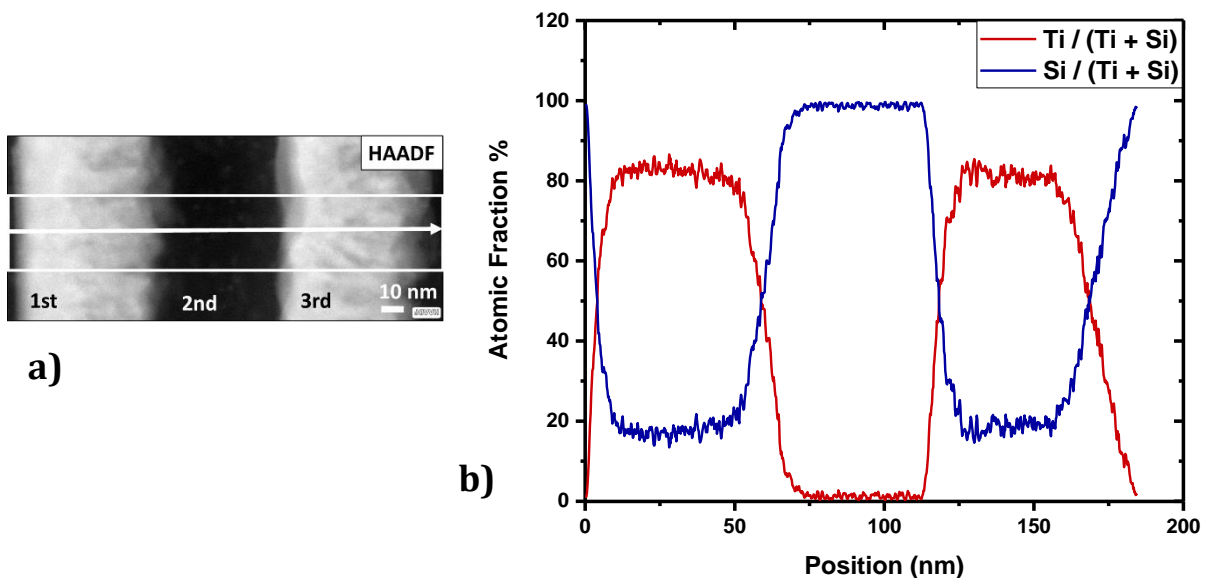


Figure 4.11: a) HAADF-STEM image indicating the area of the EDX analysis (color identification), b) atomic fraction of Ti from the total Ti + Si given with red color and atomic fraction of Si over the total Ti + Si given with blue color.

Using AFM, the surface of the total multilayer (Fig. 4.12a) and therefore the surface of the 4th SiO₂ layer was evaluated and was compared with a PECVD made SiO₂ layer deposited on a smooth SiO₂ substrate (Fig. 4.12b). The surface of the multilayer appears to have a Rq (RMS) roughness of 3 nm and some rounded domains. Compared to Figure 4.12b, where no roughness appears, the conclusion could be that these rounded domains are a memory effect of the SiO₂ layer deposited on the TiO₂ columns.

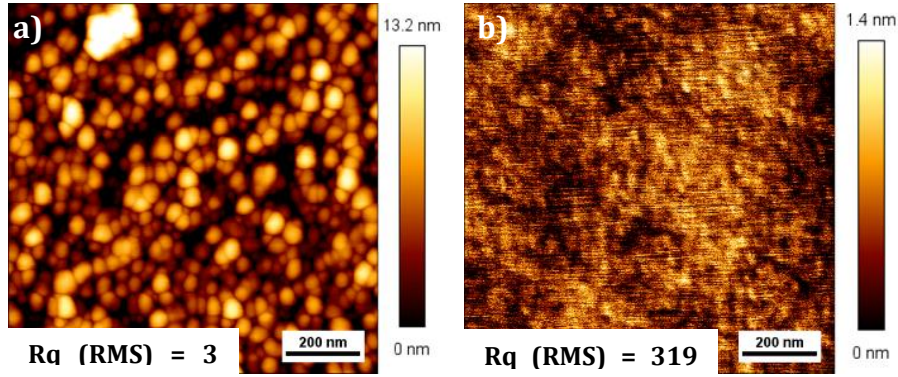


Figure 4.12: AFM scans a) of the top surface of the multilayer thin film and b) of 50 nm thick SiO₂ film on smooth Si substrate.

In line with Section 4.2.2, *in situ* ellipsometry was used, to evaluate the optical and morphological characteristics of the multilayer structure. Due to the complexity of the multilayer structure, the deduction of the final model needed to be made gradually. Consequently, the schematic representation of each model can be seen in Figure 4.13. These models were inspired by the TEM data and EDX data. At the top of each schematic the name of each model is given.

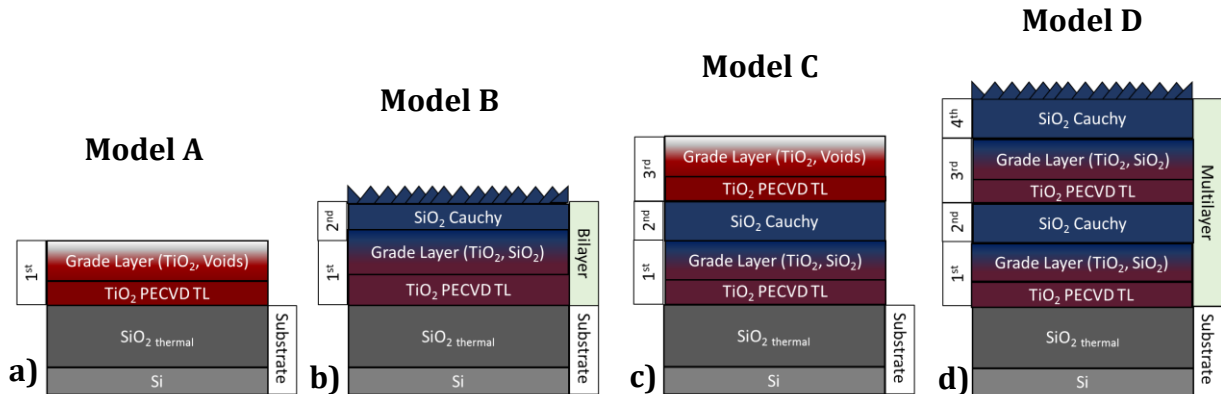


Figure 4.13: Schematic representation of the ellipsometric models used to fit the data of each elaborated layer reaching the PECVD TiO₂-SiO₂ multilayer structure

In an agreement with previous results of the group [18], the TiO₂ layers have been modeled as a two sub-layer system, one describing the dense anatase part and another one describing the anatase columns existing on the top. These TiO₂ sublayers were expressed with TL dispersion law, representing this time the PECVD made films (with lower energy gap E_g compared to the TiO₂ NPs of Section 4.2.3, determined at 3.2 eV).

Hence, the dense layer was expressed with this TL dispersion law whereas the grade grade layer was a model that was separated by the software in 10 slices and void is gradually distributed from the bottom until the top. Here, again for the SiO₂ layer the model describing the thermal silica was used based on the Cauchy dispersion law.[15]

During fitting, the thickness, the TL dispersion law and the roughness were set free. Due to the complexity of this spectroscopic ellipsometric study, each model will be presented separately. In Table 5.5, the first results from the Model A are given. Here, as only the TiO₂ layer has been deposited, the model comprises the dense part (2nd column of Table 4.5) and the graded one (3rd column of Table 4.5) having thicknesses of 22 and 36 nm accordingly. As observed in the 3rd column the voids % at the top of the graded layer is given being found at 46 %. In the 4th column of this table, the roughness is provided although in this case it cannot be accounted for, as it is actually the last slice of the grade layer. Finally, in the last column the MSE is given.

Table 4.5: Results obtained from Ellipsometry for Model A of Figure 4.13

Layer	Model A			Roughness (nm)	MSE
1 st	Dense TL	Grade TL + Voids			
	Thickness (nm)	Thickness (nm)	Voids Top%		
	22	36	46	-	6

In Table 4.6, the results from the Model B are given, including SiO₂ on top of the TiO₂ layer. The difference between Model A and B, lies also on the fact that since infiltration has been observed by EDX and TEM, the dense TiO₂ layer dispersion has been set free to account for the SiO₂ in the layer. During this process the E_g was slightly decreased from 3.2 eV to 3.1 eV. In addition, the voids existing in the TiO₂ grade layer have now been replaced by SiO₂. The Table 5.6 has been separated horizontally to describe the 1st and 2nd layer. For the 1st layer, in the third column of this Table, instead of Voids % (as in Table 4.5), the best fit led to consider the incorporation of SiO₂ of up to 49 %. Finally, the SiO₂ 2nd layer was found at 45 nm, with 4 nm roughness.

Table 4.6: Results obtained from Ellipsometry for Model B of Figure 4.13

Layer	Model B (Bilayer)			Roughness (nm)	MSE
1 st	Dense BEMA	Grade BEMA			
	Thickness (nm)	Thickness (nm)	SiO ₂ Top %		
	22	36	49		
2 nd	SiO ₂ Thickness (nm)				
	45			4	7

In Table 4.7; the Model C is given. This is a combination of the two previous as for the description of the 1st and 2nd layer, the Model B is used, and for the description of the TiO₂ deposited 3rd layer, the two sub-layer system, describing the dense anatase part and

the anatase columns existing on the top is used. This time, for the 3rd layer the dense part is found to have 18 nm thickness and the grade layer 35 nm. In addition, the 41 % of void at the top slice, do not allow to provide roughness data. Finally, the MSE still remains in low levels.

Table 4.8: Results obtained from Ellipsometry for Model C of Figure 4.13

Layer	Model C			Roughness (nm)	MSE
1 st	Dense BEMA	Grade BEMA			
	Thickness (nm)	Thickness (nm)	SiO ₂ Top %		
	22	36	41		
2 nd	SiO ₂ Thickness (nm)				
	45				
3 rd	Dense TL	Grade TL + Voids			7
	Thickness (nm)	Thickness (nm)	Voids Top %		
	18	35	41		

Moving towards the end, in Table 4.9 the Model D described the final multilayer and one could say that it could be described as two bilayers (Model B) stacked the one on top of the other. Following the same pattern as in Model B, since the SiO₂ has been deposited, the TL has been set free and the void inside the grade layer has been replaced by SiO₂. Regarding the TL dispersion law, once more a small modification of the E_g from 3.2 to 3.1 eV was observed. In addition, the void has been replaced by 43 % SiO₂ on the top of the grade layer and the SiO₂ film has a thickness of 44 nm and a roughness of 4 nm. The MSE has been slightly increased, due to the complexity of the total model.

Table 4.9: Results obtained from Ellipsometry for Model D of Figure 4.13

Layer	Model D (Multilayer)			Roughness (nm)	MSE
1 st	Dense BEMA	Grade BEMA			
	Thickness (nm)	Thickness (nm)	SiO ₂ Top %		
	22	45	41		
2 nd	SiO ₂ Thickness (nm)				
	45				
3 rd	Dense BEMA	Grade TL + Voids			
	Thickness (nm)	Thickness (nm)	SiO ₂ Top%		
	18	35	43		
4 th	SiO ₂ Thickness (nm)				
	44			4	14

Based on the fittings of the given models, the refractive index at a wavelength of 633 nm was obtained, and its variation was plotted as a function of the thickness of the multilayer (Fig 4.14). In this plot, multiple colors are given to assess the impact of the

infiltration of the optical parameters of the layers. The refractive index of the dense TiO₂ sub-layers before the infiltration, from the Model A and C, are given in red. In addition, the grade layer for the same models before the infiltration are given with pink. The refractive index of the dense TiO₂ sub-layer after the infiltration, for the Models B and D, is given with black, whereas for the grade layer is given with purple. Finally, the refractive index of the SiO₂ layer is given with blue color.

Figure 4.14 reveals the modifications of the SiO₂ infiltration induced on the optical characteristics of the TiO₂ anatase layers. Initially, before the infiltration, the TiO₂ dense layers (red lines) have a refractive index of 2.45 (1st) and 2.40 (3rd). A value that it is expected for an anatase film. In addition, for the columnar layer, as grading of void is distributed along the thickness of the film, the refractive index linearly decreases from 2.45 or 2.4 to 1.80 (pink lines). After the deposition of the SiO₂ layer, the infiltration of silica among the TiO₂ layer is expected (from TEM and EDX, verified through the Ellipsometry models) leading to a slight diminution of the refractive index of the dense part from 2.46 (1st layer) and 2.40 (2nd layer) to 2.36 and 2.39, accordingly. Nonetheless, a positive outcome of this infiltration can be seen in the grade layer (purple). Due to the fact that SiO₂ has been distributed in-between the columns and the grade layer has been transformed (SiO₂ grading along the thickness of the film and not void), the final top index of the grade layer results in a higher value of ~2 (instead of 1.8), easing at the same time the inclination of the index.

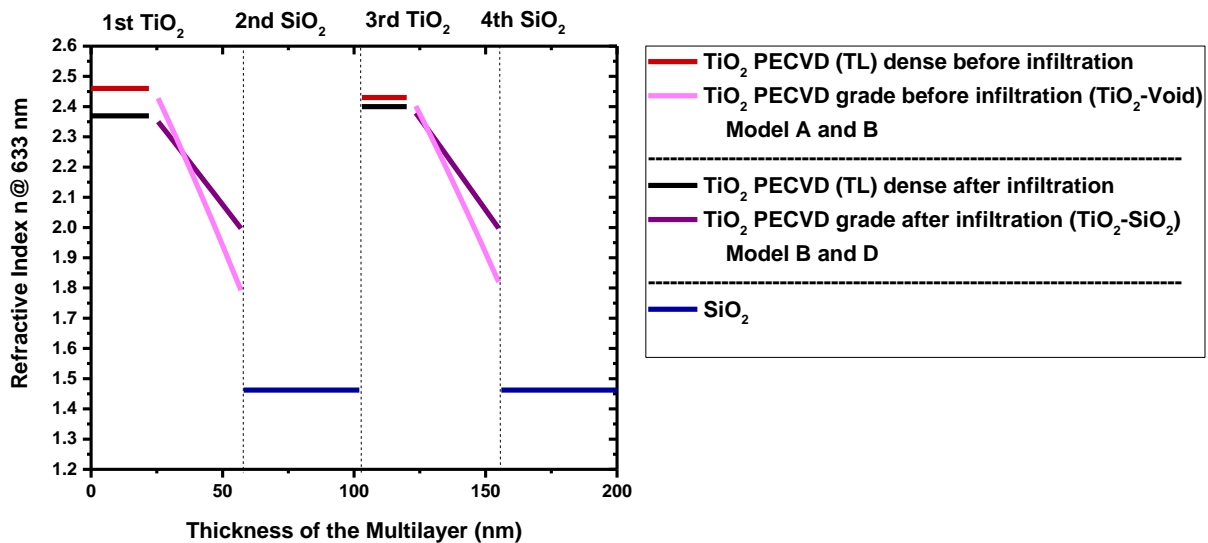


Figure 4.14: Refractive index (n) of each layer as a function of the thickness of the multilayer thin film. Red line describes the dense TiO₂ and pink the graded sub-layers coming from models A (1st layer) and C (3rd layer). Black line represents the dense TiO₂ and purple the graded sub-layers coming from models B (2nd layer) and D (4th layer). SiO₂ layers are described with the blue lines.

In this Section, the multilayer PECVD made thin film was investigated, using well established deposition conditions in the specific system. For the comparison of this type of film with the multistep multilayer one containing nanoparticles, each layer had the

same thickness and similar characterization techniques were applied. Here, we have seen that the conformal behavior is still prominent, being able to observe columnar topography of the final SiO₂ layer using AFM. Using spectroscopic ellipsometry, we were able to identify the slight decrease of the refractive index due to Silica infiltration up to 20 vol% and the decrease of the inclination of the index corresponding to the grade layer. The latter occurs between the TiO₂ and SiO₂ layers (from 1st to 2nd layer and from the 3rd to the 4th layer) and could not be accounted for using the TL dispersion, in the dense parts of the TiO₂ layers.

4.4 Discussion

In this chapter, the implementation of multilayer TiO₂-SiO₂ structures was performed. Using various characterization techniques each of the layer was identified. For the multi-step approach, despite combining two different deposition techniques TEM revealed that the layers remain intact with some infiltration of the SiO₂ occurring in the TiO₂ layer. The size of the spin coated TiO₂ NPs was not found to be drastically affected by the low pressure O₂/HMDSO plasma of the PECVD system. In accordance, an infiltration both at the columnar part and the dense one was found for the case of the PECVD made multilayer structure, using EDX.

4.4.1 Impact of the SiO₂ infiltration and conformal behavior on the amorphous-crystalline interphase

For the multi-step elaborated multilayer films, it was shown through ellipsometry that approximately 30 vol% of silica is diffused along the TiO₂ NPs layer whereas the atomic percentage detected by STEM lies between 35 and 40%. Due to the multilayered character of the sample, it is impossible to move from vol% to at% to compare those two values, since the density and molar mass of the infiltrated layer only should be assessed. Therefore, a two-step mechanism could be proposed for this infiltration. As a first step the infiltration does occur, covering the voids existing in the film and as a second step, due to this rather fast deposition (2.5 nm/min) within a few minutes a layer of SiO₂ has been created covering the TiO₂ NPs. From these results, two hypotheses regarding the structural quality of the multilayer film can be deduced. The first hypothesis proposed is the following: as the SiO₂ is infiltrated along the TiO₂ layer, it acts like a “glue” improving the adhesion between each layer. The second is that as the SiO₂ layer is deposited in a fast rate (2.5 nm/min); it covers the NPs keeping them protected from the O₂ plasma. Contrary to that, for the pure PECVD made multilayer, the degree of infiltration appears less both from ellipsometry (20 vol%) and STEM (<20 at%). This could be linked to the denser characteristics a PECVD TiO₂ layer has compared to the TiO₂ NPs with voids.

In both multi-step and pure PECVD approaches, the conformal behavior of the SiO₂ layer has been evidenced and stressed several times. It is known that conformal coatings are essential in the area of microelectronics[19] and several studies have been attempted

to investigate the conformal behavior of SiO₂. [20,21] They mainly involve Atomic Layer Deposition (ALD) processes, as it provides self-limiting growth and precursor dose sufficient to saturate all the available surface sites. [22,23] Therefore, in this study it is possible to assess the conformal properties of the SiO₂ thin films made with PECVD in significantly higher deposition rates than achieved with ALD.

4.4.2 Evaluation of the multilayer optical response based on the two implementation approaches

Multilayer TiO₂-SiO₂ structures have been widely studied and elaborated oriented towards optical applications. Thus, apart from morphological and chemical characterization techniques ellipsometry was used, to assess the refractive index of each layer. In Section 4.2.3, it was shown that the refractive index of the TiO₂ layer in accordance to what was found in Chapter 2, reveals a refractive index ($n = 1.7$) lower to the one obtained for the PECVD films ($n = 2.4$) at 633 nm. The fraction of void existing in the layer and the nanometric size of the anatase crystallites are the main reasons for this phenomenon. In contrast, the index of the SiO₂ layer was found, as expected, at 1.46. The interesting part in this study is that as the SiO₂ layer is being deposited on the TiO₂ NPs layer, it infiltrates along the film. This leads to the “healing” effect of the TiO₂ layer in terms of index. Indeed, after the infiltration part of the voids has been replaced with SiO₂ leading to the increase of the refractive index from 1.72 to 1.76 for the 1st layer and 1.67 to 1.74 for the 3rd layer.

When the same study was conducted for the PECVD made multilayer films, it was found that the TiO₂ layers reveal a completely different morphology. From TEM two sublayers were identified, a dense and a columnar one. Therefore, a two-layer material was used. As expected, before the infiltration, the dense layer has a higher refractive index (than the TiO₂ NPs layer) and the columnar one reveals a grading on its values from ~ 2.45 to 1.8. The main reason for that is that during their growth, the columns generate more voids in between them. After the infiltration, since the TiO₂ dense part accounts for some SiO₂, the index decreases. Contrary to this, for the columnar part, since the voids are now filled with SiO₂, the inclination of grading is then less steep, having a grading between 2.35 and 2.00.

Apart from knowing the optical characteristics of each layer, it would be interesting to acquire the effective ones of the total film to assess its optical response. For the calculation of the effective real and imaginary optical constants of the total film, Haija et al. [24,25] developed a formula based on which knowing the thickness of each layer and the optical constants at a given wavelength, the effective total value could be calculated. The condition for the formula to be valid would be that the layers are ultrathin and therefore our structure could not meet the requirements. Thus, in this work each layer had to be studied separately.

As a conclusion, it is clear that the infiltration affects the value of the obtained refractive index mostly in a positive way. A significant difference between these two

approaches is that with the multi-step one, we have a clear alternative variation between low and high refractive index whereas with the PECVD one, a grading of the index in the TiO₂ side until reaching the interface with the SiO₂ layer occurs.

Conclusion

In this chapter, multilayer (TiO₂-SiO₂) thin films were successfully elaborated through a two-step approach coupling wet processes such as spin coating and plasma deposition ones, such as PECVD. It has been shown that each of the 4 layers can be distinguished, having a thickness of 50 nm. The interface between each layer was well defined and an infiltration of SiO₂ inside the TiO₂ NPs was found. This infiltration provided a densification of the TiO₂ layer replacing the void percentage with SiO₂ leading to an improvement of the optical constants. Another possible effect of this infiltration was the fact that it acted as a sticking mechanism between the SiO₂ layer and the TiO₂ NPs layer improving their adhesion. The size and morphology of the spin coated NPs did not appear significantly affected by the O₂/HMDSO plasma. Furthermore, the optical constants of each layer were identified and the alternation of high to low refractive index (1.74 – 1.76 for TiO₂, 1.46 for SiO₂ at 633 nm) was verified for this specific film. The roughness of each layer was studied and the conformal behavior of the PECVD deposited SiO₂ on the nanostructured TiO₂ one was evaluated. It was observed that the top surface of the multilayer structure was nanostructured and rougher than expected.

These structural and optical results were compared with pure PECVD-made multilayer thin films. It was found that the TiO₂ layer even at 50 nm thickness comprises of two sublayers, a dense and columnar one. This morphology favored the infiltration of the SiO₂ leading to a slight decrease of its optical index. In this case, a graded refractive index was found at the columnar sublayer and a rough columnar-like surface of the SiO₂ top layer, verifying the conformal character of the SiO₂ films.

Overall, in this Chapter we have characterized the optical properties of the NPs as thin films and how they are affected by the O₂/HMDSO plasma. This interaction between the TiO₂ NPs and the PECVD made SiO₂ advantageously led to the possibility to design multi-layers with improved optical indexes.

Bibliography

- [1] Q.-X. Zhang, B. Zhu, L.-F. Zhang, S.-J. Ding, Atomic-layer-deposited SiO₂/TiO₂/SiO₂ sandwiched dielectrics for metal-insulator-metal capacitor application, *Microelectron. Eng.* 122 (2014) 1–4. <https://doi.org/10.1016/j.mee.2014.03.013>.
- [2] D. Li, M. Carette, A. Granier, J.P. Landesman, A. Goulet, In situ spectroscopic ellipsometry study of TiO₂ films deposited by plasma enhanced chemical vapour deposition, *Appl. Surf. Sci.* 283 (2013) 234–239. <https://doi.org/10.1016/j.apsusc.2013.06.091>.
- [3] H.K. Raut, V.A. Ganesh, A.S. Nair, S. Ramakrishna, Anti-reflective coatings: A critical, in-depth review, *Energy Environ. Sci.* 4 (2011) 3779. <https://doi.org/10.1039/c1ee01297e>.
- [4] J. Choi, K. Han, J.H. Kim, Enhanced near infrared reflectance of TiO₂/SiO₂/TiO₂ multilayer structure using a base-catalyzed SiO₂ film, *Thin Solid Films.* 569 (2014) 100–103. <https://doi.org/10.1016/j.tsf.2014.08.036>.
- [5] M. Faustini, L. Nicole, C. Boissière, P. Innocenzi, C. Sanchez, D. Grosso, Hydrophobic, Antireflective, Self-Cleaning, and Antifogging Sol-Gel Coatings: An Example of Multifunctional Nanostructured Materials for Photovoltaic Cells, *Chem. Mater.* 22 (2010) 4406–4413. <https://doi.org/10.1021/cm100937e>.
- [6] J. Escorcia-García, M.E. Mora-Ramos, Optical reflectivity and spatial mode localization of white-noise random dielectric oxide multilayers, *Opt. Commun.* 432 (2019) 1–7. <https://doi.org/10.1016/j.optcom.2018.09.043>.
- [7] J. Oh, H. Na, I.-S. Mok, J. Kim, K. Lee, H. Sohn, Physical and electrical properties of band-engineered SiO₂/(TiO₂)_x(SiO₂)_{1-x} stacks for nonvolatile memory applications, *Appl. Phys. A.* 108 (2012) 679–684. <https://doi.org/10.1007/s00339-012-6950-2>.
- [8] M. Magnozzi, S. Terreni, L. Anghinolfi, S. Uttiya, M.M. Carnasciali, G. Gemme, M. Neri, M. Principe, I. Pinto, L.-C. Kuo, S. Chao, M. Canepa, Optical properties of amorphous SiO₂-TiO₂ multi-nanolayered coatings for 1064-nm mirror technology, *Opt. Mater.* 75 (2018) 94–101. <https://doi.org/10.1016/j.optmat.2017.09.043>.
- [9] A. Karpinski, S. Berson, H. Terrisse, M. Mancini-Le Granvalet, S. Guillerez, L. Brohan, M. Richard-Plouet, Anatase colloidal solutions suitable for inkjet printing: Enhancing lifetime of hybrid organic solar cells, *Sol. Energy Mater. Sol. Cells.* 116 (2013) 27–33. <https://doi.org/10.1016/j.solmat.2013.04.006>.
- [10] M. El Kass, L. Brohan, N. Gautier, S. Béchu, C. David, N. Lemaitre, S. Berson, M. Richard-Plouet, TiO₂ Anatase Solutions for Electron Transporting Layers in Organic Photovoltaic Cells, *ChemPhysChem.* 18 (2017) 2390–2396. <https://doi.org/10.1002/cphc.201700306>.
- [11] D. Li, S. Elisabeth, A. Granier, M. Carette, A. Goulet, J.-P. Landesman, Structural and Optical Properties of PECVD TiO₂-SiO₂ Mixed Oxide Films for Optical Applications: Structural and Optical Properties of PECVD TiO₂-SiO₂ ..., *Plasma Process. Polym.* 13 (2016) 918–928. <https://doi.org/10.1002/ppap.201600012>.
- [12] A. Granier, G. Borvon, A. Bousquet, A. Goulet, C. Leteinturier, A. van der Lee, Mechanisms Involved in the Conversion of ppHMDSO Films into SiO₂-Like by Oxygen Plasma Treatment, *Plasma Process. Polym.* 3 (2006) 365–373. <https://doi.org/10.1002/ppap.200600022>.
- [13] D. Saha, R.S. Ajimsha, K. Rajiv, C. Mukherjee, M. Gupta, P. Misra, L.M. Kukreja, Spectroscopic ellipsometry characterization of amorphous and crystalline TiO₂ thin films grown by atomic layer deposition at different temperatures, *Appl. Surf. Sci.* 315 (2014) 116–123. <https://doi.org/10.1016/j.apsusc.2014.07.098>.
- [14] G.E. Jellison, L.A. Boatner, J.D. Budai, B.-S. Jeong, D.P. Norton, Spectroscopic ellipsometry of thin film and bulk anatase (TiO₂), *J. Appl. Phys.* 93 (2003) 9537–9541. <https://doi.org/10.1063/1.1573737>.
- [15] C.M. Herzinger, B. Johs, W.A. McGahan, J.A. Woollam, W. Paulson, Ellipsometric determination of optical constants for silicon and thermally grown silicon dioxide via a multi-sample, multi-wavelength, multi-angle investigation, *J. Appl. Phys.* 83 (1998) 3323–3336. <https://doi.org/10.1063/1.367101>.
- [16] H.G. Tompkins, ed., *Handbook of ellipsometry*, Repr, Andrew [u.a.], Norwich, NY, 2010.
- [17] D. Li, N. Gautier, B. Dey, S. Bulou, M. Richard-Plouet, W. Ravisy, A. Goulet, P. Choquet, A. Granier, TEM analysis of photocatalytic TiO₂ thin films deposited on polymer substrates by low-temperature ICP-PECVD, *Appl. Surf. Sci.* 491 (2019) 116–122. <https://doi.org/10.1016/j.apsusc.2019.06.045>.
- [18] D. Li, M. Carette, A. Granier, J.P. Landesman, A. Goulet, Effect of ion bombardment on the structural and optical properties of TiO₂ thin films deposited from oxygen/titanium tetraisopropoxide

- inductively coupled plasma, *Thin Solid Films*. 589 (2015) 783–791. <https://doi.org/10.1016/j.tsf.2015.07.015>.
- [19] K. Seshan, D. Schepis, *Handbook of thin film deposition*, 2018. <https://public.ebookcentral.proquest.com/choice/publicfullrecord.aspx?p=5309981> (accessed April 6, 2020).
- [20] M. Park, H.K. Yu, J.G. Koo, J. Jang, K.S. Nam, High-quality conformal silicon oxide films prepared by multi-step sputtering PECVD and chemical mechanical polishing, *J. Electron. Mater.* 27 (1998) 1262–1267. <https://doi.org/10.1007/s11664-998-0080-9>.
- [21] N. Sobel, C. Hess, M. Lukas, A. Spende, B. Stühn, M.E. Toimil-Molares, C. Trautmann, Conformal SiO₂ coating of sub-100 nm diameter channels of polycarbonate etched ion-track channels by atomic layer deposition, *Beilstein J. Nanotechnol.* 6 (2015) 472–479. <https://doi.org/10.3762/bjnano.6.48>.
- [22] A. Lakhtakia, R.J. Martín-Palma, eds., *Engineered biomimicry*, Elsevier, Amsterdam, 2013.
- [23] S. Hashmi, G.F. Batalha, C.J. Van Tyne, B.S. Yilbas, *Comprehensive materials processing*, Elsevier, Oxford; Walltham, MA, 2014. <http://public.ebookcentral.proquest.com/choice/publicfullrecord.aspx?p=1673593> (accessed April 6, 2020).
- [24] A.J.A. El-Haija, Effective medium approximation for the effective optical constants of a bilayer and a multilayer structure based on the characteristic matrix technique, *J. Appl. Phys.* 93 (2003) 2590–2594. <https://doi.org/10.1063/1.1543229>.
- [25] A.J. Haija, W.L. Freeman, T. Roarty, Effective characteristic matrix of ultrathin multilayer structures, (n.d.) 12.

Chapter 5

Direct Liquid Injection of TiO₂ Nanoparticles colloidal solution in low pressure O₂ Plasma Reactor

In this chapter, the novel approach using the direct liquid injection system (DLI) and the low-pressure O₂ plasma system is presented. The basic principles, from the droplet formation until the deposition of the NPs are studied. Using a theoretical model of the droplet-plasma interactions, the evaporating droplet lifetime was calculated and its value was found dependent on several factors, such as the solvent volatility, the system geometry, the plasma species characteristics and the temperature surrounding the droplets. In such study, it is crucial to understand how these factors can cause abnormal variations in the pressure, heterogeneities on the film, and contamination in the reactor due to the solvent. Based on the theoretical findings and the preliminary experimental results, we were able to optimize the TiO₂ NPs thin film deposition process. It was monitored by *in situ* ellipsometry while Optical Emission Spectroscopy (OES) gave insight on the oxidation process of the organic solvent by the O₂ plasma. The film structure was studied using Scanning Electron Microscopy (SEM), Atomic Force Microscopy (AFM) and Raman spectroscopy and its chemical analysis with X-ray Photoelectron Spectroscopy (XPS).

Table of Contents

Introduction.....	153
5.1 Material and Methods.....	154
5.2 Analysis of the Process - From the Atomization of the colloidal solution to the Deposition of the TiO ₂ NPs.....	154
5.2.1 Spraying/Atomization – Droplet Formation.....	154
5.2.1.1 The Injection System.....	154
5.2.1.2 Mean droplet size through Phase Doppler Anemometry (PDA)	155
5.2.1.3 Mass rate of the injected solvent	157
5.2.2 Transport – Evaporation of Solvent.....	157
5.2.2.1 Travel time of droplets inside the heating pipe.....	157
5.2.2.2 Evaporation of liquid droplets inside a low-pressure environment.....	159
5.2.3 Droplet Interactions with Plasma – Estimation of the droplet temperature.....	162
5.3 Deposition of the TiO ₂ NPs inside the O ₂ ICP plasma reactor: a first approach	171
5.3.1 Importance of the heating wire temperature on the deposited TiO ₂ thin films....	172
5.3.2 Impact of the liquid injection parameters on the deposited TiO ₂ thin films and the low-pressure system.....	174
5.3.4 Plasma Characterization during Injection of the TiO ₂ Colloidal Solution inside the O ₂ ICP Reactor.....	176
5.4 Optimization Strategy – Improvement on the deposition of the TiO ₂ NPs.....	179
5.4.1 Dilution with more volatile solvents (Water, Ethanol and Methanol).....	180
5.4.2 Effect of system Geometry and the Temperature	182
5.4.3 Iterative Mode of Operation.....	183
5.5 Chemical Investigation of the optimized films through XPS and Raman.....	189
5.6 Characterization of the optimized films using Ellipsometry.....	191
5.6.1 <i>In situ</i> monitoring of the TiO ₂ NPs thin film growth.....	192
5.6.2 Optical and physical characteristics of the optimized films Ellipsometric Model	195
5.7 Discussion.....	199
5.7.1 Comparison between the deposited pristine and optimized TiO ₂ NPs thin films	199
5.7.2 Iterative Process.....	201
5.7.3 From the theoretical to the experimental point of view	202
Conclusion	203
Bibliography	205

Introduction

Several industrial sectors including electronics, photocatalysis, sensors and biomedical sector demand fast and reproducible deposition of thin film on various substrates (sometimes temperature sensitive ones). In many cases, the deposition precursors have low vapor pressure, are fragile or viscous and they can even contain solid nanoparticles (NPs). The latter is of great importance as wet processes that can enable the creation of thin films containing NPs exhibit hazardous environmental human and safety issues. To address this, liquid containing plasmas (misty plasmas) were attempted over the last years, aiming in either the deposition of nanoparticles (NP) in a colloidal solution or the deposition of non-volatile precursors both in atmospheric and low-pressure plasma systems. [1-4]

Most of these studies focus on the deposition using atmospheric pressure plasma systems due to the technical challenging conditions a low pressure system containing liquid can have (e.g. risk of contamination of the vacuum chamber, malfunction of the turbomolecular pump, fast liquid vaporization without reaching the substrate, control of the plasma stability under liquid injection).[5,6] Despite this fact low pressure systems can provide a prosperous environment for high quality films and can be adapted in large scale low pressure systems used in industry.

Ross et al. and Ogawa et al. [1,7] were among the first ones to develop and implement direct liquid injection approaches for the injection of NPs inside a low pressure plasma system operated in a pressure range from 100 to 500 mTorr. In addition, Ogawa's work was the first attempt to investigate theoretically how the plasma affects the liquid droplet. In a second work [8] they focused in another important aspect of how the plasma is affected by the evaporating droplet.

In this concept, we attempt for the first time the injection of 3 nm TiO₂ NPs dispersed in a colloidal solution [9] inside a low pressure (3 mTorr) plasma reactor, for the deposition of TiO₂ nanostructured films. Therefore, in this chapter, we analyze the production, transport and evaporation of these droplets in the low pressure plasma environment. Using a theoretical model, we investigate both the temperature of the injected droplets and their lifetime. We have also characterized the plasma during the injection of liquid using Optical Emission Spectroscopy (OES). Based on the theoretical findings and the preliminary experimental results, we attempt gradually to optimize and control the process, in order to acquire homogeneous non-degraded thin films. The physical and chemical evaluation of the produced film is implemented using various characterization techniques such as Scanning Electron Microscopy (SEM), X-Ray Photoelectron Spectroscopy (XPS), Atomic Force Microscopy (AFM), Raman scattering and spectroscopic Ellipsometry.

5.1 Material and Methods

The reactor used for the injection of the colloidal solution and the creation of TiO₂ NPs thin films through this original approach was explained in detail in Chapter 2. Briefly, a low pressure inductively coupled plasma was used with O₂ as a working gas. The produced plasma was diffused in the reactor chamber where the liquid injector was also mounted, with an angle oriented towards the substrate. This configuration is provided in Chapter 2 and is given later on in Figure 5.4. The O₂ flow rate was set at 24 sccm to maintain a pressure of 3 mTorr.

5.2 Analysis of the Process - From the Atomization of the colloidal solution to the Deposition of the TiO₂ NPs

For the successful elaboration of this hybrid approach and the deposition of the TiO₂ NPs thin film, a detailed investigation was needed. The most challenging part of this study was the manipulation of the liquid colloidal solution of NPs in order to successfully inject it in the low-pressure reactor, in conditions favorable for the creation of TiO₂ NPs thin films on the substrate. Therefore, the mechanisms involved the atomization or spraying of the colloidal solution, the partial evaporation of the droplets' solvent and the deposition of the NPs on the substrate inside the ICP O₂ low-pressure plasma reactor were studied. Figure 5.1 shows a schematic illustration of the four parts of this study. The Atomization-Droplet Formation, the Transport of the droplets, the Droplet Interactions with Plasma and finally the Deposition of NPs.

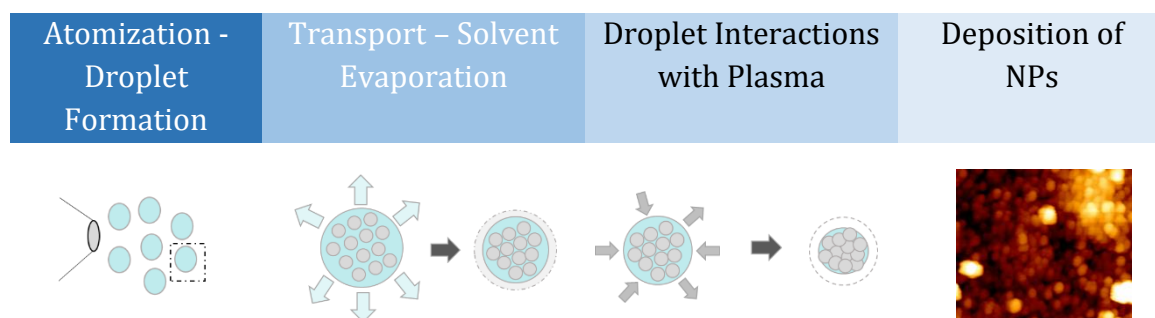


Figure 5.1: Schematic illustration of the four stages used for the analysis of the hybrid approach used.

5.2.1 Spraying/Atomization – Droplet Formation

5.2.1.1 The Injection System

An industrial injector (Kemstream Liquid Dozer) is used for the formation of droplets of the initial colloidal solution. This injection system features a normally

closed fast solenoid valve (or injector). It has a small conductance (flow coefficient), commonly called Cv and it is controlled in pulsed regime. For maintaining the low pressure (3 mTorr in standard conditions) of the plasma reactor, low injection rate is needed. Thus, the use of carrier gas to assist the droplet formation was not an appropriate strategy in our case. The injector was mounted on the reactor through a heated or not pipe, at an angle of 45° from the perpendicular to the substrate.

This injector, is actually a valve which is a normally switched off and when a positive voltage is applied the valve is opened. Using a dedicated software provided by Kemstream, we could regulate the applied frequency (f), the open time (T_{ON}) and the number of injection cycles of the injection system (Fig. 5.2). The specifications of the system from the manufacturer allowed us to regulate the parameters from 0.1 to 1 Hz and from 1 to 2 ms T_{ON} time.

In the specific liquid dozer, the difference in pressure between the reactor (at the outlet of the injector) and the atmospheric in the bottle (which is the same pressure that is at the inlet of the injector) is the “driving force”. Due to this driving force, a liquid jet is created. The droplets are generated by the rapid breakup of this liquid jet controlled by closing and opening the valve of the injector. This breakup of the columnar liquid structure is called ligament. [10] The “driving force” can be calculated by the difference in pressure between the atmospheric pressure at which the liquid is stored outside the reactional chamber and the working pressure in the reactor, as given in the next equation.

$$\Delta P = P_{liquid} - P_{reactor} = 760 \text{ Torr} - 0.003 \text{ Torr} = 759.99 \text{ Torr} \quad (\text{Equation 5.1})$$

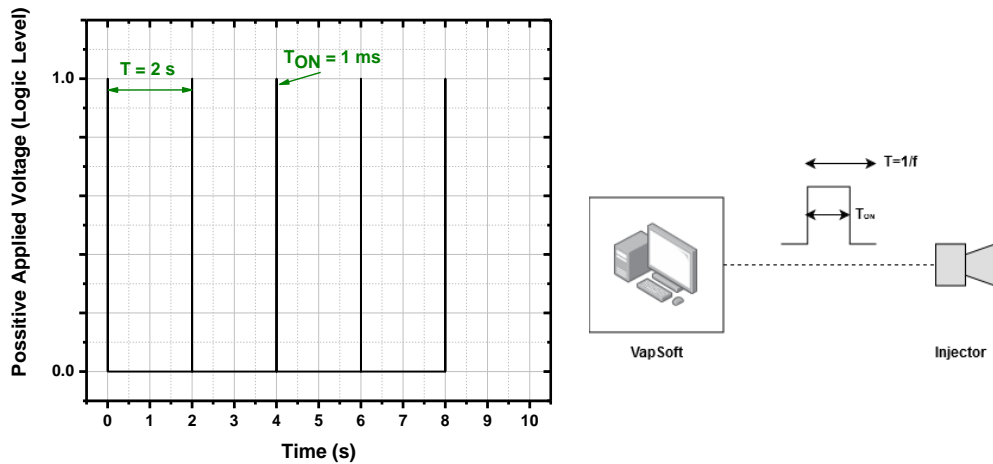


Figure 5.2: Schematic of the communication between the VapSoft software and the injector through the applied pulses for the operation of the injector.

5.2.1.2 Mean droplet size through Phase Doppler Anemometry (PDA)

Phase Doppler Anemometry (PDA) was employed for the determination of the mean size of the produced droplets from the specific injection system, at LIST in

collaboration with Dr Simon Bulou. The solution used for these experiments were the mixture of Propylene Carbonate and Propylene Glycol (in the ratio that is found in the colloidal solution of the TiO₂ NPs), water, ethanol and methanol. The measurements could not be carried out in a low-pressure system and since the driving force is what determines the droplets size, an alternative setup operated at the atmospheric pressure was used. To maintain the same pressure difference the liquid was forced through the injector by applying higher pressure inside the tank of the solution. The driving force or pressure difference was calculated as following:

$$\Delta P = P_{liquid} - P_{PDA} = 1520 \text{ Torr} - 760 \text{ Torr} = 759.99 \text{ Torr} \quad (\text{Equation 5.2})$$

Figure 5.3 shows the average mean size of the droplets produced using the liquid dozer over different solvents at 0.5 Hz and 1 ms injection parameters. As observed, the mean droplet value of water lies at 53 μm with a Standard Deviation (SD) of 20 μm, ethanol and methanol at 65 μm with SD at 29 μm and finally PCPG at 77 μm and a SD at 34 μm. As observed water has the lowest mean droplet size and methanol and ethanol do not significantly differ from each other. In contrary, for the more viscous and less volatile mixture of PC/PG, the value reaches 77 μm. These values do not lie far from other works were 50 μm droplet size was found from Ogawa et al.[1] and between 125 to 225 μm found by Kooji et al. [10] comparing different nozzle systems.

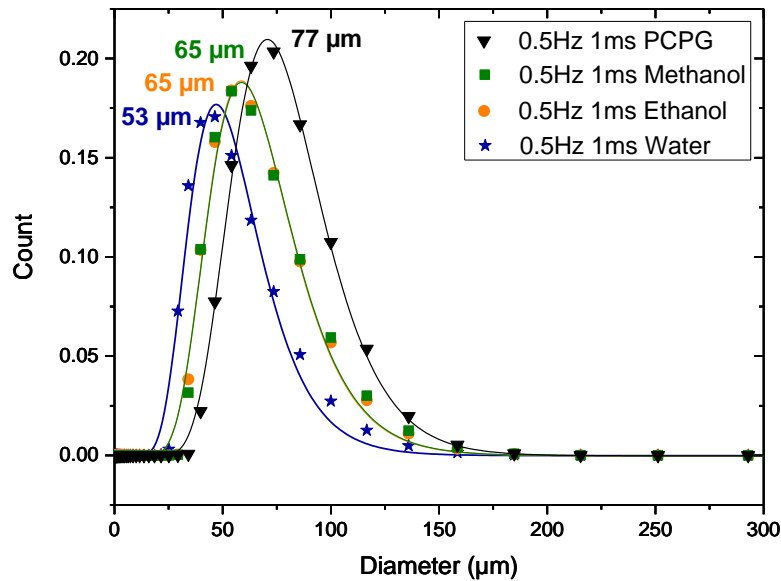


Figure 5.3: Average mean droplet size of water, ethanol, methanol and PC/PG at 0.5 Hz and 1 ms injection parameters.

Kooji et al. [10] investigated the characteristic parameters that can determine the droplet size of sprays with similar configurations. More in detail, they identified that as the pressure difference increases, the mean droplet size shifts to smaller size distributions (approximately from 200 to 150 μm). As the solvent is more viscous, this decrease in the size distributions is less pronounced. Finally, when they varied the

surface tension (mixture between ethanol-water) preserving the same density and viscosity, they observed that the peak of the droplet size distribution is slightly shifted to smaller diameters for lower surface tension but at the same time having a rather increased standard deviation. In general, they concluded that the pressure and geometry of the nozzle are the key parameters to control the drop size in this type of sprays, with the fluid parameters (viscosity and surface tension of the solution) [10] being less important. Therefore, our PDA experiment was carried out in order to verify these observations.

5.2.1.3 Mass rate of the injected solvent

In case of $T_{ON}=1$ ms, the solution mass rate was estimated at 2.33 mg per injection. This was accomplished by weighting the beaker containing the colloidal solution or solvent before and after the experiments. As the amount of injected solution increases, the solvent evaporates from the droplets and molecular species are added to the gas phase causing the pressure to increase. [1] Its monitoring, read from the gauge, revealed that during the injection, the pressure is increased instantly (within the 1st second during the injection). This pressure variation is further discussed in Section 5.3.2.

5.2.2 Transport – Evaporation of Solvent

In this Section, we will study the events occurring to the droplets after their production by the liquid dozer and during their transport towards the low-pressure plasma. More specifically, as indicated in Chapter 2 and also noted in the Section 5.2.1.1, the injector is connected to the low-pressure plasma reactor a pipe, which can be heated up to 150°C (423 K). To investigate these events, we separated this Section in two parts. In Section 5.2.2.1 great focus is given in the transport of the droplets in the heated pipe and in Section 5.2.2.2 in their evaporation leading in solvent removal and reduction of their size.

5.2.2.1 Travel time of droplets inside the heating pipe

In this section, we study the transport of the produced droplets inside the heating pipe and finally inside the plasma reactor towards the substrate. Ogawa *et al.* [1] studied the impact of pressure on the velocity of the stream as a function of different injection parameters (f , T_{ON}) using a Denso fuel injector (23209-0D040) in a pulsed mode and an estimated produced droplet diameter estimated at 50 μm , the configuration of which resembles to our system. An important similarity between these two systems is the driving force for the droplet formation, being the one of the pressure difference as well as the pulsing fashion of the injection. In this work, they observed that as the difference in pressure increases (between the reactor and the liquid), the driving force of the produced liquid droplets increases leading to a higher

travel velocity. Furthermore, they indicated that the stream velocity remains intact whatever the duration of the pulse of the injection parameter (1.3 ms and 2 ms were tested as pulse duration).

In detail, due to the difficulty to conduct these experiments in the low-pressure system, they were implemented at atmospheric pressure. To create similar pressure difference as in the low pressure, this time since their injector was in atmospheric (750 Torr), they used a higher backing pressure to thrust out the liquid and produce the stream of droplets. Therefore, as seen in Figure 5.4a, the backing pressure used was 1100, 1500 and 2000 Torr. As a result, the pressure difference could be calculated as $\Delta P = \text{Backing Pressure} - \text{Atmospheric}$. In addition, two different pulse durations were chosen, 1.3 and 3 ms. Initially, they measured the travel distance of the stream given in Figure 5.4a and from that, they calculated the stream velocity in Figure 5.4b. These results also suggest that from lower pressure difference, the liquid injected per shot is reduced since the force pushing the liquid through the injector and into the vacuum has been reduced. The liquid enters the reactor at lower velocity affecting both the atomization and the stream speed.

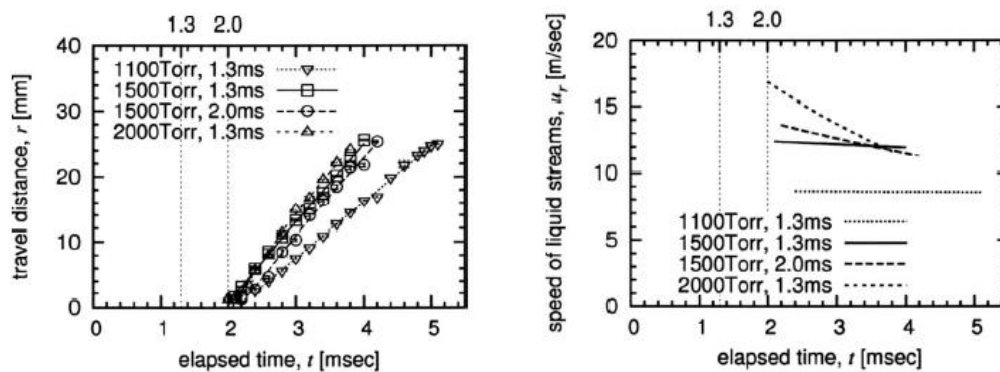


Figure 5.4: a) The distance from the fuel injector jets to the head of the spray stream as a function of the time since the voltage pulse was applied to the fuel injector valve. There is an initial delay until the valve can open. Then the spray appears and travels away from the jet openings. The four curves correspond to different pressures across the fuel injector valve forcing the ethanol liquid out of the jets. b) The calculated speed of the spray stream as a function of time based on the distance traveled in part a. [1,11]

For example, for our case, for the liquid at atmospheric pressure and a reactor at 3 mTorr, the pressure difference would be at ~ 750 Torr (as in Eq.5.1). In addition, assuming that the pulse duration in our system at 1 ms is not drastically different of the 1.3 ms proposed by Ogawa and al., the produced stream velocity would be around 13 ms^{-1} (based on Figure 5.4b). From this velocity, and knowing the distance from the injector to the substrate holder, we could calculate the travel time of the droplets from the injector to the substrate. An example of the time by adjusting the heating pipe geometry is given in Figure 5.5. In the case where the heating pipe is 5 cm long the travel time was calculated at 3.9 ms. When the pipe is increased to 20 cm it reaches 15.3 ms. Following this direction, by increasing the distance of the heating pipe, the

travel time of the droplets is increased as well, giving more time to the droplets to evaporate.

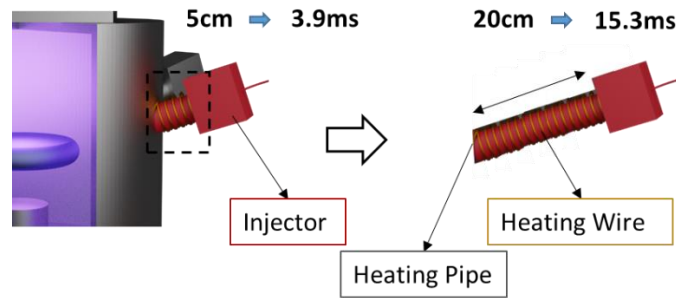


Figure 5.5: Calculated travel time of the droplets inside the heating pipe for two different pipe dimensions.

In this Section we have seen the impact of the pressure difference of injection systems like the one we use. The velocity of the produced droplets is driven by the pressure difference. Based on the results of Ogawa et al. we can understand the fashion of the droplets transport and decide of the geometrical adjustments of our system, in case an optimization of the process is needed.

Apart from the transport of these produced droplets, another important parameter that needs to be studied is their evaporation in the low-pressure medium. Hence, in the next Section 5.2.2.2 this part will be thoroughly presented.

5.2.2.2 Evaporation of liquid droplets inside a low-pressure environment

As the droplets are being transported inside the low-pressure system, they evaporate leading to solvent removal and the reduction of the droplet size. This is something quite appreciated as the more the droplets evaporate the lesser are the chances of liquid droplets landing on the substrate. Thus, in this section we have investigated the conditions in which the droplets evaporate.

The first step for moving on with this study is to specify the motion associated with the evaporation of the liquid molecules under the conditions in our system. An approach to distinguish if the motion of evaporated molecules of the droplet is diffusive (collisional) or molecular is by quantitatively distinguishing the flow regimes. This can be accomplished by calculating the dimensionless Knudsen number, Kn defined as

$$Kn = \frac{\lambda}{D} \quad (\text{Equation 5.3})$$

where λ is the mean free path of the molecule of solvent in the droplet and D is the diameter of the droplet.

The mean free path for different solvents can be calculated using the following equation:

$$\lambda = \frac{RT}{\sqrt{2}\pi d^2 N_A P} \quad (\text{Equation 5.4})$$

where R is the universal gas constant, T is the temperature, d is the molecule diameter of the solvent, N_A is the Avogadro's Number and P the absolute pressure.

For the case of small Knudsen numbers and thus when the mean free path of molecules is lower than the diameter of droplets, $\lambda < D$, the motion of evaporation is collisional. The basis of the theory of evaporation of droplets in a gaseous medium for this case, was laid by Maxwell. In an article on "Diffusion" written in 1877 for the Encyclopedia Britanica under the heading "Theory of the wet-bulb thermometer" Maxwell considered the simplest case of the stationary evaporation of a spherical droplet, motionless relative to an infinite, uniform medium. He assumed that the vapor concentration at the surface of the droplet was equal to its equilibrium concentration (i.e. the concentration of saturated vapor at the temperature of the drop, in the case of not too small droplets). [12,13] For the case of high Knudsen numbers and thus $\lambda > D$, the motion of evaporation is molecular. The molecular motion of evaporation was first derived by Hertz through the analysis of the evaporation of mercury[14] and was later verified by Knudsen[15].

Using the data given in Annex C, we were able to calculate the mean free path of the different solvents at 3 and 30 mTorr (best- and worst-case scenario of the pressure inside the system) and at three different droplet temperatures that are given in Table 5.1.

Table 5.1: Results of the mean free path for different solvents in mm.

Pressure @ 3 mTorr			
Solvent	25°C/298K	100°C/ 373K	150°C/423K
Water	30.6	38.3	43.4
Ethanol	11.8	14.9	16.9
Methanol	12.9	16.4	18.6
PG	6.3	8.0	9.1
PC	7.8	9.8	11.1
Pressure @ 30 mTorr			
Solvent	25°C/298K	100°C/ 373K	150°C/423K
Water	3.1	3.8	4.3
Ethanol	1.2	1.49	1.69
Methanol	1.3	1.64	1.86
PG	0.6	0.8	0.91
PC	0.8	0.9	1.11

The calculated mean free path for each solvent, even for the worst-case scenario, meaning the elevated pressure, lies in the case of $\lambda > D$. This means that the Knudsen number is much higher than 1 and therefore the motion of evaporation is

not diffusive (collisional) but rather molecular. Based on that, the appropriate equation can be used in order to determine the molecular flux of evaporation of the droplets. As a consequence, the molecular flux of evaporation ($\lambda > D$) based on the kinetic theory established by Hertz- Knudsen can be expressed as following:

$$W_{mol,ev} = \frac{a_c (Pd - Pr) N_A}{\sqrt{2\pi MRT_d}} \quad (\text{m}^{-2} \text{s}^{-1}) \quad (\text{Equation 5.5})$$

where a_c is the sticking coefficient of the gas molecules onto the droplet surface (condensation coefficient), Pd is the partial pressure of the droplet surface, Pr is the reactor pressure, N_A is the Avogadro constant, M is the molar mass of the solvent, R is the gas constant and T the droplet temperature.

The vapor pressure at the droplet surface Pd can be obtained using the Clausius–Clapeyron relation for an ideal gas using a reference temperature T_{ref} and the Kelvin equation to account for the surface curvature of the droplet. [16–19]

$$P_d = P_{ref} \exp \left[\frac{\Delta H_{vap}}{R} \left(\frac{1}{T_{ref}} - \frac{1}{T_d} \right) \right] \exp \left[\frac{2\sigma v}{rRT_d} \right] \quad (\text{Equation 5.6})$$

where P_{ref} is the saturated vapor pressure at the reference temperature T_{ref} , ΔH_{vap} is the latent heat of vaporization, R the gas constant, T_d the droplet temperature, σ the surface tension, v is the molar volume of the liquid of the droplet and r its droplet radius.

As the droplet evaporates, it releases vapor molecules of the colloidal solution inside the system. Although, these evaporating molecules experience only a small amount of gas-phase collisions (due to the low pressure) which could lead to re-condensation, some will reach again the droplet surface and re-condense providing heat flux and kinetic energy. Thus, the molecular flux of condensation, W_{cond} can be written as:[1]

$$W_{cond} = a_c \frac{1}{4} n_l^g \bar{u}_l \quad (\text{Equation 5.7})$$

where n_l^g is the density of the liquid molecules in the vapor phase and \bar{u}_l is their mean thermal speed. The net molecular flux, W_{net} can then be written as

$W_{net} = -W_{mol,ev} + W_{cond}$ with $W_{mol,ev}$ the flux of evaporating molecules, since evaporation is an output term and condensation an input one. From the net flux of condensing and evaporating molecules we can now calculate the decrease rate of the volume of the droplet as:[20]

$$\frac{dV}{dt} = A_{sph} W_{net} V_{mol} = 4\pi r^2 W_{net} V_{mol} = 4\pi r^2 \frac{dr}{dt} \quad (\text{Equation 5.8})$$

where A_{sph} is the area of the sphere and V_{mol} the volume of the molecule. The radius droplet decrease can be given by the equation 7 as:

$$\frac{dr}{dt} = W_{net} V_{mol} \quad (\text{Equation 5.9})$$

where $V_{mol} = M/\rho$.

In this Section, we established that the solvent evaporation is governed by molecular motion. This important aspect is dependent on the solvent nature and most importantly by the medium (pressure and temperature). When using low pressure plasma systems, the medium becomes even more complex. Especially when talking about liquid droplets inside the plasma a new term is gradually arising, that accounts for misty plasmas. Hence, in the next Section, we will propose a model for the computational analysis of these misty plasmas and we will investigate the parameters affecting their droplet size and temperature.

5.2.3 Droplet Interactions with Plasma – Estimation of the droplet temperature

Misty plasmas, being plasmas that contain liquid droplets, is a term first proposed by Coppins [152,153] in 2004. Coppins stated that these misty plasmas would not differ significantly from the dusty plasmas (plasma containing millimeter to nanometer particles) but that the liquid state of the droplets could allow droplet deformation and make surface tension forces more important. Based on this Ogawa et al. [1,11] proposed a first model to investigate this misty plasma and identify the parameters affecting the droplets temperature and lifetime.

With this approach, liquid droplets containing NPs are injected inside the reactor. Therefore, it is desirable for the specific process to evaporate faster the droplets, in order to deposit only the NPs and not the liquid droplets as well on the substrate. In this Section, we will focus on the model that will allow us to compute this droplet size reduction inside the plasma.

For the calculation of the droplet size evolution with time (Eq. 5.9), one must know the droplet temperature over time. To acquire this information, we need to account for all the energy fluxes entering in and exiting from the droplet. Since the droplet evaporates in a complex environment, that of the plasma, there are multiple components affecting the temperature of the evaporating liquid droplets. Several works [21–25] focus on the interactions of solid particles with weakly ionized, non-thermal plasmas (named also as dusty plasmas), using the energy balance equation. Such approach was followed in Chapter 3 for the interaction of the NP inside the film with the O₂ plasma. In this case, as liquid interacts with plasma, the evaporation and condensation process of the solvent are added in the equation. In Figure 5.6, the energy fluxes entering in and exiting from the droplet, meaning as well heating and cooling down the droplet are illustrated. The heating terms correspond to the collisions with the plasma species and the condensation whereas the cooling terms

include the evaporation, the conduction with gas molecules and the radiation (which can also be a heating term). Charging of the droplet as it enters the plasma sheath was not taken into consideration (which could affect the evaporation process).

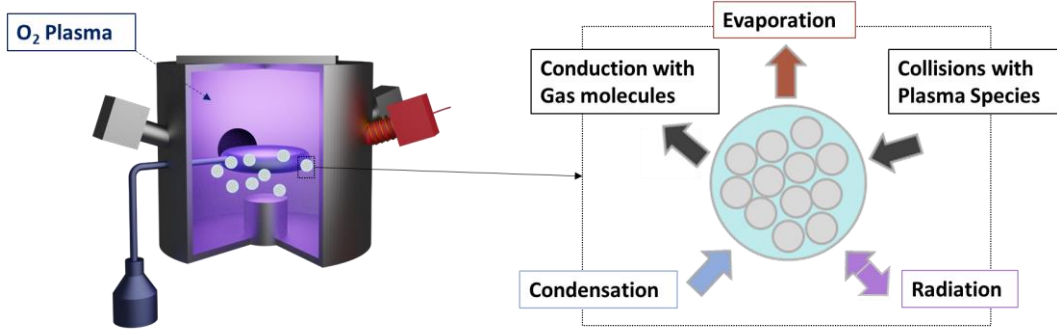


Figure 5.6: Schematic illustration of the energy fluxes entering and exiting the liquid droplet inside the plasma.

Based on these, we developed a model describing the interaction between the plasma and a single droplet inside the plasma volume using the energy balance equation.[21,24].

$$Q_{IN} = \frac{4}{3}\pi r^3 \rho C \frac{dT_d}{dt} + Q_{OUT} \quad (\text{Equation 5.10})$$

where r is the droplet' radius (considered at 25 μm), ρ is the density of the droplet solvent and C its heat capacity. Here once again, the total input power Q_{IN} and total output power Q_{OUT} at the droplets' surface can be obtained from the corresponding energy fluxes J_{IN} and J_{OUT} , $Q_{IN} = \int_A J_{IN} dA = \int_A J_{OUT} dA$, where the integrals are performed over the droplet surface area.

As stated in Section 5.2.2.2 as the droplet evaporates, it releases vapor molecules of the solvent inside the system. Although, these evaporating molecules experience only a small amount of gas-phase collisions (due to the low pressure) which could lead to re-condensation, some will reach again the droplet surface and re-condense providing heat flux and kinetic energy. Thus, inside the O₂ plasma, the main mechanisms favoring the heating of the droplet include the flux provided by the plasma species (J_{ions}, J_{ass}, J_e) and the re-condensed vapor molecules (Eq. 5.7) of the solvent (J_{condes}). In this framework, the total energy flux towards the NPs can be written as [1,21,24] :

$$J_{IN} = J_{condes} + J_{ions} + J_e + J_{ass} = a_c \frac{1}{4} n_l^g \bar{u}_l n_i (2k_B T_w + \Delta H_{vap}) + n_i \sqrt{\frac{k_B T_e}{m_i}} (E_{ion} + \Gamma_i E_i) + n_e \sqrt{\frac{k_B T_e}{m_i}} 2k_B T_e + \frac{1}{4} n_o \sqrt{\frac{8k_B T_g}{\pi m_o}} \Gamma_o E_{diss} \quad (\text{Equation 5.11})$$

where a_c is the sticking coefficient of the gas molecules onto the droplet surface (condensation coefficient considered 1), n_l^g is the density of the liquid molecules in the vapor phase and \bar{u}_l is their mean thermal speed. T_w is the wall temperature and ΔH_{vap} is the latent heat (enthalpy) of vaporization. The term k_B is the Boltzmann constant, m_i is the mass of O₂⁺, $E_{ion} = e (V_p - V_f)$ is the sheath potential (where V_p is the plasma potential, V_f is the floating potential and e is the electron charge), Γ_i is the recombination coefficient of the positive ions on the droplets (here, $\Gamma_i = 1$ is assumed), E_i is the ionization energy (12.06 eV for O₂). Moreover, m_o is the mass of O atoms, E_{diss} is the dissociation energy (5 eV for O₂), and Γ_o is the recombination coefficient of O atoms on the liquid droplet surface. Over the range of experimental conditions investigated, the Γ_o value can be estimated between 0.4 and 1 [26] (here, a maximum contribution was assumed such that $\Gamma_o = 1$).

The main mechanisms involved in the cooling of the droplet is the molecular evaporation (J_{evap}), as explained in Section 5.2.2.2, the conduction with the gas ($J_{cond,gas}$) and the radiative cooling (J_{rad}) as explained in Chapter 3. Thus, the output energy flux is written as:

$$J_{OUT} = J_{evap} + J_{cond,gas} + J_{rad} = \frac{a_c (P_d - P_r) N a}{\sqrt{2\pi M R T_d}} \Delta H_{vap} + \frac{\gamma+1}{16(\gamma-1)} \alpha \frac{p}{\sqrt{T_g}} \sqrt{\frac{8k_B}{\pi m}} (T_d - T_g) + \epsilon \sigma (T_d^4 - T_w^4) \quad (\text{Equation 5.12})$$

where γ is the adiabatic coefficient ($\gamma=1.4$ for oxygen), α is the accommodation coefficient ($\alpha=0.9$ for oxygen), p is the pressure and m is the mass of gas molecules. In the last term of Equation 5.12, the emissivity is set at $\epsilon=0.96$ for all the solvents studied and T_w is considered the wall temperature.

Table 5.2: values used to calculate the droplet evaporation kinetics [1,27,28]

Solvent	ΔH_{vap} (kJ/mol)	T_{ref} (K)	P_{ref} (Torr)	C (J/gK)	σ (nN/m)	p (g/mol)	M (g/mol)
PG	67	298	0.13	1.79	34	1.040	76
PC	60	298	0.03	1.67	41	1.205	102
Water	41	298	23.70	4.20	71	0.997	18
Ethanol	38.6	298	58.80	2.40	22	0.789	46.07
Methanol	35.2	298	126.90	3.82	27	0.792	32.04

Figure 5.7, shows the result of the energy balance equation (Eq. 5.10), calculating the temperature variation over time. The solvents used for this study, are the ones that were investigated in Section 5.2.2.2, namely the PC, PG, water ethanol and methanol. The data used to calculate the transient droplet temperature are given in Table 5.2. For these results, the pressure was set at 25 mTorr, the droplet diameter at 50 μ m and the droplet initial temperature equal to the wall temperature (T_w) at 423 K. The plasma characteristics, in order to extract these results, originate from previous works[29–31] of the group and they were measured at the center of the

diffusion chamber. Moreover, in our case, due to the system capabilities, we consider as wall temperature, the temperature of the heated pipe connecting the injector to the reactor.

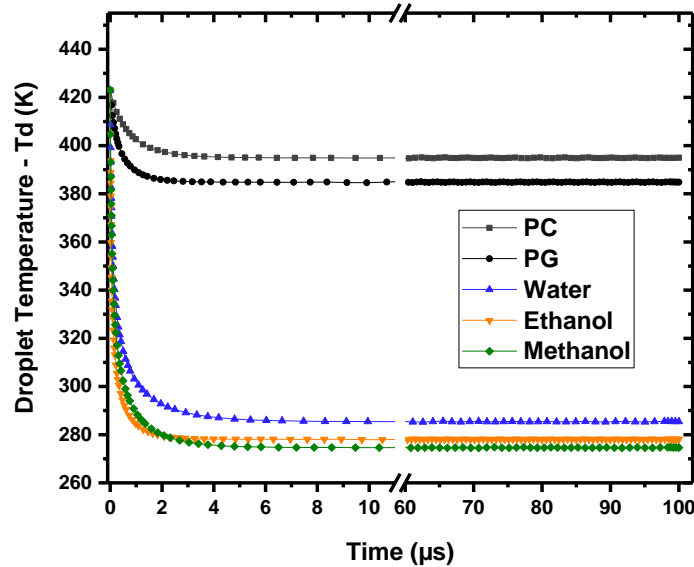


Figure 5.7: Droplet (50 μm in initial diameter) temperature evolution versus time based on solving the energy balance equation for PC, PG, water, ethanol and methanol solvents. An axis - break has been used, to given an emphasis at the transient temperature during the first μs .

As the droplet is injected inside the low-pressure system, evaporation will start immediately. As evaporation process is the main cooling term in equation 5.12, the droplet will cool down until a balance between heating and cooling terms is reached. As seen in Figure 5.7, the part of the transient time is significantly small and the temperature is stabilized within 4 μs only, meaning that the droplet evaporation and reduction in size takes place when constant temperature is reached.[32] The value of the temperature reached after 100 μs , on the right hand-side of Figure 5.7, corresponding to the steady state of each of these solvents is mainly linked to the amount of energy needed to transform the liquid into vapor (ΔH_{vap}).

Table 5.3: Low-Pressure O₂ Plasma Characteristics at the center of the diffusion chamber[29–31].

Pressure (Torr)	n_0 (cm^{-3})	$n_i=n_e$ (cm^{-3})	E_{ion} (eV)	T_e (eV)
0.002	9.4×10^{12}	5.68×10^9	16.81	5.55
0.004	1.89×10^{13}	4.39×10^9	12.96	3.9
0.007	2.57×10^{13}	3.38×10^9	10	3.3
0.01	3.9×10^{13}	3.1×10^9	9.26	2.73
0.014	7.4×10^{13}	2.3×10^9	7.71	2.58
0.021	1.47×10^{14}	1.89×10^9	6.6	2.5
0.025	1.74×10^{14}	1.59×10^9	6.04	2

Solving Eq. 5.10, leads to the determination of the temperature of the droplet over time, which allows us to calculate the radius change over time (Eq. 5.9). Therefore, coupling these two equations we can have the droplet lifetime, provided in Figure 5.8. Droplet lifetime was defined as the time needed for the droplet radius to decrease from 25 μm down to 0 nm. In Figure 5.8, the droplet lifetime is given for all the solvents under investigation and for pressure conditions inside the reactor starting from 2 to 25 mTorr. The plasma characteristics for each pressure are given in Table 5.3. As observed, the droplet lifetime is clearly dependent on the droplet characteristics. The less volatile PC and PG solvents exhibit significantly higher lifetimes than the rest. The discrepancies between the lifetime of water, ethanol and methanol are much smaller, with lower values than PC and PG. Concerning the lifetime, methanol exhibits the best process characteristics. Indeed, it is desirable for the specific process to evaporate faster the droplets, in order to deposit only the NPs and not the liquid droplets as well. A hypothetical downside of having a very volatile solvent would be that it could lead in a fast evaporation of the droplets very far from the substrate, making the deposition less efficient. The NPs inside the plasma could be trapped inside the sheath or be evacuated by the pump. Hence, the ideal condition would be to have a solvent that will “protect” and transport the NPs until the substrate having evaporated sufficiently just before reaching the substrate.

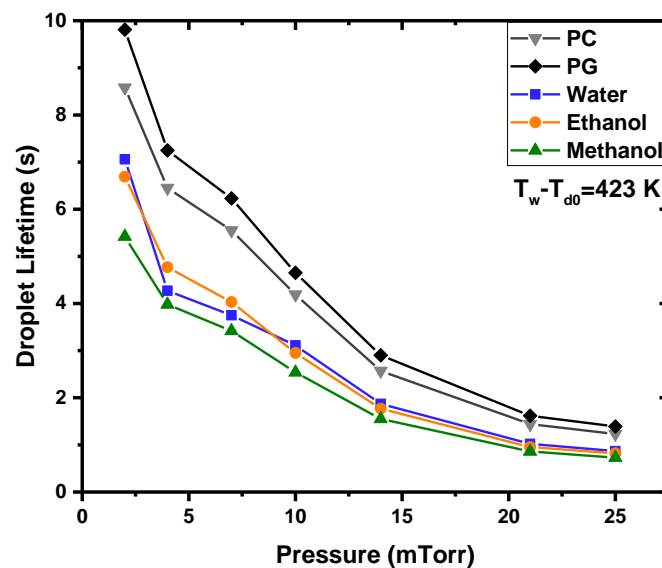


Figure 5.8: Droplet lifetime (50 μm in initial diameter) for a pressure range between 2 and 25 mTorr, for PC, PG, water, ethanol and methanol solvents. Results obtained from the energy balance equation for the stationary case.

Moreover, another interesting information Figure 5.8 provides, is the fact that as the pressure increases, the droplet lifetime significantly decreases. This observation can only be linked with higher heating droplet term in the energy balance equation. Indeed, as the pressure increases, the density of the oxygen atoms increases as well. [31] To prove this point, in Figure 5.9 (also Figure 3.10) the input flux (heating term) provided by the plasma species (J_{ions}, J_{ass}, J_e) are calculated and plotted at a

pressure range of 2 to 25 mTorr. The electron and ion flux remain the same (slightly decreased) whereas O atom flux significantly increases being the most important heating parameter leading to faster droplet evaporation.

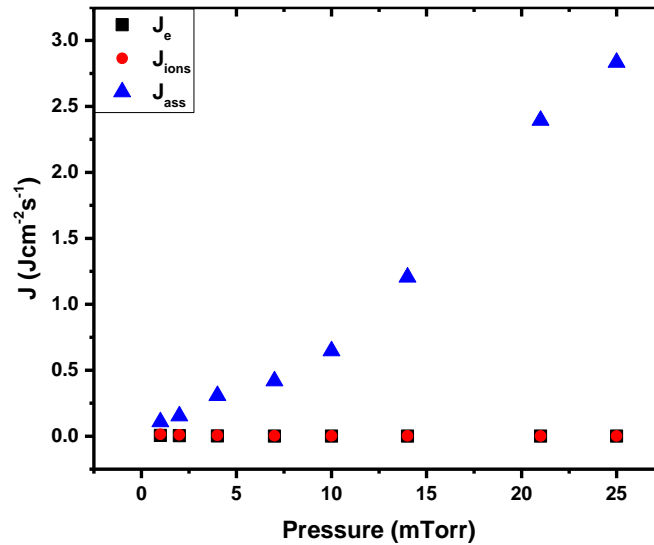


Figure 5.9: Calculated energy fluxes (J_{ions}, J_{ass}, J_e) towards the droplet for a pressure range between 2 and 25 mTorr, inside the reactor, during O₂ plasma.

From these results, we understand that the pressure increase favors the droplet lifetime reduction but a downside is that conditions at higher pressure are detrimental for the film growth (observed by previous studies of the group). This is especially important for the creation of the TiO₂-SiO₂ nanocomposites. In detail, in higher pressure the electron temperature is lower leading to less efficient dissociation of the HMDSO molecules, which can finally degrade the inorganic quality of the matrix. Moreover, from these results and knowing the impact of the pressure on the matrix quality, one could propose a periodicity of the liquid injection that would give enough time to the droplet to evaporate while maintaining the pressure at low level. This will be further discussed in Chapter 6.

Apart from the solvent volatility and the pressure during plasma, another parameter that should be considered for the efficient evaporation of the liquid droplets is the wall temperature. Moving on the study, using the solvent with the lowest droplet lifetime (methanol) and the highest droplet lifetime (PG, which is the highest also in concentration in the selected colloidal solution), we will examine the impact of the droplet lifetime for different wall temperatures. The temperatures selected are 298 K, 373 K and 423 K for the pressure range of 2 to 25 mTorr. The choice of these specific temperatures has been done to match the experimental capabilities of our system. In detail, the pipe connecting the liquid injector with the reactor is at room temperature 25°C (298 K) and can be heated up to 150°C (423 K). The initial droplet temperature was set as the wall temperature. The results of this study are given in Figure 5.10. For the case of methanol (Fig.5.10a) they show that for lower pressure, the lifetime of the droplet is significantly increased from less than 1 s

up to 10 s at room temperature. At these lower pressures, for higher temperature (423 K) the lifetime can decrease by 5 seconds compared to the one of room temperature (298 K). For pressure higher than 14 mTorr the wall temperature affects much less the lifetime, as the flux coming from the O atoms is governing the heating of the droplet. For the PG case in Figure 5.10b, we observe a similar trend and dependency on the wall temperature at low pressure, having longer lifetime than methanol by approximately 5 seconds. Again, in this case, for higher pressure the lifetime reaches a plateau at 20 mTorr, with a value of 1.5 s, it is less sensitive to the wall temperature as the O atom flux mainly heats the droplets.

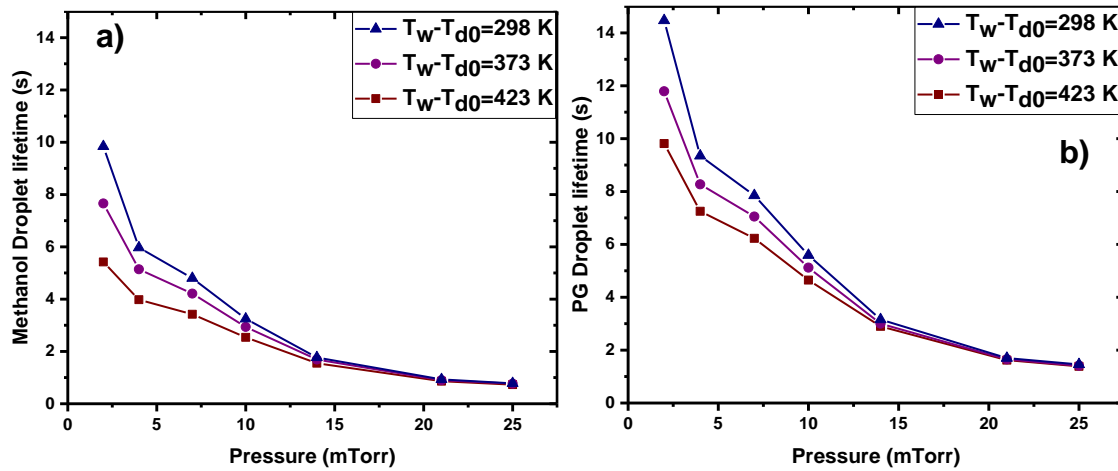


Figure 5.10: Methanol and PG droplet lifetime (50 μm in initial diameter) versus pressure for different wall temperature. Results obtained from the energy balance equation for the stationary case. The initial droplet temperature was set as the wall temperature, at 298 K given in bleu, 373K given with purple and 423K given with red.

As these interactions take place, they assist in the evaporation process of the solvent inside the droplet, decreasing its size and leading to the deposition of the remaining nanoparticles. As a last step in this study, we focus on the temperature history (Figure 5.11a) of a methanol droplet, with initial temperature equal to the wall one at 423 K and then from the steady temperature of this evaporated droplet (T_d) we investigate the temperature induced on the remaining single 5 nm in diameter nanoparticle (Figure 5.11b). This study is conducted for pressures between 2 and 25 mTorr. Apart from studying methanol, which as shown is the most volatile solvent in this study, we will also conduct this study for the PG solvent (Figure 5.11c), having the highest droplet lifetime and being the highest in concentration in our colloidal solution. From the obtained steady state temperatures (T_d) the transient temperature of the 5 nm TiO₂ NPs will be given as well. For the calculation of the NPs temperature, the Equations 3.1, 3.2 and 3.3 were used for the transient temperature of Section 3.3.2.

In general, with a first sight on these plots of Figure 5.11, we observe different behavior between the temperature of the small 5 nm TiO₂ NPs and the liquid droplets, which lie on the different heating and cooling mechanisms.

For the liquid droplet, no matter the solvent, the main mechanism when entering the medium is that of the evaporation, making the molecules exit the droplet, decreasing its size and making it cool down to its steady state temperature. As seen both in Figure 5.11a,c, this is a very fast process happening between 3 and 13 μs approximately, at 25 and 2 mTorr, respectively. The difference in the time needed for the steady state and the values of this temperature for each solvent is linked to the heating mechanism of O atoms, being much more important at higher pressure (Figure 5.9). When this term is not significantly high, it takes more time to the cooling terms to balance the small heating term, prolonging the transient duration at lower pressure (blue lines) until reaching a steady lower value. Moreover, since the droplet's partial pressure and enthalpy of vaporization are important parameters of the evaporation term (Equation 5.5 and 5.6), it explains the difference in droplet temperature between methanol and PG. Evaporation is much more efficient in methanol with the higher droplet pressure and lower enthalpy of vaporization, leading to a more efficient cooling of the droplet and hence resulting in lower temperature values than PG.

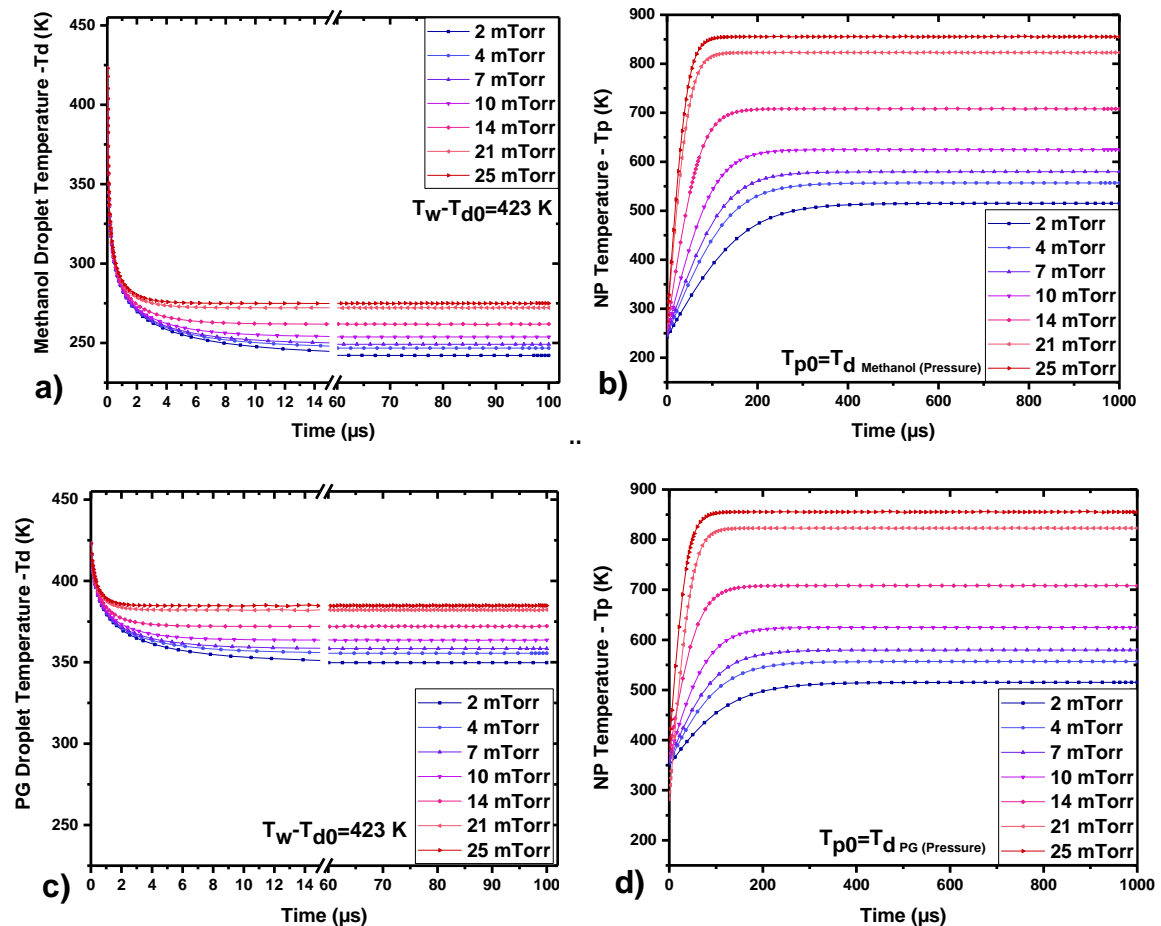


Figure 5.11: Temperature evolution versus time using the transient energy balance equation a) for a 50 μm in initial methanol diameter droplet (an axis - break has been used, to given an emphasis at the transient temperature during the first μs .) and b) for a single 5 nm in diameter NP inside the O₂ plasma. c) For a 50 μm in initial PG diameter droplet and d) the 5 nm NP.

For the TiO₂ NPs, this evaporation term does not exist. Since they are in a solid state and not in liquid, evaporation and condensation are removed from the equation. If we would imagine the NPs floating in the volume, the cooling term is only the one of the radiation and gas conduction, terms much smaller compared with the droplet evaporation/cooling term. Hence, we see in Figure 5.11b,d that the NPs are heated up. In addition, we see that their steady temperature is much higher for higher pressure thanks to the higher energy flux coming from the O atoms as explained in the comment of Figure 5.8. These calculations highlight how determining it would be to remain at low pressure if the objective is to preserve the initial NPs and avoid any annealing effect that could lead to any sintering of an assembly of NPs or a modification of the crystalline nature of the anatase. Finally, we observe that the time needed to reach steady state for the solid particles is much higher than the one of the liquid droplets having values between 100 and 400 μs. From these plots, the difference between the initial temperature of the NPs that originated from the Methanol droplet and the one originated from the PG droplet does not appear to alter the final steady state temperature of the NPs. A small difference might be observed between the transient time of Figure 5.11b and d. It seems for example that due to the lower cooling effect of PG in the case of 2 mTorr for example, the 349 K of steady state being the initial of the TiO₂ NPs lead to a smaller transient time (~350 μs) than the one observed in Figure 5.11b (~450 μs). This could be explained by this initial value being closer to the steady state.

The results obtained from this Section can be of great importance for our experimental strategy. Several factors have been identified that play a key role on the droplet evaporation, such as the solvent volatility, the plasma pressure and the wall temperature. We have seen that the solvents existing in our colloidal solution (PG and PC) are in the worst-case scenario in terms of droplet lifetime although they are very important for the stability of the monodispersed TiO₂ NPs lab-made colloidal solution. A hypothetical colloidal solution of TiO₂ NPs with a very volatile solvent such as methanol, could also not be an ideal candidate as it could hypothetically lead to a fast vaporization of the solvent letting the NPs trapped in the sheath or being discarded by the pump before reaching the substrate. One solution would be to try to dilute the existing colloidal solution with these more volatile solvents, being cautious enough to not perturb the stability of the colloidal solution. Another crucial parameter is the plasma pressure. As observed, above ~14 mTorr, the droplet lifetime for all the solvents decreases significantly. On the other side though, this increased pressure leads to higher NPs temperature, risking affecting the NPs size (sintering due to high temperature, or by enlarging the anatase nano-crystallite as seen in Chapter 3). Finally, in the case when TiO₂-SiO₂ NCs will be created in Chapter 6, higher pressure is not suitable, as the O₂ plasma dissociates the HMDSO molecules less efficiently. This less efficient plasma could degrade the quality of the inorganic matrix. Hence, it is obvious that the selection of the experimental conditions should be done carefully to address all these facts.

5.3 Deposition of the TiO₂ NPs inside the O₂ ICP plasma reactor: a first approach

Initially, the experiments were conducted using the as-synthesized colloidal solution of propylene glycol and propylene carbonate containing TiO₂ NPs (described in Chapter 2). This liquid was sprayed through the liquid dozer (Kemstream injector) placed in a 45° angle to the perpendicular, targeting towards the substrate. The reactor used for the injection of the colloidal solution and the creation of TiO₂ NPs thin films through this original approach was explained in detail in Chapter 2. O₂ was used as a working gas from the top of the Inductively Coupled Plasma Source, which was diffused inside the stainless steel diffusion chamber, where the substrate is located. The O₂ flow rate was set at 24 sccm to maintain a pressure of 3 mTorr.

The heating wire connecting the injector to the diffusion chamber was not used and therefore the droplets were produced at room temperature. The pulsing characteristics of the injection system were set at a frequency of 0.5 Hz and pulse duration T_{ON}=2 ms which led to a mass rate of 4.66 mg/injection which is translated in 69.9 mg/min (one injection every 2 seconds). The total duration of the injection was 22 minutes. During the injection, the pressure was varied between 18-20 mTorr (much higher than 3 mTorr) and drops with small sparks were evidenced with a naked eye through the chamber window. Before the deposition, O₂ plasma only was carried out for 30 minutes, in order to induce a steady plasma state and heat the substrate holder. After the deposition, during O₂ only plasma post-cleaning, OES indicated high amount of contamination (CO, OH, H Balmer lines with high emission intensities) for 4 minutes. In addition, during this time the pressure remained in high levels ~8 mTorr contrary to 3 mTorr usually measured in such conditions. After the termination of the experiment the base pressure remained in higher levels than usual (10⁻⁴ mbar contrary to 10⁻⁶ mbar usually observed as a base pressure). These observations indicate a severe contamination due to the injection of liquid in the reactor.

In Figure 5.12, the SEM characterization of the resulting films are gathered. From the low magnification image (Fig. 5.12a), a non-homogeneous deposition appears revealing some thick (flake-like) structures and micro- to millimetric-large imprints of dried droplets. The secondary electron image (Fig. 5.12b), indicates that these structures are cracked areas. Due to charging effect, the high magnification image of Figure 5.12c, led to a low-resolution image. Concerning the cross section, as shown in Figures 5.12d,e,f, a significant variation in thickness occurs, ranging from 100 to 300 nm, as a function of the chosen area. These variations are related to the flake-like structures of figure 5.12a. Nevertheless, from the high magnification of Figure 5.12f, the nanostructured morphology is clearly identified.

The results obtained from Figure 5.12, indicated that injecting the liquid droplets at room temperature leads to the deposition of large droplets in the micro-

and millimeter range, which have not sufficiently been evaporated during transport. This leads to the deposition of thick and cracked film as the droplets evaporate fast on the substrate. It has been reported by several authors that the fast drying of sol-gel films can induce cracking of the film.[33–37] Xu et al. [36] explained that the fast drying of the sol gel causes fast reduction of its volume generating strong stress in the drying film. If this stress is higher than the strength of the material, cracks are created. Finally, Kappert et al. [37] investigated the thickness dependency of the mechanical stress induced by fast drying and deduced the critical thickness upon crack-free films based on the energy released rate.

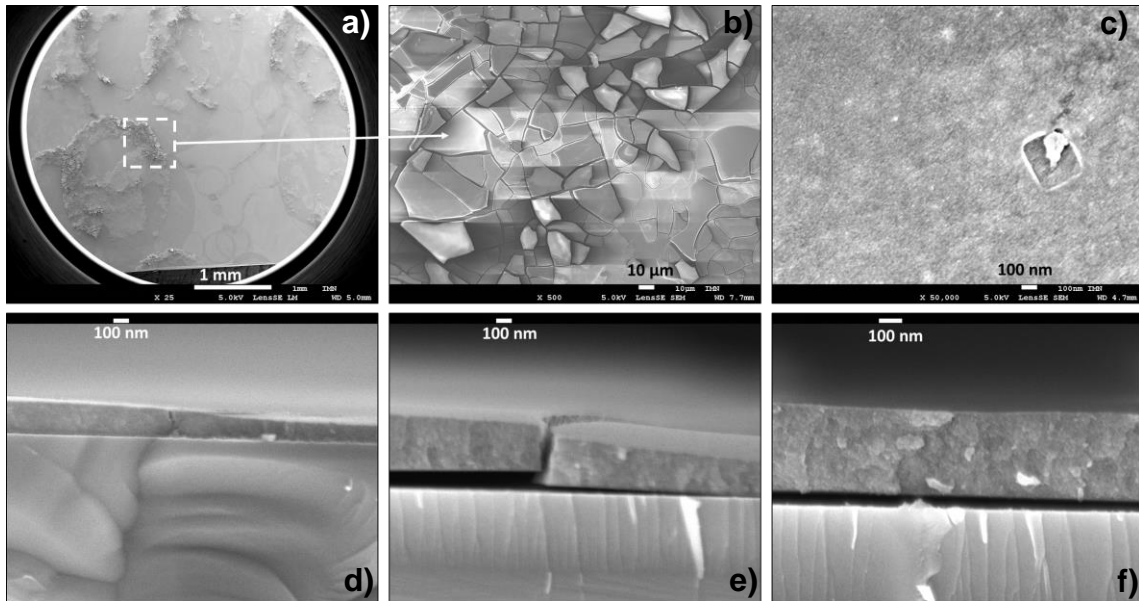


Figure 5.12: SEM images of the deposited film with a heating wire of 25°C. a) Low magnification, b) secondary electron and c) high magnification secondary electron surface view. Cross section images d, e, f) in different magnification and areas.

Similar mechanisms seem to be involved during this experiment. In addition, we evidenced indications of contamination in the reactor due to the liquid injection. Based on the theoretical calculations of Section 5.2.3, it is shown in Figure 5.10 that the droplet lifetime significantly decreases for higher wall temperatures. Hence, we conclude with this first experiment that improvement in the efficiency of evaporation has to be performed.

5.3.1 Importance of the heating wire temperature on the deposited TiO₂ thin films

In this section the heating wire surrounding the pipe that connects the injector with the reactor chamber is set at 100°C. Figure 5.13 shows the injection of the colloidal solution in the same experimental injection conditions as in the beginning of Section 5.3, with the heating wire set at 100°C. Indeed, in this case, from the low magnification image (Fig. 5.13a), the flake-like structures are less visible with some

cracks observed on some remaining dried droplets but whose sizes are now in the sub-millimeter range only (Fig. 5.13b). In the same manner, for these domains, the high magnification captures reveal the charge effect associated with the relief of the film (Fig. 5.13c). The high magnification image of Figure 5.13d was consequently recorded from an area far from the dried droplet domains. The structure of the nanoparticles seems rough, with structures inducing rough patterns and some possible agglomerations. The variation of the thickness of the deposited film is much more prominent in the cross-section images of Figure 5.13e and 5.13f where the thickness can vary between 400 nm and 1400 nm. As in Figure 5.12f, the nanostructure morphology of the cross section is also identified.

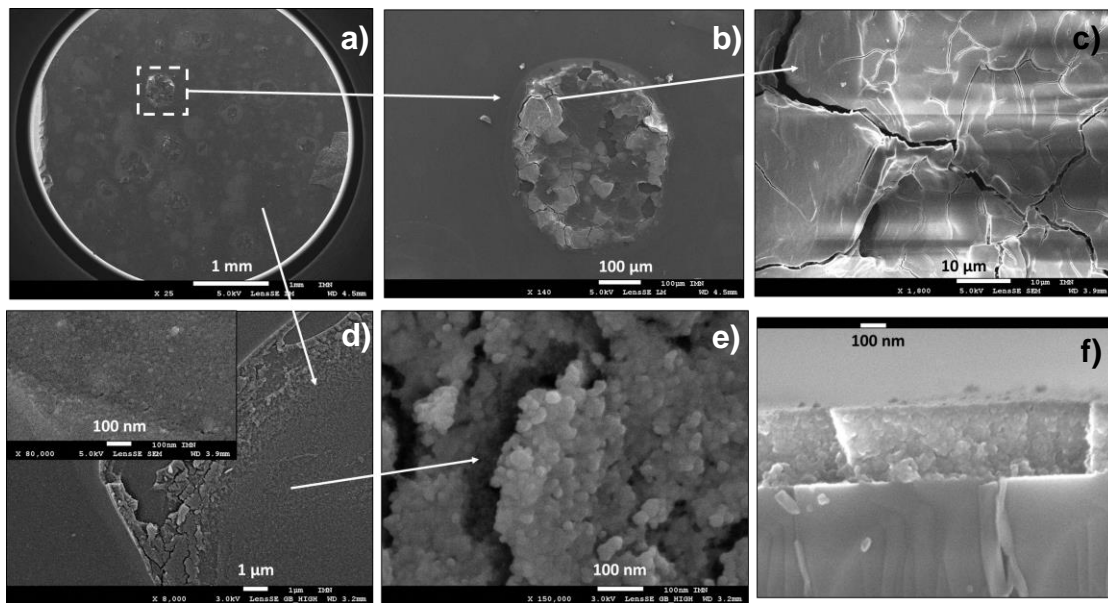


Figure 5.13: SEM images of the pristine deposited film with a heating wire of 100°C. a) Low magnification, secondary electron at b) low magnification and c) focusing on the dried droplet area. d) Low magnification image focusing on the smooth area in-between the structures with a higher magnification (x80.000) image as an inset and e) very high magnification (x150.000) secondary electron surface view focusing to the nanodomains. f) Cross section images of high magnification images.

Finally, in Figure 5.14a, the AFM scan on 1 μm x 1 μm is given. It appears rough, with large domains and its roughness was found at Rq (RMS)=5.5 nm. The produced histogram of this mean size distribution is given in Figure 5.14b. The mean domain size for this case was found at 33 nm and a standard deviation at 11 nm. From the inserted photograph in the plot, the inhomogeneity of the deposition is obvious even with a naked eye, as droplet-like patterns are identified.

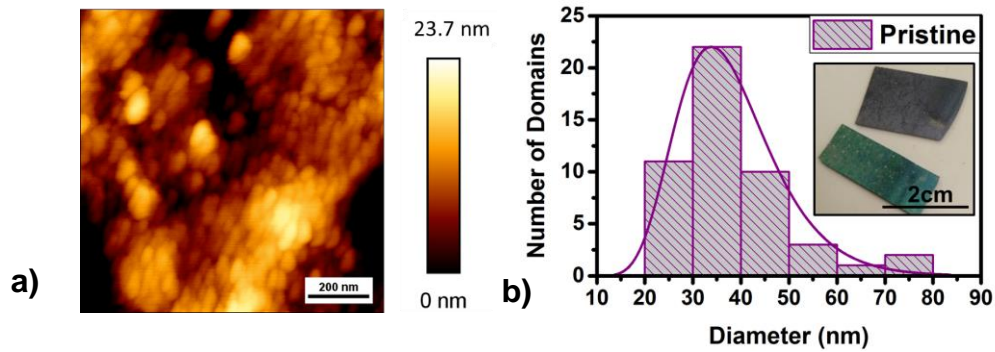


Figure 5.14: a) AFM scan (1 μm x 1 μm) and b) mean size distribution of the rounded domains based on this AFM scan. As an inset the photogram of this film is given.

As the optimization of the injection and deposition process will be studied in the next sections, this specific film will be denoted as Pristine (pristine conditions regarding heating wire and solvent).

5.3.2 Impact of the liquid injection parameters on the deposited TiO₂ thin films and the low-pressure system

As explained in Section 5.2.2.1, the injection of colloidal solution inside the low-pressure reactor requires a positive pulse to activate the injector. In the specific system, the frequency that controls the pulse generation can be regulated. For the comprehension of the impact of this frequency on the deposited films and the low-pressure system a comparative study was conducted for different total durations of deposition. As the frequency of the pulsing injection was increased, the total duration of the deposition was decreased, to compensate for the higher injected amount of solvent when the frequency is higher. Consequently, for 0.1 Hz the total deposition was at 42 minutes, for 0.2 and 0.3 Hz at 32 minutes, and finally for 0.4, 0.5 and 0.6 Hz at 22 minutes. In Figure 5.15, the top surface of the deposited films with varying injection frequency are displayed (low magnification images). In all cases, droplets on the surface are observed with various sizes. For low frequencies ($f=0.1-0.3$ Hz), some small droplets appear and the surface seems more homogeneous. For higher injection frequency, the droplets are identified larger, more numerous and the homogeneity of the surface is rather degraded. This means that for higher frequencies either larger droplets are produced close to the injector or more droplets are assembled on the substrate surface.

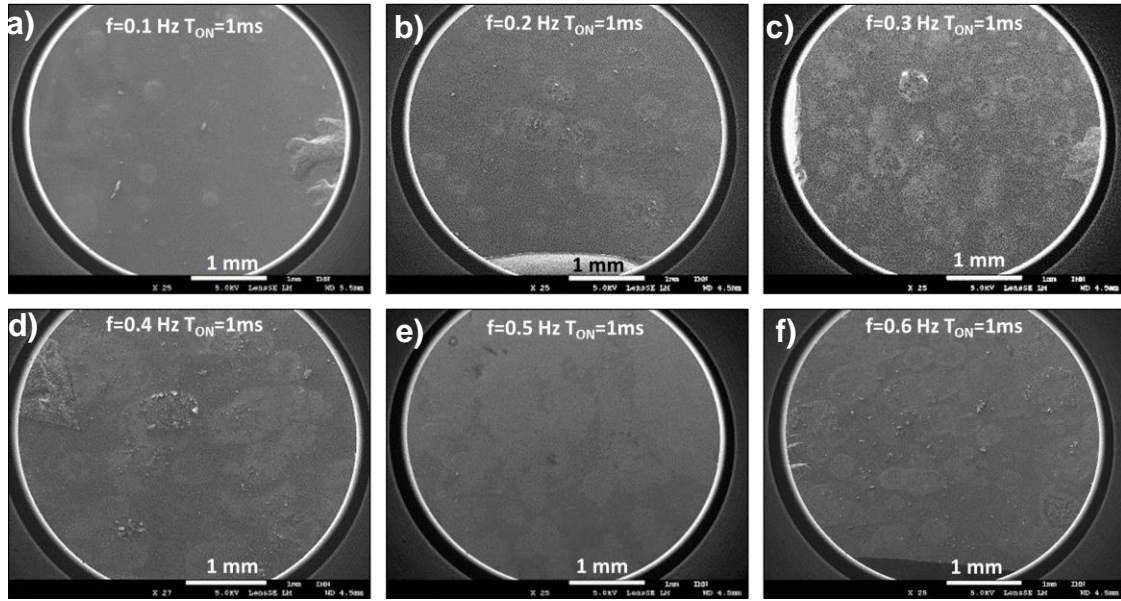


Figure 5.15: Low magnification SEM images of the films deposited at $T_{ON}=1$ ms and a) at 0.1 Hz for 42 minutes, b) at 0.2 Hz for 32 minutes c) at 0.3 Hz for 32 minutes d) at 0.4 Hz for 22 minutes, e) at 0.5 Hz for 22 minutes and f) at 0.6 Hz for 22 minutes. The pressure variation for each case is given in the second and third column of Table 5.4.

As the injected colloidal solution enters the low-pressure system, it evaporates leading to a sudden increase in the pressure of the reactor, that was detected from the gauge and read on the go. Depending on the injection parameters, this increase follows a different pattern. The observed pressure variation is given in Table 5.4. For lower frequency (0.1-0.2 Hz) and $T_{ON} = 1$ ms, when NO PULSE is applied on the injector (T_{OFF}) and hence no liquid is injected in the reactor ($T_{OFF} = Period - T_{ON}$), the pressure reaches the steady state pressure at 3 mTorr. Substantially, as the frequency increases and therefore the time between two pulses decreases, the pressure during the NO PULSE time (T_{OFF}) is at 12 mTorr reaching values up to 29 mTorr when the PULSE (injection) comes. This effect is reasonable without being favorable, as much more colloidal solution is injected and the system does not have enough time within the pulses to retrieve its steady state. Some experiments increasing the duration of the pulse (T_{ON}) were attempted and were rejected providing the prohibitive pressure variation given in Table 5.4, which is explained as more colloidal solution is injected than when $T_{ON} = 1$ ms, releasing more molecules to the vacuum system.

The observed pressure variation was for this study a significant aspect for the selection of the injection parameters. From a technical point of view, a rapid increase of the pressure each time liquid is injected is not a good qualification for the lifetime of the turbomolecular pump. Moreover, the plasma stability due to the ongoing pressure variation is altered. In addition, it has been shown by previous studies of the group, and also indicated in Table 5.3, that an increased pressure would lead to different plasma conditions. In these conditions, the reduced electron density and

electron temperature lead to less efficient dissociation of the HMDSO molecule, for the case of the TiO₂-SiO₂ NCs films (shown in Chapter 6). This less efficient plasma could degrade the quality of the inorganic matrix. On the other side, a positive observation regarding the higher-pressure levels, from the results in Section 5.2.3 and in detail in Figure 5.8, would be that in this case the droplets evaporate faster. At the same time, if the single NPs would exist in these higher-pressure levels, higher heat fluxes would be induced leading to the increase of the temperature. Hence, it is obvious that optimum injection conditions are needed, to address all these facts.

Table 5.4: Pressure variations for T_{ON} equal 1 and 2 ms for different injection frequencies.

Frequency (Hz)	Pressure (mTorr)			
	T _{ON} = 1 ms		T _{ON} = 2 ms	
	PULSE (T _{ON})	NO PULSE (T _{OFF})	PULSE (T _{ON})	NO PULSE (T _{OFF})
0.1	11	3	19	3
0.2	17	3	-	-
0.3	20	9	-	-
0.4	29	12	40	25
0.5	25	17	42	31
0.6	35	29	-	-

5.3.4 Plasma Characterization during Injection of the TiO₂ Colloidal Solution inside the O₂ ICP Reactor

As shown in Section 5.2.3, the evaporation rate of the droplet is driven by the plasma species and the nature of the solvent. Several works that focus on the complex dusty plasmas have been rigorously studied in the past. A most challenging study would be to investigate how a droplet that evaporates in the plasma can affect the latter [8].

Since it was found that the pressure varies as the colloidal solution is injected and is being evaporated inside the plasma, optical emission spectroscopy (OES) was used. Inside the O₂ gas injected, 5% Argon was added, a relative small amount, in order to not affect the experiment but assist this measurement[38,39]. Using this plasma characterization technique and a monochromator, we followed specific emission intensities. Hence, in Figure 5.16a, the time evolution of the CO (at 297.7 nm), OH (at 306.4 nm), H_δ (at 410 nm), O (at 394.5 nm) and Ar (at 419.8 nm) line intensities is plotted. These emission intensities were measured in a different time, not simultaneously and the data were aligned using the OriginPro software. In this study, the injection frequency was set at 0.1 Hz (T=10 s) and the T_{ON} at 1ms. The moment of the pulse and therefore of the injection, is given with the yellow lines. In alignment with the pressure variation (shown in the previous section), we observe in Figure 5.16 variation on the emission intensities. These variations have higher

duration (seconds range) than the residence time in the reactor, which is in our case 130 ms (based on the specifications of our pump), and therefore need to be taken into consideration.

The first information from Figure 5.16a, originates from the Ar emission intensity (blue line). In that case, when the injection of liquid takes place inside the low pressure O₂ plasma, its intensity instantly decreases. During the T_{OFF} (after the injection), the emission intensity increases again reaching the steady state value before the next injection. This decrease in the intensity of Ar (by a factor of about 10), is expected to be due to the pressure increase. Indeed, when the pressure is increased, the electron temperature is decreased (T_e) which leads to a decrease in the Ar density. To confirm this and go further, in Figure 5.17 the emission spectrum of O₂ plasma between 360 and 440 nm is given for a pressure at 25 mTorr and 3 mTorr. As observed all the intensities at the higher pressure of 25 mTorr are decreased in comparison with 3 mTorr, which is due to the electron temperature decrease from 4.5 eV to 2 eV (data obtained by previous studies and already presented in Table 5.3 of Chapter 5). The ratio between the Ar line intensities at 3 mTorr and 25 mTorr is found from this Figure at ~10, which is totally consistent with the intensity decrease of Ar line observed upon the injection of the solution.

In addition to this, for each injection, a decrease of the O emission intensity and an increase of CO, OH and H_δ emission is observed. A few seconds after the injection has passed, there is an increase of both Ar and O reaching their steady state. In a similar manner, after the injection the emission intensities of CO, OH and H have a descending pattern. The fast decrease and then increase observed on this emission intensity upon injection could be linked with transient effects caused by the abrupt liquid injection and pressure increase.

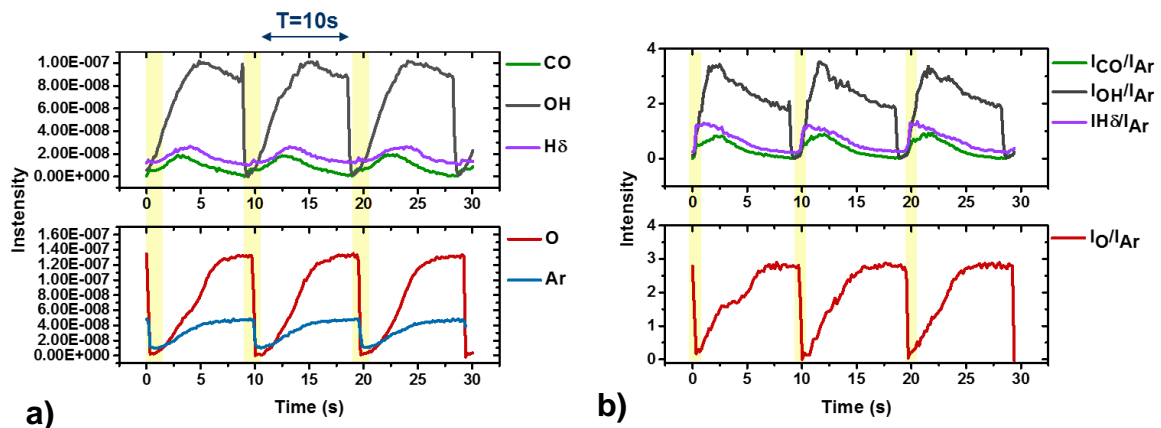


Figure 5.16: Emission Intensity of the a) CO (at 297.7 nm), OH (at 306.4 nm), H_δ (at 410 nm), O (at 394.5 nm) and Ar (at 419.8 nm) and b) intensities after normalization with Ar line intensity.

From these results, it appears that during the injection of the colloidal solution containing the NPs inside the low-pressure system, two main effects take place. First,

the variation in pressure (shown in the previous section) and second, the chemical interaction of the organic solvent with the oxygen plasma species. To acquire the information and evolution of the concentrations of O, CO, H and OH species, we will divide the emission intensities of O, CO, H and OH plotted in Figure 5.16a by the one of the Ar line (actinometry).

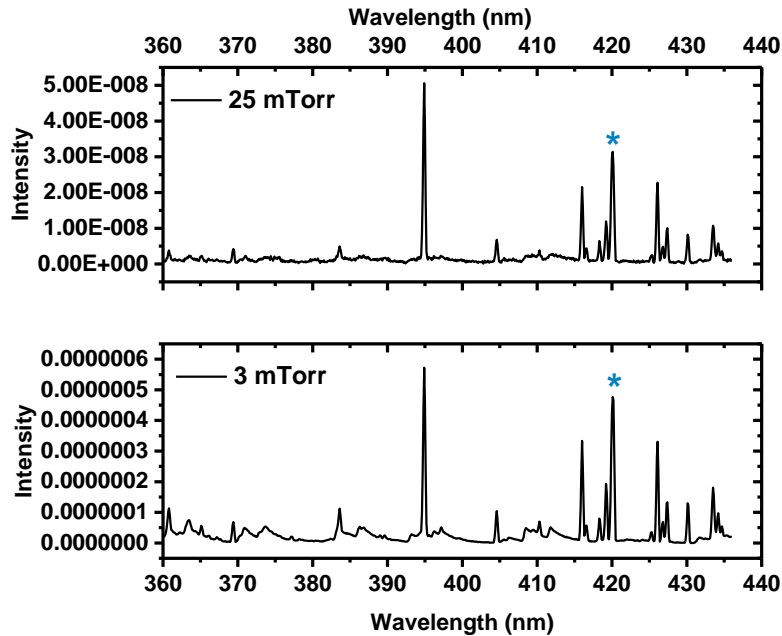


Figure 5.17: Emission spectrum for the wavelength range between 360 and 440 nm for 25 mTorr (top-side plot) and 3 mTorr (bottom side plot). Blue star for Ar emission intensity.

Actinometry relies upon normalization of the emission intensities to that from an inert gas. Since the working gas of the plasma is 95% O₂ and 5% Ar, Ar was used as actinometer. The actinometry technique[40] simply consists in normalizing the emission intensity I from a radical or molecule (I_X) to that from an inert gas such as Ar (I_{Ar}), and provided some hypotheses are fulfilled (see Annex C), the line intensity ratio I_X/I_{Ar} is proportional to the ratio of the concentrations of X (n_X) and Ar (n_{Ar}) in their ground state: $n_X/n_{Ar} \propto I_X/I_{Ar}$. In other words, dividing by the Ar line allows to get free of the variations of the electron density and electron energy distribution function due to the increase in pressure and gas composition upon the injection of the solution. We are nevertheless aware that we only partially get free of the electron density and energy distribution function and the normalized intensity I_X/I_{Ar} has to be considered only as a first approximation of the variation of the concentration of X. In actinometry measurements, the Ar line at 750 nm [18] is generally used. Nevertheless, in the case of these time resolved measurements which require the successive measurements of different lines from Ar, O, CO, OH and H as a function of time, we chose lines which could all be observed with the same grating and since OH can only be observed at ~ 310 nm, we chose the UV-blue grating (200-500nm).

According to previous studies[41] one can consider as a first approximation that I_O/I_{Ar} is proportional to O density, I_{CO}/I_{Ar} to CO density, I_H/I_{Ar} proportional to H density. In the case of OH, excited OH radicals can be created by electron impact from OH radicals and H₂O molecules, which makes the interpretation of I_{OH}/I_{Ar} more complex although clearly related to OH and H₂O.

A strong (and fast) decrease of the O density (proportional to I_O/I_{Ar}) is observed in Figure 5.16b which is almost cancelled (without reaching 0) due to the oxidation reactions upon injection of the solvent in the oxygen plasma. In addition to this, it is observed that I_{CO}/I_{Ar} , I_H/I_{Ar} , I_{OH}/I_{Ar} are increased upon the injection, which can be related to the formation of CO, H, OH (H₂O) related to the by-products of the oxidation reactions. After the injection, a different time is needed for I_{CO}/I_{Ar} , I_{OH}/I_{Ar} , I_H/I_{Ar} to reach their steady state value. Regarding the O density, approximately 6 seconds are needed whereas for the case of CO and H approximately 8 seconds. Finally, for I_{OH}/I_{Ar} it appears that the time duration between two injections (10 seconds), is not enough to reach the steady state. An accumulation of OH and/or H₂O takes place, which is likely to be linked to the accumulation of H₂O in the reactor.

From these results, it appears that the evaporation of solvent molecules increases the pressure of the reactor. The increase in pressure also results from the interaction of solvent molecules with the oxygen atoms leading to their oxidation. In addition to this, it appears that the O atom density returns to steady state faster than CO, H and OH (H₂O) indicating an accumulation of the later. The longer time needed for these species to be eliminated is coherent with the theoretical values for the PC and PG droplets lifetime. In detail, from Figure 5.8 for PC and PG the droplet lifetime is found at 9 seconds for 3 mTorr which decreases down to 1 second for 25 mTorr.

Based on the finding of these preliminary experiments in Section 5.3 and the theoretical results from the computational study in Section 5.2.3, in the next Section an optimization strategy will be followed, in order to improve the deposition and distribution of the TiO₂ NPs.

5.4 Optimization Strategy – Improvement on the deposition of the TiO₂ NPs

In Section 5.3, a first attempt to inject the colloidal solution inside the O₂ low pressure plasma system was established. In accordance to the theoretical results, it was shown that the heated wire temperature surrounding the pipe that connects the injector with the reactor chamber affects the homogeneity of the deposition, as it assists the evaporation of the droplets. The injection frequency on the other hand, was found mainly to affect the pressure. This is justified, as for higher frequency, liquid is injected more frequently. For the selection of the optimum injection frequency and T_{ON} time several parameters need to be considered. First, in order to avoid the accumulation of liquid inside the reactor one could consider the theoretical results

given in Figure 5.8 of Section 5.2.3. In this for the case of PC or PG the droplet lifetime would be around 8 to 9 seconds, for wall temperature at 423 K. This is an indication that within the injection pulses 8 or 9 seconds would be needed. Second, using the OES results, we could see that for the case of oxygen approximately 6 seconds are needed to retrieve its steady state. Hence, a good frequency selection could be 0.1 Hz as injection happens every ten seconds. Unfortunately, as seen in Figure 5.13, the deposition in that case does not appear sufficient. Therefore, in order to evidence and characterize injected NPs a slightly higher frequency between 0.3 Hz and 0.5 Hz was selected. Regarding the duration of the pulse, $T_{ON}=1$ ms was chosen as it leads to less liquid injected and a lower variation of the pressure (Table 5.4) than the $T_{ON}=2$ ms.

The aim of this chapter is to achieve the direct injection of liquid that contains NPs inside the low-pressure O₂ plasma. Using the results of the theoretical calculations in Section 5.2.3 and the preliminary results of Section 5.3, in this Section we will follow a specific optimization strategy. Since we chose to work with slightly higher frequency than 0.1 Hz, some other aspects of this process need to be improved to facilitate the evaporation of the droplets and the homogeneous distribution of the NPs on the substrate. In Figure 5.8, we show the impact of the solvent enthalpy on the droplet lifetime. Water, ethanol and methanol are solvent with significantly lower droplet lifetime, that could solve the problem of droplet formation and flake patterns on the substrate. Hence, in Section 5.4.1 the dilution of the as-synthesized colloidal solution with these more volatile solvents is attempted. Comparing the deposits after this dilution, will allow us to decide which dilution is more appropriate for our approach. Keeping the optimum dilution and bearing in mind the wall temperature impact of Figure 5.8 as well as the velocity of the droplets discussed in Section 5.2.2.1, we will move to the second optimization step. This is given in Section 5.4.2 where the impact of the system geometry and temperature is studied. Finally, as a third step, an iterative mode of injection will be proposed, in order to give to the system time to come back to steady state, both in terms of droplet evaporation time (droplet lifetime from the Section 5.2.3) and plasma species (OES). Hence, in Section 5.4.3 the mode of operation is varied by adjusting even more the injection parameters of the colloidal solution.

5.4.1 Dilution with more volatile solvents (Water, Ethanol and Methanol)

In Section 5.3.2, the droplet lifetime was calculated and plotted for PG, PC, water, ethanol and methanol. Based on these theoretical findings, experimentally, the dilution (volume ratio 3:1, dilution by a factor of 4/3) of the as-synthesized colloidal solution was attempted, since both propylene glycol and propylene carbonate (the solvent of the as-synthesized colloidal solution), are non-volatile solvents, causing the non-homogeneous droplet-like deposition on the substrate.

In Figure 5.18, the three cases of dilution between the as-synthesized colloidal solution and water (Fig a1, a2), ethanol (Fig b1, b2) or methanol (Fig c1, c2) are given.

The frequency was set at 0.5 Hz and the total deposition time was set at 30 minutes. For the dilution with water the mean droplet size was found from 35 measured droplets at 104 μm with a SD at 44 μm . For the dilution with ethanol 35 measured droplets at 123 μm with a SD at 40 μm . Finally, for the dilution with methanol for the same number of droplets the case is much more improved, as seen also in Figure 5.18c1, having a mean droplet size at 42 μm with a SD at 16 μm .

From the high magnification images in secondary electron mode, the nanostructured morphology of the TiO₂ NPs film is obtained for all the dilutions. Based on these results, and especially based on the improved/decreased droplet distribution, the next optimization step was carried out using methanol. Another important aspect that helped in this selection was based on the solvent characteristics of Table 5.2 and the theoretical results obtained through the calculations on Section 5.2.3, it is clear that the enthalpy and the vapor pressure of methanol leads to the fastest evaporation and the lowest droplet lifetime. Finally, we could imagine a droplet containing both methanol and PC/PG solvents. No data regarding the ternary phase diagram of these three solvents were reported to ascertain their miscibility or any formation of azeotropes, so, in a first approximation, we can consider that the methanol or methanol-rich mixing would evaporate fast leading to the fraction of even smaller droplets to interact with plasma and be finally deposited on the substrate. Finally the dilution (PC:PG:Methanol with the following volume fractions of 20.25:54.75:25) was selected in order to avoid the destabilization of the colloidal solution and achieve a slightly lower number of NPs in each droplet.

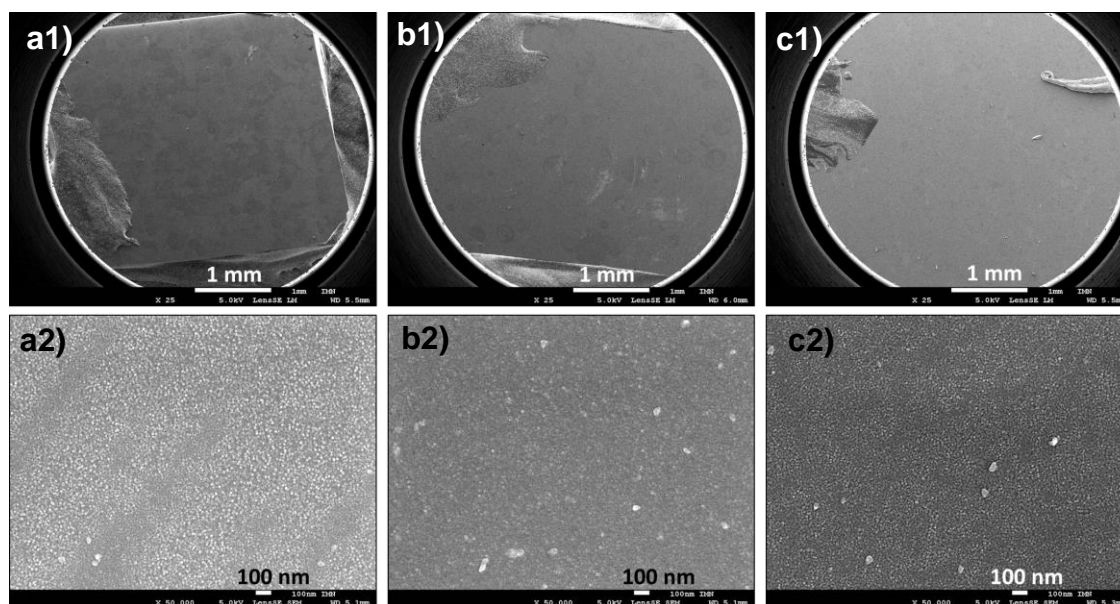


Figure 5.18: Low magnification images of the deposited film with a1) water, b1) ethanol and c1) methanol dilutions. Secondary electron high magnification images (x50.000) of the deposited NPs film with a2) water, b2) ethanol and c2) methanol dilutions.

5.4.2 Effect of system Geometry and the Temperature

The distance between the droplets production and the substrate can influence the deposition homogeneity as it had already been studied by Ogawa et al.[1] and was further explained in Section 5.2.2.1. The travel speed of these droplets for a similar configuration was estimated at 13 m s⁻¹. With a velocity like this, even for the best-case scenario (T_w=423 K, 25 mTorr, methanol) the droplet lifetime reaches a value of 0.73 seconds. Supposing that our droplet velocity is at 13 m s⁻¹, the distance needed for the droplets to fully evaporate would be 9.49 m. Since this practically was not possible, the extension of the heating pipe by 15 cm was attempted. This pipe extension provided 11.4 ms more time to the droplets to interact with the heated environment and evaporate before reaching the substrate. This value is increased compared to the initial one for a smaller heated pipe (3.9 ms) but it remains in much lower values compared to the theoretical results of Section 5.2.3. This Figure also indicated that the higher the wall temperature is, the lower the droplet lifetime becomes. Hence, at this optimization step, in addition to the pipe extension, the temperature of the heating wire surrounding this longer pipe was even more enhanced from 100°C to 150°C. The injection parameters were set at f=0.5 Hz and T_{ON}=1 ms for a duration of 50 minutes. This film will be notated as the Optimized one, in order to compare it with the Pristine one studied in Section 5.3.1.

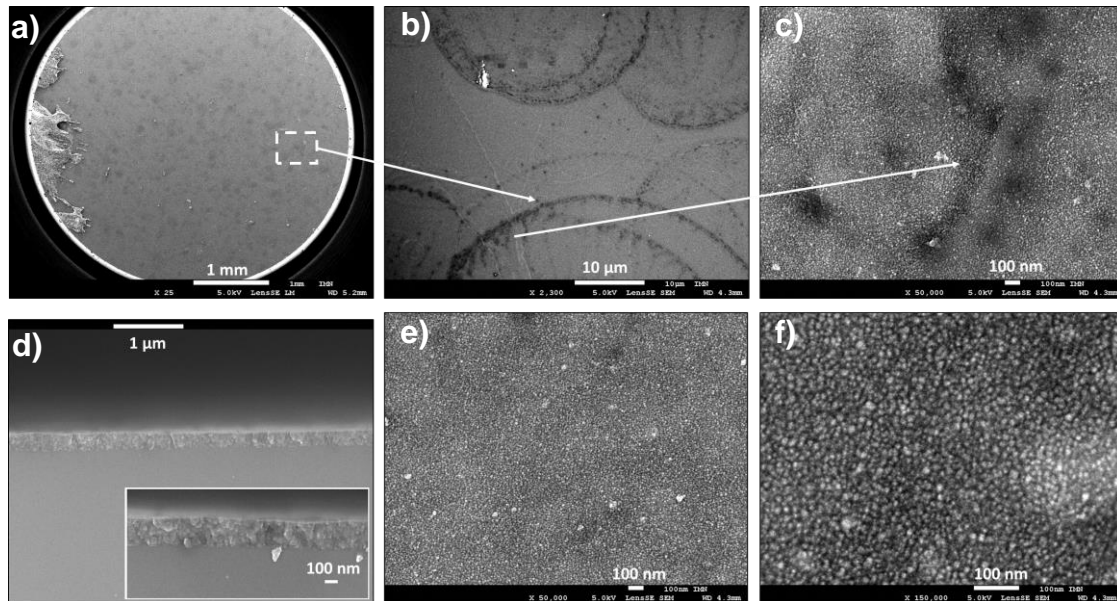


Figure 5.19: SEM images of the optimized deposited film with a heating wire of 150°C, diluted solvent with methanol and an extended heating pipe. a) Low magnification, b) secondary electron at b) low magnification and c) focusing on the dark lines. Cross section images of the TiO₂ NPs thin film .d) High magnification secondary electron surface view at e) x50.000 and f) at x100.000.

The surface view and cross section of the resulting nanostructured TiO₂ film is given in Figure 5.19. The low magnification images reveal a rather homogeneous

deposition, with only some small rounded shapes. With the secondary electron SEM images on Figure 5.19b, c focusing on these patterns, we can identify that these rounded shapes appear to present a coffee ring pattern. Along the ring a darker contrast in comparison to the total ring appears, indicating indirectly the possibility of having more carbon contamination on these areas. Figure 5.19d, reveals a homogeneous cross section in this area having much smaller variation in thickness (210 nm with standard deviation-SD at 20 nm) compared with what was previously shown for the pristine sample. Finally, high magnification images (Fig. 5.19e, f) reveal a homogeneous local nanostructuration, without rough structures as in case of the pristine sample (Section 5.3.1) and smaller possible agglomerations.

The AFM scan of the optimized sample (Figure 5.20), has small domains and with rounder shape. The reduced Rq (RMS) roughness was found having a value of 3.2 nm, indicating a low roughness. Using the specific AFM Image, the mean domain size of 50 measurements was found at 21 nm with a standard deviation of 8 nm. In Figure 5.20b, the histogram of this size domain distribution is given along with an inserted photograph of the samples. From the inserted photograph the homogeneous and uniform film of NPs is observed and the contrast with the uncoated part is seen.

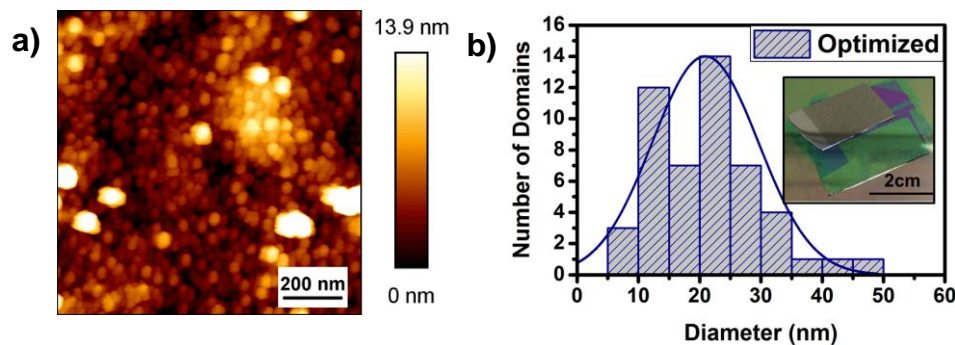


Figure 5.20: a) AFM scan (1 μm x 1 μm) and b) mean size distribution of the rounded domains based on this AFM scan. As an inset the photograph of this film is given with a uncoated part for contrast.

5.4.3 Iterative Mode of Operation

In this study, during the deposition and optimization process, the pressure variation, the reactor contamination, the control of the deposition and the formation of homogeneous thin films were identified as key points for the qualification of this novel deposition technique. To satisfy further these requirements, the deposition rate should also be controlled. Due to the limitation of the liquid injector, this could be accomplished by reducing the injection rate to the minimum and consequently using 0.1 Hz. It has been shown also both theoretically in Section 5.3.2 and through OES that the 10 seconds between each pulse, in the case of 0.1 Hz, would be a good selection regarding the droplet evaporation and the stability of the plasma species. With this frequency indeed, the injection rate is reduced and as a result the amount of material deposited on the substrate is not high enough (Figure 5.15, Section 5.3.2) rendering

it more challenging to characterize it in the nanometer range. In order to have a process that will be versatile and low cost, the duration of the deposition should not be long. In an attempt to provide an optimum compromise, a different mode of operation was selected. According to that, we optimized a program including a sequence lasting one minute which is divided into two parts. The illustration of this operation is depicted in Figure 5.20. In detail, during the first part, N pulses of 1 ms ($T_{ON} = 1\text{ ms}$) each were triggered with a period of two seconds ($T=2\text{ s}$). Thus, after this first-time lapse, during the second part of the sequence, the valve of the injector remains closed. In this condition, the N max reachable within one minute is 30. This would mean that in a minute, 30 pulses are injected ($N=30 - \text{max}$) for the optimized film of Section 5.4.2. The sequence is repeated for a total duration of 150 minutes while having 24 sccm O₂ to maintain the O₂ plasma. Before the injection, the substrate was exposed to 30 minutes O₂ plasma to achieve a steady state reactor environment.

In detail in Figure 5.21a, is plotted the sequence corresponding to N=2 which means that two pulses were applied with a period of 2 seconds and $T_{ON}=1\text{ ms}$. This ON timeframe within the one-minute sequence, will be named Direct Liquid Injection-ON (DLI-ON). After this DLI-ON, the injection was set OFF and the O₂ plasma remained ignited (this timeframe is named as DLI-OFF). This would mean that in a minute (60 s), for 4 s the solution is injected and for 56 s the injection was OFF. In the same manner, in the second (Fig. 5.21b) case with N=5, the five pulses are injected with a frequency of 0.5 Hz, having a DLI-ON duration of 10 s (as $T=2\text{ ms}$) and a DLI-OFF duration of 50 s. Finally in the third case with N=10 (Fig. 5.21c), ten pulses were injected with a DLI-ON duration of 20 s and the injection was OFF (DLI-OFF) for 40s. Therefore, by increasing the amount of pulses, the amount of injected solution is increased in a minute. In this study, the results obtained with this mode of operation are compared with the optimized sample (Section 5.5.2), where the injection is not stopped. This would mean that the optimized film has N=30 within a minute sequence at 30×2 seconds equals to 60 seconds. Hence, for this case within the one minute sequence DLI-ON lasts 60 seconds and there is no DLI-OFF.

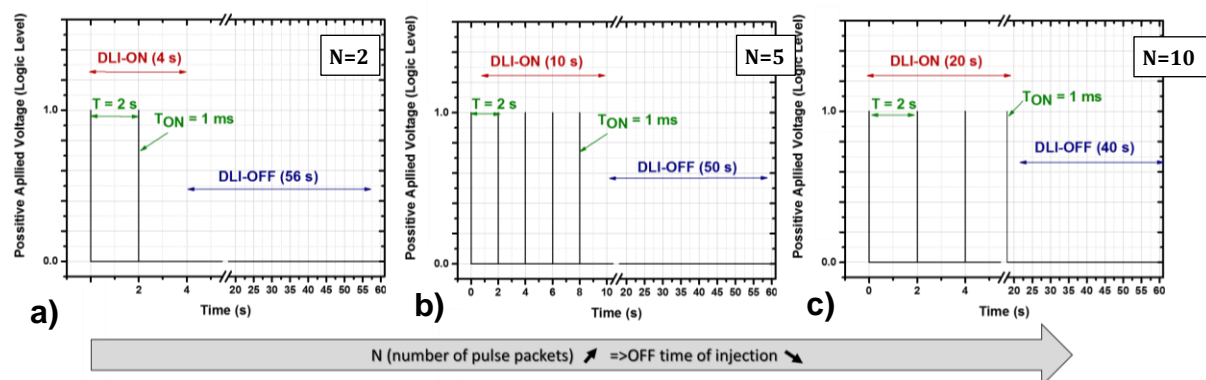


Figure 5.21: Injection procedure of the pulses applied on the liquid dozer in one minute for a) N=2, b) N=5 and c) N=10.

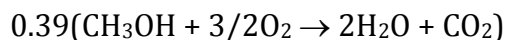
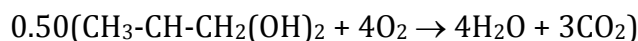
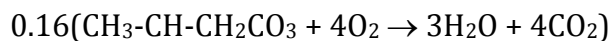
By weighing the flask containing the solution, the injected solution mass was estimated at 2.3 mg per injection. Based on this value, for the cases studied in this Section and the Optimized one (N=30) the mass rate per minute can be calculated as, $Mass\ rate = N * 2.3\ mg/inj$ and the total mass of injected solution (Total liquid mass) using the total time of injection (T injected total) as, $Total\ liquid\ mass = Mass\ rate * T_{injected\ TOTAL}$. Table 5.5 gathers the results as a function of N.

Table 5.5: Characteristics of the liquid injection elaborated with varying N.

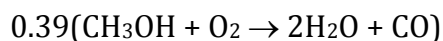
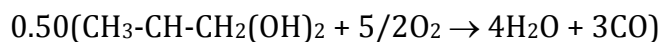
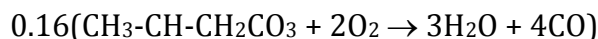
N	Mass rate (mg/min)	T _{injection} TOTAL (min)	Total injected liquid mass (g)	Pressure (mTorr)		Solution Molar flow rate (mmol min ⁻¹)	Molar flow rate of O ₂ required to oxidize (mmol min ⁻¹)		O ₂ molar flow rate / O ₂ required molar flow rate	
				PULSE	NO PULSE		CO ₂	CO	CO ₂	CO
2	4.66	150	0.70	16	3	0.07	0.23	0.13	4.3	7.4
5	11.65	150	1.75	16	3	0.17	0.58	0.33	1.7	3.0
10	23.3	150	3.50	20	3	0.33	1.16	0.67	0.9	1.5
30 (max)	69.9	50	3.50	20	6	1.00	3.47	2.00	0.3	0.5

During the injection, as mentioned previously, molecular species are added to the gas phase causing the pressure to increase, due to the evaporation of the solvent from the injected droplets. [1] This pressure was detected from the gauge and read on the go and its values are given in the fifth column of Table 5.5. PULSE corresponds to the time that a pulse is given by the injector and liquid is introduced whereas NO PULSE corresponds to time where no injection takes place i.e. in between the pulses. Their pressure results revealed that during the injection, the pressure increased instantly to a higher value. In between the pulses during the DLI-ON, the pressure was noted to come back to 3 mTorr. However, in order to steadily retrieve this 3 mTorr state once the DLI-ON timeframe was over, the system needed approximately two seconds. This was not the case for the N=30, where in this conventional pulsing mode the pressure between the pulses could reach only a value of 6 mTorr. This effect could be a presage of the decreased amount of injected solvent and in addition, of a contamination inside the reactor.

In a first approximation, without considering any further dissociation of the oxidation products, the quantity of O₂ required per minute to fully oxidize the solvent needs to be assessed to verify if these conditions are the optimal ones to limit the accumulation of species in the reactor. Since the initial PC/PG solution (for which x_{PC} equals 0.27) is diluted with MeOH in the proportion 75/25 in volume, the chemical composition of the injected solution is 0.16PC-0.50PG-0.39MeOH. The following equations gathered the quantities of O₂ necessary to oxidize the solvents as H₂O and CO₂.



Leading finally to $0.16\text{CH}_3\text{-CH-CH}_2\text{CO}_3 + 0.50\text{CH}_3\text{-CH-CH}_2(\text{OH})_2 + 0.39\text{CH}_3\text{OH} + 3.2\text{O}_2 \rightarrow 3.3\text{H}_2\text{O} + 2.5\text{CO}_2$. In case the amount of dioxygen is not high enough, CO instead of CO₂ as by-product has also to be considered, the equations are the following ones



Leading finally to $0.16\text{CH}_3\text{-CH-CH}_2\text{CO}_3 + 0.50\text{CH}_3\text{-CH-CH}_2(\text{OH})_2 + 0.39\text{CH}_3\text{OH} + 2\text{O}_2 \rightarrow 3.3\text{H}_2\text{O} + 2.5\text{CO}$.

Therefore, the final quantity of O₂ required to fully oxidize the injected solution as (H₂O and CO₂) and (H₂O and CO), is 3.2 and 2 moles of dioxygen per mole of solution, respectively.

From the mass rate reported in Table 5.5, the density ($d_{sol} = 1$) and the molar mass of the solution (69.76 g mol⁻¹), the molar flow rate can be calculated which is reported in sixth column of Table 5.5. In the same table, in the seventh column, the molar flow rates of dioxygen that would be required to fully oxidize as (H₂O and CO₂) and (H₂O and CO) are also given. From the standard flow rate (24 sscm) of O₂ the molar flow rate can be estimated to 0.99 mmol min⁻¹. Finally, the ratio between this experimental (available) O₂ molar flow rate and the former (required) ones is also given in the last column of Table 5.5. When this ratio is larger than 1, the quantity of O₂ is high enough to fully oxidize the amount of injected solution.

Considering the oxidation to lead to CO₂ or CO, the new iterative mode when the injection parameter N equals to 2 or 5, seems to be more favorable to fully oxidize the solution. For N=10, since the return to the initial pressure is achieved during NO PULSE, the ratio being 0.9 and 1.5 for CO₂ and CO, respectively tends to indicate that the amount of dioxygen is also sufficient, at least to oxidize as CO. Contrary to this, for the conventional pulsing mode (N=30), the two ratios are less than 1. This is coherent with the pressure remaining in higher levels than 3 mTorr during NO-PULSE. Based on these results it is possible to assume that for N=30 there is not enough oxygen available to oxidize the injected organic liquids, probably leading to accumulation of molecular species in the reactor, that need to be oxidized after each set of experiments.

Overall, this first approach only considers the quantity of the available molecules inside the reactor for one minute, without taking into account the

interactions occurring inside the plasma. However, it highlights that the iterative mode may be a good compromise.

Each of the films given in Table 5.5, were characterized by SEM (Figure 5.22a) and AFM (cross sectional profile, Figure 5.22b). Using the high magnification images of Figure 5.22a, we measured the diameter size of 50 domains using ImageJ and we plotted the histograms that are given in Figure 5.22c.

In Figure 5.22a, the SEM secondary electron images of the samples provided in Table 5.5 are gathered. The nanostructuring of the TiO₂ films appears in all cases. For N=2, the rounded domains observed in the image seem clearer than in the rest of the images as it is possible that they are more separated from each other. This effect could be linked with the rather low amount of injected colloidal solution possibly leading to a small thickness and a porous film. The mean domain size was found at 12 nm with SD of 2 nm. For N=5 and N=10 these rounded domains appear less separated with each other. The mean diameter for the N=5 case, was found again at 12 nm with a SD at 2 nm. For N=10, the mean diameter was found slightly shifted, at 14 nm with a SD at 2 nm and with a closer look at the histogram (purple pattern at Figure 5.22c), the size domains appear polydispersed. Finally, for N=30, which is the case analyzes in Section 5.4.2, the domains appear significantly smaller and homogeneously distributed, having a mean diameter size at 9 nm and a SD at 2 nm.

In an attempt to acquire the roughness of these films, AFM was used with the obtained roughness evolution for one scan given in Figure 5.22b. The R_q (RMS) roughness for an area 2 μm x 2 μm are inside the Figure 5.22b. In alignment with what was observed with SEM, for N=2 the scan appears having point with higher z, reaching up to 9 nm. For N=5 and N=30 the scans appear smoother with z reaching up to 5 nm. Surprisingly, for N=10 the scan follows a different pattern having possibly significant agglomerations or an error of the measurement or crossing a step that seems visible on the SEM image. The R_q (RMS) roughness lies for all the samples at 2 nm except for N=10 where the observed pattern led to higher roughness (5.4 nm).

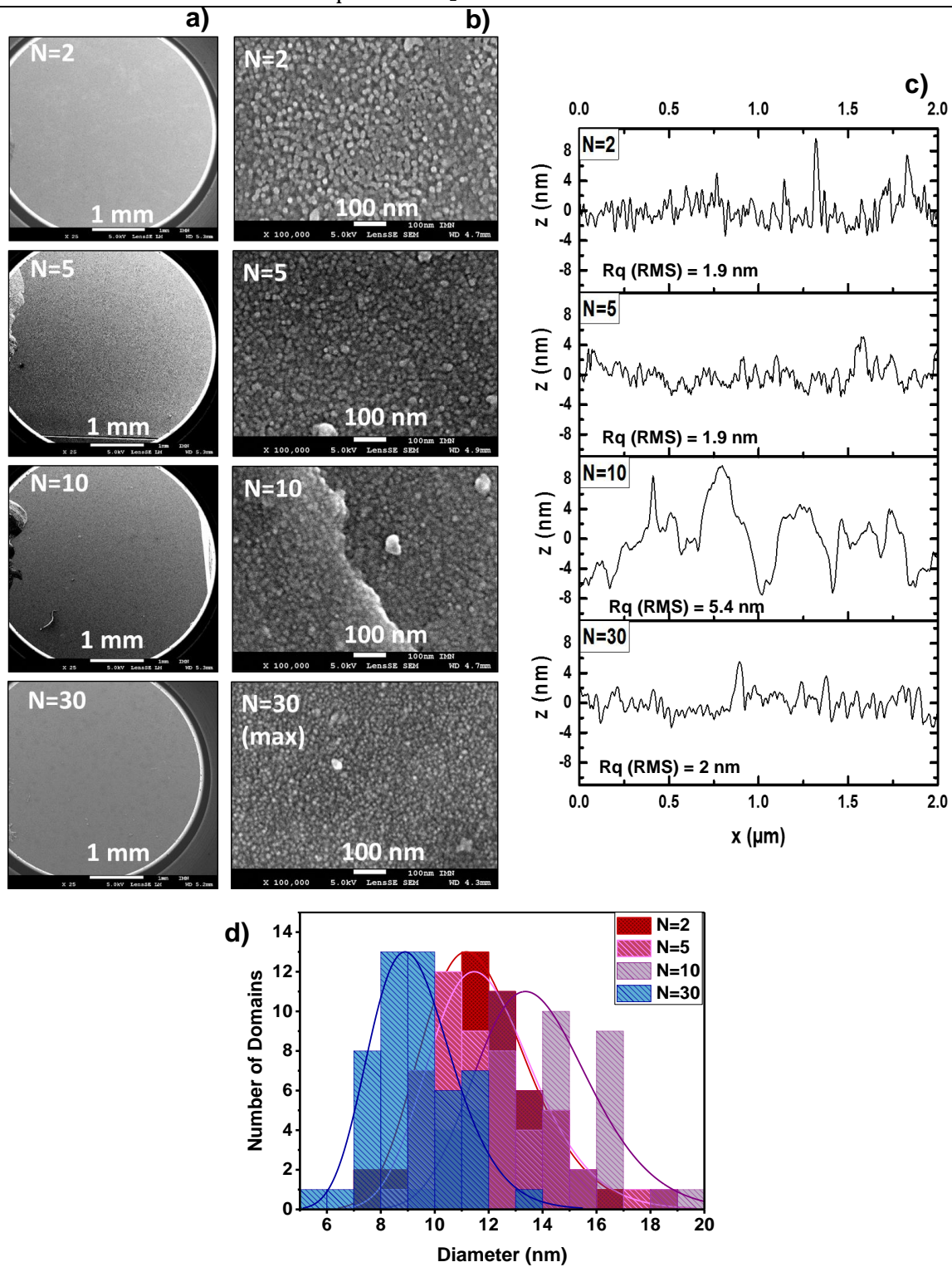


Figure 5.22: a) Low magnification and b) secondary electron surface view images in high magnification of the TiO₂ NPs thin films. c) Cross sectional profile and roughness evolution obtained with AFM at N=2, N=5, N=10 and N=30 mode (corresponding to Figure 5.19). d) Histograms of the domains sizes obtained through the high resolution SEM images.

Finally, cross sectional images are given in Figure 5.23. In general, it was challenging to recover the cross section since it appeared that all the films were significantly thin. At some local parts, corresponding to the thickest zone and

probably not totally representative of the whole sample, the film was observable, which is given in Figure 5.23. From these images, we extracted the total thickness using ImageJ software and multiple measurements. As a result, for N= 2, the thickness was estimated at 21 nm with a SD 2 nm, for N=5 at 66 nm with a SD at 3 nm and for N=10 between at 157 nm with a SD at 5 nm. All these samples were deposited for a total duration of 150 minutes. Finally, for N=30, as seen in Figure 5.19 the thickness was found at 210 nm with a standard deviation of 20 nm, for a total duration of 50 minutes. This smaller deposition duration was decided to avoid the injection of much higher amount of solvent compared to the rest of the samples.

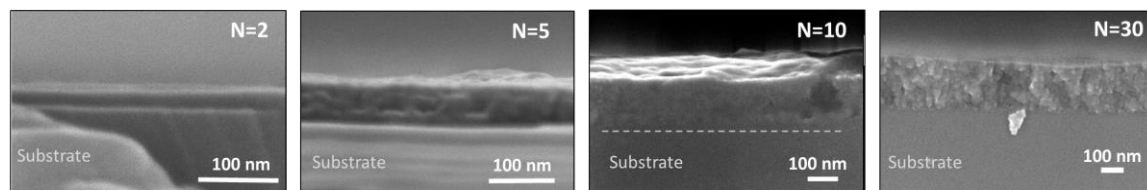


Figure 5.23: Cross sectional images of the TiO₂ NPs thin films for N=2, N=5, N=10 and N=30.

Here, after selecting the optimum dilution for the colloidal solution and adjusting the heated pipe temperature and distance, we have completed the final step of our experimental strategy. This is the use of a different and slightly more complex mode of injection. Using this mode of injection, the amount of the injected solvent is controlled and a higher time is given to the system for the liquid droplets to evaporate and the O₂ plasma to oxidize the organic solvents. It is in addition, a good way to maintain the pressure in low levels, a parameter detrimental for the good quality of the inorganic matrix (Chapter 6). In the next Section (5.5), the chemical analysis of these films will be carried out, using XPS and Raman. Finally, in Section 5.6 the in situ monitoring of these films will be accomplished and the pattern of the growth, under this iterative mode of injection, will be closely monitored.

5.5 Chemical Investigation of the optimized films through XPS and Raman

The chemical characterization of the optimized film and the optimized ones with adjusted mode of operation was conducted through XPS and Raman. The percentage of the elements found on the surface of the films are given in Figure 5.24. The atomic percentage of each element identified on the surface was extracted after the decomposition and fitting of the measured core level peaks with CasaXPS software and Gaussian-Lorentzian functions.

For the Ti 2p and Si 2p levels the typical spin-orbit splitting expected for 2p orbitals: i.e. two components 1/2 and 3/2 separated by 5 eV and 1 eV for Ti 2p and Si 2p, respectively was observed. In addition, these two spectra highlighted that the Ti and Si atoms have only one chemical environment (FWHM = 1.1 and 1.6 eV respectively). As expected the binding energy positions for Ti 2p 3/2 at 459 eV and Si

2p 3/2 at 102.4 eV are typical for such films deposited by PECVD related to TiO₂ and SiO₂ accordingly. [42–45] The contribution of oxygen bonded to titanium atoms and noted as O-Ti appears at 530.0 eV and to silicon atoms, noted as O-Si at the binding energy of 532 eV. Since the colloidal solution of TiO₂ NPs was synthesized in an organic solvent, the contribution of carbon element was considered. Therefore, three components were identified for the C 1s level. The first, at 284.8 eV, is usually assigned to C-C bonds of both adventitious elemental carbon and the solvent, while the second, at 286.0 eV, and the third, 288.5 eV, can be related to -C-O bonds and C=O bonds, respectively. In Figure 5.24, the contribution of titanium and oxygen linked to titanium is given together as a total TiO₂ percentage following the same procedure for the SiO₂.

Based on Table 5.5, one would expect that for higher amount of injected solvent a higher deposition of the NPs would be observed or at least a higher coverage of the total surface of the substrate. Unfortunately, the obtained XPS results are not so straightforward. Indeed, as the N increases, a slight increase in the TiO₂ content is observed. For all the samples, the organic species remain in low levels. However, despite that for N=2, the lowest amount of solution is injected and the longest lasts the O₂ plasma, the carbon content is surprisingly the highest. This observation may be linked to a higher sensitivity (film with the longest duration between its creation and the XPS measurement) of this film to pollution by adventitious carbon. The SiO₂ content, related to the substrate reaches an amount of approximately 65% for all the cases.

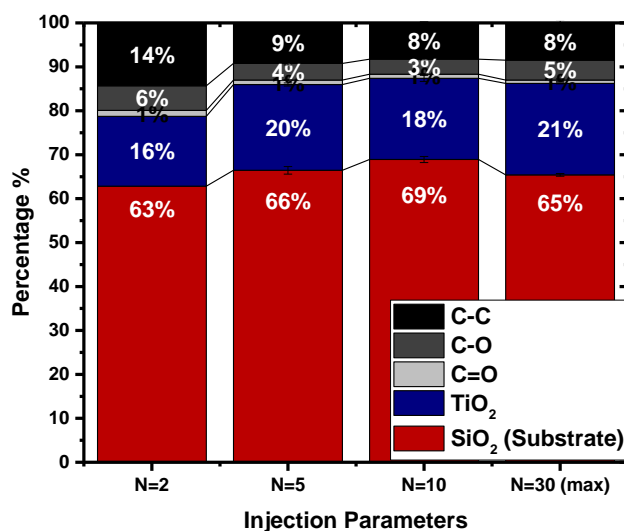


Figure 5.24: Stacked columns (%) of the chemical composition of the optimized TiO₂ NPs thin films surface.

The depth of the XPS measurement is estimated at 10 nm and the area of measurement based on the X-Ray spot used, at 700 x 300 μm². Therefore, the significant SiO₂ content measured could be linked to three assumptions. First, the porosity of the nanostructured film as significant amount of the solvent is removed

in-between the NPs. Second, the non-homogeneous covering of the substrate from the NPs. Based on the configuration of the system some areas on the substrate could be preferential for the deposition to occur having still a degree of inhomogeneity. Last, the deposition of the NPs does not lead to a thick compact thin film.

Figure 5.25 presents the Raman spectra of TiO₂ NPs optimized films with a focus on the E_g band anatase peaks. Raman modes can be assigned to the Raman spectra of the anatase crystal: 144 (E_g), 200 (E_g), 400 (B_{1g}), 513 (A_{1g}), 518 (B_{1g}) and 642 cm⁻¹ (E_g) [46,47]. The probed depth by Raman scattering includes the Silica/Si substrate meaning that polarization effects and differences in focalization of the incident beam from one sample to the other may prevent us to rely on Raman intensity. Therefore, we chose to remain cautious and comment only on modification of the peak position. In the same manner as in Chapter 3, where the spin coated TiO₂ films were studied, it can be observed that the E_g peak lies at 154 cm⁻¹: this value is shifted from the expected anatase 144 cm⁻¹ E_g peak[48,49]. It is well-established experimentally and discussed in Chapter 3 that the position of the E_g band and its shift from 144 cm⁻¹ is linked to the crystallite size.[50,51]. In this context, contrary to the shift after the plasma treatment observed in Chapter 3 (moving towards 151 cm⁻¹), for all the cases, the E_g remains close to 154 cm⁻¹. With a closer look to the Figure 5.25b, which is focused on the E_g band, we observe that for varying N, a small modification down to 153 cm⁻¹ exists. In detail for N=2, the E_g band is found at 153.6 cm⁻¹, for N=5 at 153 cm⁻¹, for N=10 at 153.1 cm⁻¹ and finally for N=30 at 153.5 cm⁻¹. This could of course be linked to the nanometric size of NPs.

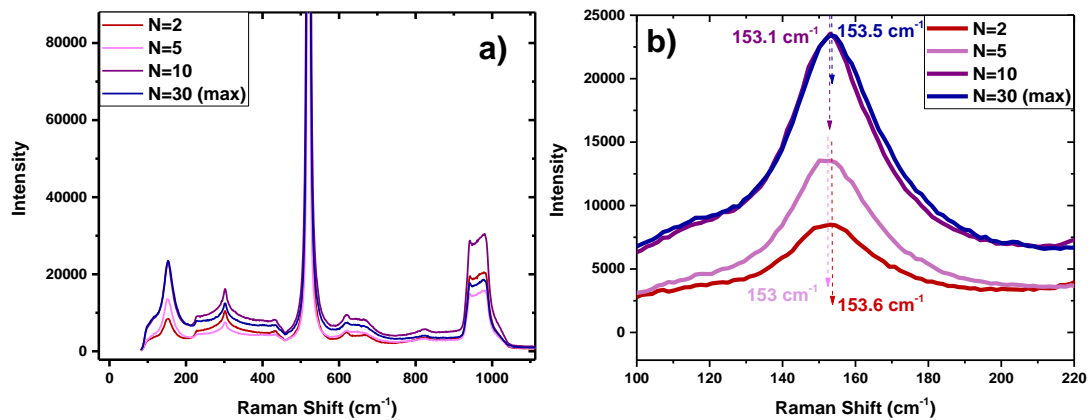


Figure 5.25: a) Raman wide spectra indicating the Anatase E_g band at 154 cm⁻¹ and the second order Si band peak at 303 cm⁻¹, among other bands as well. b) Raman spectra focusing on the Anatase E_g band at 154 cm⁻¹. The position of each E_g band, for different N is indicated inside this figure with the same color as the plot.

5.6 Characterization of the optimized films using Ellipsometry

Based on the theoretical results of Section 5.2.3 and the preliminary results of Section 5.3 we followed in Section 5.4, an optimization strategy that allowed us to

improve in a significant degree the deposition of the TiO₂ NPs and control/reduce the injected colloidal solution. A good proof indicating the improvement of the homogeneity is the fact that before the optimization it was neither possible to measure nor fit the measured data with ellipsometry. Contrary to this, for the optimized films, we were able to *in situ* monitor their growth, and used spectroscopic ellipsometry to acquire the physical and optical characteristics of the films. Hence, in Section 5.6.1, the *in situ* monitoring was accomplished by the evaluation of the Is and Ic trajectory plots and their dynamic evolution. Subsequently, using information already obtained regarding the NPs from Chapter 3, we will use the appropriate model to finally investigate in Section 5.6.2, the optical and morphological characteristics of the produced films.

5.6.1 *In situ* monitoring of the TiO₂ NPs thin film growth

During the injection of the TiO₂ NPs colloidal solution inside the low-pressure O₂ plasma reactor, the growth of the films was monitored with *in situ* ellipsometry. The recorded trajectories of the Is and Ic curves are plotted in Figure 5.26 for two wavelengths, 450 nm (Fig 5.26a) and 633 nm (Fig 5.26b). Both wavelengths are chosen to clearly illustrate the trajectory plots for photon wavelength close to the absorption of photons with the energy of TiO₂ gap and far from it, in the visible range.

In these plots, the beginning of the process is identified with t=0. During the first 30 minutes, only O₂ plasma was carried out in order to lead to the growth of a thin silica oxide layer at the surface of the substrate. This duration of O₂ plasma before the deposition has been selected in order to heat the substrate (as it is favorable condition for the droplets evaporation) and have stable O₂ plasma conditions in the reactor. By the time the injection starts (t= 30 min, 2nd arrow in the graphs), a layer of ~8 nm SiO₂ has been grown. The deposition with the N=2, N=5 and N=10 injection parameters, lasts 150 minutes (180 min in total with the 30 min O₂ plasma) and for N=30, 50 minutes (80 min in total with the 30 min O₂ plasma). In the same graphs, the trajectory plot of TiO₂ film prepared using standard PECVD process (based on O₂/TTiP plasma) is given for comparison. For the pure PECVD TiO₂ film (red dashed), the deposition starts at t=0 and lasts 50 minutes in total, reaching 50 nm in thickness. In addition to this, pure PECVD SiO₂ trajectory plot is given (based on the O₂/HMDSO plasma) corresponding to the deposition conditions of the SiO₂ matrix, which is better explained in the next Chapter. It starts from t=0 min reaching 50 nm within 25 minutes. These two trajectories are given to compare them with the ones obtained by the iterative mode of injection. The trajectory plots of N=2, 5 10 and 30 are given with continuous lines of red, pink purple and dark blue accordingly. These trajectory plots are located between the SiO₂ and TiO₂ PECVD trajectories. The lower the values of N, the closer the plot is found to the SiO₂ film. In addition, the N=2, 5 and 10 plots appear to have a dependency between the length of the plot and the total thickness obtained with SEM. The thickness obtained for this N=30 film, should lead in a much longer

trajectory plot, compared to the other cases. Here we have to remember though that the duration of the deposition for N=30 is 2 times smaller than the rest of the films. In the overall, the length of these trajectories does not comply with the rather high thicknesses obtained with SEM, on the thickest zone of the samples. Actually, for N=30 and therefore for higher amount of injected NPs in a sequence, the curve is closer to the PECVD one meaning that we can infer that its thickness lies in the range between 20 and 50 nm (if compared with the trajectories of the PECVD films).

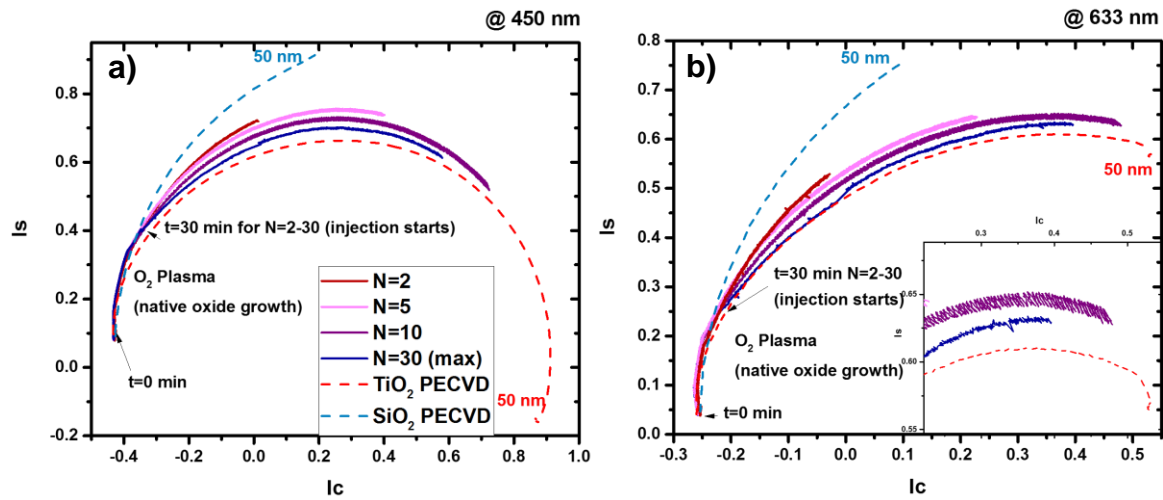


Figure 5.26: Trajectory (I_s , I_c) plots at a) 450 nm and b) 633 nm of the TiO₂ films deposited under different injection parameters (N) and compared with TiO₂ and SiO₂ PECVD made film.

In both figures a) and b), the iterative mode of injection is identified providing a less continuous (thicker) line than the one observed in PECVD TiO₂ film. To further visualize this, an inset has been placed in Figure 5.26b, that indicates clearly the difference between the films made with N=10 (purple), N=30 (bleu) and TiO₂ PECVD (dashed red)

In Figure 5.26, the non-continuous character of the I_s , I_c plots is clearly visible. Therefore, the dynamic *in situ* parameters (I_s , I_c) are given in Figure 5.27 for the first 10 minutes of injection. The 30 first minutes of O₂ plasma only have been removed in order to start the study from $t=0$ corresponding to the injection. To better identify the sequences and the Direct Liquid Injection ON (DLI), DLI-ON and DLI-OFF parts, the 10 minutes have been transformed in seconds, thus in the x axis we have 0 to 600 seconds. Each minute (60 s) corresponds to one injection sequence, as explained in Section 5.4.3. Indeed, for the N=2, N=5 and N=10 injection parameters (Fig 5.27a, b, c), a non-continuous increase of I_s and I_c is observed. More specifically, the DLI-ON and DLI-OFF timeframes follow two different trends. In detail, as the injection comes, there is a rapid increase of both the I_s and I_c and when the injection stops and only O₂ plasma exists, the curves follow a “plateau”. In the top-banner of the plots, the DLI-ON time is signaled with bleu whereas the DLI-OFF time is signaled with yellow. Contrary

to these, for the N=30 case (Fig 5.27d) the increase of both the Ic and Is curves follow a more continuous pattern.

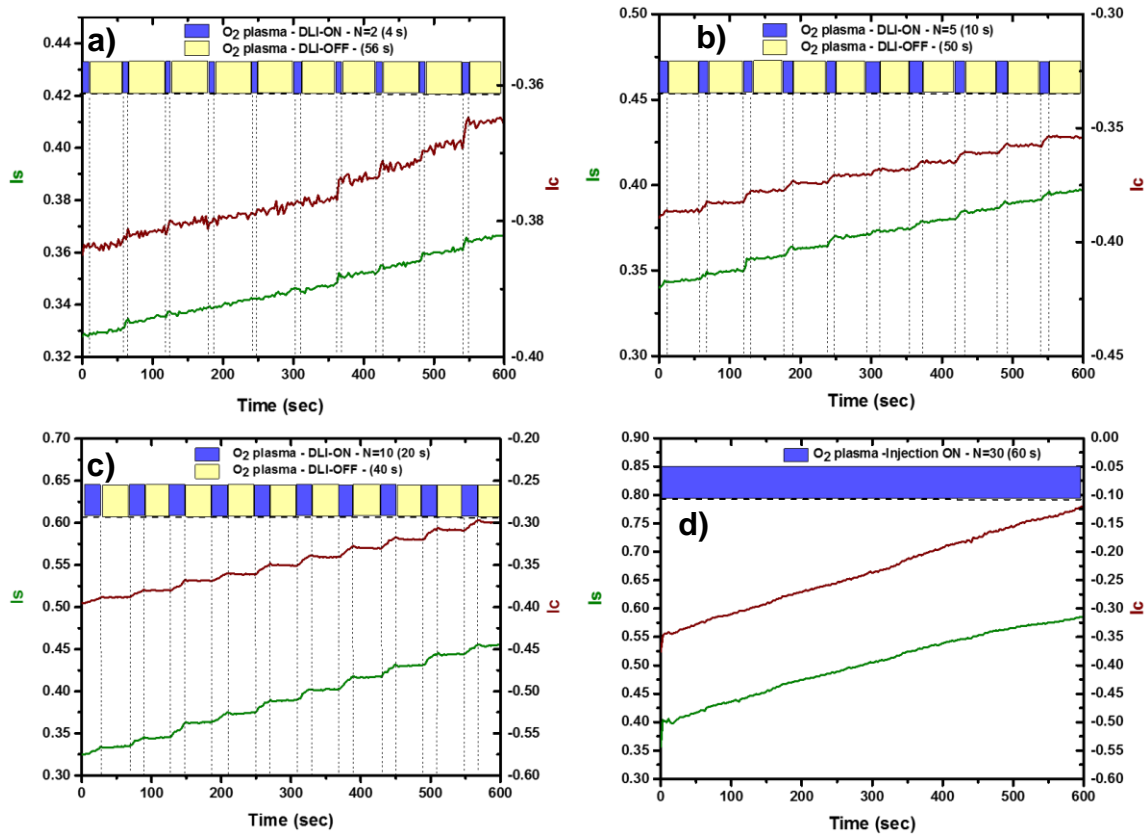


Figure 5.27: The dynamic *in situ* Is (green), Ic (red) parameters at 450 nm measured during the first 10 minutes of the liquid injection with a) N=2, b) N=5, c) N=10 and d) N=30. Each minute corresponds to one sequence (cf fig 5.21). In the top-banner of each graph, blue and yellow bars evidence the period when the liquid Injection is ON time and OFF, respectively.

To better understand the kinetics, in Figure 5.28, we focused on one injection sequence for which N=10. In this plot between the 230 and 250 seconds the DLI-OFF of the previous sequence appears. The second zone observed with 20 seconds duration corresponds to the 10 injection pulses. In this zone (DLI-ON), both Is and Ic increase, leading to the assumption that during this time the film is growing. Moreover, after the injection is finished, during the O₂ plasma only, we observe that for the first 5 seconds a slight decrease of these values occurs (indicted in the plot with a star *). This could be linked to an opposite effect than that of the growth. Since it is close to the time resolution of the ellipsometer and it is an effect observed but not along the total growth of the film, we cannot conclude whether it is an artefact of a possible indication of etching of this film or densification (as in Chapter 3). Accordingly, during the remaining 35 seconds (DLI-OFF), both Is and Ic seem almost constant.

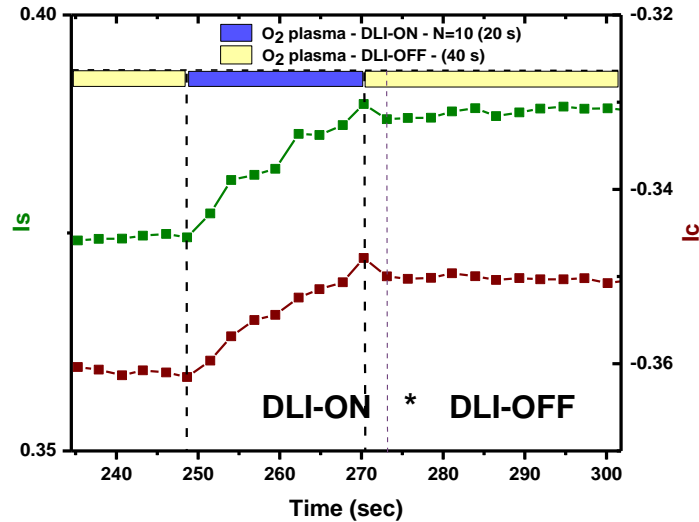


Figure 5.28: The dynamic in situ I_s (green), I_c (red) parameters at 450 nm for $N=10$ focused on one sequence. In the top-banner of each graph, blue and yellow bars evidence the period when the liquid Injection is ON time and OFF, respectively.

5.6.2 Optical and physical characteristics of the optimized films Ellipsometric Model

Using the data obtained by ellipsometry, we can acquire important information regarding the optical and physical characteristics of the film. To achieve this, a model describing the material is needed. The validity of the model and therefore the evaluation of the accuracy of the fit was estimated by the Mean Square Error MSE factor. [52] These samples, obtained by the iterative mode of injection, were accounted for as homogenous layers on silicon substrate with a native oxide layer, without top-layer roughness. Due to heterogeneities observed and these coffee-ring patterns, a more pronounced diffusion of the incident light was observed (in the measurement) at shorter wavelengths. Hence, the fitting was carried out in the limited range of 550 - 1000 nm (instead of 240 to 1000 nm).

The choice of the model was taken based on the results obtained in Chapter 3. In this Chapter, we saw that for the spin coated TiO₂ NPs film (using the colloidal solution of TiO₂ NPs) a model using the Tauc Lorentz dispersion law to describe the PECVD TiO₂ bulk films is not suitable. Instead, a Bruggeman Effective Medium Approximation Model (BEMA) was used describing the TiO₂ NPs and Voids (Figure 3.2, Section 3.2.1). Before the plasma treatment the fraction of Voids was estimated at 19 % whereas after the plasma treatment this void was fitted to 0. At the same time, the bandgap of the film was slightly decreased. Using multiple characterization techniques, it was possible to verify that small variation on the anatase nanocrystallite may occur due the energy flux brought to the small particles by the 25 mTorr O₂ plasma.

Here, in the same manner as in Chapter 3, the model used was based on BEMA between TiO₂ NPs and void. An important parameter indicating the existence of voids is the XPS results, where for all the N parameters a significant amount of the silica substrate is measured. An example of the fit quality and the model used, is given in Figure 5.29. The results describing the structure of the film that were obtained by this spectroscopic ellipsometry are given in Table 5.6 along with the MSE. During the fit, the void fraction, thickness and the optical energy gap (E_g) parameter of the TL dispersion law were set free.

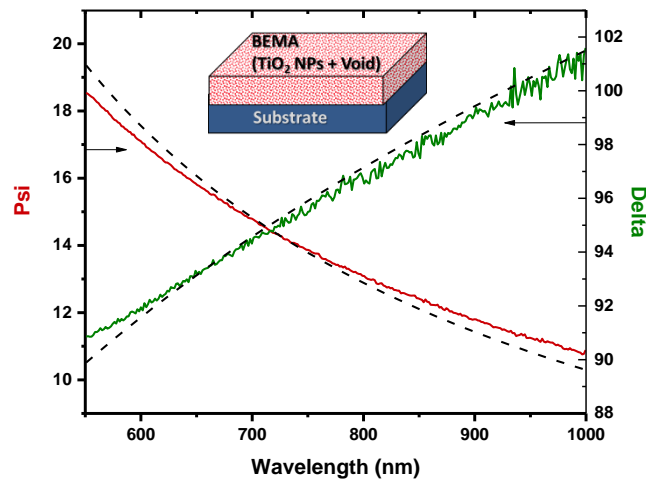


Figure 5.29: Psi (red) and Delta (green) results of the measured (continuous) and modeled (dashed) data with ellipsometry, based on the Bruggeman Effective Medium (BEMA) model.

Table 5.6: NCs characteristics with varying injection parameter

N	Thickness (nm)	Void %	T _{injection} TOTAL (min)	Total injected liquid weight (g)	Dep. Rate (nm/min)	MSE (550-100 nm)
2	19	20	150	0.70	0.13	7
5	32	14	150	1.75	0.21	13
10	43	8	150	3.50	0.29	26
30	36	12	50	3.50	0.72	23

The attained results from spectroscopic ellipsometry, indicate that the produced films have significantly low thickness such as 19 nm for N=2, 32 nm for N=5, 43 nm for N=10 and 36 for N=30. As a reminder, it is quite coherent that the film produced in the condition N=30 has similar thickness as with N=10 as the liquid has been injected for 50 minutes instead of 150, leading to the same total injected colloidal solution (given in Table 5.5 and 5.6). These thickness results could now explain the trajectory plots of Figure 5.25, where their length was found comparable to the trajectory plots of 50 nm SiO₂ and TiO₂ PECVD made films. Moreover, a significant amount of voids was found in these films with N=2 having the highest amount at 20%, N=5 at 14%, N=10 at 8% and finally for N=30 at 12%. These results could also explain

the deviation of the trajectory plots from the TiO₂ PECVD made film. It could actually indicate that the higher the void, the higher is the influence of the substrate leading to plots closer to the SiO₂ PECVD reference. Dividing the final film thickness with the total duration of the deposition, in the 6th column of Table 5.6, we indicate the deposition rate. It appears that for higher N, the higher the deposition is, still remaining below 1 nm/min.

From these thickness data and the total duration of the deposition, we can plot the deposition rate as a function of the injection parameter or as a function of the DLI-ON (=N*2 s) time divided by the total time of the sequence (1 min). Hence, in Figure 5.30, both the Injection Parameter (N) and the fraction of the DLI-ON from the sequence are given in the x-axis. As expected, for the maximum N = 30, the fraction equals to 1 (“conventional pulsing mode”). In the y-axis of the figure the deposition rate is given. With red line the linear fit of these points is plotted. This means that through the process parameters there is a linear control of the TiO₂ NPs thin film growth. In addition to this, from the Table in Figure 5.30b, we see that for N=2, E_g is found at 3.4 eV, for N=5 at 3.3 eV, for N=10 at 3.3 eV and N=30 at 3.4 eV. These values as expected are slightly higher than the bulk TiO₂ PECVD films (3.2 eV). No significant modification of these films from the 3.4 eV representing the 5 nm TiO₂ NPs can be ascertained regarding the induced alterations on the TiO₂ anatase crystallites as it has been already observed in Chapter 3, after the plasma treatment of the spin coated NPs. This is coherent with the very small variations in the position of the Raman Eg band described in Section 5.5 (Fig. 5.25). Finally, the optical refractive index of the TiO₂ NPs at 633 nm in Figure 5.30b, does not appear significantly affected having a value of approximately ~2 (2.01 for N=2, 2.01 for N=10 and 2.03 for N=30). Only for the case of N=5 a slight decrease is observed having a value of 1.92.

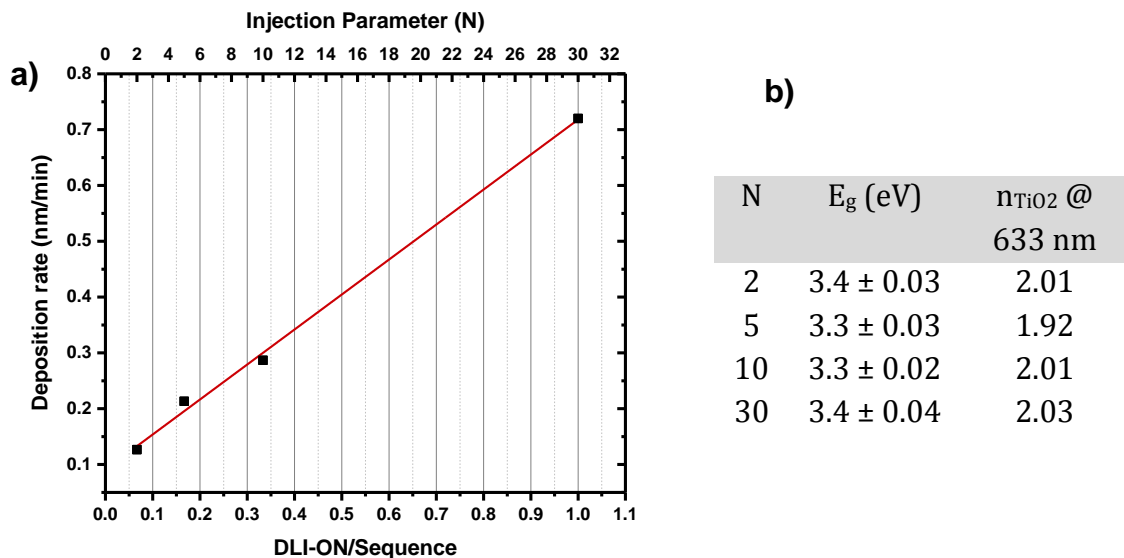


Figure 5.30: a) Deposition rate of the TiO₂ NPs versus the injection parameter N or the DLI-ON/ Sequence. Red line represents the linear fit of the scatter points. b) Optical energy gap (E_g) and refractive index of the TiO₂ layer obtained by the spectroscopic ellipsometry for the optimized films with varying injection parameter (N).

From these results, the absorption coefficient (α) was extracted (Ellipsometry CompleteEASE Software) and the Tauc plots were created, which are given in Figure 5.31. A Tauc plot is a method to determine the optical band gap in semiconductors. In this figure, both cases of a direct and an indirect bandgap are given. As seen in Figure 5.31, in the x-axis of the figures the photon energy ($h\nu$) is given whereas in y-axis the $(\alpha h\nu)^{1/r}$. The value of the exponent r denotes the nature of the transition with $\frac{1}{2}$ for the direct allowed transitions (Figure 5.31a) and 2 for the indirect allowed ones. Extrapolating in both cases the linear region from this curve can lead to the extraction of the optical band gap, as seen in Figure 5.31a,b with dotted lines. From these plots we see that the bandgap obtained by the indirect transitions lies closer to the one expected and verifies the indirect nature of the gap of the TiO₂ anatase materials from literature.[53] In addition to this, from these Tauc plots, we observe that the TiO₂ NPs, for different N, reveal small alterations to their optical bandgap.

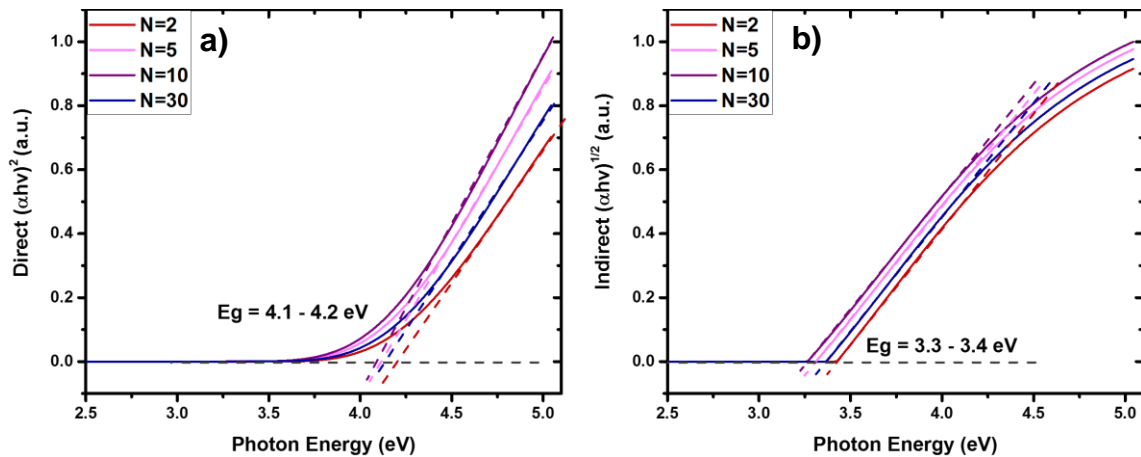


Figure 5.31: Tauc plots for all the injection parameters (N) used for the deposition of the TiO₂ NPs optimized thin films, for the determination of the a) direct and b) indirect optical band gap.

Ellipsometry has a probed area of 25 mm², meaning that it is a technique that gives a mean field view of the composition. From these results, having thickness below 40 nm and a fraction of void, the XPS data could be explained. With XPS, the depth profile of the measurement is at 10 nm. Hence, it could be possible that for these rather thin films with voids, X-rays are reaching the substrate leading to emission of photoelectrons, indicating the existence of the SiO₂ in the measurements. Moreover, an important discrepancy observed through the characterization of the optimized films, is between the cross sectional images with SEM and the thickness obtained with ellipsometry. As explained in Section 5.4.3, the identification of the cross sectional layer was challenging. It is therefore possible that this local (nm range) images given in Figure 5.23, to be taken at remaining droplet and are not completely representative of the whole sample. If despite the optimization strategy, some droplet patterns still exist on the substrate, this could explain in addition the scattering effects observed in the low wavelengths through ellipsometry. Finally, using *in situ* ellipsometry it was

possible to follow even at the beginning of the growth the deposition pattern and identify through the Is and Ic plots the DLI-ON and DLI-OFF zones. This way of deposition significantly resembled to an ALD-like process. having a resolution close to 0.1 nm. It is noteworthy to say that *in situ* ellipsometry is a useful tool to monitor the growth of the film.

5.7 Discussion

5.7.1 Comparison between the deposited pristine and optimized TiO₂ NPs thin films

The degree of improvement, from the present study, can be clearly identified by comparing two chosen films. First, the pristine film, studied in Section 5.3.1 as it is considered the basis of the study in terms of experimental conditions (colloidal solution, distance from the pipe, temperature of the heating wire). Second, the optimized film studied in Section 5.4.2, as all the important parameters of the pristine sample affecting the quality of deposition have been improved maintaining the same injection frequency. To assess the discussion and the comparison, in Figure 5.32, the AFM scan and mean domain size distribution are gathered. In addition, as inset in the size distribution plot, a photograph of the deposited thin films is given.

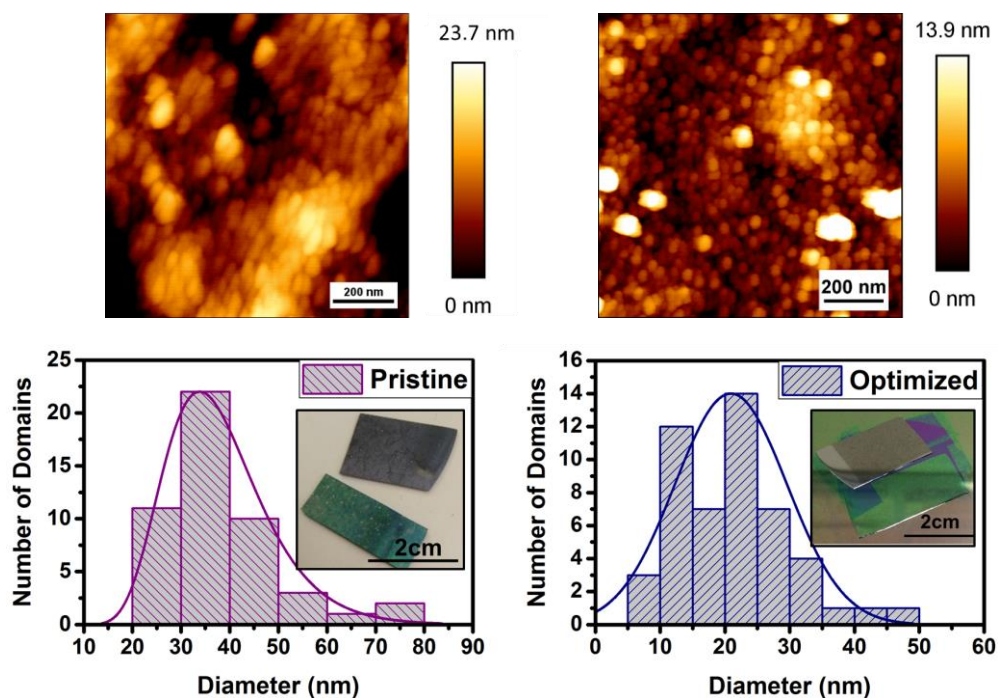


Figure 5.32: AFM and size distribution of the pristine (left hand-side) and optimized (right hand-side) samples. The optical images of the films are given with a photo inserted in the plots.

In accordance with what was shown from SEM, the scan of the pristine sample appears rough, with large domains and its roughness was found at Rq (RMS)=5.5 nm.

The mean domain size for this case was found at 33 nm and a standard deviation at 11 nm. Furthermore, from the inserted photograph the inhomogeneity of the deposition is obvious even with a naked eye, as droplet-like patterns are identified. The scan of the optimized sample, is much clearer, having smaller domains and with rounder shape. The reduced Rq (RMS) roughness verifies this observation having a value of 3.2 nm. In this case, the mean domain size was found at 21 nm with a standard deviation of 8 nm. From the inserted photo the importance of these optimization steps is clearly proven, indicating a much more homogeneous and uniform film of NPs.

To reply to two important questions, in Figure 5.33, the Raman spectrum of the pristine, optimized and spin coated film before the O₂ plasma are compared. The two questions that need to be answered are the following. First, whether the O₂ plasma affects the injected NPs in the same manner as in Chapter 3, by slightly increasing the size of the nanocrystals as suggested by the analysis of the *in situ* ellipsometry data (Section 5.6). Second, if the domains measured in Figure 5.32, are the NPs themselves which would have aggregated to produce larger particles or agglomerated NPs.

Aggregation of particles is an irreversible process involving sintering of NPs, forming a bigger one, whereas agglomeration is caused due to the breakdown of the mechanisms that allow the NPs to remain far from each other leading NPs in close proximity forming a bigger agglomerate.

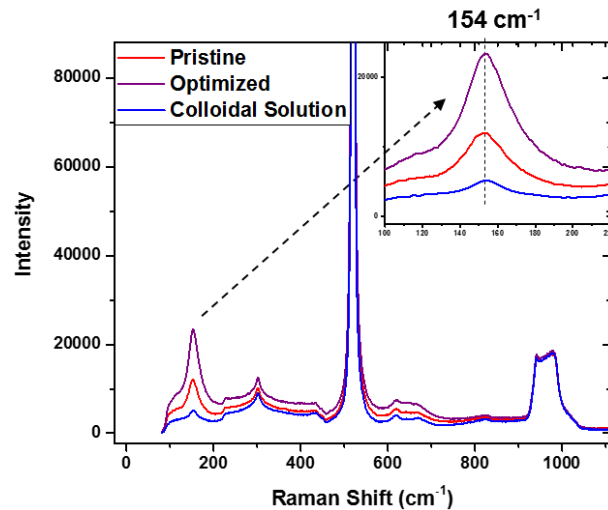


Figure 5.33: Raman spectra indicating the Anatase Eg band at 154 cm⁻¹ and the second order Si band peak at 303 cm⁻¹ for the spin coated film from Chapter 3, the pristine and optimized films from Chapter 5.

From this Figure 5.33, we observe that all of the compared films have values close to the 154 cm⁻¹ with the optimized having a slightly lower value at 153.6 cm⁻¹. Contrary to these results, in Chapter 3 it was found that this Eg peak shifts to 151 cm⁻¹ after the exposure of the spin coated TiO₂ NPs film in the O₂ plasma. Hence, this is an indication that the crystallites remain in their initial state having though some

possible agglomerations but not aggregations. When varying the N injection parameter and introducing some DLI-OFF in the sequence, some clues such as the E_g slight shift in Figure 5.25 and the optical E_g from Ellipsometry in Figure 5.30b and 5.31b could indicate that the O₂ plasma between the DLI-ON times does not slightly affect the anatase nanocrystallite. Based on the E_g variation (3.4 to 3.3 eV) and the E_g band shift (154 to 153 cm⁻¹), these variations remain in the uncertainty of measurements compared to what was observed in Chapter 3 (E_g from 3.4 to 3.2 eV, E_g band from 154 to 150 cm⁻¹).

5.7.2 Iterative Process

As last part of the optimization strategy, the iterative mode of operation was proposed. According to this, different number of injection pulses (N) were selected, in a sequence of one minute. The produced films with N=2, 5, 10 and 30, were thoroughly investigated concerning their physical and chemical characteristics. For all the cases the nanometric anatase was identified using Raman despite the different amount of N. In addition to this, based on the chemical analysis of the films surface, a slight increase of the TiO₂ content was found as N increases. At the same time, a significant amount of the native oxide of the substrate was detected. This inconclusive finding could be linked to the area or the depth of the XPS measurement. As stated in Section 5.5, this characterization could lead to the following information about the samples. First, based on the configuration of the system some areas on the substrate could be preferentially favorable for the deposition to occur having still a degree of inhomogeneity and second that the deposition of the NPs does not lead to a thick compact thin film. With spectroscopic ellipsometry, it was in Section 5.6 verified that the films have thickness lower than 36 nm and that voids are incorporated in the film.

The growth of the film was monitored *in situ* with ellipsometry and the Is Ic trajectories were plotted for the first ten minutes of the deposition. Using this technique we were able to capture the iterative mode of operation which resembles studies carried out using Atomic Layer Deposition (ALD).[54] Using this approach, two kinetics were identified within one sequence. First, at the DLI-ON time, both Is and Ic increase, leading to the assumption that during this time the film is growing. Second, as long as the injection is OFF (DLI-OFF), and only O₂ plasma exists, we observe that for the first 5 seconds a decrease of these values which could be linked to an inverse effect than growth. This observation was inconclusive as it could mean that the O₂ plasma either densifies the film or chemically etches the organic solvent surrounding the NPs. Given that it is in the limit of the resolution of this system, it was not accounted as a reliable result. Finally, during the DLI-OFF it was shown that no growth exists.

5.7.3 From the theoretical to the experimental point of view

In Section 5.2.3 we studied theoretically the interactions between the liquid droplet (with different solvents) and the plasma and using the energy balance equation we were able to investigate the parameters affecting the droplet lifetime. It was found that the enthalpy of vaporization of each solvent affects the speed of evaporation rendering methanol the easiest solvent to evaporate in this environment and PC and PG the most difficult ones. Given that our initial colloidal solution comprises of PC and PG, we diluted it with the more volatile solvent, in order to assist the evaporation rate. That was achieved as it allowed us to decrease the number of NPs in a droplet and thus having a way to decrease the size of the droplet interacting with the plasma once methanol is evaporated (assuming, in a first approximation, there is no azeotrope phase in the ternary mixture). Indeed, it was proven experimentally that the deposition and distribution of the NPs on the substrate was improved rendering the dilution with methanol the most promising choice.

In addition to this, the wall temperature inside this system was found to influence the evaporation rate of the solvent especially for lower pressure values. Technically in our system the possibility to increase the total diffusion chamber wall temperature was not possible. Alternatively, we were able to increase the temperature of the pipe connecting the injector to the reactor. In accordance to the theoretical study, instead of a cracked film (due to the rapid evaporation of solvent) while injecting at 25 °C we were able to acquire more crack-free films at 100 °C and even more homogeneous deposits at 150 °C.

Finally, even for the best-case scenario ($T_w=423$ K, 25 mTorr, methanol) the droplet lifetime reaches a value of 0.73 seconds. Supposing that our droplet velocity is at 13 m s^{-1} , the distance needed for the droplets to fully evaporate would be 9.5 m. Since this practically was not possible, the extension of the heating pipe by 15 cm was attempted. With this addition in the system, the deposition was significantly improved having only smaller in size shaped patterns resulting from coffee-ring effect upon drying.

There are several additions and adjustments that could be proposed to improve even better this novel and versatile approach of depositing nanoparticles in a plasma environment. First, the solvent of the colloidal solution should be volatile enough, in order to play the role of the “NPs carrier”, and not be involved in the film chemical composition. At the same time, it should not be too volatile and injected in very small volumes as the efficiency of the deposition could be decreased (evaporate very fast leading to trapping of the NPs in the plasma sheath or dramatic increase in pressure leading the plasma to switch off). In addition, adjusting the wall temperature of the reactor at around 450 K could all be a step of improvement. Moreover, we saw that the heating terms of plasma can influence the droplet lifetime. In our case, the O atom density was the main performer. Ogawa and all showed that both the plasma density and the electron temperature can increase the droplet temperature and

therefore the evaporation rate. Finally, based on the coffee-ring findings, we could assume that deliberately controlling and increasing the substrate temperature could lead in a positive outcome in terms of film homogeneity.

Conclusion

In this chapter, the injection of the TiO₂ NPs colloidal solution inside the low pressure O₂ plasma was attempted. As a first step, the analysis of the process was conducted focusing on the injection system and the characteristics of the produced droplets. As a second step, their transport and evaporation inside the low-pressure system were studied. Finally, as a third step, their interactions with the low pressure O₂ plasma were unraveled. Based on the mean free path of the evaporating molecules, the motion of evaporation was identified as molecular. As a result, the appropriate equation was added in the energy balance equation, to calculate the droplet temperature and accordingly the droplet lifetime. It was found that the droplet lifetime for the less volatile solvents existing in our colloidal solution (PG and PC), is much higher than the rest of the studied solvents (water, ethanol and methanol) having a lifetime up to 15 seconds, at room temperature. The increased pressure (from 3 towards 25 mTorr) and therefore the increased heating term provided by the O atom energy flux indicated a decrease in this lifetime down to 1 second. For the more volatile solvent such as methanol the droplets lifetime at 3 mTorr was found much less, at 5 seconds. In general, this step was of great importance as it gave insight in the mechanisms affecting the evaporation process. These types of calculations could allow the improvement of both the system and the injected solution and lead to estimations regarding the quality of the NPs deposition.

Preliminary experiments were conducted indicating a pressure variation as the droplet molecules evaporate inside the low-pressure system and the oxidation process of the organic solvent was captured using OES. From these experiments, the importance of the process optimization was clarified. Bearing in mind, that only the TiO₂ NPs should be deposited and not the organic colloidal solution three optimization steps were followed. Initially, the dilution of the initial colloidal solution with more volatile solvents was carried out. Methanol was identified as the most favorable solvent at this step. In addition, the geometry of the system was adjusted, increasing the distance between the injector and the substrate as well as increasing the temperature of this part. Furthermore, in order to have a process that will be versatile and low cost, the duration of the deposition should not be long. In an attempt to provide an optimum compromise, a different mode of operation was selected. It was called iterative mode of operation and in a sequence lasting one minute, a varying number (N) of injection pulses was selected. The physical and chemical characteristics of the optimized films (N=2, 5, 10 and 30) were investigated, verifying the nanometric anatase deposition. The growth of the film was monitored with *in situ* ellipsometry and this DLI-ON and DLI-OFF mode of operation was detected in the Is

and I_c curves. From this, it was identified that during on time, injection and deposition occurs whereas during off time mainly the O₂ plasma acts. Using spectroscopic ellipsometry, it was identified that the deposition rates are found between 0.13 and 0.72 nm/min for N=2 to N=30, accordingly. An amount of void was also found in the film indicating a degree of porosity on the film. Finally, through the slight modification of the optical bandgap (E_g), the Raman band E_g and the mean size of the measured domains using SEM images, no significant modification of the crystallite was clearly induced by the O₂ plasma. An indication of severe agglomerations or aggregation is not evidenced.

In general, this chapter was of great importance for understanding the mechanisms affecting the NPs deposition and identifying modes of operation of the system compatible with the SiO₂ matrix deposition developed in Chapter 6.

Bibliography

- [1] D. Ogawa, I. Saraf, A. Sra, R. Timmons, M. Goeckner, L. Overzet, The direct injection of liquid droplets into low pressure plasmas, *J. Vac. Sci. Technol. Vac. Surf. Films.* 27 (2009) 342–351. <https://doi.org/10.1116/1.3081965>.
- [2] M. Vervaele, B. De Roo, O. Deschaume, M. Rajala, H. Guillon, M. Sousa, C. Bartic, C. Van Haesendonck, J.W. Seo, J.-P. Locquet, Development of a new direct liquid injection system for nanoparticle deposition by chemical vapor deposition using nanoparticle solutions, *Rev. Sci. Instrum.* 87 (2016) 025101. <https://doi.org/10.1063/1.4940937>.
- [3] J. Profili, O. Lévassieur, J.-B. Blaisot, A. Koronai, L. Stafford, N. Gherardi, Nebulization of Nanocolloidal Suspensions for the Growth of Nanocomposite Coatings in Dielectric Barrier Discharges: Nebulization of Nanocolloidal Suspensions..., *Plasma Process. Polym.* 13 (2016) 981–989. <https://doi.org/10.1002/ppap.201500223>.
- [4] P. Brunet, R. Rincón, J.-M. Martínez, Z. Matouk, F. Fanelli, M. Chaker, F. Massines, Control of composite thin film made in an Ar/isopropanol/TiO₂ nanoparticles dielectric barrier discharge by the excitation frequency, *Plasma Process. Polym.* (2017) n/a-n/a. <https://doi.org/10.1002/ppap.201700049>.
- [5] F. Fanelli, A.M. Mastrangelo, F. Fracassi, Aerosol-Assisted Atmospheric Cold Plasma Deposition and Characterization of Superhydrophobic Organic–Inorganic Nanocomposite Thin Films, *Langmuir.* 30 (2014) 857–865. <https://doi.org/10.1021/la404755n>.
- [6] P.J. Bruggeman, M.J. Kushner, B.R. Locke, J.G.E. Gardeniers, W.G. Graham, D.B. Graves, R.C.H.M. Hofman-Caris, D. Maric, J.P. Reid, E. Ceriani, D. Fernandez Rivas, J.E. Foster, S.C. Garrick, Y. Gorbanev, S. Hamaguchi, F. Iza, H. Jablonowski, E. Klimova, J. Kolb, F. Krcma, P. Lukes, Z. Machala, I. Marinov, D. Mariotti, S. Mededovic Thagard, D. Minakata, E.C. Neyts, J. Pawlat, Z.L. Petrovic, R. Pflieger, S. Reuter, D.C. Schram, S. Schröter, M. Shiraiwa, B. Tarabová, P.A. Tsai, J.R.R. Verlet, T. von Woedtke, K.R. Wilson, K. Yasui, G. Zvereva, Plasma–liquid interactions: a review and roadmap, *Plasma Sources Sci. Technol.* 25 (2016) 053002. <https://doi.org/10.1088/0963-0252/25/5/053002>.
- [7] A.D. Ross, K.K. Gleason, The CVD of Nanocomposites Fabricated via Ultrasonic Atomization, *Chem. Vap. Depos.* 12 (2006) 225–230. <https://doi.org/10.1002/cvde.200506368>.
- [8] D. Ogawa, C.W. Chung, M. Goeckner, L. Overzet, Transient effects caused by pulsed gas and liquid injections into low pressure plasmas, *Plasma Sources Sci. Technol.* 19 (2010) 034013. <https://doi.org/10.1088/0963-0252/19/3/034013>.
- [9] A. Karpinski, S. Berson, H. Terrisse, M. Mancini-Le Granvalet, S. Guillerez, L. Brohan, M. Richard-Plouet, Anatase colloidal solutions suitable for inkjet printing: Enhancing lifetime of hybrid organic solar cells, *Sol. Energy Mater. Sol. Cells.* 116 (2013) 27–33. <https://doi.org/10.1016/j.solmat.2013.04.006>.
- [10] S. Kooij, R. Sijs, M.M. Denn, E. Villermaux, D. Bonn, What Determines the Drop Size in Sprays?, *Phys. Rev. X.* 8 (2018). <https://doi.org/10.1103/PhysRevX.8.031019>.
- [11] M. Goeckner, D. Ogawa, I. Saraf, L. Overzet, Progress report: Direct injection of liquids into low-pressure plasmas, *J. Phys. Conf. Ser.* 162 (2009) 012014. <https://doi.org/10.1088/1742-6596/162/1/012014>.
- [12] P.C. Reist, *Aerosol science and technology*, 2. ed, McGraw Hill, New York, 1993.
- [13] W.C. Hinds, *Aerosol technology: properties, behavior, and measurement of airborne particles*, 2. ed, Wiley, New York, 1999.
- [14] H. Hertz, Ueber die Verdunstung der Flüssigkeiten, insbesondere des Quecksilbers, im luftleeren Raume, *Ann. Phys.* 253 (1882) 177–193. <https://doi.org/10.1002/andp.18822531002>.
- [15] M. Knudsen, Die maximale Verdampfungsgeschwindigkeit des Quecksilbers, *Ann. Phys.* 352 (1915) 697–708. <https://doi.org/10.1002/andp.19153521306>.
- [16] V.A. Kuz, A vapor pressure equation for droplets, (n.d.) 2.
- [17] A.V. Kozyrev, A.G. Sitnikov, Evaporation of a spherical droplet in a moderate-pressure gas, *Phys.-Uspekhi.* 44 (2001) 725–733. <https://doi.org/10.1070/PU2001v044n07ABEH000953>.
- [18] D.M. Murphy, T. Koop, Review of the vapour pressures of ice and supercooled water for atmospheric applications, *Q. J. R. Meteorol. Soc.* 131 (2005) 1539–1565. <https://doi.org/10.1256/qj.04.94>.

- [19] P.R. Chakraborty, K.R. Hiremath, M. Sharma, Evaluation of evaporation coefficient for micro-droplets exposed to low pressure: A semi-analytical approach, *Phys. Lett. A.* 381 (2017) 413–416. <https://doi.org/10.1016/j.physleta.2016.11.036>.
- [20] A.V. Kozyrev, A.G. Sitnikov, Evaporation of Charged Drops, *Russ. Phys. J.* 46 (2003) 646–655. <https://doi.org/10.1023/B:RUPJ.0000008193.53695.30>.
- [21] G.H.P.M. Swinkels, H. Kersten, H. Deutsch, G.M.W. Kroesen, Microcalorimetry of dust particles in a radio-frequency plasma, *J. Appl. Phys.* 88 (2000) 1747–1755. <https://doi.org/10.1063/1.1302993>.
- [22] L. Mangolini, U. Kortshagen, Selective nanoparticle heating: Another form of nonequilibrium in dusty plasmas, *Phys. Rev. E.* 79 (2009). <https://doi.org/10.1103/PhysRevE.79.026405>.
- [23] H.R. Maurer, H. Kersten, On the heating of nano- and microparticles in process plasmas, *J. Phys. Appl. Phys.* 44 (2011) 174029. <https://doi.org/10.1088/0022-3727/44/17/174029>.
- [24] N.J. Kramer, R.J. Anthony, M. Mamunuru, E.S. Aydil, U.R. Kortshagen, Plasma-induced crystallization of silicon nanoparticles, *J. Phys. Appl. Phys.* 47 (2014) 075202. <https://doi.org/10.1088/0022-3727/47/7/075202>.
- [25] S. Prasanna, A. Michau, K. Hassouni, S. Longo, Effect of charge fluctuation on nanoparticle heating in dusty plasma, *Plasma Sources Sci. Technol.* 28 (2019) 03LT03. <https://doi.org/10.1088/1361-6595/ab094d>.
- [26] A. Granier, S. Jacq, D. Li, M. Carette, A. Goulet, Investigation of plasma surface interactions in pulsed O₂/TTIP low pressure ICP plasma by time resolved optical emission spectroscopy, in: ESCAMPIG XXI, Viana do Castelo, Portugal, 2010: p. 2.
- [27] V. Shen, Standard Reference Simulation Website, NIST Standard Reference Database 173, (2006). <https://doi.org/10.18434/T4M88Q>.
- [28] CRC handbook of chemistry and physics: a ready-reference book of chemical and physical data., 2017.
- [29] D. Li, M. Carette, A. Granier, J.P. Landesman, A. Goulet, Effect of ion bombardment on the structural and optical properties of TiO₂ thin films deposited from oxygen/titanium tetraisopropoxide inductively coupled plasma, *Thin Solid Films.* 589 (2015) 783–791. <https://doi.org/10.1016/j.tsf.2015.07.015>.
- [30] F. Nicolazo, A. Goulet, A. Granier, C. Vallee, G. Turban, B. Grolleau, Study of oxygen/TEOS plasmas and thin SiO_x films obtained in an helicon diffusion reactor, *Surf. Coat. Technol.* 98 (1998) 1578–1583.
- [31] A. Granier, G. Borvon, A. Bousquet, A. Goulet, C. Leteinturier, A. van der Lee, Mechanisms Involved in the Conversion of ppHMDSO Films into SiO₂-Like by Oxygen Plasma Treatment, *Plasma Process. Polym.* 3 (2006) 365–373. <https://doi.org/10.1002/ppap.200600022>.
- [32] H.J. Holterman, Kinetics and evaporation of water drops in air, (n.d.) 67.
- [33] T.J. Garino, The Cracking of Sol-Gel Films During Drying, *MRS Proc.* 180 (1990) 497. <https://doi.org/10.1557/PROC-180-497>.
- [34] J.N. Hart, Y.-B. Cheng, G.P. Simon, L. Spiccia, Challenges of producing TiO₂ films by microwave heating, *Surf. Coat. Technol.* 198 (2005) 20–23. <https://doi.org/10.1016/j.surfcoat.2004.10.097>.
- [35] M. Bockmeyer, P. Löbmann, Crack formation in TiO₂ films prepared by sol-gel processing: Quantification and characterization, *Thin Solid Films.* 515 (2007) 5212–5219. <https://doi.org/10.1016/j.tsf.2006.11.193>.
- [36] P. Xu, A.S. Mujumdar, B. Yu, Drying-Induced Cracks in Thin Film Fabricated from Colloidal Dispersions, *Dry. Technol.* 27 (2009) 636–652. <https://doi.org/10.1080/07373930902820804>.
- [37] E.J. Kappert, D. Pavlenko, J. Malzbender, A. Nijmeijer, N.E. Benes, P.A. Tsai, Formation and prevention of fractures in sol-gel-derived thin films, *Soft Matter.* 11 (2015) 882–888. <https://doi.org/10.1039/C4SM02085E>.
- [38] A. Granier, D. Chéreau, K. Henda, R. Safari, P. Leprince, Validity of actinometry to monitor oxygen atom concentration in microwave discharges created by surface wave in O₂-N₂ mixtures, *J. Appl. Phys.* 75 (1994) 104–114. <https://doi.org/10.1063/1.355897>.
- [39] D.V. Lopaev, A.V. Volynets, S.M. Zyryanov, A.I. Zotovich, A.T. Rakhimov, Actinometry of O, N and F atoms, *J. Phys. Appl. Phys.* 50 (2017) 075202. <https://doi.org/10.1088/1361-6463/50/7/075202>.
- [40] R.A. Gottscho, V.M. Donnelly, Optical emission actinometry and spectral line shapes in rf glow discharges, *J. Appl. Phys.* 56 (1984) 245–250. <https://doi.org/10.1063/1.333954>.
- [41] A. Bousquet, Dépôt de couches minces par plasma pulsé radiofréquence et basse pression en mélange hexaméthylsiloxane / oxygène, Thesis Manuscript, 2005.

- [42] M. El Kass, L. Brohan, N. Gautier, S. Béchu, C. David, N. Lemaitre, S. Berson, M. Richard-Plouet, TiO₂ Anatase Solutions for Electron Transporting Layers in Organic Photovoltaic Cells, *ChemPhysChem*. 18 (2017) 2390–2396. <https://doi.org/10.1002/cphc.201700306>.
- [43] D. Li, S. Elisabeth, A. Granier, M. Carette, A. Goullet, J.-P. Landesman, Structural and Optical Properties of PECVD TiO₂-SiO₂ Mixed Oxide Films for Optical Applications: Structural and Optical Properties of PECVD TiO₂-SiO₂ ..., *Plasma Process. Polym.* 13 (2016) 918–928. <https://doi.org/10.1002/ppap.201600012>.
- [44] J.F. Moulder, W.F. Stickle, P.E. Sobol, K.D. Bomben, J. Chastain, R.C. King Jr., Physical Electronics, Incorporation, eds., *Handbook of X-ray photoelectron spectroscopy: a reference book of standard spectra for identification and interpretation of XPS data*, Physical Electronics, Eden Prairie, Minn., 1995.
- [45] P. Ondračka, D. Nečas, M. Carette, S. Elisabeth, D. Holec, A. Granier, A. Goullet, L. Zajíčková, M. Richard-Plouet, Unravelling local environments in mixed TiO₂-SiO₂ thin films by XPS and ab initio calculations, *Appl. Surf. Sci.* 510 (2020) 145056. <https://doi.org/10.1016/j.apsusc.2019.145056>.
- [46] W.F. Zhang, Y.L. He, M.S. Zhang, Z. Yin, Q. Chen, Raman scattering study on anatase TiO₂ nanocrystals, *J. Phys. Appl. Phys.* 33 (2000) 912–916. <https://doi.org/10.1088/0022-3727/33/8/305>.
- [47] T. Ohsaka, F. Izumi, Y. Fujiki, Raman spectrum of anatase, TiO₂, *J. Raman Spectrosc.* 7 (1978) 321–324. <https://doi.org/10.1002/jrs.1250070606>.
- [48] W. Ma, Z. Lu, M. Zhang, Investigation of structural transformations in nanophase titanium dioxide by Raman spectroscopy, *Appl. Phys. Mater. Sci. Process.* 66 (1998) 621–627. <https://doi.org/10.1007/s003390050723>.
- [49] C. Pighini, D. Aymes, N. Millot, L. Saviot*, Low-frequency Raman characterization of size-controlled anatase TiO₂ nanopowders prepared by continuous hydrothermal syntheses, *J. Nanoparticle Res.* 9 (2007) 309–315. <https://doi.org/10.1007/s11051-005-9061-6>.
- [50] Y. Gao, X. Zhao, P. Yin, F. Gao, Size-Dependent Raman Shifts for nanocrystals, *Sci. Rep.* 6 (2016). <https://doi.org/10.1038/srep20539>.
- [51] A.G. Rolo, M.I. Vasilevskiy, Raman spectroscopy of optical phonons confined in semiconductor quantum dots and nanocrystals, *J. Raman Spectrosc.* 38 (2007) 618–633. <https://doi.org/10.1002/jrs.1746>.
- [52] D. Saha, R.S. Ajimsha, K. Rajiv, C. Mukherjee, M. Gupta, P. Misra, L.M. Kukreja, Spectroscopic ellipsometry characterization of amorphous and crystalline TiO₂ thin films grown by atomic layer deposition at different temperatures, *Appl. Surf. Sci.* 315 (2014) 116–123. <https://doi.org/10.1016/j.apsusc.2014.07.098>.
- [53] J. Zhang, P. Zhou, J. Liu, J. Yu, New understanding of the difference of photocatalytic activity among anatase, rutile and brookite TiO₂, *Phys Chem Chem Phys.* 16 (2014) 20382–20386. <https://doi.org/10.1039/C4CP02201G>.
- [54] T. Muneshwar, K. Cadien, Probing initial-stages of ALD growth with dynamic in situ spectroscopic ellipsometry, *Appl. Surf. Sci.* 328 (2015) 344–348. <https://doi.org/10.1016/j.apsusc.2014.12.044>.

Chapter 6

Novel one-step approach for the creation of TiO₂-SiO₂ NCs through PECVD and Sol Gel

TiO₂ nanoparticles (NPs), 3 nm in size, were injected inside a low-pressure O₂/hexamethyldisiloxane plasma reactor using a liquid injector and following an iterative injection sequence. The initial plasma condition was chosen from previous PECVD experiments in order to get a high quality dense SiO₂ matrix and finally produce TiO₂-SiO₂ nanocomposite (NC) thin films. However, to ascertain the SiO₂ quality while injection is processing, a first set of experiments was conducted. Actually, studying the elaboration of the SiO₂ matrix by injecting only the solvent without the TiO₂ NPs indicated a good matrix quality, as it was found to exhibit optical properties similar to thermal silica, as extracted from ellipsometry. Optical Emission Spectroscopy (OES) on these conditions revealed the impact of liquid injection on the plasma chemistry indicating that O₂ plasma can retrieve its steady state after a few seconds. Furthermore, based on the positive indications about the SiO₂ matrix and the findings of the Chapter 5, both the liquid injection and vapor precursor parameters were established aiming to address the main challenges observed when creating NCs. Transmission Electron Microscopy (TEM) indicated good distribution and non- agglomeration of the NPs. The fraction of the TiO₂ NPs inside the SiO₂ matrix was evaluated. Coherent results between Scanning Electron Microscopy (SEM) and ellipsometry were obtained, with a volume percentage of 16% and 19%, respectively for the N=10 case. From X-ray photoelectron spectroscopy (XPS) the amount was slightly smaller, 12 %, which could be explained due to the limitation of the measurement (in depth). Nonetheless, for varying injection parameter, the surface composition can be controlled. Using *in situ* ellipsometry data the alternating mode of this approach was evidenced, identifying in real time two different kinetics according to injection phases of TiO₂ NPs into SiO₂ or not. Finally, using ellipsometry and the appropriate model, the ability of this process to tune the NCs composition and optical response by tuning the injection parameters was proven.

Table of Contents

Introduction.....	211
6.1 Materials and Methods.....	212
6.1.1 TiO ₂ NPs colloidal solution	212
6.1.2 Deposition of TiO ₂ -SiO ₂ NCs thin films through the hybrid approach.....	213
6.2 Elaboration of the PECVD made SiO ₂ matrix	214
6.2.1 Deposition conditions of the SiO ₂ matrix without any injection.....	214
6.2.2 Investigation of the SiO ₂ matrix characteristics during the creation of the NCs ...	217
6.2.3 Plasma behavior during the creation of the NCs	217
6.3 TiO ₂ -SiO ₂ NCs thin films through the hybrid approach.....	225
6.3.1 Structural characterization of the TiO ₂ -SiO ₂ NCs and TiO ₂ crystallinity.....	225
6.3.2 Morphological analysis of the TiO ₂ -SiO ₂ NC surface	227
6.4 Chemical analysis of the NCs in various injection parameters using XPS	229
6.5 Characterization of the NCs using Ellipsometry.....	233
6.5.1 <i>In situ</i> monitoring of the NCs' growth	233
6.5.2 Optical and physical characteristics using Bruggeman Effective Medium Approximation (BEMA) Model.....	236
6.5.3 Following the growth and composition of a deposited layer within a one minute sequence	239
6.6 Discussion.....	242
6.6.1 Estimation of the amount of NPs distribution in the matrix through the characterization techniques	242
6.6.2 Comparison with other studies.....	243
6.6.3 The outcome of this hybrid approach.....	244
Conclusion	245
Bibliography	247

Introduction

Nowadays, there is an ongoing demand of smaller, faster and low-cost integrated systems. Achieving this often requires new materials and new processes that combine the existing ones. In this context, nanocomposites (NCs) and nanostructured materials have gained great attention, as the enhanced surface-area-to-volume ratio is a key factor for the different properties of NCs material compared to the bulk one. The properties of the resulting composite may be more likely to resemble those of the interface zones rather than those of the original constituents[1].

One of the most significant challenge in the development of such nanocomposites is the control of the growth mechanisms, of the final morphology and the level and homogeneity of incorporation of the nanoparticles using reproducible, versatile and low-cost processes. Several conventional methods have been used in the past involving soft chemistry or vacuum processes. More specifically, sol-gel method is a well-established process which is based on hydrolysis and condensation reactions.[2,3] The drawback of processes like this is the several steps until acquiring a nanocomposite thin film as well as the toxicity that of the NPs if they have to be manipulated as powder at some step of the process. [4] Moreover, vacuum processes such as PECVD or CVD, have also been used for the creation mainly of mixed oxide films, by varying the fraction of the precursor[5,6]. Sputtering approaches have been also used using a metal cathode as a precursor for the creation of metal or metal-oxide NPs. [4,7]

Recently, there have been some attempts using hybrid (aerosol-assisted, direct liquid injection etc.) approaches for the creation of nanocomposite thin films. Profili et al. [8] implemented a one-step approach for the deposition of ZnO-SiO₂ nanocomposite coatings on wood by the atomization of a stable suspension of ZnO dispersed in hexamethylsiloxane (HMDSO) in an atmospheric pressure dielectric barrier discharge (DBD). Ross et al.[9] elaborated composite films using an ultrasonic atomizer and a PECVD system using Tetraethoxysilane (TEOS) as a matrix precursor and polystyrene nanoparticles with a mean size of 96 nm. The pressure in the specific system was varied between 100 and 500 mTorr. More recently, Carnide et al. reported a new method that allowed to synthesize NPs from organometallic precursor in the reactor-injector prior to their injection in the RF low-pressure plasma reactor at 750 mTorr. The resulted nanocomposites consisted of small (6 ± 3 nm) and isolated ZnO NPs homogeneously dispersed in an amorphous hydrogenated carbon matrix. This increased interest in hybrid approaches led to the development of new direct liquid injection systems[10] and studies regarding the interactions of the liquid droplets with the low pressure plasma systems [11]. Most of these studies focus on the deposition of inorganic NPs-organic matrix NC film (also observed in the comparative table in Section 1.1.4.3, Chapter 1).

The main bottlenecks for producing nanocomposite thin films are incorporating a high-volume fraction, preventing the agglomeration of nanoparticles and dispersing them homogeneously in the matrix. Using this low-pressure system, we intend to deposit thin films incorporating the 3 nm TiO₂ NPs in a high quality inorganic SiO₂ matrix. This is accomplished by the direct liquid injection of the 3 nm TiO₂ NPs colloidal solution without a carrier gas and the addition of HMDSO vapor precursor in the low-pressure O₂ plasma. Furthermore, as several works involving atmospheric pressure plasma systems report challenges to deposit in one-step and acquire good quality NC films, we intend to investigate the differences and prospects in using low-pressure hybrid systems. Initially, the matrix quality and characteristics were studied separately and the impact of the iterative injection of the organic solvent (existing in the colloidal solution), was evaluated. Secondly, the evaluation of the nanocomposites' quality, homogeneity and distribution of the TiO₂ NPs are achieved by various characterization techniques such as High Resolution Transmission Electron Microscopy (HRTEM), Energy Dispersive X-ray spectrometry (EDX), Atomic Force microscopy (AFM) and X-ray photoelectron spectroscopy (XPS). Finally, with this work, we aim to establish this novel and versatile approach and we aim to identify the conditions for acquiring thin films oriented towards optical applications. Therefore, the optical characteristics of the film, such as its refractive index, are being extracted with spectroscopic Ellipsometry.

6.1 Materials and Methods

6.1.2 TiO₂ NPs colloidal solution

The NPs, used in these experiments, enclosed in the colloidal solution are well-defined and monodispersed with a mean hydrodynamic diameter (including species of the solvent surrounding the NP to counterbalance surface charge) centered on 3.7 nm, as it can be seen by the Dynamic Light Scattering (DLS) with Zetasizer NanoZS (Malvern) in Figure 6.1. As indicated in Chapter 2, some variation in the water content during the synthesis may change the size of the NPs. Hence, to limit possible clogging of the nozzle, we selected smaller NPs for this study than the ones used for Chapter 3 and 4. Moreover, it has been previously estimated that the double layer surrounding the NPs lies at 1 nm [13] and therefore we can assume that the actual TiO₂ nanocrystallite diameter lies at 2.7 nm. As synthesized, the solvent of this solution is a mixture of 4-methyl-1,3-dioxolan-2-one also known as propylene carbonate (PC) and 1,2-propanediol or propylene glycol (PG), with a molar fraction of 27 %:73 % respectively.

For the effective injection and evaporation of the colloidal solution inside the low pressure PECVD system (based on Chapter 5), the dilution of the colloidal solution with a more volatile one was carried out. Therefore, the final colloidal solution used was a mixture of PC:PG:Methanol with a volume fraction of 20.25:54.75:25 . The size

distribution of the diluted solution was verified with DLS and no alterations were found upon time (typically several months).

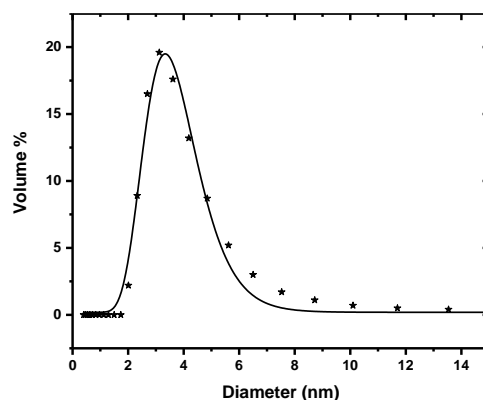


Figure 6.1: Hydrodynamic size distribution of the TiO₂ NPs used in the experiments of this Chapter inside the as-prepared (PC-PG) colloidal solution deduced from DLS.

6.1.2 Deposition of TiO₂-SiO₂ NCs thin films through the hybrid approach

For the elaboration of the TiO₂-SiO₂ NCs thin film, the colloidal solution was injected in a low-pressure reactor. The mode of injection of the colloidal solution inside the low pressure O₂ plasma has been thoroughly analyzed in Chapter 5. This time for the deposition of the SiO₂ matrix, hexamethyldisiloxane HMDSO vapor was introduced from the heated container (at 35.8 °C) without a carrier gas through a distribution ring, located 8 cm above the substrate.

For the deposition of the NC film, the colloidal solution of TiO₂ NPs was injected using the iterative mode of injection, as already described in Section 5.4.3. A scheme of this mode of injection is given in Figure 6.2. The temperature of the heated pipe was set at 150°C. As previously described, the injection can be controlled through the VapSoft software (Kemstream).

The solvent mass rate was estimated at 2.33 mg per injection. During this intermittent mode of injection (Fig. 6.1), the oxygen flow of the working gas was set at 24 sccm while the continuous flow of HMDSO precursor was maintained at 0.11 sccm. The fraction between HMDSO and O₂ was chosen in a way to facilitate the dissociation of the HMDSO molecules as well as the oxidation of the silicon precursor organic species and colloidal solution.

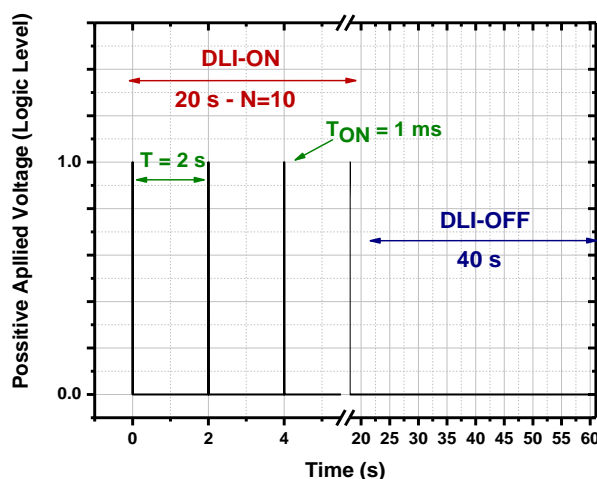


Figure 6.2: Description of the sequence including the first part of pulsed injection of the solution (Direct Liquid Injection DLI-ON) and the second part without liquid injection (DLI-OFF). T_{ON} corresponds to the duration of each pulse and T to the period between two pulses.

6.2 Elaboration of the PECVD made SiO₂ matrix

In Chapter 5, the injection of the colloidal solution inside the low pressure O₂ plasma system was thoroughly studied and explained. In order to have a better insight of the final goal of this work, which is the elaboration and characterization of the TiO₂-SiO₂ nanocomposite thin films, in this Section 6.2, the produced matrix only, is being investigated. More in detail, in Section 6.2.1, the SiO₂ matrix is elaborated under standard Plasma Enhanced Chemical Vapor (PECVD) deposition and characterized. In Section 6.2.2, the deposited matrix during the injection of the organic solvent only of the colloidal solution (without NPs) was attempted. This experiment was conducted to investigate whether the pressure variation induced by the evaporating solvent organic molecules affects the deposition rate of the SiO₂ matrix or its inorganic quality.

6.2.1 Deposition conditions of the SiO₂ matrix without any injection

The deposition of the SiO₂ matrix was carried out on a Si substrate with a precursor HMDSO flow rate set at 0.11 sccm and O₂ flow rate at 24 sccm. The valve of the turbomolecular valve was fully open to ensure the pressure set at 3 mTorr. Under these conditions, the HMDSO / O₂ fraction is at 0.005, which leads to an efficient dissociation of the HMDSO molecule and favors the oxidation of the organic groups. In Figure 6.3, the top view and the cross section of the deposited film are given. As expected, the SiO₂ layer surface is very smooth and from the cross-section view its thickness using ImageJ software was calculated at 97 ± 2 nm. Based on this small fraction between HMDSO and O₂, the inorganic quality of the matrix is expected to be high. To verify this assumption, the elaborated film was characterized with ellipsometry and its optical characteristics were compared with the thermal SiO₂ one.

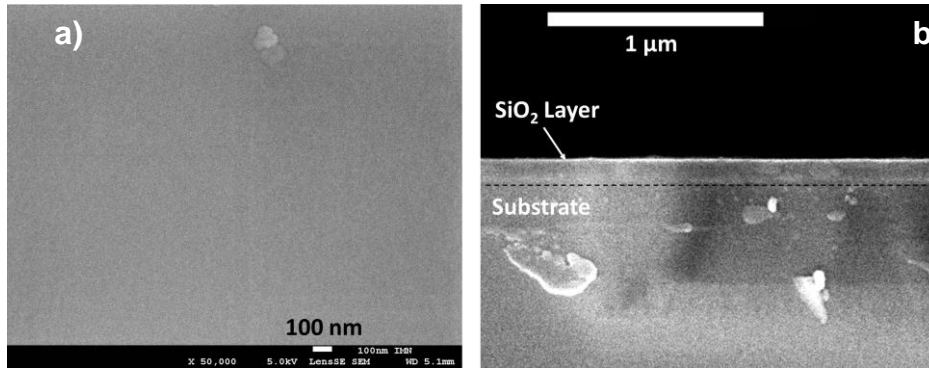


Figure 6.3: Scanning electron microscopy of the SiO₂ thin film under standard PECVD conditions with a flow rate of 0.11 sccm. a) Top view image and b) cross-section of the film.

This comparison was implemented using spectroscopic ellipsometric study. In this study, the thermal silica model was used, which is given schematically in Figure 6.4. It is a tabulated (by the software) model proposed by Herzinger et al. [14] based on the Sellmeier/Cauchy dispersion law. The measured Psi and Delta data (colored lines) and the simulated (by the thermal silica model) are given in Figure 6.4. In the overall, from Figure 6.4, despite some discrepancies found at 350 to 450 nm, the Psi and Delta data (measured and simulated) have a good matching. This means that the fit using the thermal silica model is good. The accuracy of the model and the fit is also provided by the software using the Mean Standard Error (MSE). In this case, the provided MSE had a value of 9.

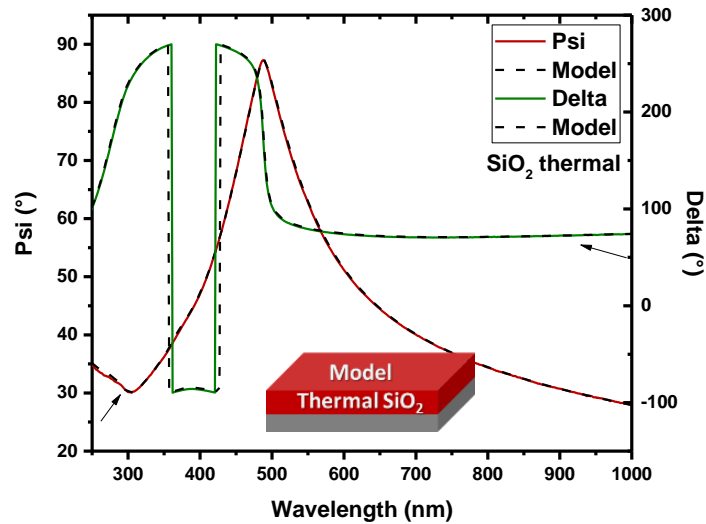


Figure 6.4: Psi-Delta values obtained from spectroscopic ellipsometry (full lines) and from simulations (dashed lines). The results are shown as a function of the photon wavelength. The model used for the simulations is based on thermal SiO₂ material. The schematic representation of the model is also shown in the figure.

In an attempt to improve the fit and reach lower MSE values, the parameters (A, B, C) describing the Cauchy dispersion law were set “free” (meaning that the software could fit its values to reach an even better MSE result). This resulted in A

equal to 1.4590 ± 0.0005 , B equal to 0.0028 ± 0.0002 , C equal to $8.7670 \times 10^{-5} \pm 9.950 \times 10^{-6}$ and a MSE at 7.

Apart from the quality of the fit, the software can provide information regarding the physical characteristics of the film such as its thickness and the optical constants such as the refractive index and extinction coefficient. For the case of the thermal silica, the thickness was found at 106.0 ± 0.2 nm and for the second fit with the “freed” parameters at 105.0 ± 0.2 nm. From this total thickness and the total duration of the deposition, the deposition rate was found at 2.1 nm/min.

Since the error of both fits, (MSE equals 9 versus 7) and the physical characteristics lie very close to each other, it appears that the two models are very similar. A way to identify this is to plot the optical constants of these two models. Hence, in Figure 6.5, the optical constants for the wavelength range of 250 to 1000 nm are plotted.

Figure 6.5 shows the refractive index (n) and the extinction coefficient (k) versus wavelength for the two models used. As expected, the extinction coefficient for all the wavelength range is at 0 for both cases. The refractive index follows the same pattern, for both models having slightly lower values for the thermal silica. Finally, at 633 nm wavelength for the thermal SiO₂ the refractive index equals to 1.46 and whereas for the second model (freed Cauchy parameters) equals to 1.47.

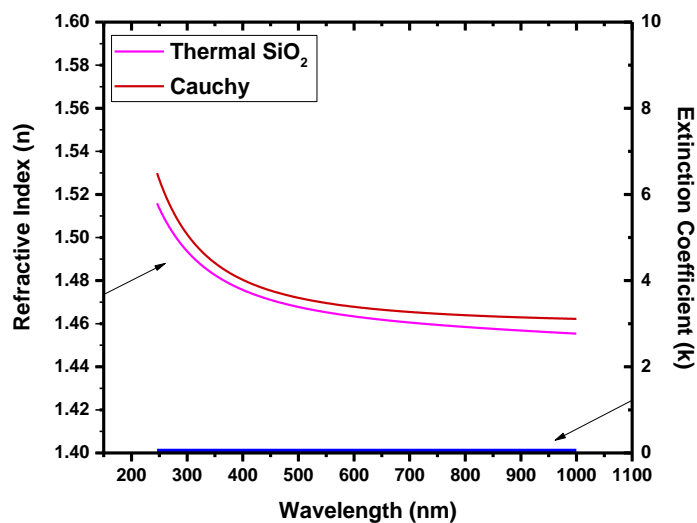


Figure 6.5: Refractive index and extinction coefficient versus wavelength for the two models used, pink and red traces for Thermal SiO₂ and Cauchy model, respectively.

Compared to 1.457 generally reported for thermal silica [15] our SiO₂ film, made under the conditions explained above, lies very close. The value of the index is found only slightly (by 0.01) higher. This is a proof of the inorganic quality of the produced PECVD-made silica along the total volume of the film.

Hence, in the following Section, preserving the specific deposition conditions, we will investigate the impact of the injected solvent on the SiO₂ matrix quality. To achieve that, the solvent of the colloidal solution without the NPs will be injected.

6.2.2 Investigation of the SiO₂ matrix characteristics during the creation of the NCs

In Section 6.2.1, the characteristics and the inorganic quality of the SiO₂ matrix were studied using mainly ellipsometry and compared with thermal silica data. Unfortunately, during the injection of the NPs the pressure variation (due to the injection of the solvent as discussed in Chapter 5) and the release of organic molecules (from the solvent) inside the low-pressure O₂ plasma system may alter the characteristics mentioned above. Consequently, we conducted the experiments of depositing the SiO₂ matrix (analyzed in Section 6.2.1) while injecting the solvents of the colloidal solution without the NPs.

The injection parameter (N) was varied and the films were elaborated with N=2, 5, 10 and 30, for 50 minutes. As expected, for different N, different pressure variation (read on the go from the gauge) was measured as reported in Table 6.1. During the injection DLI-ON time (which is N*2sec), each pulse injects liquid in the low pressure system which leads to an increase in pressure. The pressure at this time of the pulse can reach up to 20 mTorr (column PULSE in Table 6.1) and as long as there is no injection (NO PULSE column in Table 6.1), the pressure decreases. When the pulsing stops (DLI-ON is over) for all the cases apart N=30 and no injection takes place, the pressure comes back to the steady state 3 mTorr within approximately 2 seconds. For N=30, since no OFF time exists (DLI-OFF) within the one-minute sequence (30*2 s = 60 s case of conventional pulsing mode), during the pulse the pressure reaches 20 mTorr and then it decreases only to 16 mTorr. This possibly happens as, in this mode of operation, the system does not have enough time (no DLI-OFF time) to discard the extra accumulated molecules in the volume and reach its steady state before another injection pulse begins.

Table 6.1: Experimental and ellipsometric results of the elaborated SiO₂ matrixes.

N	Pressure (mTorr)		Thickness (nm)	Dep. Rate Total (nm/min)	MSE
	PULSE	NO PULSE			
2	12	3	95	1.9	12
5	16	3	83	1.7	9
10	20	3	69	1.4	11
30 (max)	20	16	23	0.5	8

During this matrix deposition, we were able to monitor *in situ* the growth with ellipsometry, acquiring the ellipsometric data. Using the model of Section 6.2.1 (Cauchy dispersion law with fixed parameters which significantly resembles the one of the classical thermal SiO₂) we fitted these data and extracted information regarding

the physical characteristics of the film. Therefore, the results are given in Table 6.1 and the thickness evolution versus time of the deposition is given in Figure 6.6, for all the cases. In detail, the thickness given in Table 6.1 is obtained at the end of the deposition and the deposition rate is extracted from the slope of the linear curves plotted in Figure 6.6. Finally, MSE is the Mean Square Error indicating how accurate the fit is. It appears that for higher N, and for the same duration of deposition, the thickness reached is lower, meaning that the injection of solvents and the associated pressure variation seems to hamper the deposition rate of silica. Moreover, the MSE remains in low levels, indicating that the quality of the matrix is not degraded by the solvent injection or the hampered deposition rate, preserving its inorganic quality.

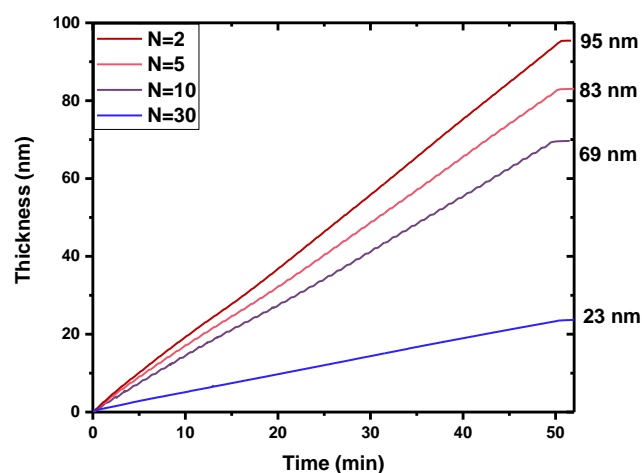


Figure 6.6: Thickness evolution versus time extracted from the dynamic fitting of the *in situ* ellipsometry data, for different solvent only injection parameters (N). At the end of each curve the final thickness is given.

In Figure 6.6, it appears that the growth of the film exhibits some discontinuous variations, which are more pronounced for N=5 and N=10. To investigate whether or not this deposition rate variation for different N is linked with the pressure variation, the dynamic trajectories of Is and Ic are plotted in Figure 6.7, both for N=5 and N=10.

Indeed, the evolution of the Is and Ic curves in Figure 6.7, is disrupted by the solvent injection. This pattern is the exact opposite from the findings of Chapter 5, as the plateau is reached during the injection. Actually, during the injection of the colloidal solution in the O₂ plasma (Section 5.6, Chapter 5), the Is and Ic were evolving whereas during the OFF time they were stable. Using the model of thermal silica (Section 6.2.1), the dynamic thickness evolution is plotted in Figure 6.8, for the first ten minutes.

The results of Figure 6.8 indicate that during the DLI-ON time, for both cases, the thickness does not evolve as expected (the deposition rate is severely decreased) whereas during the DLI-OFF time the growth continues, following the usual deposition rate. Except for N=2, this discontinuity finally leads to a lower average

deposition rate compared to the standard SiO₂ film of Section 6.2.1 (2.1 nm/min). The higher the value of N, the longer the duration of the pressure being at higher levels is. Finally, this results in the disruption of the growth and a decrease in the deposition rate.

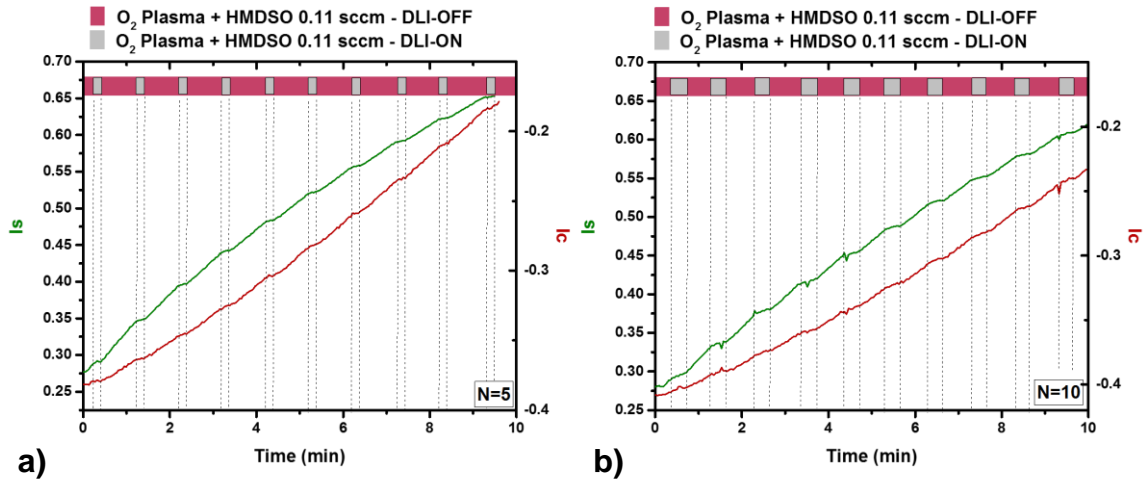


Figure 6.7: Dynamic Is and Ic trajectories in the first 10 minutes of the deposition, for N=5 and N=10. The gray and red parts in the top bar corresponds to the DLI-ON and DLI-OFF injection time, respectively.

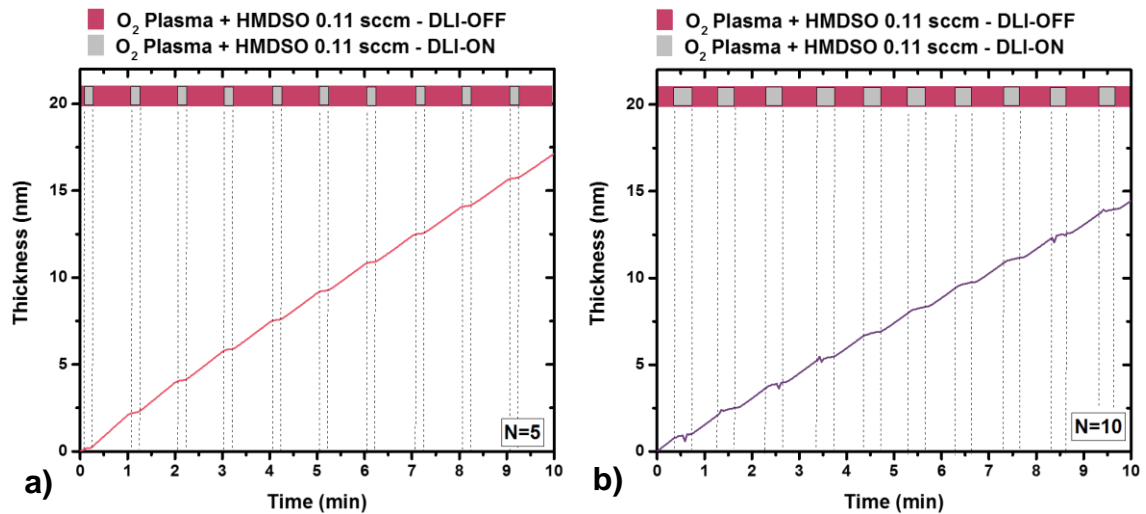


Figure 6.8: Dynamic evolution of thickness in the first 10 minutes of the deposition for a) N=5 and b) N=10. The gray and red parts in the top bar corresponds to the DLI-ON and DLI-OFF injection time, respectively.

From the data obtained from Table 6.1, we can plot the deposition rate as a function of the injection parameter or as a function of the DLI-ON (=N*2 s) time divided by the total time of the sequence (1 min). Hence, in Figure 6.9, both the Injection parameter (N) and the fraction of the DLI-ON from the total sequence are given. In the x-axis as expected, for the maximum N = 30, the fraction equals to 1 (“conventional pulsing mode”). In the y-axis of the figure the deposition rate is given, which as stated previously decreases for higher N meaning higher injected solvent.

This decrease appears experimentally to be linear (red fitted line). This means that the plasma efficiency in the deposition depends on the duration of the injection step and hence on the resulting pressure increase.

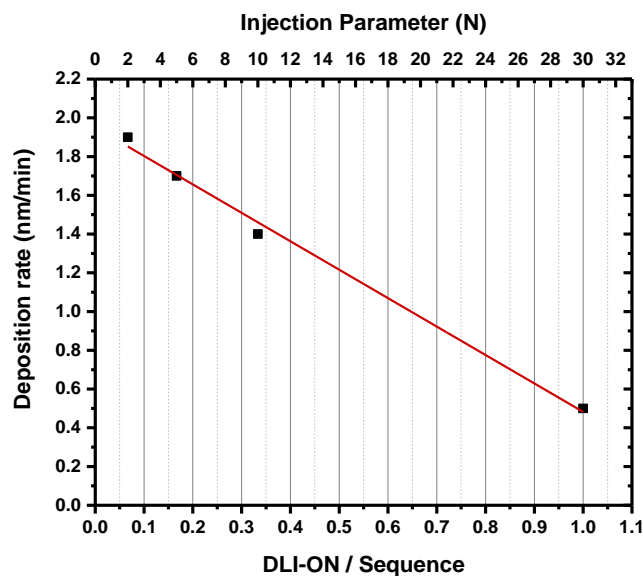


Figure 6.9: Deposition rate of the SiO₂ matrix versus the injection parameter, N, (top x-axis) or the DLI-ON/ Sequence (bottom x-axis). Red line represents the linear fit of the scatter points.

Based on these findings, one would wonder, what is the exact mechanism leading to this less efficient deposition for higher pressures. It was shown Chapter 5 that in the specific O₂ low-pressure plasma a significant variation concerning the plasma density, electron temperature, ion energy and O atoms density occurs, for different pressures. As the pressure increases from 3 mTorr towards 25 mTorr, the plasma density, electron temperature, ion energy decrease whereas the O atoms density increases. It is known from literature that the HMDSO vapor molecules are preferentially broken by electron impact and the deposited fragments are being oxidized on the substrate surface by the O atoms. Hence, the plasma characteristics found at higher pressures do not favor the fragmentation of the HMDSO vapor molecule leading to a lower deposition rate.[16]

As a conclusion, this study gives insight in the impact of this iterative mode of NPs injection on the matrix quality. Ellipsometry did not reveal significant discrepancies from a good quality inorganic film, with the refractive index lying at 1.47 vs 1.46 for the thermal SiO₂[14,15]. In addition to this, the pressure variation indicated a vice versa effect than the one observed during injection of the colloidal solution in an O₂ plasma (Chapter 5). This is a presage that during the simultaneous deposition (NPs and matrix) an alternating deposition of the NPs and the matrix driven by the N parameter will occur.

6.2.3 Plasma behavior during the creation of the NCs

In the previous Section we have seen that the value of N affects the pressure variation leading to a decrease of the deposition rate of the SiO₂ matrix for higher N injection parameter. To investigate further the impact of this solvent injection inside the O₂/HMDSO plasma, Time Resolved Optical Emission Spectroscopy (OES) was conducted. As in the case of the injection of the colloidal solution in the O₂ plasma (Chapter 5), we followed the emission intensities of Ar and O lines at 419.8 nm and 394.5 nm respectively as well as the ones of CO at 297.7 nm, OH at 306.4 nm and H δ at 410 nm. The latter correspond to the emission of excited CO, OH and H species formed by electron impact reactions with the by-products of the oxidation of HMDSO and the solvent. Each emission was measured for approximately 2 sequences. Since we used a photomultiplier as a detector, the data for the different lines were not recorded simultaneously. Hence, the data were post-treated in order to be aligned with each other. As a reminder, during these experiments, in the solvent, no NPs were included.

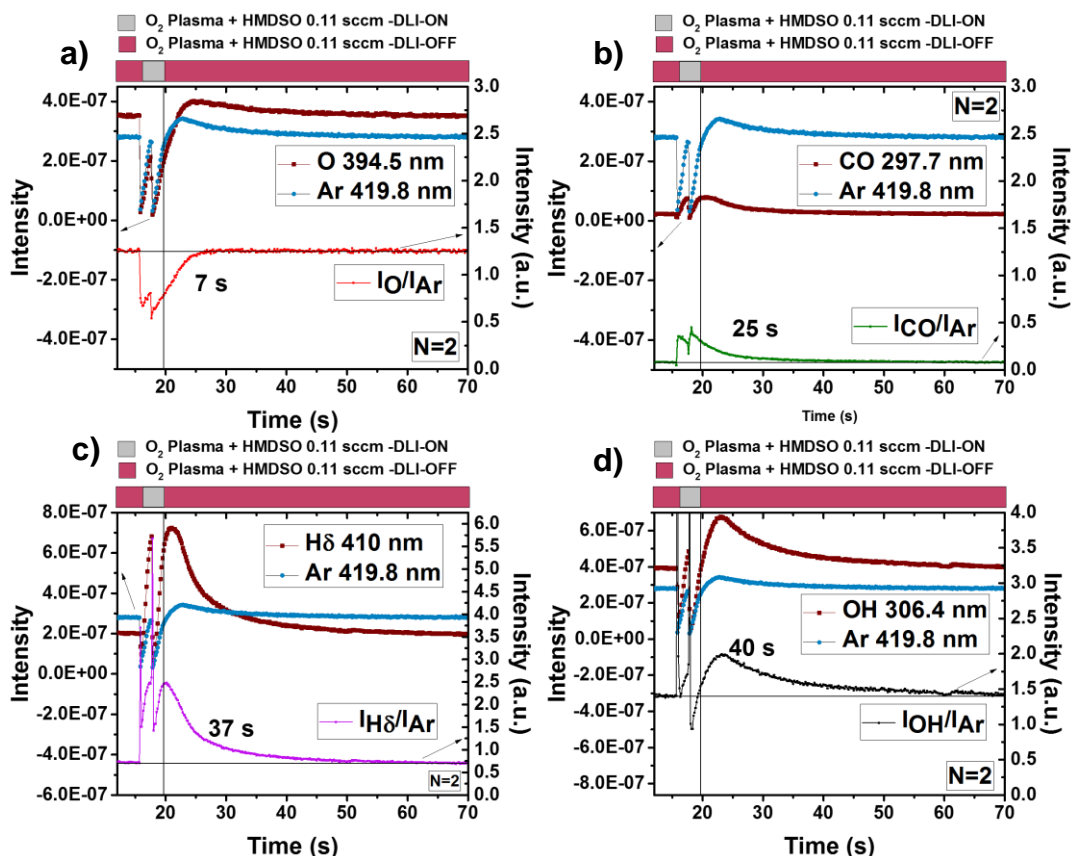


Figure 6.10: Time Resolved Emission intensities of and Ar at 419.8nm, O at 394.5nm, CO at 29.67 nm, H δ at 409.9nm and OH at 306.4 nm for N=2. The gray and red parts in the top bar correspond to the DLI-ON and DLI-OFF injection time during O₂/HMDSO Plasma, respectively. No NPs were injected, only the solvents of the colloidal solution. In figure a) O and Ar emission intensities are given. In figure b) the CO and Ar ones. In figure c) H δ and Ar ones. Finally, in figure d) OH and Ar ones. The normalized intensity of each emission is given in the right-hand side y-axis.

In Figures 6.10, 6.11 and 6.12 the time variations of these emission intensities are given for N=2, 5 and 10, accordingly. In these figures, the gray and red parts in the top bar correspond to the DLI-ON and DLI-OFF injection time, respectively. In each of these sub-figures, on the left hand axis the a) O, Ar emission intensities b) CO and Ar emission intensities c) H δ and Ar emission intensities and d) OH and Ar emission intensities are given.

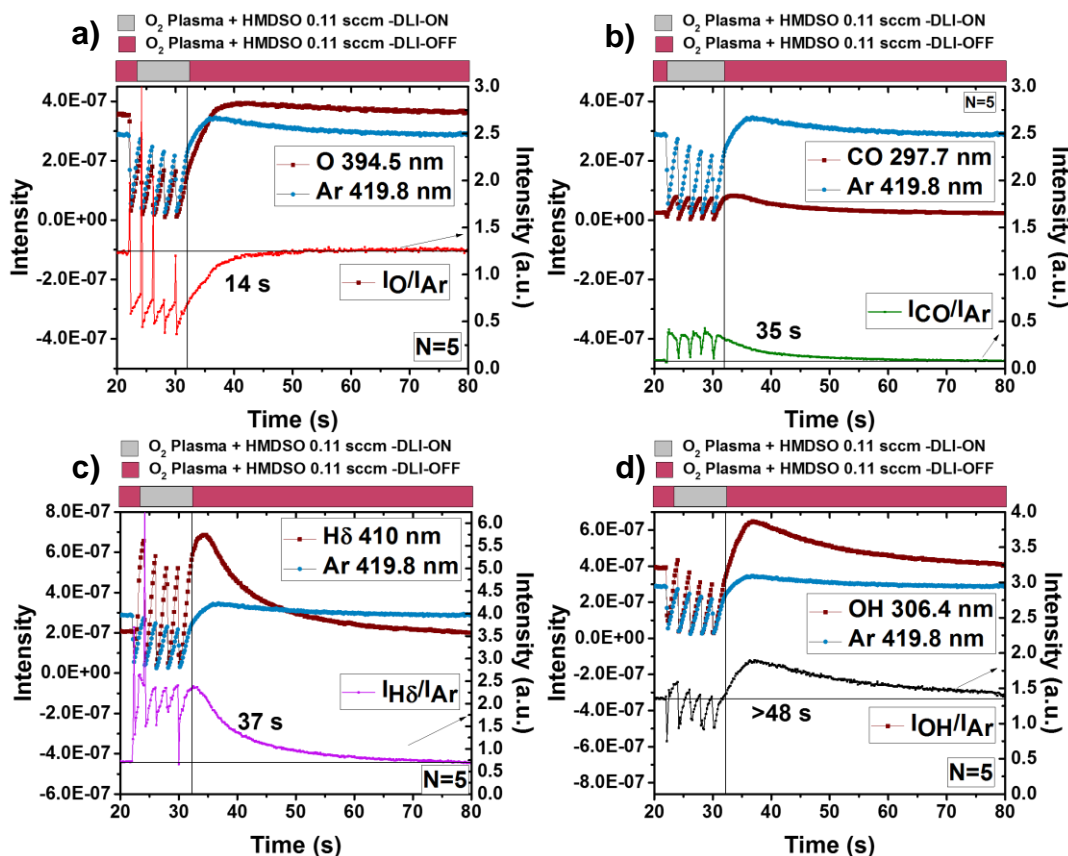


Figure 6.11: Time Resolved Emission intensities of and Ar at 419.8nm, O at 394.5nm, CO at 29.67 nm, H δ at 409.9nm and OH at 306.4 nm for N=5. The gray and red parts in the top bar correspond to the DLI-ON and DLI-OFF injection time during O₂/HMDSO Plasma, respectively. No NPs were injected, only the solvents of the colloidal solution. In figure a) O and Ar emission intensities are given. In figure b) the CO and Ar ones. In figure c) H δ and Ar ones. Finally, in figure d) OH and Ar ones. The normalized intensity of each emission is given in the right-hand side y-axis.

From the emission intensities of Figures 6.10, 6.11 and 6.12, several things are observed. First, due to the measurement resolution of the OES having a measurement every 0.16 seconds, it is possible to follow each pulse (each solvent injection) of the DLI-ON. Moreover, from a closer look in the figures, it appears that during each injection, the emission intensities of the Ar and O lines are decreased trying to retrieve their steady state value within the pulses. As the delay is not long enough after one pulse (~ 2 s), a new pulse comes along inducing again a decrease in the emission intensity. The same observation in the opposite direction is attained by the emission

intensities of CO, OH and H δ . This time, with each pulse a rapid decrease and then increase of the intensities are observed preserving higher values than the steady state one when the injection is stopped. For all the N injection parameters, the minimum and maximum value of all the intensities appear to be similar. The ratio of this decrease of Ar is found by these figures at around ~ 10 , a value that can be justified by the pressure increase during the injection. This ratio has already been proven in Chapter 5, Section 5.3.4 and Figure 5.17. There it was shown that all the intensities at the higher pressure (25 mTorr) are decreased, as the collisions are less efficient and the electron temperature has lower values than that at 3 mTorr. Hence, from 3 to 25 mTorr there is a decrease in the Ar emission intensity by a factor of 10.

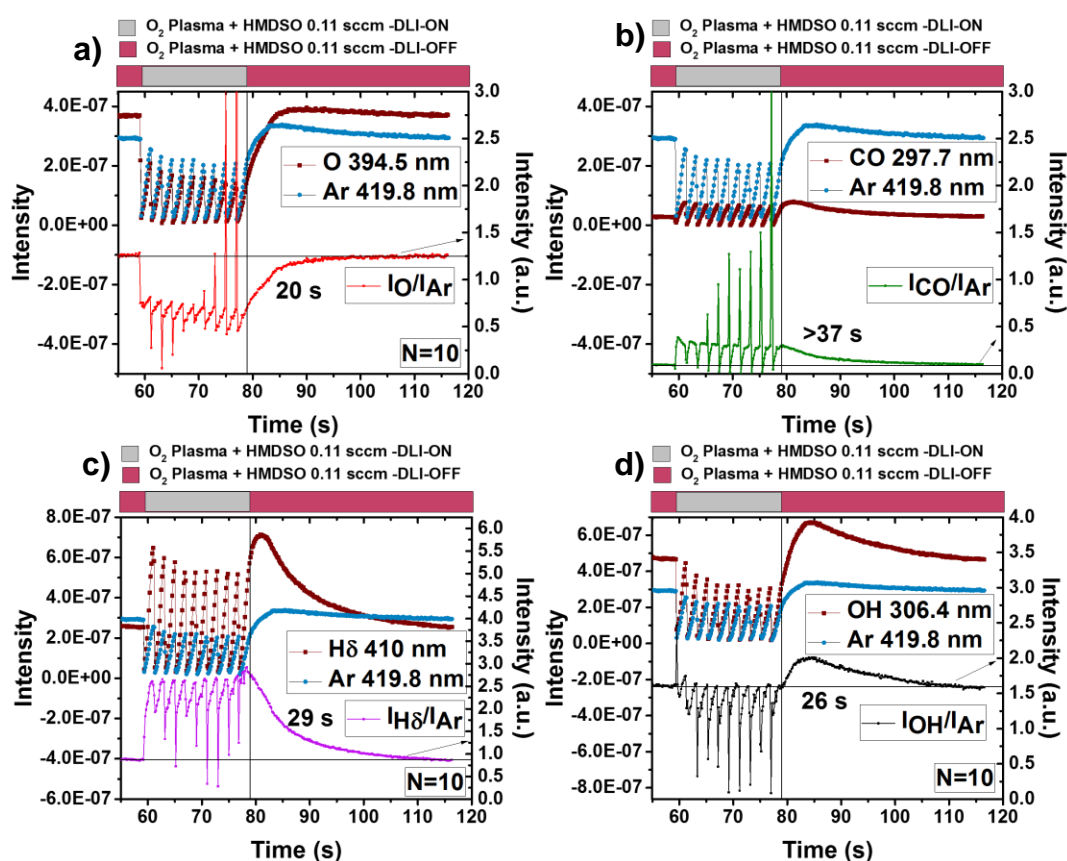


Figure 6.12: Time Resolved Emission intensities of and Ar at 419.8nm, O at 394.5nm, CO at 29.67 nm, H δ at 409.9nm and OH at 306.4 nm for N=10. The gray and red parts in the top bar correspond to the DLI-ON and DLI-OFF injection time during O₂/HMDSO Plasma, respectively. No NPs were injected, only the solvents of the colloidal solution. In figure a) O and Ar emission intensities are given. In figure b) the CO and Ar ones. In figure c) H δ and Ar ones. Finally, in figure d) OH and Ar ones. The normalized intensity of each emission is given in the right-hand side y-axis.

For all the N injection parameters, the minimum and maximum value of all the intensities appear to be similar whereas small differences are observed on the time needed right after DLI-ON (first seconds of red bar indicating DLI-OFF) for the values

to reach the steady state. Hence, for the Ar line, the time for going back to the steady state is 3 seconds for N=2 and 5 seconds for N=5 and 10.

However, to get more insight regarding those different delays, actinometry [17] has to be carried out, in the same way as described in Chapter 5. The results of this normalization are given in the right-hand side of Figure 6.10, 6.11 and 6.12, for N=2, N=5 and N=10 accordingly. In these figures, some spikes are observed being related to some discrepancies in the millisecond range during the alignment of O, CO, OH or H δ and Ar emission intensities and their division.

From the normalized intensities, the decrease of O and the increase of H and CO densities at the beginning of the DLI-ON are thus clearly evidenced. The normalized OH intensity evolves more singularly. From these plots, it is also interesting to note that during the DLI-ON the time in-between 2 pulses (2 seconds) is insufficient to allow the return to the steady state concentration of all these species. At the end of DLI-ON, H and CO densities decrease directly towards the steady state whereas the OH one exhibits a peak-like shape (indicating an accumulation), before reaching the steady-state. From these normalized data, the time delay from the point where the DLI-ON time is over until reaching the steady state have been extracted and are plotted in Figure 6.13.

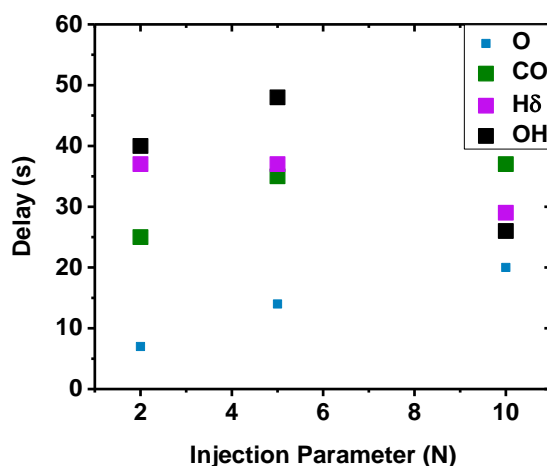


Figure 6.13: Time delay for varying N injection parameter, extracted from the normalized data of Figures 6.10, 6.11 and 6.12, from the point where the DLI-ON time is over until reaching the steady state. Small square blue symbol represents O normalized emission intensities, big green square the CO, big purple square the H δ and big black square the OH.

From these results, the delay for O is in the range of 10 s and increases with the injection parameter N. For CO and H, the dependence on N is more difficult to assess but the delays now range between 20 and 40 s. This value is coherent with the lifetime of solvent droplet (refer to chapter 5). However, from the delayed decrease of the normalized intensity of OH, the hypothesis that water molecule also formed during the oxidation of solvent or HMDSO may be adsorbed on surfaces can be formulated thus delaying the return of OH emission to its steady state value. Actually,

the amount of HMDSO is very low compared to the O₂ molecules and the solvent content.

Given to the complex conditions during the injection further experiments need to be done, using a CCD to get free of errors in the time scale due to the division of intensities which are not recorded simultaneously, to discriminate if different reactions regarding OH radicals and water, are involved and get more insight of the emissions evolution with N.

From this study, we have identified significant points of this complex deposition process. We have seen that time resolved OES is a sensitive tool allowing us to observe with high resolution each solvent injection and its impact on the O₂ plasma. This also indicates that as N increases and more solvent is injected, the DLI-OFF is reduced (DLI-OFF=1 minute – DLI-ON), leading to the accumulation of species in the reactor and saturation of the system. This could be the reason why the experimentally observed linear dependence of the deposition rate decreases with the N parameter (Figure 6.9). Finally, this work is a proof that despite the low-pressure system and the injection of liquid inside the plasma, Ar and O emission intensities never reach the value of zero, indicating that with this approach we could indeed perturb the plasma chemistry but maintain the plasma ignited.

In the following Section, the simultaneous deposition of the SiO₂ matrix and the injection of the TiO₂ NPs in the colloidal solution will be attempted. A great emphasis will be given on the distribution of the NPs inside the matrix and in the next Sections, 6.4 and 6.5, XPS and ellipsometric analysis will involve the validation of the agility of this hybrid process. In other words, Section 6.3 establishes the possibility of creating actual nanocomposite films and Sections 6.4 and 6.5 explore the possibilities of tuning the chemical and optical properties of the films through the process.

6.3 TiO₂-SiO₂ NCs thin films through the hybrid approach

In this Section, using the initial injection case of N=10, will be established the hybrid approach which enables the creation of NCs thin films. The structural and physical characteristics of the produced film will be analysed using various characterization techniques.

6.3.1 Structural characterization of the TiO₂-SiO₂ NCs and TiO₂ crystallinity

Cross section structural analysis of the elaborated NC thin film (with N=10 and deposition duration of 50 minutes) was conducted with TEM and S-TEM with the results given in Figure 6.14. For the effective characterization of the samples through TEM, the deposition was carried on Tin doped Indium oxide deposited on polyethylene terephthalate (ITO (50nm)/PET(125µm), Sheldahl). Through multiple measurements on low magnification images (images such the one of Fig. 6.14a), the

thickness of the film was measured at 85 ± 6 nm providing a variation of thickness along the film. The roughness of the substrate seen in Figure 6.14 is possibly accounted at the (thin slices) preparation method, and it was considered for the measurements of the thickness. The contrast difference from the ITO and the substrate was the initial point of each thickness measurement. Using high-resolution images on the rectangular area (black contour) shown in Fig. 6.14b and based on the contrast between the amorphous matrix and the basal planes of the nanocrystals, some TiO₂ NPs were identified and stressed with white rounded contour shapes (Figure 6.14c). An agglomeration of these NPs is not identified but rather assembling of two or three NPs having the SiO₂ matrix between them. The latter could be a result of observing nanoparticles deeper in the thickness of the cross section. Using ImageJ software, the size of each of these NPs (14 nanoparticles identified) was extracted and their mean value lied at 2.7 ± 0.4 nm. Consequently, if compared to the DLS results shown in the previous section, which gives us the hydrodynamic diameter of the NPs (2.7 nm + 1 nm), the assumption that upon injection the NPs' size remains intact, is confirmed. Finally, the NPs seem well dispersed inside the matrix. The HAADF-STEM images given in the same figure confirm that both oxygen and silicon (Fig. 6.14e,f) are homogeneously distributed along the cross section of the film. Ti on the other hand, (Fig. 6.14g), linked to the TiO₂ NPs is identified with some small dots verifying the TEM images (Fig. 6.14c) and their distribution along the film.

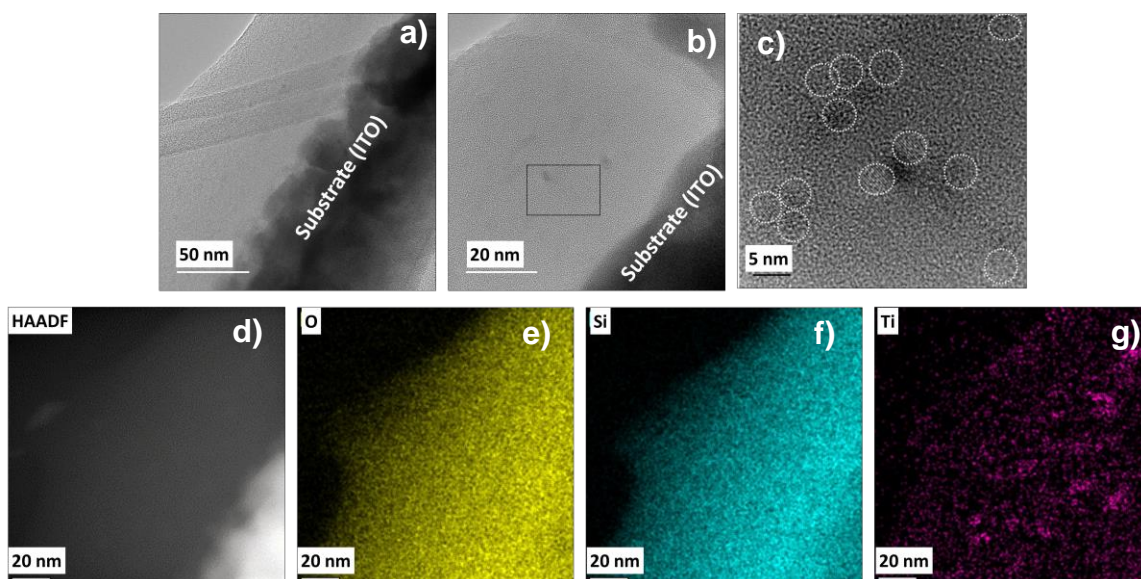


Figure 6.14: TEM cross section of the NC thin film a) at low magnification, b) at high magnification and c) higher magnification image focusing on the distributed TiO₂ NPs inside the SiO₂ matrix. HAADF-STEM images of the SiO₂-TiO₂ NCs d) in a selective area. Elemental mapping for e) O, f) Si and g) Ti.

The crystalline phase of the TiO₂ NPs was identified using Raman. Figure 6.15 presents the Raman spectra of the elaborated NC with a focus on the Eg anatase peak. Raman modes can be assigned to the Raman spectra of the anatase crystal: 144 (Eg), 200 (Eg), 400 (B1g), 513 (A1g), 518 (B1g) and 642 cm⁻¹ (Eg) [19,20]. Since the

analysis of intensity requires to be done cautiously, especially for thin films, the comments were focused on the peak position shifting. In this figure, it can be observed that the Eg peak lies at 154 cm⁻¹, a value shifted from the anatase expected at 144 cm⁻¹ [21,22]. It is well-established experimentally that Raman spectra of low-dimensional crystals of semiconductors are modified when compared to the corresponding bulk crystal spectra namely, (1) the Raman peaks are asymmetrically broadened and (2) their positions are shifted [23,24]. In this context, the results presented in Figure 6.10 confirm that the deposited TiO₂ NPs distributed in the SiO₂ matrix are anatase crystallites and in nanometric size, as observed by TEM.

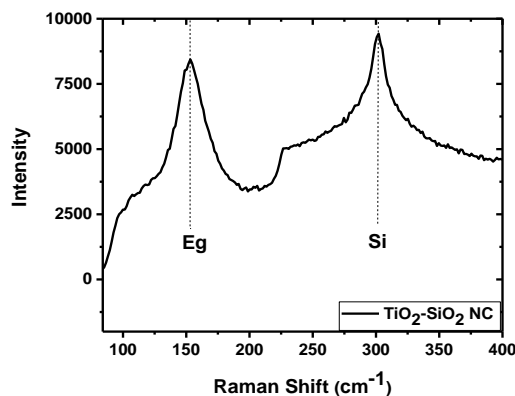


Figure 6.15: Raman spectra indicating the Anatase Eg band at 154 cm⁻¹ and the second order Si band peak at 303 cm⁻¹.

6.3.2 Morphological analysis of the TiO₂-SiO₂ NC surface

The surface morphological analysis of the TiO₂-SiO₂ NC thin film was investigated with SEM and AFM as shown in Figure 6.16. From the SEM top view image (Fig. 6.16a), the surface of the film is homogeneous and nanostructured, revealing some rounded domains. Since the resolution of the SEM is at 10 nm, one can understand that the exact identification and quantification of these domains is impossible. From the AFM scan (Fig. 6.16b), the Rq (RMS) roughness of the nanocomposite film was deduced at 2 nm. Since the deposition on silicon substrate should not lead to additional roughness or nanostructuration especially for the deposition of amorphous SiO₂ (matrix), the nanostructured pattern also observed with AFM can be linked to the NC morphology. These same rounded domains (as in SEM) appear with a bright yellow-white contrast, as they are located higher on the z-axis and their size is higher than the one of the initial NPs in solution measured by DLS in Figure 6.1. From detailed analysis of multiple AFM scans at low and high magnification, the mean size of the domains was extracted and plotted as a histogram in Fig. 6.16c. The fitting by a Log-Normal distribution, provided a mean size of 23.0 nm of these rounded domains and a standard deviation of 5 nm.

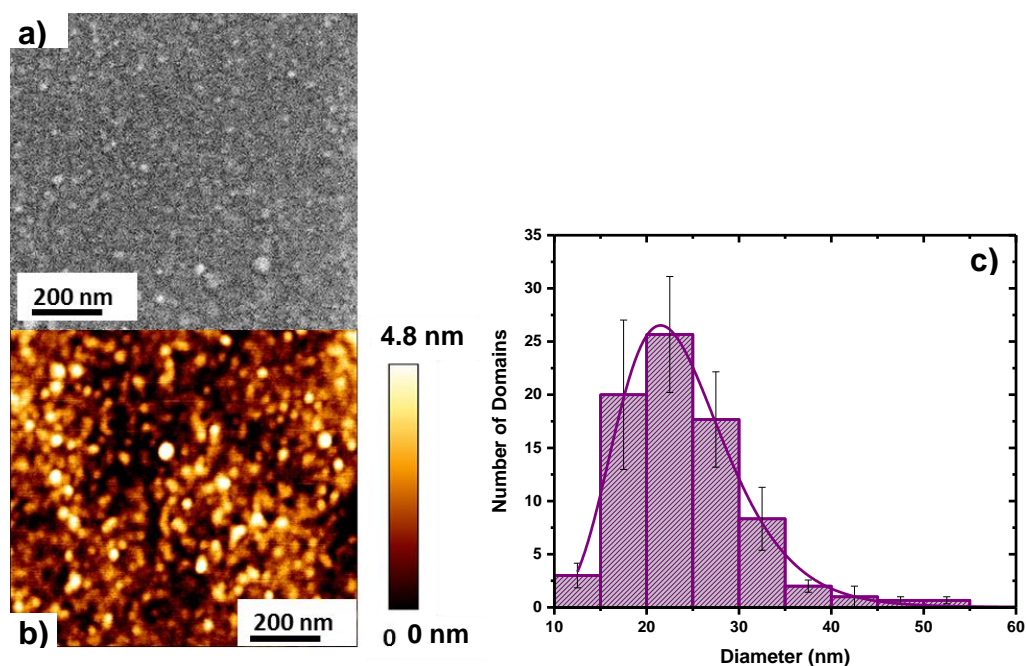


Figure 6.16: a) SEM secondary electron image of the surface, b) AFM scan of the TiO₂-SiO₂ NCs thin film and c) size distribution of the rounded domains deduced from the AFM scans.

From TEM analysis, singular NPs were identified without a clear indication of agglomerations but a rather assembling of two to three NPs in their proximity. In addition to this, from the Raman spectra a shift from the nanometric Anatase Eg band in Figure 6.10 is not observed, leading to the conclusion that the size of the initial NPs remains. This time, from the size distribution of the rounded domains in Figure 6.16b, a higher mean size of 23 nm arises. This could be a possible indication of NPs agglomerations or domains created by the distribution of the TiO₂ NPs inside the SiO₂ molecules of the matrix.

From the high magnification local analysis both from TEM and SEM/AFM, the elaborated NC film indicated a rather homogenous structural profile. To have an overall view of this film, low magnification EDS mapping of the film surface was established. In order to extract adequate resolution of each element, a thicker film was used ($d=224$ nm). The results are given in Fig. 6.17, and reveal a singular distribution of the titanium element over a 2552 μm^2 surface. In contrary, both silicon and oxygen elements are homogeneously distributed over the surface of the film, confirming the local HAADF-STEM results shown in Figure 6.14. The distribution of the titanium element relates to rounded ring shape formation. A first hypothesis could be the well-known coffee-ring effect, happening when the solute is likely to migrate in the edge of the evaporating droplet due to the formation of preferential flow and faster evaporation at this area. [25–27] Overlapping of this coffee ring during the growth of the SiO₂ matrix, could be the explanation of the thickness variation (± 6 nm) deduced from TEM cross-sections (Figure 6.14a).

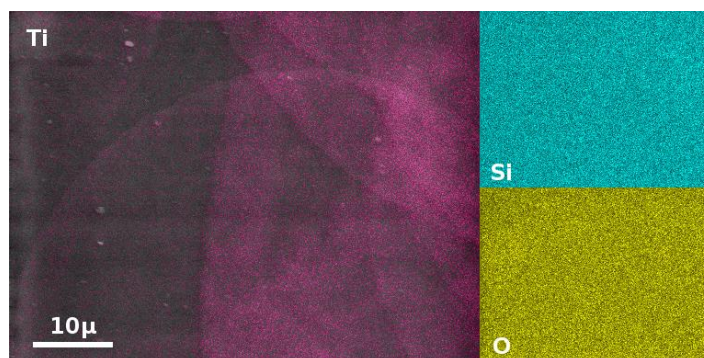


Figure 6.17: SEM image and EDX map of Ti superimposed (left) and corresponding EDX maps of Si and O (right).

Avoiding the superimposed areas shown by the EDX map, a quantitative EDX analysis was conducted on a large surface area (2640 μm²) to overcome the problem of homogeneity. Hence, measuring large area allowed us to ensure a more representative result. In the present case, in order to increase the EDX signals. We deposited on ITO/PET such as no additional Si coming from the substrate would interfere with the quantification of the SiO₂ matrix. Therefore, the sample is a multilayer including: first, 224 nm of NC including Ti, Si, O, second, 50 nm of ITO constituted of Sn, In and O third PET incorporating C and O. The weak energy of the EDX peaks for carbon and oxygen and the strong interactions throughout the layers for these elements do not allow us to rely on the results. Several factors reduce the accuracy of the quantitative analysis by EDX. The analysis depth prevents a measurement of the first layer only (without the substrate) that would lead to more reliable results. This is due to the energy of the electron beam that passes through the layer during the measurement. Stratagem (chapter2) enables to overcome this problem. Hence, from this analysis the fraction of titanium over silicon content is given in Table 6.2. For N=10, 15 at% of Ti and thus of TiO₂ could be incorporated in the nanocomposite.

Table 6.2: Quantitative results by EDX on large surface (2640 μm² - magnification X1000).

	Weight %	Atomic %
Silicon	76.9	85
Titanium	23.1	15

6.3.3 Plasma characteristics during the TiO₂-SiO₂ NC deposition

In the same fashion as in Section 6.2.3, the emission intensities of Ar and O lines at 419.8 nm and 394.5 nm respectively as well as the ones of CO at 297.7 nm, OH at 306.4 nm and H_δ at 410 nm were followed. This was carried out with Time Resolved OES for the N=10 injection parameter (the case of the NC studied in this Section 6.3). The difference with Section 6.2.3 is that this time, TiO₂ NPs are included in the

colloidal solution. In addition, these emission intensities were normalized with that of the Ar, and the results are given in Figure 6.18. More explicitly, on the left-hand axis, the initial data are given whereas on the right hand axis the normalized ones.

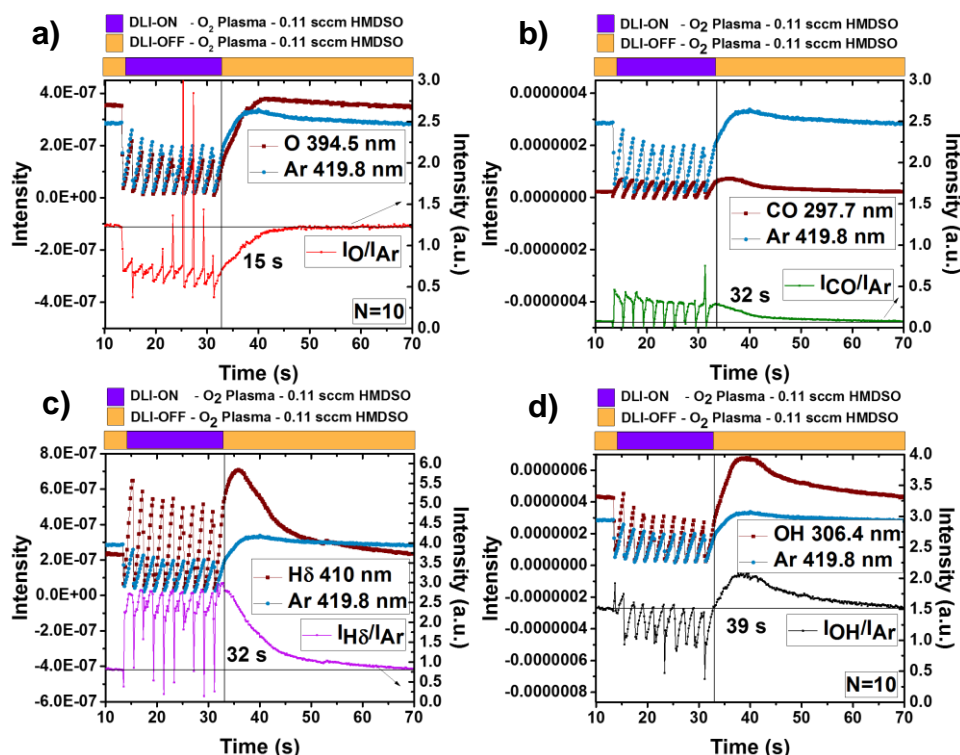


Figure 6.18: Time Resolved Emission intensities of and Ar at 419.8nm, O at 394.5nm, CO at 29.67 nm, H δ at 409.9nm and OH at 306.4 nm for N=10. The purple and orange parts in the top bar correspond to the DLI-ON and DLI-OFF injection time during O₂/HMDSO Plasma, respectively. Here, the TiO₂ NPs were included in the colloidal solution. In figure a) O and Ar emission intensities are given. In figure b) the CO and Ar ones. In figure c) H δ and Ar ones. Finally, in figure d) OH and Ar ones. The normalized intensity of each emission is given in the right-hand side y-axis.

If compared with the results in Section 6.2.3 we observe that the maximum and minimum intensities of this emissions lie on the same levels. In addition, it appears that the delay when DLI-ON is over until the steady state has similar duration. Actually, the delay of the normalized intensity of O and CO is found at 5 seconds lesser than in Section 6.2.3 whereas H δ and OH have an increased delay by 3 and 13 seconds accordingly.

This indicates that presence of the NPs inside the colloidal solution does not seem to significantly affect the chemistry of the plasma. Further experiments need to be carried out to discriminate the influence of the different reactants (HMDSO, solvent, NPs), in particular how they affect the OH radicals and the accumulation of H₂O.

6.4 Chemical analysis of the NCs in various injection parameters using XPS

The chemical analysis of the NC surface was carried out with XPS. In Figure 6.19, the atomic concentration of O 1s, Ti 2p, C 1s and Si 2p can be seen, for the case N=10 studied in Section 6.3. In each figure, the atomic concentration in percentage is given, considering the components included in each XPS peak. The contribution of oxygen bonded to silicon atoms, noted as O-Si appears at the binding energy of 532.6 eV whereas the one corresponding to the bond with titanium, noted as O-Ti, at 530.5 eV. [6] A noteworthy observation in this figure is the fact that no peak corresponding to Ti-O-Si can be found, as expected for a nanocomposite, confirming that only two different phases are detected in the film.[28] As reported by many authors [13,29], the signal of titanium element in XPS results from two separated peaks that can be attributed to Ti 2p_{3/2} and Ti 2p_{1/2}. The 2p_{3/2} peak lies at 458.5 eV as expected for Ti⁴⁺ cations in TiO₂. Since the injected colloidal solution of TiO₂ NPs was synthesized in an organic solvent, the contribution of carbon element was investigated. Therefore, three components were identified in the C 1s peak.

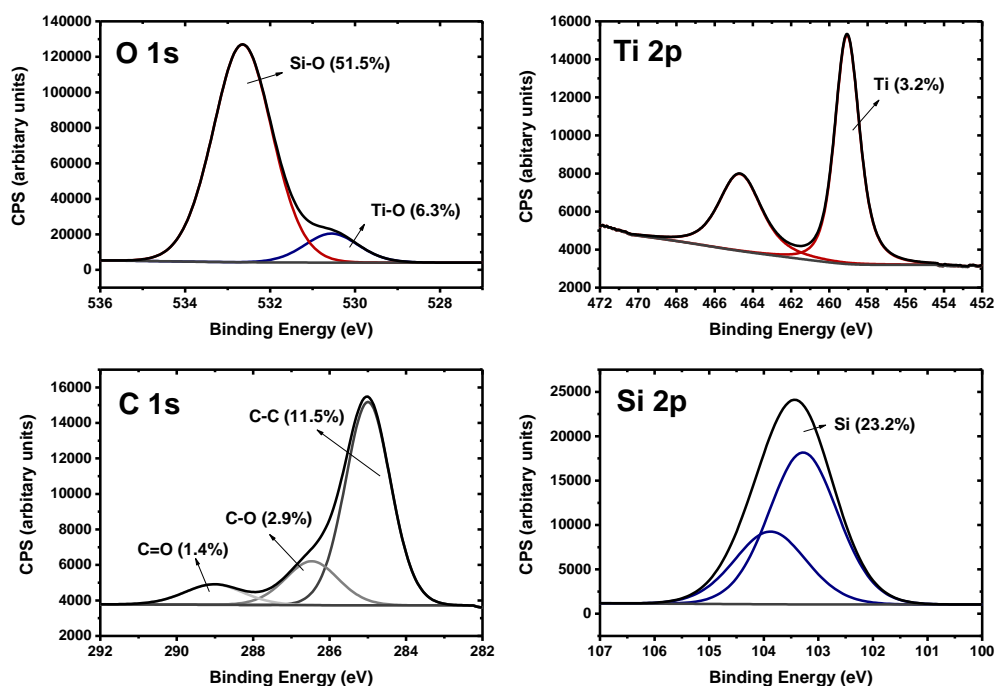


Figure 6.19: O 1s, Ti 2p_{3/2} and Ti 2p_{1/2}, C 1s and Si 2p_{3/2} and Si 2p_{1/2} peaks of the TiO₂-SiO₂ NC thin film measured by XPS (atomic percentages of the components in between brackets).

The first and most prominent one, at 285 eV, is usually assigned to C-C bonds of both adventitious elemental carbon and the solvent, while the second, at 286.0 eV, and the third, 288.5 eV, can be related to -C-O bonds and C=O bonds, respectively. Finally, the Si 2p_{3/2} peak has a binding energy of 103 eV, which is related to the fully

oxidized SiO₂ matrix [29]. Consequently, from the Ti2p and Si 2p signals, the estimated percentage on the surface of the NC for the TiO₂ NPs is at 12% and 88% for the SiO₂ matrix for the N=10 case.

To investigate the impact of the amount of the injected nanoparticles on the chemical composition, the same XPS experiments were conducted for films with various injection parameters (N) and for the same deposition duration (50 minutes). Therefore, in Table 6.3, the value of N is given as well as the concentration of elements in percentage. Carbon lies at rather low levels, even for the highest N value. In addition, for a higher N, the Ti 2p percentage increases and at the same time the Si 2p decreases as well.

Table 6.3: Concentration of elements for NC films with various injection parameters

N	concentration of elements (at%)			
	C 1s (%)	O 1s (%)	Ti 2p (%)	Si 2p (%)
1	5.5	65.8	0.02	28.6
2	6.2	65.8	0.13	27.8
5	5.5	66.1	0.46	28.0
10	15.9	57.8	3.1	23.1
30	7.8	64.8	6.1	21.3

From these percentages and using the Ti2p and Si 2p signals, the estimated percentage on the surface of the NC for the TiO₂ NPs and the SiO₂ matrix are plotted in stacked columns in Figure 6.20. The dependence of the NPs content on the amount of injected colloidal solution (N) is clear. For N=1 and 2 the amounts of TiO₂ NPs detected in the first 10 nm of the surface are rather low 0.1 and 0.5 mol% in TiO₂ accordingly whereas for N=30 (the highest value of N) it reaches 22 mol% in TiO₂.

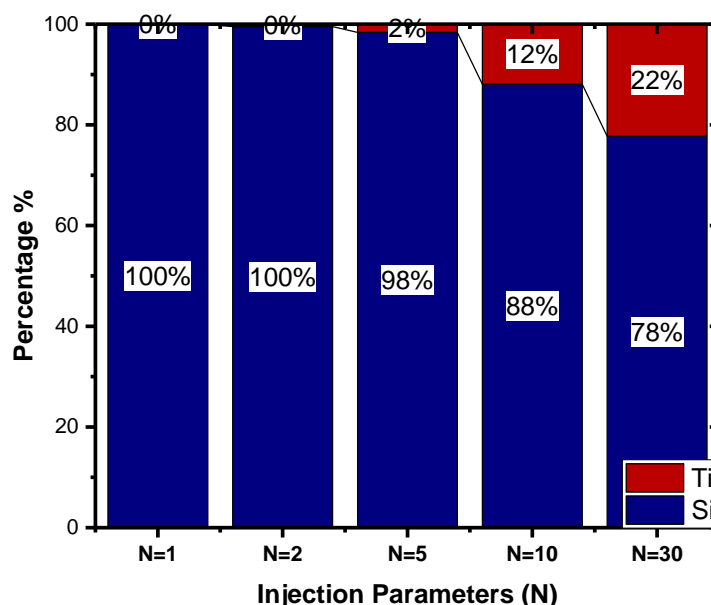


Figure 6.20: Stack column indicating the percentage between TiO₂ and SiO₂ in the NC for different injection parameters.

To further investigate this, in the next Section, the characterization of the NC thin films will be carried out using Ellipsometry. This way, a larger area of the film will be probed and along the volume of the NC film.

6.5 Characterization of the NCs using Ellipsometry

Based on the results obtained in Section 6.2 regarding the quality of the SiO₂ matrix and the distribution of the NPs in the latter from Section 6.3, we can now examine the growth of the NC thin film. Initially, this will be accomplished by the evaluation of the Is and Ic trajectory plots and their dynamic evolution. Subsequently, using information already obtained regarding the matrix and the NPs, we will use the appropriate model to finally investigate the optical and morphological characteristics of the produced films.

6.5.1 *In situ* monitoring of the NCs' growth

As the first step of this study, the Is/Ic trajectory plots for two different wavelengths, 450 nm and 633 nm are given in Figure 6.21. The plots involving NCs with varying N injection parameter correspond to the growth of approximately the first 50 nm thickness as well as the pure SiO₂ matrix studied in Section 6.2.1. In addition, for comparison, the plots of pure PECVD TiO₂ and mixed oxide Ti_{0.5}Si_{0.5}O₂, 50nm thick films are given. All the standard PECVD made films are plotted with dashed lines. The N=2 film, incorporating a significantly low amount of TiO₂ NPs (measured by XPS and expected due to the low mass injection rate), lies very close to the trajectory plot of the pure SiO₂ matrix (dotted dark blue line). As the value of N increases, the plot shifts towards the one of the pure TiO₂ PECVD (dotted red line) film. In addition to this, the trajectories of N=20 (pink) and N=30 (light blue) that are the trajectories with the highest amount of TiO₂ NPs with this approach, are closer to the PECVD mixed oxide Ti_{0.5}Si_{0.5}O₂ (purple dotted line).

On a close inspection of the traces (inset in Figure 6.21b), due to the injection of the colloidal solution, a non-continuous growth appears on the trajectory plots. This was previously reported for injection of colloidal solution in the O₂ plasma in Chapter 5 and upon solvent injection in the O₂/HMDSO plasma in Section 6.2.2.

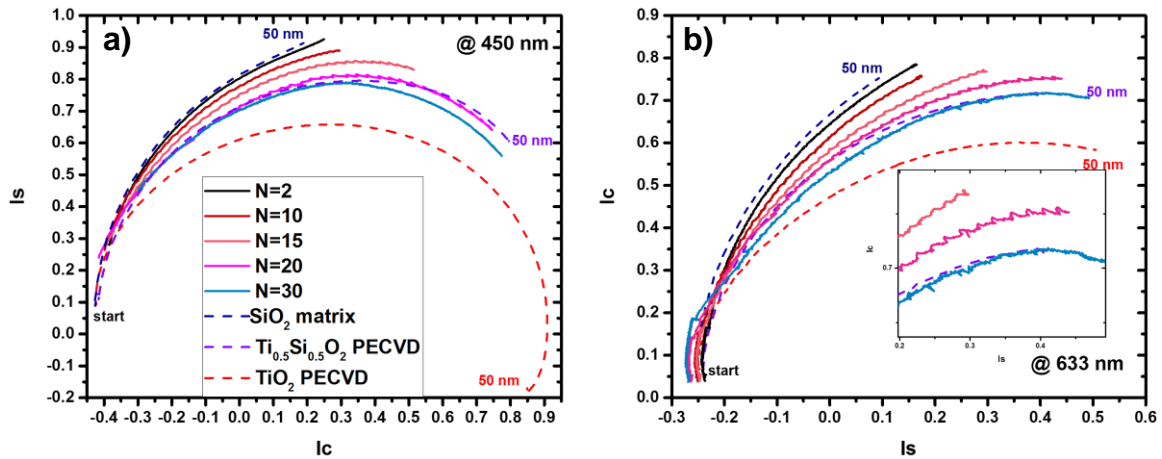


Figure 6.21: Trajectory (I_s , I_c) plots at a) 450 nm and b) 633 nm of the NC films deposited under different injection parameters (N) and compared with SiO₂ PECVD made matrix, the mixed oxide Ti_{0.5}Si_{0.5}O₂ and the TiO₂ PECVD made film.

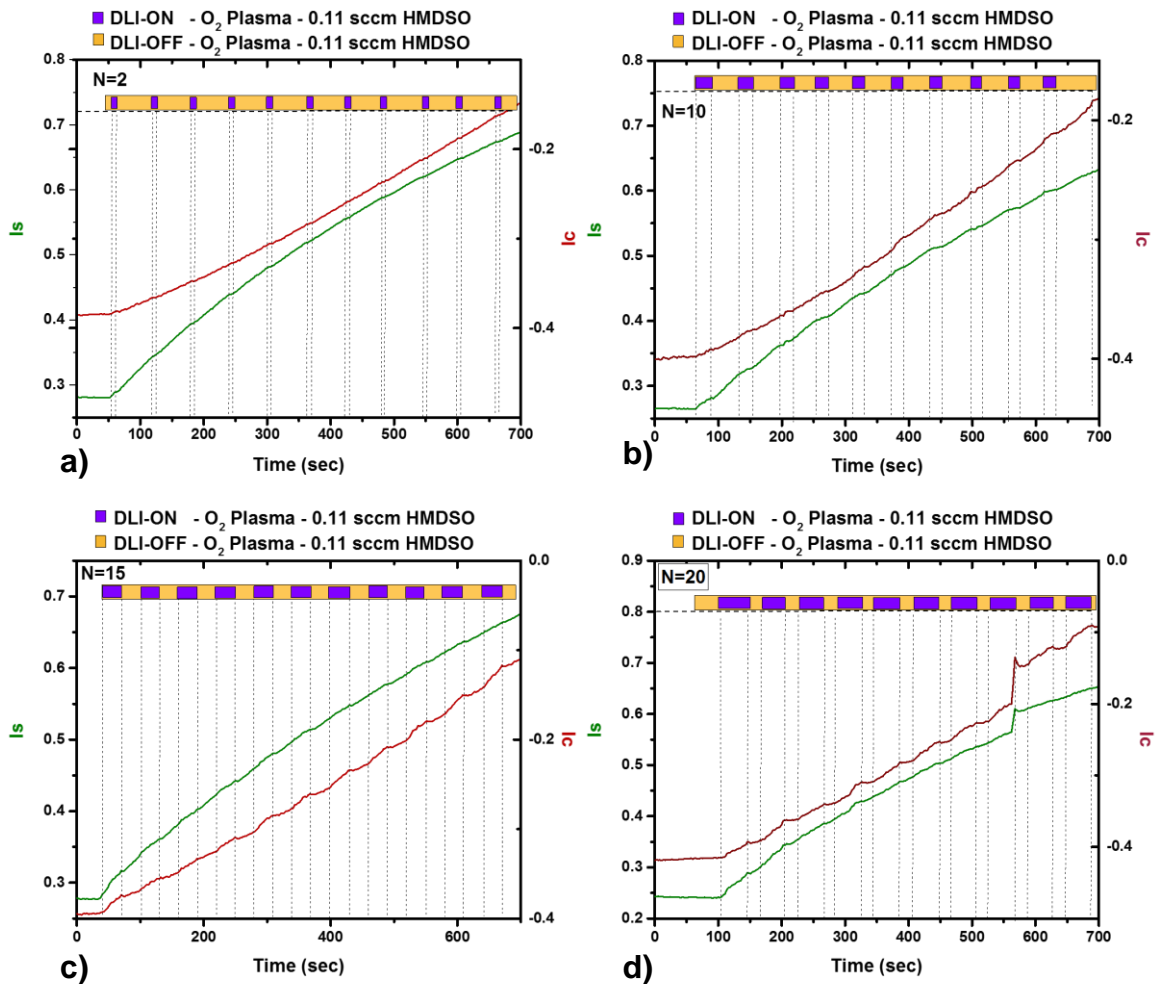


Figure 6.22: The dynamic in situ I_s , I_c parameters at 450 nm measured during the first 10 minutes of the liquid injection with a) $N=2$, b) $N=10$, c) $N=15$ and d) $N=20$. Each minute corresponds to one sequence. In the top bar, with purple is signaled the Injection ON and with orange the injection OFF part.

Therefore, to evaluate this growth we conducted the dynamic study monitoring the *I_s* and *I_c* curves for the 10 first minutes of the growth. This dynamic study is provided in Figure 6.22. Despite the non-continuous character observed in the trajectory plots of Figure 6.22, from the dynamic curves, the two different zones of the sequence (DLI-ON and DLI-OFF) are not easily distinguished. This phenomenon is a result of the opposite behaviors observed between the NPs injection in an O₂ plasma and the solvent injection in the O₂/HMDSO one. Zooming in, in the Figure 6.22b, and plotting it in Figure 6.23, we could discriminate better these two zones that exhibit two different slopes. During the DLI-ON time mainly the NPs are deposited as due to the elevated pressure the HMDSO vapor dissociation is not so efficient (a small amount of SiO₂ growth exists as well) whereas during the DLI-OFF the SiO₂ matrix is deposited. Hence, in Figure 6.22, gradually for higher N the growth of the TiO₂ NPs is more prominent than the one of SiO₂.

Generally, from this dynamic study, it appears that for all cases of Figure 6.22 the total evolution of the *I_s* and *I_c* curves is similar for the first 10 minutes of the growth. In addition, we have seen in Figure 6.23, that the slopes are different for the DLI-ON and DLI-OFF zones. Hence; these findings indicate that this alternating mode of deposition is a complementary one. This means that as the N increases, the amount of the TiO₂ NPs increases and the amount of the SiO₂ decreases leading possibly to an average similar deposition rate for all the cases with different composition.

These general trends, based on the dynamic ellipsometric data will be further investigated and ascertained in the next Section, using spectroscopic ellipsometry.

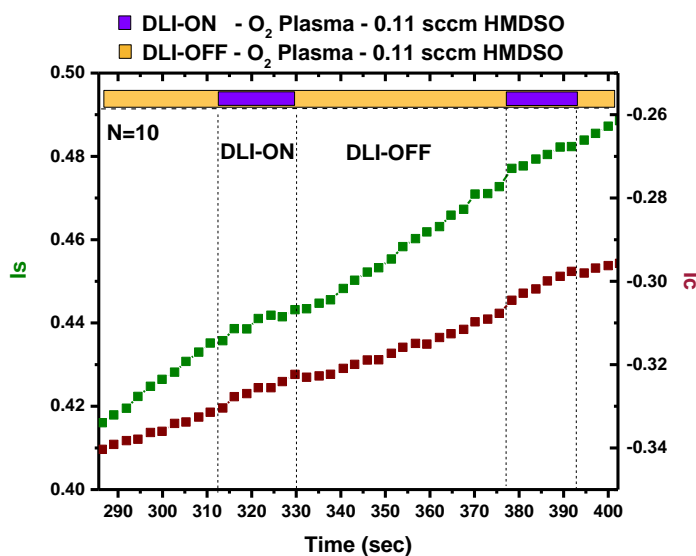


Figure 6.23: Dynamic in situ *I_s*, *I_c* parameters at 450 nm measured during the first 10 minutes of the liquid injection with N=10 focused on one injection cycle. In the top bar, with purple is signaled the Injection ON and with orange the injection OFF part.

6.5.2 Optical and physical characteristics using Bruggeman Effective Medium Approximation (BEMA) Model

To extract the structural and optical information from these data, the samples are modeled as homogenous layers on silicon substrate, without any top-layer roughness. Due to heterogeneities observed at low magnification in the Section 6.3, a more pronounced diffusion of the incident light was observed (in the measurement) at shorter wavelengths. Hence, the fitting was carried out in the limited range of 550 - 1000 nm (instead of 240 to 1000 nm). The validity of the model and therefore the evaluation of the accuracy of the fit was estimated by the Mean Square Error MSE factor. [30]

Initially, assuming the ellipsometry is not sensitive enough to detect the nanocomposite nature of the sample, the first ellipsometric model used, was based on a one phase material with Tauc-Lorentz dispersion law as shown in Figure 6.24a.[30] In this Figure, the experimental and simulated data show discrepancies, providing a high value of the error value (MSE=22). Therefore, a two-phase material (SiO₂ and TiO₂) was set up to account for the ellipsometric data of the NC. Based on the cross section results obtained with TEM (Fig. 6.14, Section 6.3), the Bruggeman Effective Medium Approximation (BEMA) shown in Figure 6.24b was used, to model the TiO₂ distributed NPs in the SiO₂ matrix.

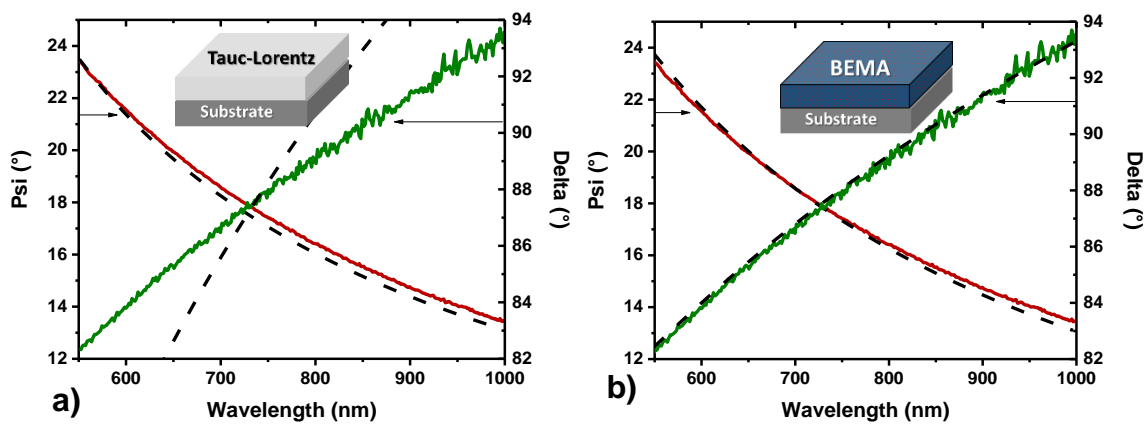


Figure 6.24: Psi (red) and Delta (green) results of the measured (continuous) and modeled (dashed) data with ellipsometry, based on Tauc-Lorentz model (a) and (b) on the Bruggeman Effective Medium (BEMA) model.

The model used to fit the ellipsometry data of the silica matrix was the one of Section 6.2.1 using the Cauchy dispersion law which significantly resembles the one of the classical thermal SiO₂ material, as expressed by Herzinger et al. [14]. For the TiO₂ NPs, the Tauc-Lorentz dispersion law was used based on a spin coated 50 nm TiO₂ NPs film studied thoroughly in Chapter 3. The fit using the second model, resulted in an improved error (MSE=4). From the BEMA, the fraction of TiO₂ NPs in the film could be deduced reaching 19 vol% and 81 vol% of SiO₂ for the N=10 case. This observation, confirms the XPS results (Section 6.4), where no mixed (Ti-O-Si)

bonding was observed. The results for all the NCs (with varying N) extracted using the Bruggeman Effective Medium Approximation (BEMA) at the end of the deposition are given in Table 6.4.

Table 6.4: NCs characteristics with varying injection parameter

N	Pressure (mTorr)		Thickness (nm)	Dep.Rate Total (nm/min)	MSE (550-100 nm)
	PULSE	NO PULSE			
2	14	3	50	1.7	1
10	20	3	46	1.4	4
15	20	3	49	1.5	5
20	20	3	56	1.6	19
30 (max)	20	16	51	1.4	23

From this Table 6.4, some differences are observed if compared with the data of the Table 6.1, where the matrix was deposited only with the solvents under the iterative mode of injection. First, the pressure (read on the go from the gauge) is increased slightly more than what is given in Table 6.1 when the PULSE is applied and liquid is introduced, possibly due to the existence of the NPs as well. As a reminder, column PULSE corresponds to the time when colloidal solution is injected and as long as there is no injection, the pressure decreases, the value of which is given in the NO PULSE column of Table 6.4. Moreover, for all the cases apart the N=30, when the pulsing stops (DLI-ON is over) the pressure reaches a steady state within approximately 2 seconds. The MSE has significantly lower values than the ones obtained for the matrices only, and this is linked to the wavelength range of the fit. Most discrepancies between the measured and simulated data, even for the silica matrix without any solvent injection in Section 6.2.1, were found between 300-450 nm wavelengths. Here, these wavelengths are excluded as stated above leading therefore in an improvement of the fit and the MSE. Moreover, comparing the MSE values of this Table we observe that for higher N, a higher MSE is attained. This can be linked with the higher injected colloidal solution, resulting in a higher filling of the matrix with NPs, which finally induces inhomogeneities possibly favoring scattering effects.

In the BEMA model used for the spectroscopic ellipsometry, as stated in the previous paragraph, the Cauchy dispersion law from Section 6.2.1 was used for the SiO₂ NPs and the Tauc-Lorentz describing the spin coated TiO₂ NPs of Chapter 3. In Chapter 3, we had indicated that the NPs are not degraded severely from the ICP O₂ plasma, but that their nanocrystallite size slightly increases. This was based on several characterization techniques with the most prominent being a shift observed on the Eg band using Raman and the slight decrease in the Eg parameter on the Tauc Lorentz material. In Chapter 5, during the injection of the TiO₂ NPs only, no shift was observed on the Raman spectra. The same trend appeared in Figure 6.14 where once more the Eg band lied at 154 cm⁻¹. Despite this fact, in the Tauc-Lorentz model used in the

BEMA, the E_g parameter was set free and its values for all the N remained almost unchanged.

From these results, the absorption coefficient (α) was extracted (Ellipsometry CompleteEASE Software) and the Tauc plots were created, which are given in Figure 6.25. A Tauc plot is a method to determine the optical band gap in semiconductors. In this figure, both cases of a direct and an indirect bandgap are given. As seen in Figure 6.25, in the x-axis of the figures the photon energy ($h\nu$) is given whereas in y-axis the $(\alpha h\nu)^{1/n}$. The value of the exponent n denotes the nature of the transition with $\frac{1}{2}$ for the direct allowed transitions (Figure 2.25a) and 2 for the indirect allowed (Figure 2.25b) ones. Extrapolating in both cases the linear region from this curve can lead to the extraction of the optical band gap, as seen in Figure 6.25 with dotted lines. From these plots we see that the bandgap obtained by the indirect transition lies closer to the one expected and verifies the indirect nature of the gap of the TiO₂ anatase materials from literature.[31] In addition to this, from these Tauc plots, it appears that the TiO₂ NPs do not reveal an alteration to their optical bandgap for different N injection parameter and that as expected they have a slightly higher bandgap than the bulk TiO₂.

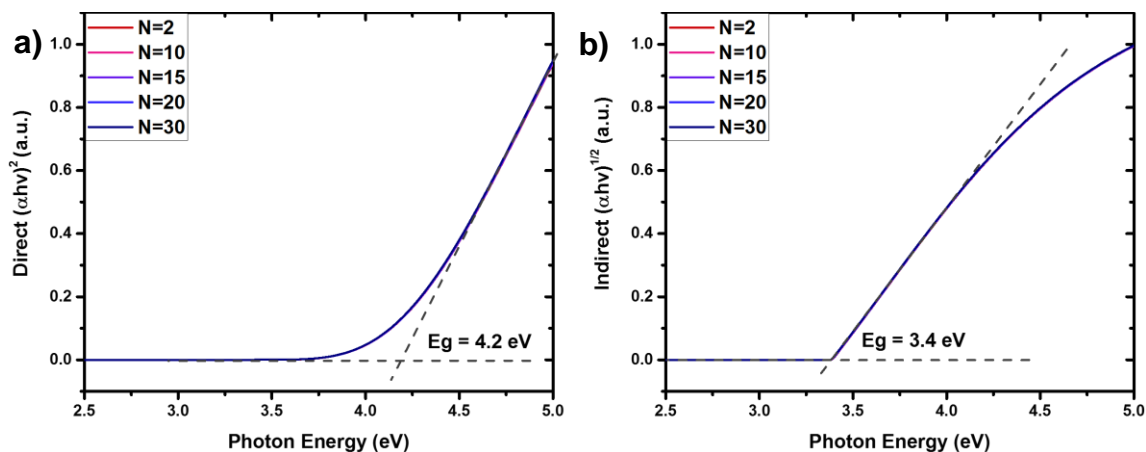


Figure 6.25: Tauc plots for all the injection parameters (N) used for the deposition of the NC thin films, for the determination of the a) direct and b) indirect optical band gap.

Subsequently, the volume fractions of the TiO₂ NPs distributed in the SiO₂ matrix and the effective refractive index of the NC based on the Bruggeman Effective Medium Approximation (BEMA) are plotted Figure 6.26a for varying injection parameter (N). The fraction of NPs for $N=1$ has a value of 2.5 vol%, an effective refractive index at 1.48 and it can reach up to 58 vol% for $N=30$, having an effective refractive index of 1.78. Hence, an almost linear dependency of both the NC composition and the refractive index on the injection parameter N . In addition to this, in Figure 6.26b, the same data are plotted but this time to better correlate the NC composition with the refractive index of the film.

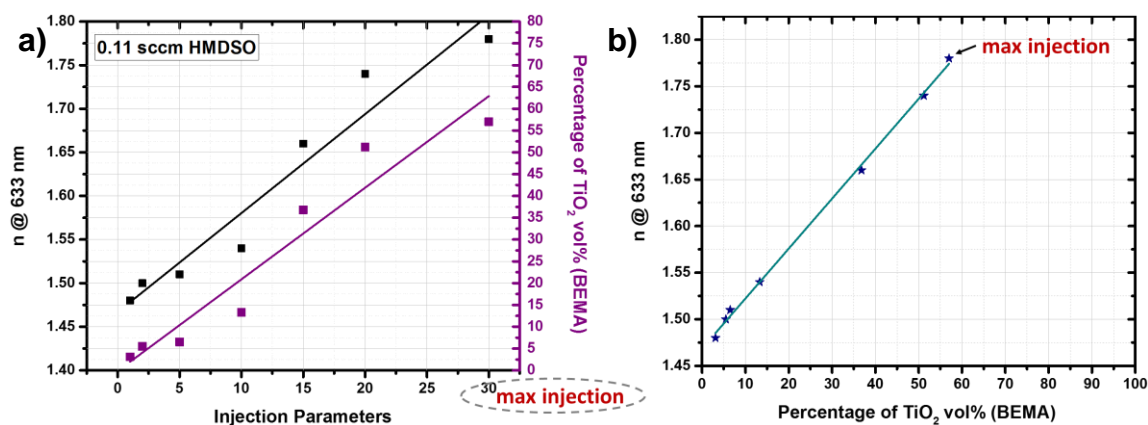


Figure 6.26: a) Effective refractive index at 633 nm and percentage of TiO₂ NPs extracted from the Bruggeman Effective Medium Approximation (BEMA) for varying injection parameter (N). Lines are used for guidance. b) Effective refractive index as a function of the volume TiO₂ percentage in the matrix.

From these results, we observe an accurate control of the NC composition and effective optical index through the deposition conditions. In addition to this, a very good trend of linear increase of the index with the TiO₂ content is observed from 1.47 the silica index to 2.00 if we consider the extrapolation of the linear relationship up to 100 vol% and titania only. It's worth noting that the extrapolated n index slightly differs from the expected one for bulk anatase but is still higher than the index found for the NPs plasma treated (chapter 3). Actually, for a 20 minutes plasma treatment on a spin coated TiO₂ NPs deposited film, the optical index at 633 nm was equal 1.65. The mineralization of the NPs by plasma during their transport towards the substrate *i.e.* in volume seems far more efficient than when the particles are arranged as thin films. Consequently, we could conclude that with this approach we are capable to improve the optical quality of the TiO₂ NPs, together with to tune and control the properties of the NCs in which they are dispersed.

6.5.3 Following the growth and composition of a deposited layer within a one-minute sequence

Studying the dynamic Is and Ic curves for the first ten minutes of the injection in Chapter 5, indicated that the growth of the film due to the TiO₂ NPs injection occurs mainly during the DLI-ON time and then during the DLI-OFF only O₂ plasma exists, mineralizing possibly the deposited layer. In contrary, the same curves for the deposition of the matrix during the injection of colloidal solution indicate that the growth mainly occurs during the DLI-OFF time where only O₂/HMDSO plasma takes place. As small growth of the SiO₂ matrix is observed during the DLI-ON time as well, although during this time the increase in pressure significantly affects the efficient dissociation of the HMDSO vapor molecule in the plasma volume. Furthermore, in Section 6.5.1 once again from the Is and Ic curves we could observe the two different

zones, one referring to the NPs deposition and one to the SiO₂ matrix. Hence, one could consider that this approach of deposition is an alternating one.

To validate this assumption, using the model proposed in Section 6.5.2 we conducted the following experiment, of evaluating the growth and the NPs percentage identified during the DLI-ON period and during the DLI-OFF one, within one-minute sequence. The data with N=20 was used, as we could clearly identify the two zones. The dynamic fit was carried out at a timeframe where a significant amount of layer was already grown. In this case, based on the BEMA model of Section 6.5.2 (consisting of TiO₂ NPs with Tauc-Lorentz and the SiO₂ matrix with the Cauchy dispersion law) we initially consider the layer after 29 minutes of deposition whose thickness was fitted to 47 nm thickness with 49 vol% of TiO₂ NPs. Then, to follow the growth within the next minute (next sequence), the 47 nm thick layer was considered known and all its parameters were fixed and a new very thin layer was accounted for, on top, by the BEMA model. On this new thin layer, the fraction between the TiO₂ and SiO₂ was set free as well as the thickness.

A schematic illustration of this model is given in Figure 6.27a. In this figure, the results of the fit are also given within this one-minute sequence, including the volume percentage in TiO₂ NPs (left hand side axis), the Thickness (blue symbols and right hand side axis) and the MSE (red symbols and right hand side axis) as a function of time. Light purple background color corresponds to the 40 seconds (N=20*2sec) of DLI-ON time and light yellow color corresponds to the 20 seconds of DLI-OFF time. In addition to this, in Figure 27b, the results of the fit are given within four-minute sequence, including once again the volume percentage in TiO₂ NPs, the thickness and the MSE (red symbols and right-hand side axis) as a function of time. In the figure, the schematic illustration of the model used is also given.

Regarding the figure with the one sequence (Fig 6.27a), during the DLI-ON a variation in the TiO₂ NPs amount is detected, having up to 78 vol% NPs and a growth up to 1.5 nm. As a result, during this time the prominent deposition is the one of the TiO₂ NPs having as well a small SiO₂ matrix growth. In addition, during the DLI-OFF as expected only some SiO₂ growth exists, going from 1.5 to 2.1 nm.

Having four sequences could be more reliable as the thin top layer reaches only a few nanometers in thickness during the first sequence. Observing more than one, (four in this case) leads to a thickness of 6 nm as seen in Figure 26b, resulting in a better overall view of the alternating deposition. Therefore, during the first sequence as already seen and during the DLI-ON the TiO₂ percentage reaches up to 78% whereas during the following sequences this percentage reaches values of approximately 70%. During the DLI-OFF, and as the SiO₂ matrix mainly grows, as expected the NPs percentage decreases to lower values of approximately 30-40%. The result obtained by this approach, fitting more than one sequence indicates that after the second or third sequence a more stable profile of the growth is seen.

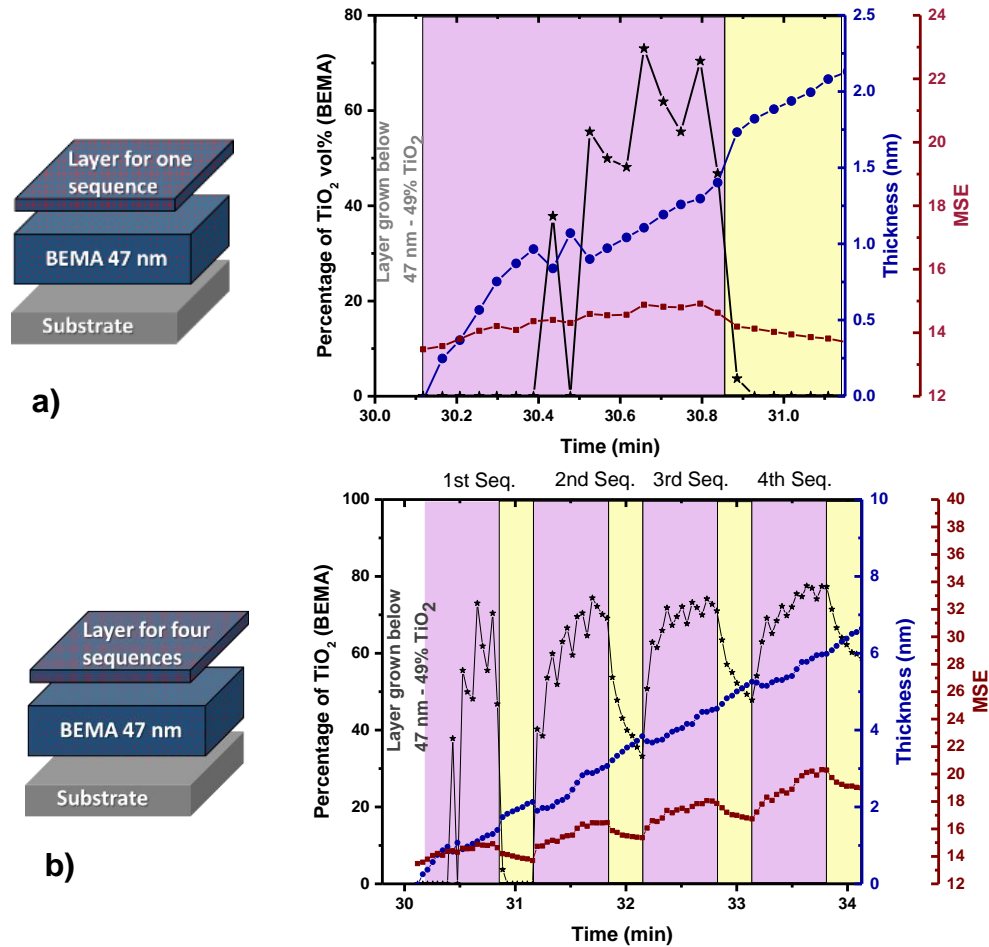


Figure 6.27: a1) Schematic illustration of the fitting approach used to investigate the deposition pattern in one sequence with N=20 on 47 nm film. a2) The results obtained for the TiO₂ NPs percentage, the layer thickness and the MSE in the one-minute sequence. b1) Schematic illustration of the fitting approach used to investigate the deposition pattern in four sequence. b2) The results obtained for the TiO₂ NPs percentage, the layer thickness and the MSE in the four-minute sequence. Light purple corresponds to the DLI-ON time whereas light yellow to the DLI-OFF time.

As a conclusion, this experiment allowed us to verify that this approach induces an alternating profile with mainly deposition of TiO₂ NPs and inhibition of Silica growth due to the increase in pressure (during DLI-ON) followed by the deposition of the silica matrix (during DLI-OFF) in each sequence. It also indicates that the 50% final composition of TiO₂ NPs for this case as given in Figure 6.26, is an average coming from the DLI-ON and DLI-OFF of the total injection cycles.

6.6 Discussion

6.6.1 Estimation of the amount of NPs distribution in the matrix through the characterization techniques

From the structural characterizations, we demonstrate the capability to produce nanocomposite thin films through this hybrid process. In order to compare the content in NPs measured by SEM and ellipsometry, the atomic percentage in TiO₂ has to be converted as a volume one.

$$\%vol_{TiO_2} = \frac{V_{TiO_2}}{V_{NC}} = \frac{n_{TiO_2} \times M_{TiO_2}/d_{TiO_2}}{n_{NC} \times M_{NC}/d_{NC}} = \%at_{TiO_2} \frac{M_{TiO_2}/d_{TiO_2}}{M_{NC}/d_{NC}}$$

where V_{TiO_2} and V_{NC} are the volume and n_{TiO_2} , M_{TiO_2} , d_{TiO_2} and n_{NC} , M_{NC} , d_{NC} are the number of mole, molar mass and density of TiO₂ and nanocomposite, respectively. First, we need to take into consideration that the formula of the NPs is not rigorously TiO₂, because the shell of the NPs is composed of hydroxyl and solvent molecules grafted to the TiO₂ core. Hence, the molar mass was estimated from previous work[12] to be 90 g mol⁻¹. This value takes into account the hydroxide shell surrounding the NPs only, meaning that this is a lower limit. The density was assessed, by weighting a 50 nm thick spin-coated NPs film, to be 3.3 g cm⁻³ (*i.e.* 83 % of the anatase density). The formula of NC can be written $\%at_{TiO_2} TiO_2 + \%at_{SiO_2} SiO_2$ and in the same manner the density was calculated by weighting a dedicated sample and reached 2.5 g cm⁻³ and the molar mass was found to be 64.5 g mol⁻¹ (molar mass for TiO₂ NPs equal 90 g mol⁻¹). Thus, the volume percentage corresponding to 15 at% was estimated to reach 16%. The content in NPs is quite coherent between SEM and ellipsometry, with a volume percentage of 16% and 19%, respectively, for the N=10 case. The difference can be related to the lateral dimensions of the probed zone which is 2640 μm² and 25 mm², by SEM and ellipsometry, respectively. Ellipsometry gives a mean field view of the composition, numerous EDX analyses should lead to equivalent content. As mentioned above, it has to be noted that the molar mass of the NPs estimated takes into account the hydroxide shell surrounding the NPs only and is a lower value. Making an accurate measurement in the NCs is not possible but if the real value is higher due to the grafting of solvent molecule, the discrepancy between both percentages is expected to be reduced. The atomic percentages from XPS can be treated in the same manner leading to a slightly smaller volume percentage of 13 %, but it has to be noticed that if the lateral analyzed area is 700 × 300 μm² (comparable to EDX analysis) the probed depth, is limited to the very surface. This could be linked to the final step of the deposition process (at the end of the sequence, injection is OFF) during which only silica is deposited. Consequently, it could also explain the low roughness nanostructured surface obtained by AFM. As already known in Chapter 4, amorphous SiO₂ deposited by PECVD is (significantly) conformal, following the surface pattern on which it is being deposited.[32–36] Based on what has been

already found in TEM, an explanation for this nanostructuration could be that as the NPs are being deposited, the SiO₂ matrix is being attached on, leading to their dispersion. This mechanism could also be the reason for not having significant large agglomerates in the film.

In Section 6.1.2, it has been indicated that the mass rate of injection is 2.33 mg/injection. Hence, the total amount of the solution injected for the thick (224 nm) sample (N=10 for duration of 160 min) used to perform EDX can be estimated to 3.72 g. Using a density of 1.0 (density of the solution) and [TiO₂]=3.75.10⁻² mol/L in the diluted solution, the calculated amount of the TiO₂ injected as NPs is 1.4.10⁻⁴ mol (mass of injected solution / density x [TiO₂]). Second, in order to calculate how much of these NPs were incorporated in the NCs, we need to assess the amount of NCs deposited over an area of 13×13 cm² (~corresponding to the sample holder surface). Based on the thickness of NCs (N=10 prepared for EDX), its density and its molar mass used in the previous paragraph, the number of NCs mole is equal to 1.5.10⁻⁴ mol (thickness x surface x density / molar mass). Then knowing that the atomic percentage in TiO₂ in the NCs is 15 at%; the number of moles incorporated in the chosen volume is 2.2 10⁻⁵ mol. Hence, for the selected area, the ratio of NPs incorporated in the NCs film is 16 % of the total amount of NPs injected. This estimation of the process efficiency strongly depends on the area we take into account and probably represent a minimum value. In order to render the process more competitive, this efficiency would need to be more precisely measured by depositing on large areas and then to be improved, by limiting deposition on the vertical wall of the reactor, for instance.

6.6.2 Comparison with other studies

Our strategy involving simultaneous and direct liquid injection of colloidal solutions in a plasma successfully leads to limited agglomeration of the NPs in the nanocomposite and a control of their dispersion in the matrix, compared to processes operated at atmospheric pressure[37–41]. Especially on these works and based on the spay-casting theory[42], it has been identified that the evaporation of the droplets leads to the agglomeration of the NPs.[38] In an attempt to reduce this effect several works, using atmospheric pressure systems attempted a two-step process of first depositing the colloidal solution and then allowing the matrix deposition with plasma.[37,43]

Regarding low pressure systems, Vervaele et al. [10] using the direct liquid injection in a low pressure CVD system, clearly identified that the low flow rate (0.25 g/min) for the solution injection favors the dispersion of the nanoparticles whereas in higher rates (1 g/min) they coalesce shifting the mean size distribution towards higher values. This finding is important as in our case being able to vary the injection flow rate from 2.33 mg/min (for N=1) to 69 mg/min (for N=30) we remain in

favorable conditions for the dispersion of the NPs, thus demonstrating the rapidity of injection we could reach with the experimental set-up.

An important difference between low pressure and atmospheric systems affecting the creation of agglomerations, could be linked to the motion of solvent evaporation being molecular (for the low pressure) instead of diffusive. [11,44,45]

6.6.3 The outcome of this hybrid approach

Because of the overall good homogeneity of the film, we were able to retrieve the optical and dielectric properties by producing proper modelling of the ellipsometric signals (especially in the 550 to 1000 nm wavelength range). This feature qualifies the process as suitable for the preparation of nanocomposites, for optical applications, at these wavelengths. Despite the solvent injection, the obtained matrix proved to be of high quality as the fit with thermal silica parameters was significantly accurate. This could be a proof that the deposited matrix exhibits a strong inorganic character. By tuning the injection sequence from N=1 to N=30, we were able to modify both the percentage of the TiO₂ inside the SiO₂ matrix (Section 6.5.3) and the resulted refractive index, having the possibility to reach up to 58 vol% in TiO₂ content. To the best of our knowledge, these results are unique compared to the reported approaches. [11,37–40,46]

Due to our experimental choice, a downside of these liquid droplets as observed by the low magnification SEM-EDX images leads to coffee ring patterns for the TiO₂ NPs. Several works report the depiction of droplets due to the limited volatility of the injected solution[9,47] or the too large size (due to system limitations) of the produced droplets (for example in one work droplets were ranging from 5 to 200 μm[43]). Given that some of the produced droplets by the direct liquid injector do not have enough time to evaporate (low volatility of the solvent), the evaporation process happens at the surface of the film. However, this also appears as an advantage. Actually, the combination of low volatility of solvents, remarkable stability of the colloidal solution and condition of spraying in the reactor resulted in an efficient transport of the droplets containing the non-agglomerated NPs towards the substrate. The optimization of the injection sequence permitted to keep the NPs protected inside the liquid droplets almost until the substrate preventing them to aggregate during the interaction with the plasma species. Additionally, we infer that this allows us to prevent from some preferential reaction to the reactor wall and therefore to observe less loss of matter. Finally, one way to decrease the size of droplets would be to dilute the colloidal solution in a higher proportion than the tested one, with a very highly volatile solvent (alkanes for instance). The latter would be evaporated very fast at the exit of the injector allowing the less volatile solvent to form smaller droplets. A compromise would have to be found, in case of high dilution, to adjust the NPs content and to verify the stability of the solution. Moreover, another possibility would also be to change the injector orifice. In our choice, we had an orifice with 8 holes in view of

limiting any clogging upon injection the holes. With the experience attained from this work, we could consider the implementation of an injector orifice with 5 holes. Since we have identified that the temperature plays a key role in the vaporization process of the solvent, the experiments using a heating substrate holder or/and a heated reactor is to be implemented. Finally, bearing in mind that the pressure difference (between the reactor and the solvent container) is the driving force for the droplet production and velocity, pumping the solvent container in order to achieve lower pressure than the atmospheric could be an interesting improvement. That way could achieve lower velocity and provide more time to the droplets to evaporate before reaching the substrate.

In this Chapter some of the questions we had set at the beginning of this work are answered. We have successfully established a hybrid approach coupling the direct injection of colloidal solution and the plasma process for the creation of nanocomposites. In addition to this, despite the iterative injection of liquid, plasma characterization showed that plasma is indeed perturbed but does not switch off. After getting a first level of understanding of the mechanisms by combining calculations and systematic experimental approach in Chapter 5, here, both the matrix itself and the nanocomposites were evaluated. Finally, we showed that it is possible to control the NC properties through the control of the system parameters and revealing the potential of this approach to be an agile one.

Conclusion

In this present chapter, we reported for the first time the creation of TiO₂-SiO₂ NC thin film by injecting a colloidal solution in a low pressure O₂/HMDSO plasma. The iterative injection sequence was selected in a way to control the deposition rate of both the NPs and the matrix and in that way by adjusting the iterative injection control the properties (filling factor of the NPs) of the NC films. The pressure was maintained at 3 mTorr (with slight variations) allowing to maintain the plasma ignited (evidenced with OES) and leading to the deposition of good quality inorganic SiO₂ matrix, without any intentional heating. Experiments which involved the deposition of the SiO₂ matrix while injecting the solvent only *i.e.* without the NPs, proved to be of great importance for acquiring information regarding the high matrix quality and the material characteristics for ellipsometry use. The resemblance of the produced matrix (for all the cases) with the thermal silica material (based on ellipsometry) could be a proof of the inorganic nature of the silica matrix. Regarding the implementation of the NCs, the cross section of the film revealed a good distribution of the NPs along the depth. The amount of these 3 nm NPs, was evaluated by multiple characterization techniques and was estimated at 16 vol%, and 19 vol% for N=10 case. The surface composition revealed a lower value (13 vol%), which could be explained due to the coating effect of the SiO₂ matrix (during the last second of the sequence). Notably, not significant agglomeration of NPs was observed. Finally, adjusting the parameters of the injection

sequence (from N=2 to N=30), revealed the possibility to adjust the TiO₂ content of the NC leading to controlled optical properties. Thus, based on ellipsometry, the TiO₂ content was varied from 2.5 vol% to 58 vol% having an effective refractive index at 633 nm from 1.48 to 1.78. The process offers the possibility to adjust the latter in a wide range by managing the volume proportion of NPs in the matrix thanks to the linear relationship between both parameters. Potentially, an agile approach like this could give the freedom to tune and adjust the NCs properties by adjusting both the nature of the NPs and the matrix but also of the injection parameters reaching a large range of NPs content inside the matrix.

Bibliography

- [1] J.K. Nelson, ed., Dielectric polymer nanocomposites, Springer, New York, 2010.
- [2] S. Guldin, P. Kohn, M. Stefik, J. Song, G. Divitini, F. Ecarla, C. Ducati, U. Wiesner, U. Steiner, Self-Cleaning Antireflective Optical Coatings, *Nano Lett.* 13 (2013) 5329–5335. <https://doi.org/10.1021/nl402832u>.
- [3] S. Kermadi, N. Agoudjil, S. Sali, L. Zougar, M. Boumaour, L. Broch, A. En Naciri, F. Placido, Microstructure and optical dispersion characterization of nanocomposite sol-gel TiO₂-SiO₂ thin films with different compositions, *Spectrochim. Acta. A. Mol. Biomol. Spectrosc.* 145 (2015) 145–154. <https://doi.org/10.1016/j.saa.2015.02.110>.
- [4] C.A. Charitidis, P. Georgiou, M.A. Koklioti, A.-F. Trompeta, V. Markakis, Manufacturing nanomaterials: from research to industry, *Manuf. Rev.* 1 (2014) 11. <https://doi.org/10.1051/mfreview/2014009>.
- [5] S. Larouche, H. Szymanowski, J.E. Klemberg-Sapieha, L. Martinu, S.C. Gujrathi, Microstructure of plasma-deposited SiO₂/TiO₂ optical films, *J. Vac. Sci. Technol. Vac. Surf. Films.* 22 (2004) 1200–1207. <https://doi.org/10.1116/1.1763912>.
- [6] D. Li, S. Elisabeth, A. Granier, M. Carette, A. Goulet, J.-P. Landesman, Structural and Optical Properties of PECVD TiO₂-SiO₂ Mixed Oxide Films for Optical Applications: Structural and Optical Properties of PECVD TiO₂-SiO₂ ..., *Plasma Process. Polym.* 13 (2016) 918–928. <https://doi.org/10.1002/ppap.201600012>.
- [7] N. Nedfors, O. Tengstrand, A. Flink, A.M. Andersson, P. Eklund, L. Hultman, U. Jansson, Reactive sputtering of NbCx-based nanocomposite coatings: An up-scaling study, *Surf. Coat. Technol.* 253 (2014) 100–108. <https://doi.org/10.1016/j.surfcoat.2014.05.021>.
- [8] J. Profili, O. Lévasseur, A. Koronai, L. Stafford, N. Gherardi, Deposition of nanocomposite coatings on wood using cold discharges at atmospheric pressure, *Surf. Coat. Technol.* 309 (2017) 729–737. <https://doi.org/10.1016/j.surfcoat.2016.10.095>.
- [9] A.D. Ross, K.K. Gleason, The CVD of Nanocomposites Fabricated via Ultrasonic Atomization, *Chem. Vap. Depos.* 12 (2006) 225–230. <https://doi.org/10.1002/cvde.200506368>.
- [10] M. Vervaele, B. De Roo, O. Deschaume, M. Rajala, H. Guillon, M. Sousa, C. Bartic, C. Van Haesendonck, J.W. Seo, J.-P. Locquet, Development of a new direct liquid injection system for nanoparticle deposition by chemical vapor deposition using nanoparticle solutions, *Rev. Sci. Instrum.* 87 (2016) 025101. <https://doi.org/10.1063/1.4940937>.
- [11] D. Ogawa, I. Saraf, A. Sra, R. Timmons, M. Goeckner, L. Overzet, The direct injection of liquid droplets into low pressure plasmas, *J. Vac. Sci. Technol. Vac. Surf. Films.* 27 (2009) 342–351. <https://doi.org/10.1116/1.3081965>.
- [12] A. Karpinski, S. Berson, H. Terrisse, M. Mancini-Le Granvalet, S. Guillerez, L. Brohan, M. Richard-Plouet, Anatase colloidal solutions suitable for inkjet printing: Enhancing lifetime of hybrid organic solar cells, *Sol. Energy Mater. Sol. Cells.* 116 (2013) 27–33. <https://doi.org/10.1016/j.solmat.2013.04.006>.
- [13] M. El Kass, L. Brohan, N. Gautier, S. Béchu, C. David, N. Lemaitre, S. Berson, M. Richard-Plouet, TiO₂ Anatase Solutions for Electron Transporting Layers in Organic Photovoltaic Cells, *ChemPhysChem.* 18 (2017) 2390–2396. <https://doi.org/10.1002/cphc.201700306>.
- [14] C.M. Herzinger, B. Johs, W.A. McGahan, J.A. Woollam, W. Paulson, Ellipsometric determination of optical constants for silicon and thermally grown silicon dioxide via a multi-sample, multi-wavelength, multi-angle investigation, *J. Appl. Phys.* 83 (1998) 3323–3336. <https://doi.org/10.1063/1.367101>.
- [15] I.H. Malitson, Interspecimen Comparison of the Refractive Index of Fused Silica*,†, *J. Opt. Soc. Am.* 55 (1965) 1205–1209. <https://doi.org/10.1364/JOSA.55.001205>.
- [16] A. Bousquet, Dépôt de couches minces par plasma pulsé radiofréquence et basse pression en mélange hexaméthylsiloxane / oxygène, Thesis Manuscript, 2005.

- [17] R.A. Gottscho, V.M. Donnelly, Optical emission actinometry and spectral line shapes in rf glow discharges, *J. Appl. Phys.* 56 (1984) 245–250. <https://doi.org/10.1063/1.333954>.
- [18] A. Granier, D. Chéreau, K. Henda, R. Safari, P. Leprince, Validity of actinometry to monitor oxygen atom concentration in microwave discharges created by surface wave in O₂-N₂ mixtures, *J. Appl. Phys.* 75 (1994) 104–114. <https://doi.org/10.1063/1.355897>.
- [19] W.F. Zhang, Y.L. He, M.S. Zhang, Z. Yin, Q. Chen, Raman scattering study on anatase TiO₂ nanocrystals, *J. Phys. Appl. Phys.* 33 (2000) 912–916. <https://doi.org/10.1088/0022-3727/33/8/305>.
- [20] T. Ohsaka, F. Izumi, Y. Fujiki, Raman spectrum of anatase, TiO₂, *J. Raman Spectrosc.* 7 (1978) 321–324. <https://doi.org/10.1002/jrs.1250070606>.
- [21] W. Ma, Z. Lu, M. Zhang, Investigation of structural transformations in nanophase titanium dioxide by Raman spectroscopy, *Appl. Phys. Mater. Sci. Process.* 66 (1998) 621–627. <https://doi.org/10.1007/s003390050723>.
- [22] C. Pighini, D. Aymes, N. Millot, L. Saviot*, Low-frequency Raman characterization of size-controlled anatase TiO₂ nanopowders prepared by continuous hydrothermal syntheses, *J. Nanoparticle Res.* 9 (2007) 309–315. <https://doi.org/10.1007/s11051-005-9061-6>.
- [23] Y. Gao, X. Zhao, P. Yin, F. Gao, Size-Dependent Raman Shifts for nanocrystals, *Sci. Rep.* 6 (2016). <https://doi.org/10.1038/srep20539>.
- [24] A.G. Rolo, M.I. Vasilevskiy, Raman spectroscopy of optical phonons confined in semiconductor quantum dots and nanocrystals, *J. Raman Spectrosc.* 38 (2007) 618–633. <https://doi.org/10.1002/jrs.1746>.
- [25] R.D. Deegan, O. Bakajin, T.F. Dupont, G. Huber, S.R. Nagel, T.A. Witten, Capillary flow as the cause of ring stains from dried liquid drops, *Nature.* 389 (1997) 827–829. <https://doi.org/10.1038/39827>.
- [26] K.L. Maki, S. Kumar, Fast Evaporation of Spreading Droplets of Colloidal Suspensions, *Langmuir.* 27 (2011) 11347–11363. <https://doi.org/10.1021/la202088s>.
- [27] P.J. Yunker, T. Still, M.A. Lohr, A.G. Yodh, Suppression of the coffee-ring effect by shape-dependent capillary interactions, *Nature.* 476 (2011) 308–311. <https://doi.org/10.1038/nature10344>.
- [28] P. Ondračka, D. Nečas, M. Carette, S. Elisabeth, D. Holec, A. Granier, A. Goulet, L. Zajíčková, M. Richard-Plouet, Unravelling local environments in mixed TiO₂-SiO₂ thin films by XPS and ab initio calculations, *Appl. Surf. Sci.* 510 (2020) 145056. <https://doi.org/10.1016/j.apsusc.2019.145056>.
- [29] J.F. Moulder, W.F. Stickle, P.E. Sobol, K.D. Bomben, J. Chastain, R.C. King Jr., Physical Electronics, Incorporation, eds., *Handbook of X-ray photoelectron spectroscopy: a reference book of standard spectra for identification and interpretation of XPS data*, Physical Electronics, Eden Prairie, Minn., 1995.
- [30] D. Saha, R.S. Ajimsha, K. Rajiv, C. Mukherjee, M. Gupta, P. Misra, L.M. Kukreja, Spectroscopic ellipsometry characterization of amorphous and crystalline TiO₂ thin films grown by atomic layer deposition at different temperatures, *Appl. Surf. Sci.* 315 (2014) 116–123. <https://doi.org/10.1016/j.apsusc.2014.07.098>.
- [31] J. Zhang, P. Zhou, J. Liu, J. Yu, New understanding of the difference of photocatalytic activity among anatase, rutile and brookite TiO₂, *Phys Chem Chem Phys.* 16 (2014) 20382–20386. <https://doi.org/10.1039/C4CP02201G>.
- [32] G.B. Raupp, D.A. Levedakis, T.S. Cale, Conformality of SiO₂ films from tetraethoxysilane-sourced remote microwave plasma-enhanced chemical vapor deposition, *J. Vac. Sci. Technol. Vac. Surf. Films.* 13 (1995) 676–680. <https://doi.org/10.1116/1.579806>.
- [33] M. Park, H.K. Yu, J.G. Koo, J. Jang, K.S. Nam, High-quality conformal silicon oxide films prepared by multi-step sputtering PECVD and chemical mechanical polishing, *J. Electron. Mater.* 27 (1998) 1262–1267. <https://doi.org/10.1007/s11664-998-0080-9>.

- [34] I. Savin de Larclause, T. Paulmier, I. Enache, H. Caquineau, P. Raynaud, F. Massines, N. Gherardi, Conformity of Silica-like Thin Films Deposited by Atmospheric Pressure Townsend Discharge and Transport Mechanisms, *IEEE Trans. Plasma Sci.* 37 (2009) 970–978. <https://doi.org/10.1109/TPS.2009.2017023>.
- [35] N. Sobel, C. Hess, M. Lukas, A. Spende, B. Stühn, M.E. Toimil-Molares, C. Trautmann, Conformal SiO₂ coating of sub-100 nm diameter channels of polycarbonate etched ion-track channels by atomic layer deposition, *Beilstein J. Nanotechnol.* 6 (2015) 472–479. <https://doi.org/10.3762/bjnano.6.48>.
- [36] K. Arts, M. Utriainen, R.L. Puurunen, W.M.M. Kessels, H.C.M. Knoop, Film Conformality and Extracted Recombination Probabilities of O Atoms during Plasma-Assisted Atomic Layer Deposition of SiO₂, TiO₂, Al₂O₃, and HfO₂, *J. Phys. Chem. C.* 123 (2019) 27030–27035. <https://doi.org/10.1021/acs.jpcc.9b08176>.
- [37] J. Profili, O. Levasseur, J.-B. Blaisot, A. Koronai, L. Stafford, N. Gherardi, Nebulization of Nanocolloidal Suspensions for the Growth of Nanocomposite Coatings in Dielectric Barrier Discharges: Nebulization of Nanocolloidal Suspensions..., *Plasma Process. Polym.* 13 (2016) 981–989. <https://doi.org/10.1002/ppap.201500223>.
- [38] J. Profili, O. Levasseur, N. Naudé, C. Chaneac, L. Stafford, N. Gherardi, Influence of the voltage waveform during nanocomposite layer deposition by aerosol-assisted atmospheric pressure Townsend discharge, *J. Appl. Phys.* 120 (2016) 053302. <https://doi.org/10.1063/1.4959994>.
- [39] P. Brunet, R. Rincón, J.-M. Martinez, Z. Matouk, F. Fanelli, M. Chaker, F. Massines, Control of composite thin film made in an Ar/isopropanol/TiO₂ nanoparticles dielectric barrier discharge by the excitation frequency, *Plasma Process. Polym.* (2017) n/a-n/a. <https://doi.org/10.1002/ppap.201700049>.
- [40] J. Profili, S. Dap, O. Levasseur, N. Naude, A. Belinger, L. Stafford, N. Gherardi, Interaction of atomized colloid with an ac electric field in a dielectric barrier discharge reactor used for deposition of nanocomposite coatings, *J. Phys. Appl. Phys.* 50 (2017) 075201. <https://doi.org/10.1088/1361-6463/aa515f>.
- [41] D.P. Denis, T. Barry, B. Gerry, Effect of Titanium Oxide Nanoparticle Incorporation into nm Thick Coatings Deposited Using an Atmospheric Pressure Plasma, *J. Nanosci. Nanotechnol.* 10 (2010) 2746–2752. <https://doi.org/10.1166/jnn.2010.1432>.
- [42] A.B.D. Nandiyanto, K. Okuyama, Progress in developing spray-drying methods for the production of controlled morphology particles: From the nanometer to submicrometer size ranges, *Adv. Powder Technol.* 22 (2011) 1–19. <https://doi.org/10.1016/j.apt.2010.09.011>.
- [43] R. Mauchauffé, M. Moreno-Couranjou, N.D. Boscher, A.-S. Duwez, P. Choquet, Liquid-Assisted Plasma-Enhanced Chemical Vapor Deposition of Catechol and Quinone-Functionalized Coatings: Insights into the Surface Chemistry and Morphology: Liquid-Assisted Plasma-Enhanced Chemical Vapor Deposition of Catechol..., *Plasma Process. Polym.* 13 (2016) 843–856. <https://doi.org/10.1002/ppap.201600002>.
- [44] P.C. Reist, *Aerosol science and technology*, 2. ed, McGraw Hill, New York, 1993.
- [45] W.C. Hinds, *Aerosol technology: properties, behavior, and measurement of airborne particles*, 2. ed, Wiley, New York, 1999.
- [46] N. De Vietro, A. Conte, A.L. Incoronato, M.A. Del Nobile, F. Fracassi, Aerosol-assisted low pressure plasma deposition of antimicrobial hybrid organic-inorganic Cu-composite thin films for food packaging applications, *Innov. Food Sci. Emerg. Technol.* 41 (2017) 130–134. <https://doi.org/10.1016/j.ifset.2017.02.010>.
- [47] M. Goeckner, D. Ogawa, I. Saraf, L. Overzet, Progress report: Direct injection of liquids into low-pressure plasmas, *J. Phys. Conf. Ser.* 162 (2009) 012014. <https://doi.org/10.1088/1742-6596/162/1/012014>.

General Conclusion & Perspectives

Due to the prosperous properties nanocomposites (NCs) can have, a great interest has been given in the processes for their preparation. Two of them are the main and well-established categories taking place in the liquid phase and in the gas phase. Aiming in having a versatile and safe-by-design process led to the much recent attempt of creating hybrid approaches coupling the gas and liquid phase ones. Based on these, the objective of this work was the creation of TiO₂-SiO₂ NCs thin films through a hybrid approach coupling chemically synthesized NPs with plasma process. This was attempted for the first time in such a low pressure (3 mTorr) using an O₂ Inductively Coupled Plasma (ICP) source compared to the literature. Through theoretical and experimental results, important questions were replied. Our work was separated in four experimental steps using initially conventional methods to deposit the TiO₂ NPs and the SiO₂ matrix, in order to assess for any modification of the NPs upon plasma treatment in O₂-only plasma and in O₂/hexamethydisiloxane plasma. Then the two next steps were dedicated to the implementation of the novel hybrid one where the lab-made colloidal solutions were directly injected in two low pressure plasmas.

Through the first experimental step, **in Chapter 3**, we investigated the impact of a low pressure O₂ plasma on thin films formed of spin-coated anatase TiO₂ nanoparticles (NPs) with a core shell configuration. Some modifications were observed on the NPs structure and two kinetics were identified during O₂ plasma processing. Based on the obtained results, it was proposed that, following the chemical etching of the hydroxyl and organic shell, the O₂ plasma treatment can induce the crystallization of an additional TiO₂ layer surrounding the initial TiO₂ core through the formation of O-Ti-O bonds. This mineralization was explained based on the relatively high temperature of TiO₂ nanoparticles provided by the energy balance between input energy fluxes and output energy fluxes. In the overall, we concluded that such low-pressure O₂ plasma treatments represent fast and efficient post-deposition tools for mineralizing and tailoring, with a degree of control, the optical properties and nano-crystallinity of the TiO₂ thin films. This study also allowed stating that the NPs prepared at low temperature are not degraded upon O₂-only plasma treatment.

Moreover, the second experimental step was detailed in **Chapter 4**, where multilayer (TiO₂-SiO₂) thin films were successfully elaborated through a two-step approach coupling wet processes such as spin coating (for TiO₂ NPs) and plasma deposition ones (for SiO₂) such as Plasma Enhanced Chemical Vapor Deposition (PECVD). Though a significant infiltration of SiO₂ (~30 %) inside the TiO₂ NPs was found, the interface between each layer was well defined. This infiltration provided a densification of the TiO₂ layer replacing the void with SiO₂ leading to an improvement of the optical constants. This infiltration may also act as a sticking interfacing between the SiO₂ layer and the TiO₂ NPs layer improving their adhesion. The size and morphology of the spin

coated NPs, did not appear significantly affected by the O₂/HMDSO Plasma. Moreover, the optical constants of each layer were identified and the alternation of high to low refractive index (1.74 – 1.76 for the “effective” TiO₂, 1.46 for SiO₂ at 633 nm) was verified for this specific film. The roughness of each layer was studied and the conformal behavior of the PECVD deposited SiO₂ on the nanostructured TiO₂ one, was evaluated. These structural and optical results were compared with pure PECVD-made multilayer thin films for which a grading of the index in the TiO₂ side until reaching the interface with the SiO₂ layer, is observed. A significant difference between these two approaches is that the multi-process one offers a clear alternating variation between low and high refractive index.

After these two steps were completed, and it was demonstrated that the preservation of the NPs under the O₂ ICP but also under the O₂/HMDSO plasma is retained, the experiments using the novel approach were initiated, in **Chapter 5**. This involved the direct injection of the TiO₂ NPs lab-made colloidal solution inside the low pressure O₂ plasma reactor. Due to the constrain linked to working at low pressure, the determining preliminary step was the choice of the most suitable injection system, without any gas carrier. Initially, the characterization of the process was conducted focusing on the injection system and the produced droplets. Subsequently, their transport inside the low-pressure system was studied leading to establish that the solvent evaporation is governed by molecular motion. Finally, the interactions of solution droplets with the low pressure O₂ plasma were unraveled leading to the production of misty plasma and using the appropriate equations based on energy balance for evaporating liquid droplets, we calculated the droplet temperature and accordingly the droplet lifetime, for different solvents of the colloidal solution. The droplet lifetime for the less volatile solvents of the colloidal solution (PG and PC), is much higher than for the rest of the studied solvents (water, ethanol and methanol) having a lifetime up to 15 seconds. The parameters decreasing even more this lifetime (below 1 second) were identified. Namely, these were the increased pressure (from 3 towards 25 mTorr) leading to an increased heating term provided by the O atom energy flux and the increased temperature of the walls. In general, this step was of great importance as it gave insight in the mechanisms affecting the evaporation process. This type of calculations allowed the improvement of both the system and the injected solution and led to estimations regarding the quality of the NPs deposition. Preliminary experiments were conducted indicating a pressure variation as the droplet molecules evaporate inside the low-pressure system and the oxidation process of the organic solvent was captured using Time Resolved Optical Emission Spectroscopy. From these experiments, the importance of the process optimization was clarified. Following a specific optimization strategy, we were able to improve in an important degree the deposition of the TiO₂ NPs. This was a crucial step for understanding the mechanisms affecting the NPs deposition and identifying operating modes of the injection system compatible with the SiO₂ matrix deposition.

When the optimum conditions for the injection and the deposition of the TiO₂ NPs were defined (dilution of the colloidal solution with methanol, elevation of the temperature, extension of the distance of the heated pipe connecting the injector to the

reactor and iterative mode of injection), we reported for the first time, in **Chapter 6**, the creation of TiO₂-SiO₂ nanocomposite thin film by injecting a lab-made colloidal solution in a low pressure (3 mTorr) O₂/HMDSO plasma. The iterative injection sequence was selected in a way to control the deposition rate of both the NPs and the matrix. Hence, by adjusting the iterative injection, the control of the properties such as the filling factor of the NC films was achieved. The pressure was maintained at 3 mTorr (with slight variations) allowing to maintain the plasma ignited (evidenced with OES) and leading to the deposition of good quality inorganic SiO₂ matrix. Experiments which involved the deposition of the SiO₂ matrix while injecting the solvent only *i.e.* without the NPs, proved to be of great importance for acquiring information regarding the high matrix quality and the material characteristics. *In situ* spectroscopic ellipsometry was used as a smart characterization technique to monitor the growth of NCs film. Finally, adjusting the parameters of the injection sequence revealed the possibility to tune the TiO₂ content of the NC leading to controlled optical properties. Thus, based on ellipsometry, the TiO₂ content was varied from 2.5 vol% to 58 vol% having an effective refractive index at 633 nm from 1.48 to 1.78.

In the overall, with this work, we established for the first time the direct injection of liquid droplets inside the 3 mTorr O₂ plasma, while maintaining the plasma ignited and its dissociative efficiency. In addition to low pressure, it is worth noting that the process operates at moderate temperature typically less than 120°C, potentially rendering it compatible with deposition on thermally sensitive substrate (like polymer for instance). This work, was a first attempt to understand the mechanisms driving the interactions between the evaporating droplets and the plasma, and a way to highlight this rather new chapter into the area of misty plasmas. As the efficiency of the plasma was not lost, it was possible for us to introduce from a different source than the liquid injection, the HMDSO vapor and attain a high-quality inorganic matrix. Significant agglomerations of the injected TiO₂ NPs were not evidenced. Thanks to the control of both the NPs deposition and matrix growth, the deposition rate was maintained in low level enough to produce ultra-thin NC films. Finally, thanks to the linear relationship between the injection parameters and the effective optical characteristics of the NCs, we could conclude saying that this is an agile process.

Since this work is the first approach of our group towards this direction, many perspectives could be proposed. Below they are gathered in three main categories namely understanding the mechanisms of interactions inside the plasma, the process and the produced nanocomposites.

Interactions

The better understanding of the interactions happening during this process is very important as it can provide useful information regarding the state of the plasma, the nanoparticles and the matrix. These could be: a) the interactions between nanoparticles

(within the droplet), b) the interactions between particles and plasma species during their transport to the substrate and c) the interaction of the plasma with the nanoparticles and the matrix during deposition d) the interaction with the surface of the substrate and growing NC film. Finally, it is important to investigate the chemical and electrical (plasma impedance) response of the plasma due to these interactions. In particular, in solution, the NPs exhibit a positive charge at their surface which prevents the NPs to settle down by maintaining repulsive interactions between them. The stability of the colloidal solution is a required statement for its injection but further studies are mandatory in order to understand how the charge of the NPs inside a droplet evolves (i) upon evaporation of the solvent in the reactor, (ii) upon interaction with the plasma and particularly the sheath and charged species till (iii) the total vaporization of the solution before reacting with the substrate or growing film.

Process

In this work, the optimization of the process for acquiring a homogeneous distribution of the NPs was an important part of our study. It did improve significantly our deposits. Since there is still some room for improvements, some modifications can be proposed. First, to decrease the droplet lifetime the solvent of the colloidal solution should be adjusted, as well as the temperature in which this process take place should be increased (heated substrate and heated walls). Managing the solvent evaporation just before the droplet reaches the surface would actually be the ideal situation. Hence, the compromise has to be found between the protection offered to the TiO₂ NPs by the low volatile solvent and its evaporation in order to limit the coffee ring effect we were still facing. Second, another parameter that could favor the droplet lifetime would be a system to reduce the pressure difference (driving force of the injection system) between the liquid and the reactor. This could lead to lower velocity, resulting in longer travel time for the droplets until they reaching the substrate. Consequently, they could have more time to evaporate before reaching the substrate. Here, it should be considered that for lower pressure difference the mean droplet size could be increased, as the force for the droplet production will be “softer”. Third, the orifice of the injector could be adjusted in order to provide less liquid droplets in each injection. Finally, from the results obtained from the theoretical study, the identification of the plasma parameters that could provide the most prominent heating terms could be achieved experimentally aiming in improving the evaporation rate of the liquid droplets.

Regarding the TiO₂-SiO₂ NPs, up to now the injection of HMDSO was maintained in a continuous mode during the simultaneous iterative injection of TiO₂ NPs. One could attempt to pulse the TiO₂ NPs and the HMDSO alternately, which could also offer new opportunities and more degrees of freedom.

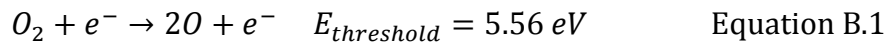
Nanocomposites

We have stated that this approach aims in the creation of a versatile process where the nature of both the NPs and the matrix could vary. Here, it was shown that through the injection parameters, the filling factor of the TiO₂ NPs can be varied. Spectroscopic ellipsometry modelling led to establish a linear correlation between the optical refractive index of the NC and its TiO₂ fraction, indicating the agile character of the process. Given that the size of the filler can induce different characteristics on the NC properties, the experiments using different NPs sizes could be proposed. Finally, the alteration of both the nature of the NPs and the matrix should be attempted, to prove the versatility of the system.

These first works open up a whole field of research and future prospects regarding the possibility to set-up NC thin films with tunable dielectric and optical properties, since the injection of the NPs and the deposition of the matrix can be managed with time, separately. Providing a deeper understanding of the mechanisms involved in this hybrid process coupling injection of lab-made solution and Plasma Enhanced Chemical Vapor Deposition, the production of thin films with dedicated specifications should be rendered accessible.

Annex B

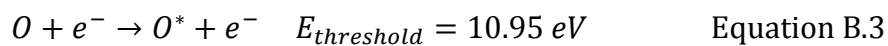
Previous studies by mass spectroscopy and actinometry have shown that in the specific conditions oxygen is weakly dissociated (5%). The neutral species included in this plasma, are the oxygen atoms (O) and the molecule of dioxygen (O₂). The O atom is created by dissociation of the O₂ and is lost by recombination after reacting with the reactor walls. Hence, the following equations exist: [1]



With coefficient k_p being dependant on the recombination coefficient γ of the O atoms on the walls.

In addition to this, the excited species that can be found in this O₂ plasma system are based on two principle reactions:

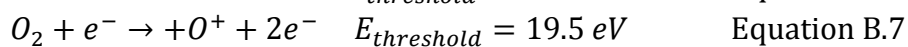
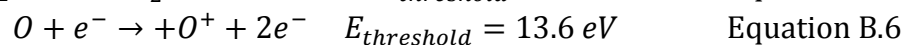
The direct excitation of the oxygen atom from its ground state



And the dissociative excitation of the O₂ molecule



Regarding the positive ions, two types are considered. The O₂⁺ and O⁺ with the O₂⁺ being considered the most dominant one. The reactions for this positive ion production are based on the direct ionization of the O atoms and the dissociative ionization of the O₂ molecule, and are listed below.



[1] A. Bousquet, Dépôt de couches minces par plasma pulsé radiofréquence et basse pression en mélange hexaméthylsiloxane / oxygène, Thesis Manuscript, 2005.

Annex C

Table C.1

Solvent	Molecule Diameter (10^{-10} m)	Molar Mass (g/mol)	Molar Volume (m^3/mol)	ρ (g/cm^3)
Water	2.75	18	18.05	0.997
Ethanol	4.4	46	58.4	0.789
Methanol	4.2	32	40.45	0.792
PG	5-7	76	73.17	1.040
PC	5-7	102	84.72	1.205

Table C.2

Solvent	T (K)	Po saturated vapor (Pa)	Hvap (kJ/mol)	Cp (J/gK)	σ (nN/m)
Water	273	611	43.99	4.20	71
	<i>Triple Point</i>				
Ethanol	150	$4.3 \cdot 10^{-4}$	42.41	2.40	22
	<i>Triple Point</i>				
Methanol	175	$1.86 \cdot 10^{-1}$	37.4	3.82	22.7
	<i>Triple Point</i>				
PG	298	0.13	76	1.79	34
PC	298	0.03	71.3	1.67	41

Annex D

Actinometry is a method of analysis using optical emission spectroscopy which allows one to determine the density of the species existing in the plasma in a ground state. This nondestructive technique is based on the proportionality between the emission intensities of the excited radicals and the concentration of these atoms in the ground state in the plasma. [1–3]

In the case of low pressure plasmas the conditions required to ensure the validity of actinometry can be summarized as follows:

1. The introduction of the actinometer (inert gas such as Ar) should not modify the discharge. The density of the actinometer must be known and constant.
2. The excited state of the actinometer from the ground state is created by electronic impact. As the actinometer is generally monoatomic, no dissociative excitation is possible. The excited state is created by the following reaction:

$$Ar + e^- \rightarrow Ar^* + e^-$$
 with the excitation coefficient $k_{exc}(Ar)$
3. The oxygen excited level O^* must be populated not by dissociative excitation of O_2 but by direct excitation of O , which means that $[O]$ must be high enough and/or the tail of the electron distribution function not too highly populated.

The theoretical expression of the actinometric signal I_O/I_{Ar} (corrected from the response of the optical system) takes into account the population of O^* by electron excitation of O (k_{exc}^O) and dissociative excitation of O_2 ($k_{diss}^{O_2}$) and is given by:

$$\frac{I_O}{I_{Ar}} = \frac{k_{exc}^O [O]}{k_{exc}^{Ar} [Ar]} + \frac{k_{diss}^{O_2} [O_2]}{k_{exc}^{Ar} [Ar]} \quad \text{Equation D.1}$$

This equation can be coupled to the mass conservation law between argon and oxygen atoms contained in the O_2/Ar feed, defined by η as follows:

$$\eta = \frac{[O_2]}{[Ar]} = \frac{2[O_2] + [O]}{2[Ar]} \quad \text{Equation D.2}$$

From (D.1) and (D.2), the following relation between the degree of oxygen dissociation and the actinometric signal can be deduced:

$$\frac{1}{\eta} \frac{I_O}{I_{Ar}} = \frac{k_{diss}^{O_2} [O_2]}{k_{exc}^{Ar} [Ar]} + a_d \left[2 \frac{k_{exc}^O}{k_{exc}^{Ar}} - \frac{k_{diss}^{O_2}}{k_{exc}^{Ar}} \right] \quad \text{Equation D.3}$$

This equation makes it possible to determine dissociation coefficient a_d as a function of the ratio of the intensities between O and Ar , with the condition of knowing exactly the values of the k coefficients.

The dissociation coefficient a_d is also defined as:

$$a_d = \frac{[O]}{[O] + 2[O_2]} \quad \text{Equation D.4}$$

and mass conversion law between argon and oxygen atoms contained in the O₂/Ar feed, defined by η as:

$$\eta = \left[\frac{[O_2]}{[Ar]} \right]_{feed} = \frac{\%Ar}{\%O_2} = \left[\frac{2[O_2] + [O]}{2[Ar]} \right]_{plasma} \quad \text{Equation D.5}$$

We also define the proportion of atomic oxygen as the ratio of [O] to the total concentration of neutral species in plasma (N). We have, by definition, the following equality

$$[O] + [O_2] + [Ar] = N \quad \text{Equation D.6}$$

N is directly related to the pressure in the reactor by the ideal gas relation $P = NkT$, with N the number of moles per unit of volume considering that the temperature of neutral species does not vary.

By combining equations (D.4), (D.5) and (D.6), we connect the rate of oxygen atoms and the dissociation coefficient to the molecule by the equation:

$$\frac{[O]}{N} = \left[\frac{2a_d}{a_d + (1 + \eta)} \right] \quad \text{Equation D.7}$$

Hence, we have established the equations which allow us to calculate a_d and [O]/N as a function of actinometric signal, provided that the spectral responses and the excitation coefficients of O, Ar and O₂ are known.

- [1] Granier A, Nicolazo F, Vallée C, Goulet A, Turban G and Grolleau B 1997 Diagnostics in helicon plasmas for deposition *Plasma Sources Sci. Technol.* **6** 147–56
- [2] Nicolazo F, Goulet A, Granier A, Vallee C, Turban G and Grolleau B 1998 Study of oxygen/TEOS plasmas and thin SiO_x films obtained in an helicon diffusion reactor *Surf. Coat. Technol.* **98** 1578–1583
- [3] Bousquet A 2005 *Dépôt de couches minces par plasma pulsé radiofréquence et basse pression en mélange hexaméthylsiloxane / oxygène* Thesis Manuscript (Nantes)

Scientific Production

Articles in international peer-review journals

1- Modification of the optical properties and nano-crystallinity of anatase TiO₂ nanoparticles thin film using low pressure O₂ plasma treatment, M. Mitronika, J. Profili, A. Goulet, Agnès Granier, L. Stafford, Mireille Richard-Plouet (accepted Thin Solid Films)

2- TiO₂-SiO₂ Nanocomposite thin films deposited by Direct Liquid Injection of colloidal solution in a O₂/HMDSO low pressure plasma, Maria Mitronika, Jacopo Profili, Antoine Goulet, Nicolas Gautier, Nicolas Stephant, Luc Stafford, Agnès Granier, Mireille Richard-Plouet, under revision in Journal of Physics D : Applied Physics

3- TiO₂-SiO₂ mixed oxide deposited by low pressure PECVD: insights on optical and nanoscale electrical properties, M. Mitronika, C. Villeneuve-Faure, L. Boudou, W. Ravisy, M.P. Besland, A. Goulet, M. Richard-Plouet, submitted in Applied Surface Science

Communications in Conferences

1- 16th International Conference on Plasma Surface Engineering, September 17 - 21, 2018, in Garmisch-Partenkirchen, Germany, Association of PECVD process and chemical synthesis for the development of TiO₂/SiO₂ nanocomposite material : a new approach. Authors: Maria Mitronika, Jacopo Profili, Antoine Goulet, Luc Stafford, Agnès Granier, Mireille Richard-Plouet (Oral Presentation)

2- 20th International Thematic Conference-School "Advanced Materials and Technologies", 27-31/8/2018, Palanga, Lithuania PECVD PROCESS AND CHEMICAL SYNTHESIS TO DESIGN TIO₂/ SIO₂ NANOCOMPOSITE THIN FILMS Authors: Maria Mitronika, Jacopo Profili, Antoine Goulet, Luc Stafford, Agnès Granier, Mireille Richard-Plouet (Poster & Awarded)

3- SFP 2019, Nantes Etude de l'effet de l'injection pulsée de nanoparticules de TiO₂ dans un plasma basse pression de O₂/HMDSO par diagnostics optiques et électriques résolus en temps Authors: Maria Mitronika, Jacopo Profili, Antoine Goulet, Agnès Granier, Mireille Richard-Plouet (Poster)

4- Plathinium 23-27/9/2020 Antibes, France A novel one-step approach for Nanocomposite Thin Films coupling PECVD and colloidal solutions (Oral Presentation) Authors: Maria Mitronika, Jacopo Profili, Antoine Goulet, Agnès Granier, Mireille Richard-Plouet

5- Plathinium 23-27/9/2020 Antibes, France Physicochemical modification of spin-coated TiO₂ nanoparticle thin film by ICP low pressure oxygen plasma (Poster) Authors: Maria Mitronika, Jacopo Profili, Antoine Goulet, Agnès Granier, Mireille Richard-Plouet

6- 17th International Conference on Plasma Surface Engineering 2020 Hybrid PECVD / direct liquid injection of a Colloidal Solution for SiO₂:TiO₂ nanocomposite thin film

deposition Authors : Maria Mitronika¹, Jacopo Profili², Antoine Gullet, Luc Stafford, Nicolas Gautier, Agnès Granier, Mireille Richard-Plouet (Oral Presentation- Applied)

7- 5th (14-16/5/2018) GDRI Nanomateriaux Multifonctionnels Contrôlés Meeting (Port Argeles, France 14-16/5/2018) Nanocomposite TiO₂/ SiO₂ thin films: A new approach by coupling PECVD process and chemical synthesis (Poster) Authors: Maria Mitronika, Jacopo Profili, Antoine Gullet, Agnès Granier, Mireille Richard-Plouet

8-6th GDRI Nanomateriaux Multifonctionnels Contrôlés Meeting (Quebec, Canada 22-24/5/2019) Analysis of nanocomposite TiO₂/ SiO₂ thin films modified by low pressure plasma processes (Oral Presentation) Authors: Maria Mitronika, Jacopo Profili, Antoine Gullet, Luc Stafford, Agnès Granier, Mireille Richard-Plouet

9- WinterSchool 2019, Chip Fab of the Future, Infineon Technologies Austria AG - Villach, Carinthia (Austria) (Oral Presentation) Authors: Maria Mitronika, Jacopo Profili, Antoine Gullet, Luc Stafford, Agnès Granier, Mireille Richard-Plouet

10- PSE Satellite, 10-11/2/2020, Prague Hybrid approach coupling Plasma Processes and injection of Colloidal Solutions for customized Nanocomposite thin films (Oral presentation) Authors: Maria Mitronika, Jacopo Profili, Antoine Gullet, Luc Stafford, Agnès Granier, Mireille Richard-Plouet

Other actions

1- Two oral presentations (15 minutes) regarding plasma for the Lycéens' visit, 22/02/2018

2-Fête de la Science October 2018

Titre : Dépôt de couches minces de $\text{TiO}_2 - \text{SiO}_2$ par association plasma et sol-gel : impact du procédé de dépôt et de la composition sur les propriétés, application à l'optique intégrée

Mots clés : nanocomposites, injection directe de liquide, PECVD, TiO_2 NPs, matrice SiO_2

Résumé : Ce travail décrit une approche hybride couplant le procédé de dépôt chimique en phase vapeur assistée par plasma (PECVD) avec l'injection d'une solution colloïdale fabriquée au laboratoire pour la synthèse de films inorganiques nanocomposites (NC) incluant des nanoparticules de TiO_2 (NPs) dans une matrice SiO_2 . Deux études préliminaires ont été réalisées en utilisant les deux méthodes classiques de dépôt : enduction centrifuge et PECVD. La première nous a permis de mieux comprendre les interactions des NPs de TiO_2 avec un plasma O_2 à basse pression (3m Torr) et la seconde d'élucider la nature de l'interface entre les NPs cristallines et la silice amorphe préparée par PECVD. Pour l'approche hybride en une étape, tout d'abord, l'optimisation de la procédure d'injection des NPs de TiO_2 dans un plasma O_2 basse pression a été mise en œuvre.

Il a été démontré par calcul et prouvé expérimentalement que les principaux paramètres prolongeant la durée de vie des gouttelettes de solution colloïdale (ce qui peut induire des hétérogénéités du film et une pollution dans le réacteur) sont la volatilité du solvant, la géométrie du système, les espèces de plasma et la température entourant les gouttelettes. Ensuite, les nanocomposites ont été préparés en injectant simultanément des NPs de TiO_2 dans le plasma O_2 -hexaméthylsiloxane (HMDSO) comme précurseur d'une matrice de silice inorganique. Dans l'ensemble, la structure anatase et la taille des NPs de TiO_2 sont conservées dans le film NC. En faisant varier les paramètres d'injection, il a été montré que, dans la matrice SiO_2 , qui est de bonne qualité optique, la teneur en NPs peut être réglée de 1 à 50% conduisant à des propriétés optiques ajustables.

Title : Deposition of $\text{TiO}_2 - \text{SiO}_2$ thin films by associating plasma and sol-gel: impact of the deposition process and the composition on the properties, application to integrated optics

Keywords : nanocomposites, direct liquid injection, PECVD, TiO_2 NPs, SiO_2 matrix

Abstract: With the present work we propose a hybrid approach coupling the Plasma Enhanced Chemical Vapor Deposition (PECVD) process with injection of lab-made colloidal solution for the synthesis of inorganic TiO_2 - SiO_2 nanocomposite (NC) films. Two preliminary studies were carried out using the conventional deposition methods: spin coating and PECVD. The first one allowed us to gain insights on the low O_2 plasma – NPs interactions and the second one on the nature of the interface between the crystalline NPs and the amorphous PECVD SiO_2 . For the one-step hybrid approach, first, the optimization of the injection procedure of TiO_2 NPs in an O_2 low-pressure plasma was implemented. It was shown computationally and

proven experimentally that the main parameters prolonging the lifetime of the solution droplets (causing heterogeneities in the film and pollution in the reactor) is the solvent volatility, the system geometry, the plasma species and the temperature surrounding the droplets. Second, the nanocomposites were prepared by simultaneously injecting TiO_2 NPs into the O_2 -hexamethylsiloxane (HMDSO) plasma leading to a inorganic silica matrix of optical quality. In the overall, both the anatase structure and the 3 nm size of the TiO_2 NPs were retained in the NC film. By varying the injection parameters, it was shown that the anatase NP content in the SiO_2 matrix can be tuned from 1 to 50% leading to adjustable optical properties.